Understanding of Weak Turbulence of Capillary Waves

by

Yulin Pan

Submitted to the Department of Mechanical Engineering
in partial fulfillment of the requirements for the degree of

Doctor of Philosophy in Mechanical Engineering

at the

MASSACHUSETTS INSTITUTE OF TECHNOLOGY

February 2017

Author . . . .
Department of Mechanical Engineering
November 15, 2016

Certified by . . . .
Dick K.P. Yue
Philip J. Solondz Professor of Engineering
Professor of Mechanical and Ocean Engineering
Thesis Supervisor

Accepted by . . . .
Rohan Abeyaratne
Chairman, Department Committee on Graduate Theses

Understanding of Weak Turbulence of Capillary Waves

by

Yulin Pan

Submitted to the Department of Mechanical Engineering
on November 15, 2016, in partial fulfillment of the
requirements for the degree of
Doctor of Philosophy in Mechanical Engineering

Abstract

First developed by Zakharov, Weak Turbulence Theory (WTT) aims at describing the steady-state statistical property of an ensemble of waves in weakly nonlinear interactions. In the wavenumber k domain, the WTT steady-state analytical solution yields a power-law inertial-range spectrum $I \sim k^{\alpha}$, with a constant energy flux P from large forcing scales to small dissipative scales. Over the years, this result has found applications in various physical contexts including plasma physics, optics, internal waves, surface gravity and capillary waves. As a representative physical system with three-wave resonant interactions, capillary wave turbulence has been the subject of many investigations. In addition to the fundamental interest of this problem, an accurate representation of capillary waves on water surface is also important in understanding the air-sea interaction and remote sensing of the ocean.

We study capillary wave turbulence from both theoretical and computational considerations. The original theoretical derivation, from the primitive Euler equations to the Kinetic Equation (KE) which yields the final power-law solution $I \sim CP^{1/2}k^{-19/4}$, is re-formulated. While an emphasis is placed on understanding the assumptions in wave turbulence, we correct the analytical evaluation of the Kolmogorov Constant, with $C = 6.97$, different compared to the original derivation.

We then develop a tool, based on the High Order Spectral (HOS) method, to simulate the primitive Euler equations on a Cartesian grid. The simulation confirms the theoretical results, which can be approached at sufficiently high nonlinearity level, and uncovers the physics at insufficient nonlinearity, namely with the steepened power-law spectral slope and reduced capability of energy flux. These phenomena, earlier observed experimentally in finite wave basin, are shown to be caused by the finite-box effect, i.e., nonlinear resonance broadening becomes insufficient to overcome the discreteness in k.

The mechanism of finite-box effect is further elucidated in the framework of the KE. In order to incorporate the quasi-resonant interaction on a discrete grid, we develop the quasi-resonant kinetic equation (QRKE) with the introduction of an additional parameter κ, which governs the ratio of nonlinear resonance broadening and wavenumber discreteness. We show that the physics at sufficient and insufficient nonlinearity, as obtained in the simulation of primitive Euler equations, are recovered in the results of $\kappa = \kappa_0$ and $\kappa < \kappa_0$, where κ_0 represents an upper limit of energy flux by quasi-resonance approaching that of exact resonance in theoretically infinite domain. This thus establishes the physical connection between nonlinearity level and the features of the power-law spectrum, through the nonlinear broadening.

We finally apply the developed tool of primitive Euler equations to study the freely-decaying capillary wave turbulence. The problem considered here is an extension of WTT, where the turbulence is allowed to evolve freely in the presence of physically realistic broad-scale dissipation and finite-box effect. Based on our numerical findings, we obtain a simple mathematical model, describing the evolution of the power-law spectrum in the form of exponential modal decay from an initial power-law spectrum. The evolving dynamics involved in this process is elucidated.

The investigations in this thesis are for the special case of capillary wave turbulence, while our main findings are expected to also hold for weak turbulence in other similar physical systems.

Thesis Supervisor: Dick K.P. Yue
Title: Philip J. Solondz Professor of Engineering
Professor of Mechanical and Ocean Engineering

Acknowledgments

I would like to express my sincere gratitude to my advisor, Prof. Dick K.P. Yue, for his immeasurable amount of support throughout this study. His continuous guidance is invaluable not only in educating me with wave mechanics, but more importantly, in shaping me to an independent researcher in the field. "Give a man a fish, and you feed him for a day; teach a man to fish, and you feed him for a lifetime." I would never have been qualified as a "fisher" without this journey with Prof. Yue.

Dr. Yuming Liu is another most influential person during my graduate study. His attitude to science is what I could ever imagine for a great scholar, and discussion with him always brings me wisdom and encourages me to stay optimistic with my academic future.

I am indebted to my other two thesis committee members, Prof. Triantaphyllos Akylas and Prof. Pierre Lermusiaux. Their erudition has kept inspiring me to deepen my understanding of the problem. The committee meetings I have been through with them are especially enjoyable experiences along the way to this final thesis.

The seven-year odyssey for Ph.D. would be less memorable without my friends at MIT. It is not possible to name them all, but I would like to especially thank people of the VFRL: Zao, Areti, Wenting, Grgur, Bryce, Sankha, Meng, Yusheng, Sha, Xiangming, Chengxi and Emma. They have made VFRL a family for me, and I have learned great amount from each one of them over the years. My thanks also goes to Mary Thompson and Leslie Regan for their longtime administrative help, and to John Capomaccio for his friendly face which lightens up many of my otherwise lonely midnight.

This is the best time of life, this is the worst time of life. All the bewilderment, torment and struggles I have had tend to become inconsiderable at the moment of final achievement of my Ph.D., but they do have genuinely existed in my life. Without the unbounded love and support from my parents, Zhigang Pan and Peixuan Ma, I could have never survived from them. They have revealed on me how delicate a man could inherently be, yet taught me how to overcome all these fragility in life. My gratefulness for them is truly beyond words.

My deep appreciation also goes to my girlfriend Hui Wang, for her understanding on my predicament and tolerance of my imperfection. It seems to be destined to meet her during this special stage of my life, and it is my fortune.

Finally, I dedicate this thesis to my grandma in heaven. May you rest in peace, grandma.

Contents

List of Figures

List of Tables

Chapter 1

Introduction

A description of the wind-generated waves on the ocean surface is of vital importance for both engineering and oceanographic purposes. The wavelength of waves in a typical wind sea ranges from O(1mm) to O(100m), and rich mechanisms are involved, including energy input from wind, gravity/capillary wave-wave interactions, wave-current-bathymetry interactions, and energy dissipation by viscosity and wave breaking. While a complete and accurate modelling of all these multi-scale mechanisms are beyond the physical understanding and computational capability of today, the interest of our research is focused on the capillary wave regime, which is the dominant part of ocean surface with wavelength less than 17mm (see figure 1-1 for a sketch of the wind-wave spectrum). Despite the narrow range in the wave spectrum, capillary waves play an important role on the dynamics of the sea surface, e.g., the air-sea interactions and energy transport and dissipation at small scales. Physically, we know little of the wavenumber spectral distribution of these short waves, as well as their modulation by and energy exchange with the underlying long swell. This information is crucial in calculation of the acoustic and electromagnetic back-scattering, and thus sheds light on the interpretation of microwave remote sensing of the ocean.

We consider the statistical property, at zero gravity, in the inertial range of a capillary wavefield under weakly nonlinear interactions. This problem can be generalized to nonlinear dispersive waves in different physical contexts, and bears fundamental interests to physicists. It can be considered as a special case under

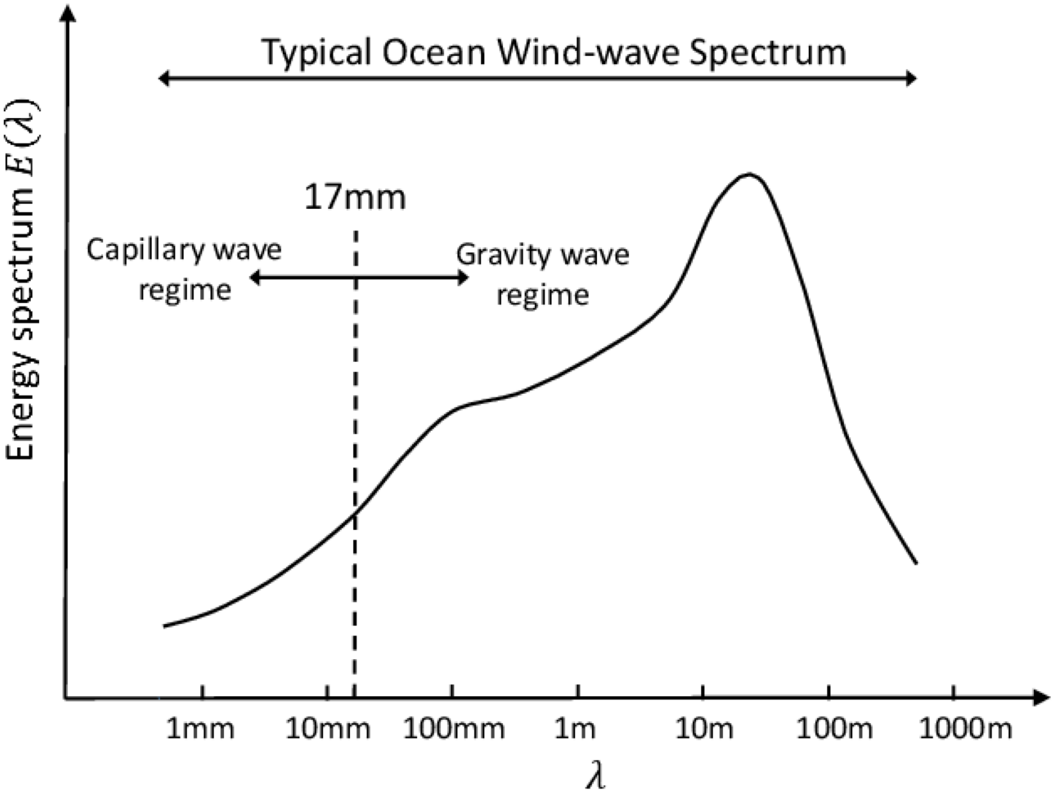

Figure 1-1: Typical wind-wave spectrum of the ocean.

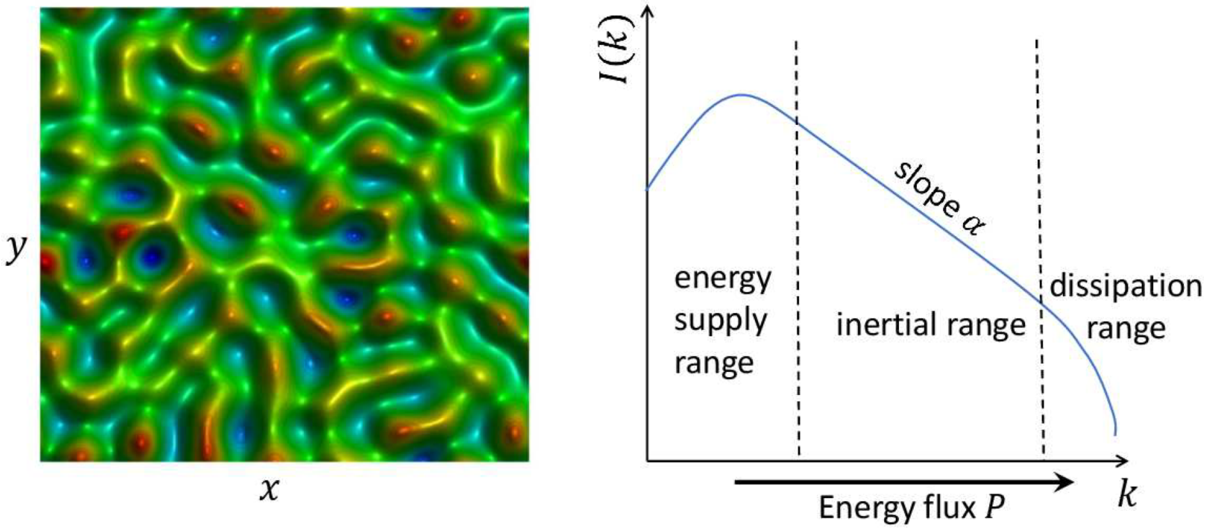

Figure 1-2: (left) A statistically stationary wavefiled; (right) its associated energy spectrum.

weak nonlinearity to Kolmogorov's general description of power-law cascade process in the inertial range of turbulent flows (Kolmogorov, 1941) (see figure 1-2 for a sketch of a statistically stationary wavefield and its associated energy spectrum). Due to the additional assumption of weak nonlinearity, mathematical formulations are more accessible and the cascade spectrum can be obtained as an exact stationary solution of the Kinetic Equation (KE), which governs the evolution of wave spectrum due to nonlinear resonant interactions. This methodology, named the Weak Turbulence Theory (WTT) (Newell & Rumpf, 2011; Zakharov *et al.*, 1992), has found applications in various contexts of nonlinear waves, including plasma physics (Galtier *et al.*, 2002), optics (Dyachenko *et al.*, 1992), internal waves (Lvov *et al.*, 2004), surface gravity and capillary waves (Zakharov & Filonenko, 1966, 1967). Despite the importance, the validity and limitations of the WTT solutions are not fully understood.

1.1 WTT of capillary waves

As a representative physical system with three-wave resonant interactions, capillary wave turbulence has been the subject of many investigations. The theoretical framework of WTT of capillary waves is developed by Zakharov & Filonenko (1967) (and reformulated in (Pushkarev & Zakharov, 2000; Stiassnie *et al.*, 1991)). Under WTT assumptions, including weak nonlinearity, infinite domain and dissipation at only high wavenumbers, the isotropic spectrum of surface elevation yields a closed-form stationary solution (with energy supply at large scales balanced by energy dissipation at small scales) in the inertial range:

$$I_\eta(\mathbf{k}) = I_\eta(k) = C\frac{P^{1/2}\rho^{1/4}}{\sigma^{3/4}}k^{-19/4}. \tag{1.1}$$

Here and hereafter we use $\mathbf{k}$ to represent vector wavenumber and $k = |\mathbf{k}|$. In (1.1), P (kg/s^3) is the energy (density) flux to large wavenumbers, σ (kg/s^2) the surface tension coefficient and ρ (kg/m^3) the fluid density. I_η (m^4) is defined (Zakharov & Filonenko, 1967; Pushkarev & Zakharov, 2000) by $\langle\hat{\eta}(\mathbf{k})\hat{\eta}^*(\mathbf{k}')\rangle = I_\eta(\mathbf{k})\delta(\mathbf{k}-\mathbf{k}')$, with the angle bracket denoting ensemble average, star denoting complex conjugate, and $\hat{\eta}(\mathbf{k}) = 1/(2\pi)\iint_{-\infty}^{\infty}\eta(\mathbf{r})e^{-i\mathbf{k}\cdot\mathbf{r}}d\mathbf{r}$ being the Fourier transform of surface elevation $\eta(\mathbf{r}) \equiv \eta(x,y)$. Leaving the proof in Chapter 2, we claim here that this definition of I_η is equivalent to the definition of energy density spectrum (see Phillips, 1985) with a proportional factor. C is the non-dimensional Kolmogorov Constant, analytically evaluated in Pushkarev & Zakharov (2000), with a value of $C_0 = 9.85$. Physically, it represents the amount of energy flux that can be carried by a power-law spectrum at certain magnitude, i.e., the capability of a power-law spectrum to transfer energy.

The validity of this solution (1.1), and especially the assumptions made in the derivation, have received many investigations. In particular, the scaling of the spectrum with respect to wavenumber $I_\eta \sim k^\alpha$ has been tested experimentally (Falcon *et al.*, 2007; Wright *et al.*, 1996; Brazhnikov *et al.*, 2007; Xia *et al.*, 2010) and numerically (Pushkarev & Zakharov, 1996, 2000; Deike *et al.*, 2014*b*). While the exponents found in Falcon *et al.* (2007); Xia *et al.* (2010); Pushkarev & Zakharov (1996, 2000); Deike *et al.* (2014*b*) are consistent with the theoretical value, deviations are reported in Xia *et al.* (2010); Wright *et al.* (1996) with $\alpha = -5.3$, and Brazhnikov *et al.* (2007) with $\alpha = -6.0$ under weak or narrow-band forcing.

The scaling of I_η with P, and the value of Kolmogorov constant C, have remained open questions. Recent experimental observations from two independent groups Falcon *et al.* (2007); Xia *et al.* (2010) suggest that a linear scaling relation $I_\eta \sim P$ should apply, in apparent disagreement with (1.1). This controversy is summarized in Newell & Rumpf (2011), and appears now resolvable (Deike *et al.*, 2014*a*) by a better experimental estimation of P that distinguishes the energy flux from the energy dissipation at large scales. There is no direct numerical investigation of this scaling.

Attempts at estimating C numerically are given in Pushkarev & Zakharov (2000) and Deike *et al.* (2014*b*), by respectively a potential flow simulation and a Navier-Stokes simulation, with reported values of $C_{pot} = 1.7$ and $C_{NS} = 5.0$. This value is only recently measured experimentally (Deike *et al.*, 2014*a*) with $C_{exp} = 0.5$. The reasons for these discrepancies remain unclear. Resolving these controversies requires both a close scrutiny of the theoretical derivation and understanding of the physical discrepancy between WTT and simulations/experiments, e.g., finite box effect (see Pushkarev & Zakharov, 1996) which limits the nonlinear resonance due to wavenumber discreteness, occurring generally in finite computational domain/wave basin.

1.2 Quasi-resonance in finite wave domain

In spite of the assumption of theoretically infinite domain in the derivation, the tempted validation of (1.1) is usually conducted in a finite domain. This posed questions including why the theoretical spectrum, derived based on the assumption of infinite wave domain, can be recovered in realistic condition of finite wave domain, and how the wavenumber discreteness in a finite domain affects the dynamics. Indeed, these questions can be originated from the mathematical property of the exact triad resonant conditions: In a rectangular finite domain, it is shown in Kartashova (1990) that there is no solution of exact triad resonance, as the frequency-matching condition turns into a particular case of Fermat's last theorem. It has been shown in experiment

(Denissenko *et al.*, 2007) that the nonlinearity level plays a key role in the dynamics: While the theoretical result can be approached at sufficient nonlinearity level, insufficient nonlinearity results in the steepened power-law spectral slope $|\alpha| > |\alpha_0|$. To understand this phenomenon, it is qualitatively argued (e.g. Pushkarev & Zakharov, 2000; Connaughton *et al.*, 2001) that the energy transfer in finite domain is only possible under sufficient nonlinear broadening. However, a quantitative description of this mechanism is still lacking, and an explanation on how nonlinearity level modifies these spectral properties is still under investigation.

There is no attempts, till today, of understanding the problem regarding the discrete capillary wave turbulence in the framework of the KE. Indeed, the equation is not directly applicable, as the wavenumber discreteness in finite domain restricts the triad resonance, rendering the collision integral which represents nonlinear interaction to be zero. It is, however, desirable to establish this framework, which is physically more tangible than that of the primitive Euler equations, in terms of its explicit mathematical description of energy transfer by triads. We postulate that the influence of the nonlinearity level on the dynamics of energy transfer can be elucidated after the corresponding parameter is properly introduced.

1.3 Decaying capillary wave turbulence with broad-scale dissipation

While there are many investigations of the weak turbulence in stationary regime, where energy input is balanced by energy dissipation, the freely decaying non-stationary capillary wave turbulence is much less studied. A notable exception is the theoretical work of Falkovich *et al.* (1995), where the decaying spectrum is considered in the framework of the Kinetic Equation (KE). Under the WTT assumptions, the unsteady solution of the KE yields a time-varying spectral amplitude inversely proportional to time, and a power-law spectrum within an inertial range of fixed width that decays with constant spectral slope $\alpha = -19/4$:

$$I_\eta(k,t) \sim k^{-19/4} t^{-1}, \text{ for } t > t^0, \tag{1.2}$$

where t^0 is the initial time of the evolution of the power-law spectrum. The total energy is obtained in Falkovich *et al.* (1995) by analytical integration of (1.2) in k, to yield $E(t) \sim t^{-1}$.

In physically-realistic situations, finite box effect is always present; and dissipation exists over broad scales. The validity of (1.2) under these effects must be checked by experimental and numerical studies. While there is no numerical investigation of this problem, experimental investigations show that, during the decay, the inertial range varies, with the cutoff wavenumber k_c moving towards lower k as time increases (Deike *et al.*, 2012, 2013; Kolmakov *et al.*, 2004). The spectral slope α is, in general, found to be time-varying (e.g. Miquel & Mordant, 2011; Deike *et al.*, 2013, 2014*a*), depending on the nonlinearity level and viscosity of the fluid. The time decay of the modal amplitudes obtained in all the experiments is exponential, rather than t^{-1}. In terms of the total energy $E(t)$, the only direct measurement is Deike *et al.* (2012), which also shows an exponential decay, in disagreement with the theory (notwithstanding possible effects of gravity waves on the energy measurement which may affect the direct comparison). It is postulated that at least some of these apparent discrepancies can be attributed to the inherent WTT assumptions underlying (1.2) (e.g. Kolmakov *et al.*, 2004; Miquel & Mordant, 2011; Deike *et al.*, 2013). This leaves the modification of (1.2) under finite box effect and broad-scale dissipation an open issue.

The broad-scale dissipation present in the actual physics is especially important for decaying turbulence, as it enhances unsteadiness by allowing a faster spectral energy variation at broad scales. Yet it introduces an extra dynamics into the weak turbulence problem. Deike *et al.* (2014*a*) shows, for stationary turbulence, that dissipation within the inertial range results in a nonconstant inter-modal energy transfer. This is in contrast to WTT which assumes a constant energy flux P transferring energy across k from large to small scales. The variation of energy transfer in k affects the experimental (or numerical) quantification of P. For the case of stationary-state forced turbulence, earlier measurements of P (e.g. Falcon *et al.*, 2007; Xia *et al.*, 2010) rely on the assumption that P is equal to the total energy input rate, or equivalently the total rate of dissipation Γ. The obtained results are in apparent disagreement with the WTT scaling of $I_\eta \sim P^{1/2}$. This controversy is later shown resolvable (Deike *et al.*, 2014*a*), in limited range of nonlinearity, by defining P as the average of the inter-modal energy transfer over the entire inertial range. In decaying turbulence with broad-scale dissipation, the inter-modal energy transfer is further affected by the unsteadiness of the spectrum, and an effective way to evaluate P is not available.

The complexities associated with the unsteadiness in the decaying turbulence, broad-scale dissipation and finite box effect, inevitably present in realistic physical experiments, are closely coupled. The general problem is difficult, and there is still not a clear elucidation, especially in the context of direct numerical investigation, of the underlying dynamics. In particular, it would be desirable to obtain a modified form of (1.2) (or (1.1)) for the spectral evolution, as well as that for $E(t)$, applicable to the general physical problem of decaying capillary wave turbulence. Physically, the role of unsteadiness in the spectrum evolution and dynamics, the time dependence of the spectral slope $\alpha(t)$, as well as its inherent connection to the wave field and dissipation magnitude, remain unknown.

1.4 Long-short wave and wave-current interactions

Investigation of the interactions of these short (capillary) waves with long waves or currents is another key step in understanding the upper ocean dynamics. These phenomena are in essence multi-scale, which is an indispensable component in many other studies of physical oceanography, for example at larger scale, the interactions of internal tide with gulf stream, bathymetry and horizontal density variation. In particular, the propagation of internal tide under these influences is recently analyzed at Middle Atlantic Bight region using the decomposition of field variables with the hydrostatic assumption (Kelly & Lermusiaux, 2016; Kelly *et al.*, 2016).

For long-short wave interactions, the first effort is Longuet-Higgins & Stewart (1960), who considers the modulation of linear short waves by a weakly nonlinear long wave, and derives the formulae for modulated short-wave wavenumber and amplitude. This is extended in Longuet-Higgins (1987) by a numerical solution which allows the long-wave amplitude to be finite, and in Zhang & Melville (1990) by removing the linearity limitation of the short wave. More sophisticated investigation on the evolution of a short-wave spectrum on a long-wave background is provided in Gramstad & Trulsen (2010). Another phenomenon involving the long-short wave interactions is the generation of parasitic capillary waves on steep gravity or gravity-capillary waves. Since the first observation of this phenomenon by Cox (1958), it has been extensively studied in experiments (Fedorov *et al.*, 1998; Chang *et al.*, 1978; Zhang, 1995; Perlin *et al.*, 1993), numerics (Longuet-Higgins, 1963; Fedorov *et al.*, 1998; Longuet-Higgins, 1995) and theory (Jiang *et al.*, 1999; Dommermuth, 1994; Hung & Tsai, 2009; Watson & Buchsbaum, 1996; Watson, 1999; Watson & Mcbride, 1993; Ceniceros & Hou, 1999).

All the above theoretical and numerical studies rely more or less on the assumptions amongst linearity, steadiness and narrow-bandedness. To obtain a comprehensive study on the long-short wave interactions, a fully-nonlinear unsteady solver is desirable. The most popular choice in this category is the High-Order Spectral (HOS) method, developed independently by Dommermuth & Yue (1987) and West *et al.* (1987). The key step in HOS solution is a Dirichlet-to-Neumann Operator (DNO), which maps the surface potential to the derivative of surface potential. The accuracy of the DNO, can be increased as needed, by increasing the nonlinearity order in the boundary perturbation method applied in HOS. This procedure, however, involves a known difficulty in solving the long-short wave interactions with disparate wavelengths. Indeed, the boundary perturbation method is historically controversial (Holliday, 1977; Zhang *et al.*, 1993) in its capability of solving the long-short wave interactions. Although vindicated theoretically (Brueckner & West, 1988), difficulty remains in high-order numerical solutions (Nicholls & Reitich, 2001). A robust approach which remedies this numerical difficulty, for modelling long-short wave interactions, is yet to be established.

For wave-current interactions, existing studies mainly focus on the influence of a prescribed current on the surface waves. Longuet-Higgins & Stewart (1961) considers the modulation of a weakly nonlinear wave by a slowly-varying current, from a perturbation analysis. The major results are later shown to be obtainable from principle of conservation of apparent frequency and wave action (Phillips, 1981; Shyu & Phillips, 1990; Bretherton & Garrett, 1968). The current field is also shown to be one of the major concerns for rogue wave generation (Mallory, 1974; Dysthe *et al.*, 2008; Wu & Yao, 2004; Merkoune *et al.*, 2013; White & Fornberg, 1998; Lavrenov & Porubov, 2006; Lavrenov, 1998; Smith, 1976). On the other hand, studies on the influence of surface waves on the underlying currents, which is also expected to be physically in-negligible, are generally lacking. Numerical study provides a viable means to elucidate the physics involved in these problems, and a reliable way for prediction. For this purpose, an efficient numerical solver is desirable. This requires a first effort to include the influence of a prescribed current field on nonlinear surface wave simulation, with a fully-nonlinear coupled current-wave solver to be developed next.

1.5 Outline of current work

This thesis is mainly devoted to the study of capillary wave turbulence from both theoretical and computational considerations, with the last two chapters discussing simulations of long-short wave and wave-current interactions.

1.5.1 Re-formulation of WTT derivation

For the purpose of building a solid theoretical background, we re-formulate the derivation of WTT for capillary waves. The original derivation outlined in Zakharov & Filonenko (1967); Pushkarev & Zakharov (2000) is substantially expanded, from the primitive Euler equations to the final stationary power-law solution of the wave spectrum. In the midst, the obtained kinetic equation (KE) is accentuated, which directly governs the spectral evolution due to triad resonant interactions. The assumptions involved in the derivation is elucidated, which facilitates the ensuing analysis of the deviation to the theoretical results in numerical simulations incorporating realistic conditions. Two errors involved in the original derivation (Pushkarev & Zakharov, 2000), regarding the Komogorov Constant, are emphasized, including a normalization factor and the evaluation of a key integral. These yield an updated value of $C_0 = 6.97$ along with a modification of (1.1).

1.5.2 Simulation of the primitive Euler equations

A direct numerical investigation of capillary wave turbulence can be performed via simulation of the primitive Euler equations. To this end, it is crucial to develop an efficient numerical technique for the simulation. This is achieved based on the High Order Spectral (HOS) method, which is widely applied in the simulation of gravity wave field. We develop a modification which incorporates capillarity in HOS, by adding surface tension term in the governing equation.

In HOS, the primitive Euler equations are truncated up to an arbitrary order M in wave steepness ϵ. We develop two schemes to include the surface tension term $\nabla_{\mathbf{x}} \cdot (\nabla_{\mathbf{x}}\eta/\sqrt{1+\nabla_{\mathbf{x}}\eta\cdot\nabla_{\mathbf{x}}\eta})$, either as a whole or truncated to order M using Taylor expansion. The two implementations are respectively consistent with gravity-wave HOS originated from two independent groups, Dommermuth & Yue (1987) and West *et al.* (1987), and should be used accordingly. In practical consideration, these two implementations yield truncation errors of the same order ϵ^{M+1} even though the former includes random terms higher than order M in the governing equations. Notwithstanding, the exact truncation (exclusive of all terms higher than order M) of the latter bears slight theoretical advantage of exact conservation of energy within order M, as the truncated equations form an exact Hamiltonian system.

Extensive validations and analysis of the developed method are pursued, including a validation against the Crapper analytical solution for a one-dimensional capillary wave of finite amplitude (Crapper, 1957); and a numerical instability analysis. In particular, it is shown that the inclusion of the surface tension term aggravates the numerical restriction on the time step size. In order to accelerate the simulation, we develop an implicit Runge-Kutta time-marching method which combines a linear propagator method (Hou *et al.*, 1994) and the 4th-order Runge-Kutta scheme. This allows larger time steps to be used in the simulation (with the inevitable cost of decreased accuracy). In addition, we upgrade the 1/2-rule de-aliasing scheme in the original HOS to the more popular 2/3 rule, which allows more wave modes to be simulated for a given grid.

The first application of the developed method is to investigate isotropic turbulence of capillary waves, and evaluate the validity of WTT, by direct numerical simulation of the primitive Euler equations. The aim is to obtain a clean development of the wave spectrum not obscured by complexities associated with the mechanical forcing of the waves (Pushkarev & Zakharov, 1996, 2000; Falcon *et al.*, 2007; Xia *et al.*, 2010; Deike *et al.*, 2014*a*) and difficulties associated with the estimation of P (Falcon *et al.*, 2007; Xia *et al.*, 2010; Deike *et al.*, 2014*a*). Furthermore, we seek to uncover the physics at a substantially broader range of nonlinearity level relative to existing measurements (Falcon *et al.*, 2007; Xia *et al.*, 2010; Deike *et al.*, 2014*a*) and numerics (Pushkarev & Zakharov, 1996, 2000; Deike *et al.*, 2014*b*). To achieve this, we consider the free evolution of an arbitrary initial wavefield represented by a general isotropic spectrum. We then look for the development of a power-law spectrum in the evolution process from different initial nonlinearity levels. In the simulation, the dissipation effect is represented by additional terms in the primitive Euler equations which exponentially damps the wave amplitude at high wavenumbers. The energy flux P is evaluated, without ambiguity, by direct evaluation of the energy dissipation rate in the dissipation range. We expect to elucidate the scaling of I with k and P, and value of C in this study, and understand the influence on the results by interplay between finite box effect and nonlinearity level.

We then employ the developed method on decaying capillary wave turbulence with realistic broad-scale dissipation. In contrast to WTT in stationary regime, we simulate the evolving spectrum for a long enough time scale to investigate the time-varying dynamics. We expect that these configurations are sufficient to replicate the results from experiments on a power-law spectrum with exponential modal decay, as well as monochromatic decrease of the cut-off wavenumber k_c and variation of α during the decay. Based on the simulation results, we seek a modified form of (1.2), which describes the time-dependent power-law spectrum within the inertial range under broad-scale dissipation. The physical roles of unsteadiness, finite box effect and dissipation magnitude in the decaying process are elucidated.

1.5.3 Study of quasi-resonant kinetic equation (QRKE)

For the purpose of understanding wave turbulence, the KE is superior to the primitive Euler equations in terms of its explicit description of energy transfer by triads. The KE of capillary waves reads

$$\frac{\partial n_{\mathbf{k}}}{\partial t} \sim \iint_{-\infty}^{\infty} F(\mathbf{k}, \mathbf{k}_1, \mathbf{k}_2, n_{\mathbf{k}}, n_{\mathbf{k}_1}, n_{\mathbf{k}_2}) \delta(\mathbf{k} - \mathbf{k}_1 - \mathbf{k}_2) \delta(\omega_{\mathbf{k}} - \omega_{\mathbf{k}_1} - \omega_{\mathbf{k}_2}) d\mathbf{k}_1 d\mathbf{k}_2, \quad (1.3)$$

where $n_{\mathbf{k}}$ is the spectral density of wave action, $\omega_{\mathbf{k}} = |\mathbf{k}|^{3/2}$ is the angular frequency determined from the linear dispersion relation, and $F(\mathbf{k}, \mathbf{k}_1, \mathbf{k}_2, n_{\mathbf{k}}, n_{\mathbf{k}_1}, n_{\mathbf{k}_2})$ is a particular function that will be specified in a later chapter.

The term $\partial n_{\mathbf{k}} / \partial t$ takes nonzero value when the arguments of the two delta functions in (1.3) simultaneously vanish. This is only possible with exact resonant interactions in the limit of theoretically infinite domain, as $\mathbf{k}$ takes continuous values. In contrast, it is shown in Kartashova (1990) that there is no exact triad resonance in a finite rectangular domain, as the frequency condition, turning into a particular case of Fermat's last theorem, does not satisfy. This imposes a difficulty in understanding discrete turbulence in finite domain in the framework of (1.3).

Physically under the situation of grid discreteness, nonlinearity broadens the linear dispersion relation (e.g. Pushkarev & Zakharov, 2000; Herbert *et al.*, 2010), making possible the energy transfer within quasi-resonant triads. To account for this mechanism, a technique can be applied which represents the exact delta function on frequency in (1.3) with a generalized finite-width delta function δ_g. The width of δ_g

thus characterizes the nonlinear broadening. This approach has been developed for shallow-water gravity waves as a simulation tool, validated against experimental data (Piscopia *et al.*, 2003; Zaslavskii & Polnikov, 1998). It is worthwhile to develop the corresponding approach for the capillary-wave KE, with the purpose of studying the capillary wave turbulence. We point out that although this broadening technique is inspired by the physical reasoning of quasi-resonance, the particular form of the finite-width delta function is mathematically derivable from the primitive Euler equations by assuming discreteness in wavenumber.

Following this reasoning, and guided by a quantitative study of the broadening mechanism using results from the Euler equations, we develop a quasi-resonant kinetic equation (QRKE) for capillary waves, which takes into consideration the wavenumber discreteness, nonlinear resonance broadening and quasi-resonant triad interactions. An additional non-dimensional parameter κ is introduced in this developed QRKE, which exclusively governs the ratio of nonlinear broadening and wavenumber discreteness. This thus provides a framework in which the influence of nonlinear broadening on discrete wave turbulence can be directly evaluated. By simulating the QRKE with different values of κ, and correlating with the features of the power-law spectrum at different nonlinearity levels (obtained in the simulation of primitive Euler equations), we establish the physical connection between nonlinearity level and wave turbulence, through the nonlinear resonance broadening.

1.5.4 Long-short wave and wave-current interactions

We first consider long-short wave interactions with disparate wavelengths ($\gamma \equiv k_S/k_L \gg 1$). We illustrate the ill-conditioning of the boundary perturbation method in solving the boundary value problem regarding velocity potential ϕ, which is due to the presence of "divergently" large terms proportional to the multiplication of short-wave wavenumber and long-wave amplitude, raised to power $m-1$ in the mth order calculation in the boundary perturbation method. Although these terms can be shown to exactly cancel one another at each order (for which we provide a general theoretical proof), they amount to the calculation of small numbers as differences of very large numbers in the numerical solution. This inaccuracy in numerics significantly limits the capability of HOS in dealing with a wave field with $\gamma \gg 1$. As a remedy, we can either use accordingly higher precision arithmetics, or introduce a mapping scheme, which fundamentally removes the difficulty regarding long-short wave interactions. The computational cost is however increased as the scheme requires additional vertical discretization of the wave field. The efficacy of the developed approach is demonstrated by applying it to a prescribed boundary value problem involving the long-short wave interaction.

For wave-current interactions, we first develop the framework of nonlinear surface wave simulation superposed on a prescribed current. The derived governing equations are then casted in a Hamiltonian formulation to elucidate the conservation of coupled wave-current energy. A simulation is conducted for a long-crested wave spectrum passing a realistic current field. The effects of following/opposing current on the evolution of waves are elucidated, accompanied with physical interpretations. We finally present algorithms for a fully nonlinear coupled simulation of wave-current interactions, where the waves and currents are both allowed to evolve in time.

1.5.5 Thesis organization

The remainder of this thesis is organized as follows: We start in Chapter 2 by reformulating the theoretical derivation of WTT for capillary waves. In Chapter 3, the numerical tool for simulation of the primitive Euler equations is developed, along with multiple validations and analysis. The studies of stationary capillary wave turbulence via simulations of primitive Euler equations and QRKE are respectively described in Chapter 4 and 5. Chapter 6 is devoted to the study of decaying capillary wave turbulence. The long-short wave interaction and wave-current interaction are respectively discussed in Chapter 7 and 8. Summary and possible future extensions are described in Chapter 9.

Chapter 2

Theoretical Derivation

In this chapter, we re-formulate the derivation of WTT for capillary waves. The original derivation outlined in Zakharov & Filonenko (1967); Zakharov *et al.* (1992); Pushkarev & Zakharov (2000) is substantially expanded. We show two errors involved in Pushkarev & Zakharov (2000) regarding the analytical evaluation of the Kolmogorov Constant C, including the normalization for (2.85) and the evaluation of a key integral (2.68). This results in a final solution written in the form of (2.90) and (2.91). The inherent assumptions involved in the derivation are summarized.

2.1 Canonical formulation of governing equations

We consider capillary waves in two surface dimensions on the free surface of an ideal incompressible fluid. For small Bond number, gravity is neglected. Without loss of generality, the time and mass units are chosen so that the surface tension coefficient σ and fluid density ρ are unity. The system is described in the context of potential flow (velocity potential $\phi(x, y, z, t)$) in terms of nonlinear evolution equations (Zakharov & Filonenko, 1967) for surface elevation $\eta(x, y, t)$ and velocity potential at the surface $\phi^s(x, y, t) \equiv \phi(x, y, \eta, t)$:

$$\eta_t + \nabla_{\mathbf{x}}\phi^s \cdot \nabla_{\mathbf{x}}\eta - (1 + \nabla_{\mathbf{x}}\eta \cdot \nabla_{\mathbf{x}}\eta)\phi_z = 0, \tag{2.1}$$

$$\phi_t^s - \nabla_{\mathbf{x}} \cdot \frac{\nabla_{\mathbf{x}}\eta}{\sqrt{1+\nabla_{\mathbf{x}}\eta\cdot\nabla_{\mathbf{x}}\eta}} + \frac{1}{2}\nabla_{\mathbf{x}}\phi^s\cdot\nabla_{\mathbf{x}}\phi^s - \frac{1}{2}(1+\nabla_{\mathbf{x}}\eta\cdot\nabla_{\mathbf{x}}\eta)\phi_z^2 = 0, \qquad (2.2)$$

where $\nabla_{\mathbf{x}} = (\partial/\partial x, \partial/\partial y)$ denotes the horizontal gradient. ϕ_z is the vertical velocity evaluated at the free surface.

The first task is to transform (2.1) and (2.2) to Fourier space, by defining a two-dimensional (2D) Fourier transform of a function $f(\mathbf{x})$ as (For simplicity, we use $\int_{-\infty}^{\infty} d\mathbf{x}$ to denote the 2D integration $\iint_{-\infty}^{\infty} dxdy$ in the rest of this thesis as long as no confusion is incurred.)

$$\widehat{f}(\mathbf{k}) = \frac{1}{2\pi}\int_{-\infty}^{\infty} f(\mathbf{x})e^{-i\mathbf{k}\cdot\mathbf{x}}d\mathbf{x}. \qquad (2.3)$$

The transform of nonlinear terms formed by multiplication of functions are described below, taking $(\nabla_{\mathbf{x}}\phi^s)\cdot(\nabla_{\mathbf{x}}\eta)$ as an example:

$$\begin{aligned}
\nabla_{\mathbf{x}}\widehat{\phi^s\cdot\nabla_{\mathbf{x}}}\eta &= \frac{1}{2\pi}\int_{-\infty}^{\infty} \nabla_{\mathbf{x}}\phi^s\cdot\nabla_{\mathbf{x}}\eta e^{-i\mathbf{k}\cdot\mathbf{x}}d\mathbf{x} \\
&= \frac{1}{(2\pi)^3}\int_{-\infty}^{\infty} e^{-i\mathbf{k}\cdot\mathbf{x}}d\mathbf{x}\cdot\int_{-\infty}^{\infty}(\widehat{\nabla_{\mathbf{x}}\phi^s})_1 e^{i\mathbf{k}_1\cdot\mathbf{x}}d\mathbf{k}_1\int_{-\infty}^{\infty}(\widehat{\nabla_{\mathbf{x}}\eta})_2 e^{i\mathbf{k}_2\cdot\mathbf{x}}d\mathbf{k}_2 \\
&= \frac{1}{(2\pi)^3}\iiint_{-\infty}^{\infty}(\widehat{\nabla_{\mathbf{x}}\phi^s})_1\cdot(\widehat{\nabla_{\mathbf{x}}\eta})_2 e^{i(\mathbf{k}_1+\mathbf{k}_2-\mathbf{k})\cdot\mathbf{x}}d\mathbf{x}d\mathbf{k}_1d\mathbf{k}_2 \\
&= -\frac{1}{2\pi}\iint_{-\infty}^{\infty}\mathbf{k}_1\cdot\mathbf{k}_2\widehat{\phi}^s(\mathbf{k}_1,t)\cdot\widehat{\eta}(\mathbf{k}_2,t)\cdot\delta(\mathbf{k}-\mathbf{k}_1-\mathbf{k}_2)d\mathbf{k}_1d\mathbf{k}_2.
\end{aligned}$$

where we have used two identities:

$$\delta(\mathbf{k}) = \frac{1}{(2\pi)^2}\int_{-\infty}^{\infty} e^{i\mathbf{k}\cdot\mathbf{x}}d\mathbf{x}, \qquad (2.4)$$

and

$$(\widehat{\nabla_{\mathbf{x}}\phi^s})_j = i\mathbf{k}_j\widehat{\phi}^s(\mathbf{k}_j,t), \text{ for } j=1,2. \qquad (2.5)$$

Following the above procedures, equations (2.1) and (2.2) can be transformed to:

$$\widehat{\eta}_t(\mathbf{k},t) - \frac{1}{2\pi}\iint_{-\infty}^{\infty}(\mathbf{k}_1\cdot\mathbf{k}_2)\widehat{\phi}^s(\mathbf{k}_1,t)\cdot\widehat{\eta}(\mathbf{k}_2,t)\cdot\delta(\mathbf{k}-\mathbf{k}_1-\mathbf{k}_2)d\mathbf{k}_1d\mathbf{k}_2 - \widehat{\phi}_z = 0, \quad (2.6)$$

$$\widehat{\phi^s}_t(\mathbf{k},t) + k^2\widehat{\eta}(\mathbf{k},t) - \frac{1}{4\pi}\iint_{-\infty}^{\infty}(\mathbf{k}_1\cdot\mathbf{k}_2)\widehat{\phi^s}(\mathbf{k}_1,t)\cdot\widehat{\phi^s}(\mathbf{k}_2,t)\cdot\delta(\mathbf{k}-\mathbf{k}_1-\mathbf{k}_2)d\mathbf{k}_1 d\mathbf{k}_2$$
$$-\frac{1}{4\pi}\iint_{-\infty}^{\infty}\widehat{\phi_z}(\mathbf{k}_1,t)\cdot\widehat{\phi_z}(\mathbf{k}_2,t)\cdot\delta(\mathbf{k}-\mathbf{k}_1-\mathbf{k}_2)d\mathbf{k}_1 d\mathbf{k}_2 = 0. \tag{2.7}$$

Here we have made the assumptions of small wave steepness $||k\eta|| \sim O(\epsilon)$ (week nonlinearity), and that three-wave interactions are dominant for capillary waves. As a result, only terms up to second order (ϵ^2) are retained in (2.6) and (2.7).

Let us eliminate the surface vertical velocity $\widehat{\phi_z}$ so that the two governing equations involve only two unknowns $\widehat{\phi^s}(\mathbf{k},t)$ and $\widehat{\eta}(\mathbf{k},t)$. For this purpose, we must express $\widehat{\phi_z}$ in terms of $\widehat{\phi^s}$ and $\widehat{\eta}$. The procedure is outlined below.

To satisfy the Laplace equation, the velocity potential $\widehat{\phi}(\mathbf{k},z,t)$ in deep water can be expressed as:

$$\widehat{\phi}(\mathbf{k},z,t) = \widehat{\Phi}(\mathbf{k},t)e^{kz}, \tag{2.8}$$

where $k = |\mathbf{k}|$. By substituting $z = \eta(\mathbf{x},t)$ in (2.8), the surface potential can be obtained:

$$\widehat{\phi^s}(\mathbf{k},t) = \widehat{\phi}(\mathbf{k},\eta,t) = \widehat{\Phi}(\mathbf{k},t)e^{k\eta} \tag{2.9}$$

In physical domain, this can be expressed as:

$$\phi^s(\mathbf{x},t) = \frac{1}{2\pi}\int_{-\infty}^{\infty}\widehat{\Phi}(\mathbf{k},t)e^{k\eta}e^{i\mathbf{k}\cdot\mathbf{x}}d\mathbf{k}. \tag{2.10}$$

Similarly, taking the derivative of (2.8) in z direction and substituting $z = \eta(\mathbf{x},t)$, we obtain the vertical velocity in physical domain:

$$\phi_z(\mathbf{x},t) = \frac{1}{2\pi}\int_{-\infty}^{\infty}k\widehat{\Phi}(\mathbf{k},t)e^{k\eta}e^{i\mathbf{k}\cdot\mathbf{x}}d\mathbf{k}. \tag{2.11}$$

We now truncate equation (2.10) up to $O(\epsilon^2)$:

$$\phi^s(\mathbf{x},t) = \frac{1}{2\pi}\int_{-\infty}^{\infty}\widehat{\Phi}(\mathbf{k}_1,t)(1+k_1\eta)e^{i\mathbf{k}_1\cdot\mathbf{x}}d\mathbf{k}_1. \tag{2.12}$$

Substituting $\eta(\mathbf{x},t) = \frac{1}{2\pi}\int_{-\infty}^{\infty}\widehat{\eta}(\mathbf{k}_2,t)e^{i\mathbf{k}_2\cdot\mathbf{x}}d\mathbf{k}_2$ in (2.12) and transforming to wavenumber domain, equation (2.12) becomes:

$$\widehat{\phi}^s(\mathbf{k},t) = \widehat{\Phi}(\mathbf{k},t) + \frac{1}{2\pi}\iint_{-\infty}^{\infty} k_1\widehat{\Phi}(\mathbf{k}_1,t)\widehat{\eta}(\mathbf{k}_2,t)\delta(\mathbf{k}-\mathbf{k}_1-\mathbf{k}_2)d\mathbf{k}_1 d\mathbf{k}_2. \tag{2.13}$$

Applying the same procedure to (2.11), we obtain

$$\widehat{\phi}_z(\mathbf{k},t) = k\widehat{\Phi}(\mathbf{k},t) + \frac{1}{2\pi}\iint_{-\infty}^{\infty} k_1^2\widehat{\Phi}(\mathbf{k}_1,t)\widehat{\eta}(\mathbf{k}_2,t)\delta(\mathbf{k}-\mathbf{k}_1-\mathbf{k}_2)d\mathbf{k}_1 d\mathbf{k}_2. \tag{2.14}$$

We now invert (2.13) iteratively to express $\widehat{\Phi}(\mathbf{k},t)$ in terms of the surface quantities $\widehat{\phi}^s$ and $\widehat{\eta}$. For the zeroth iteration, we retain terms of order $O(\epsilon)$ in (2.13) and obtain

$$\widehat{\Phi}^{(0)}(\mathbf{k},t) = \widehat{\phi}^s(\mathbf{k},t) + O(\epsilon^2) \tag{2.15}$$

For the next iteration, we obtain terms up to $O(\epsilon^2)$ in (2.13) (sufficient for three-wave interactions):

$$\widehat{\phi}^s(\mathbf{k},t) = \widehat{\Phi}^{(1)}(\mathbf{k},t) + \frac{1}{2\pi}\iint_{-\infty}^{\infty} k_1\widehat{\Phi}^{(0)}(\mathbf{k}_1,t)\widehat{\eta}(\mathbf{k}_2,t)\delta(\mathbf{k}-\mathbf{k}_1-\mathbf{k}_2)d\mathbf{k}_1 d\mathbf{k}_2. \tag{2.16}$$

$\Rightarrow$

$$\widehat{\Phi}^{(1)}(\mathbf{k},t) = \widehat{\phi}^s(\mathbf{k},t) - \frac{1}{2\pi}\iint_{-\infty}^{\infty} k_1\widehat{\phi}^s(\mathbf{k}_1,t)\widehat{\eta}(\mathbf{k}_2,t)\delta(\mathbf{k}-\mathbf{k}_1-\mathbf{k}_2)d\mathbf{k}_1 d\mathbf{k}_2. \tag{2.17}$$

Substituting (2.17) into (2.14), we obtain (consistently truncated to $O(\epsilon^2)$)

$$\widehat{\phi}_z(\mathbf{k},t) = k\widehat{\phi}^s(\mathbf{k},t) - \frac{1}{2\pi}\iint_{-\infty}^{\infty} (kk_1 - k_1^2)\widehat{\phi}^s(\mathbf{k}_1,t)\widehat{\eta}(\mathbf{k}_2,t)\delta(\mathbf{k}-\mathbf{k}_1-\mathbf{k}_2)d\mathbf{k}_1 d\mathbf{k}_2. \tag{2.18}$$

The primitive Euler equations truncated up to $O(\epsilon^2)$ in wavenumber space can now be obtained by substituting (2.18) into (2.6) and (2.7):

$$\widehat{\eta}_t(\mathbf{k},t) - k\widehat{\phi}^s(\mathbf{k},t) = \frac{1}{2\pi}\iint_{-\infty}^{\infty} (\mathbf{k}_1\cdot\mathbf{k} - k_1 k)\widehat{\phi}^s(\mathbf{k}_1,t)\cdot\widehat{\eta}(\mathbf{k}_2,t)\cdot\delta(\mathbf{k}-\mathbf{k}_1-\mathbf{k}_2)d\mathbf{k}_1 d\mathbf{k}_2. \tag{2.19}$$

$$\widehat{\phi^s}_t(\mathbf{k},t)+k^2\widehat{\eta}(\mathbf{k},t) = \frac{1}{4\pi}\iint_{-\infty}^{\infty}(\mathbf{k}_1\cdot\mathbf{k}_2+k_1k_2)\widehat{\phi^s}(\mathbf{k}_1,t)\cdot\widehat{\phi^s}(\mathbf{k}_2,t)\cdot\delta(\mathbf{k}-\mathbf{k}_1-\mathbf{k}_2)d\mathbf{k}_1d\mathbf{k}_2. \tag{2.20}$$

We now introduce the canonical variables:

$$\widehat{\eta}(\mathbf{k},t) = \frac{k^{-1/4}}{\sqrt{2}}(a(\mathbf{k},t)+a^*(-\mathbf{k},t)). \tag{2.21}$$

$$\widehat{\phi^s}(\mathbf{k},t) = \frac{-ik^{1/4}}{\sqrt{2}}(a(\mathbf{k},t)-a^*(-\mathbf{k},t)). \tag{2.22}$$

$\Rightarrow$

$$a(\mathbf{k},t) = \frac{\sqrt{2}}{2}k^{1/4}\widehat{\eta}(\mathbf{k},t)+i\frac{\sqrt{2}}{2}k^{-1/4}\widehat{\phi^s}(\mathbf{k},t). \tag{2.23}$$

To obtain the canonical form of the governing equations, we multiply (2.19) by $\sqrt{2}k^{1/4}/2$ and (2.20) by $i\sqrt{2}k^{-1/4}/2$, and add up the two equations. After some algebraic manipulations, we obtain

$$\begin{aligned} i\frac{\partial a_{\mathbf{k}}}{\partial t}-\omega_{\mathbf{k}}a_{\mathbf{k}} =&\frac{\sqrt{2}}{16\pi}\iint_{-\infty}^{\infty}\{[2(\frac{kk_1}{k_2})^{1/4}(\mathbf{k}\cdot\mathbf{k}_1-kk_1)+(\frac{k_1k_2}{k})^{1/4}(\mathbf{k}_1\cdot\mathbf{k}_2+k_1k_2)]a_{\mathbf{k}_1}a_{\mathbf{k}_2} \\ &+[2(\frac{kk_1}{k_2})^{1/4}(\mathbf{k}\cdot\mathbf{k}_1-kk_1)-(\frac{k_1k_2}{k})^{1/4}(\mathbf{k}_1\cdot\mathbf{k}_2+k_1k_2)]a_{\mathbf{k}_1}a^*_{-\mathbf{k}_2} \\ &-[2(\frac{kk_1}{k_2})^{1/4}(\mathbf{k}\cdot\mathbf{k}_1-kk_1)+(\frac{k_1k_2}{k})^{1/4}(\mathbf{k}_1\cdot\mathbf{k}_2+k_1k_2)]a^*_{-\mathbf{k}_1}a_{\mathbf{k}_2} \\ &-[2(\frac{kk_1}{k_2})^{1/4}(\mathbf{k}\cdot\mathbf{k}_1-kk_1)-(\frac{k_1k_2}{k})^{1/4}(\mathbf{k}_1\cdot\mathbf{k}_2+k_1k_2)]a^*_{-\mathbf{k}_1}a^*_{-\mathbf{k}_2}\} \\ &\delta(\mathbf{k}-\mathbf{k}_1-\mathbf{k}_2)d\mathbf{k}_1d\mathbf{k}_2, \end{aligned} \tag{2.24}$$

where $a_{\mathbf{k}} = a(\mathbf{k},t)$ and we use this short notation throughout this thesis. Making use of the symmetrical properties of functions: $\int_{-\infty}^{\infty} f(\mathbf{k}_1)d\mathbf{k}_1 = \int_{-\infty}^{\infty} f(-\mathbf{k}_1)d\mathbf{k}_1$;

$\iint_{-\infty}^{\infty} f(\mathbf{k}_1, \mathbf{k}_2) d\mathbf{k}_1 d\mathbf{k}_2 = \iint_{-\infty}^{\infty} f(\mathbf{k}_2, \mathbf{k}_1) d\mathbf{k}_1 d\mathbf{k}_2$, we obtain

$$\begin{aligned} i\frac{\partial a_{\mathbf{k}}}{\partial t} - \omega_{\mathbf{k}} a_{\mathbf{k}} = \iint_{-\infty}^{\infty} [&\overline{V}^{(1)}(\mathbf{k}, \mathbf{k}_1, \mathbf{k}_2) a_{\mathbf{k}_1} a_{\mathbf{k}_2} \delta(\mathbf{k} - \mathbf{k}_1 - \mathbf{k}_2) \\ &+ \overline{V}^{(2)}(\mathbf{k}, \mathbf{k}_1, \mathbf{k}_2) a_{\mathbf{k}_1} a^*_{\mathbf{k}_2} \delta(\mathbf{k} - \mathbf{k}_1 + \mathbf{k}_2) + \overline{V}^{(3)}(\mathbf{k}, \mathbf{k}_1, \mathbf{k}_2) a^*_{\mathbf{k}_1} a_{\mathbf{k}_2} \delta(\mathbf{k} + \mathbf{k}_1 - \mathbf{k}_2) \\ &+ \overline{V}^{(4)}(\mathbf{k}, \mathbf{k}_1, \mathbf{k}_2) a^*_{\mathbf{k}_1} a^*_{\mathbf{k}_2} \delta(\mathbf{k} + \mathbf{k}_1 + \mathbf{k}_2)] d\mathbf{k}_1 d\mathbf{k}_2, \end{aligned} \tag{2.25}$$

where

$$\overline{V}^{(1)}(\mathbf{k}, \mathbf{k}_1, \mathbf{k}_2) = U(\mathbf{k}_1, \mathbf{k}_2, \mathbf{k}) - U(\mathbf{k}, -\mathbf{k}_1, \mathbf{k}_2) - U(\mathbf{k}, -\mathbf{k}_2, \mathbf{k}_1), \tag{2.26}$$

$$\overline{V}^{(2)}(\mathbf{k}, \mathbf{k}_1, \mathbf{k}_2) = U(\mathbf{k}, \mathbf{k}_2, \mathbf{k}_1) - U(\mathbf{k}_1, -\mathbf{k}, \mathbf{k}_2) - U(\mathbf{k}_1, -\mathbf{k}_2, \mathbf{k}), \tag{2.27}$$

$$\overline{V}^{(3)}(\mathbf{k}, \mathbf{k}_1, \mathbf{k}_2) = U(\mathbf{k}, \mathbf{k}_1, \mathbf{k}_2) - U(\mathbf{k}_2, -\mathbf{k}, \mathbf{k}_1) - U(\mathbf{k}_2, -\mathbf{k}_1, \mathbf{k}), \tag{2.28}$$

$$\overline{V}^{(4)}(\mathbf{k}, \mathbf{k}_1, \mathbf{k}_2) = U(\mathbf{k}_1, \mathbf{k}_2, \mathbf{k}) + U(\mathbf{k}, \mathbf{k}_1, \mathbf{k}_2) + U(\mathbf{k}, \mathbf{k}_2, \mathbf{k}_1), \tag{2.29}$$

with $U(\mathbf{k}, \mathbf{k}_1, \mathbf{k}_2) = \frac{\sqrt{2}}{16\pi}(\frac{kk_1}{k_2})^{1/4}(\mathbf{k} \cdot \mathbf{k}_1 + kk_1)$.

The symmetrical properties of these functions can be found as:

$$\overline{V}^{(2)}(\mathbf{k}, \mathbf{k}_1, \mathbf{k}_2) = \overline{V}^{(1)}(\mathbf{k}_1, \mathbf{k}, \mathbf{k}_2), \tag{2.30}$$

$$\overline{V}^{(3)}(\mathbf{k}, \mathbf{k}_1, \mathbf{k}_2) = \overline{V}^{(1)}(\mathbf{k}_2, \mathbf{k}, \mathbf{k}_1). \tag{2.31}$$

Let

$$V(\mathbf{k}, \mathbf{k}_1, \mathbf{k}_2) = \overline{V}^{(1)}(\mathbf{k}, \mathbf{k}_1, \mathbf{k}_2), \tag{2.32}$$

$$\widetilde{V}(\mathbf{k}, \mathbf{k}_1, \mathbf{k}_2) = \overline{V}^{(4)}(\mathbf{k}, \mathbf{k}_1, \mathbf{k}_2), \tag{2.33}$$

equation (2.25) is transformed to

$$\begin{aligned} i\frac{\partial a_{\mathbf{k}}}{\partial t} - \omega_{\mathbf{k}} a_{\mathbf{k}} = \iint_{-\infty}^{\infty} & [V(\mathbf{k}, \mathbf{k}_1, \mathbf{k}_2) a_{\mathbf{k}_1} a_{\mathbf{k}_2} \delta(\mathbf{k} - \mathbf{k}_1 - \mathbf{k}_2) \\ & + V(\mathbf{k}_1, \mathbf{k}, \mathbf{k}_2) a_{\mathbf{k}_1} a^*_{\mathbf{k}_2} \delta(\mathbf{k} - \mathbf{k}_1 + \mathbf{k}_2) + V(\mathbf{k}_2, \mathbf{k}, \mathbf{k}_1) a^*_{\mathbf{k}_1} a_{\mathbf{k}_2} \delta(\mathbf{k} + \mathbf{k}_1 - \mathbf{k}_2) \\ & + \widetilde{V}(\mathbf{k}, \mathbf{k}_1, \mathbf{k}_2) a^*_{\mathbf{k}_1} a^*_{\mathbf{k}_2} \delta(\mathbf{k} + \mathbf{k}_1 + \mathbf{k}_2)] d\mathbf{k}_1 d\mathbf{k}_2. \end{aligned} \tag{2.34}$$

Equation (2.34) is the canonical formulation of the truncated primitive Euler equations. The framework of the above formulation follows Stiassnie & Shemer (1984) for gravity waves. We note that (2.34) is alternatively derivable using the traditional and general technique of Zakharov & Filonenko (1967), by truncating the Hamiltonian form of (2.1) and (2.2).

2.2 Definition of statistical variables

The following task is to obtain the statistical (spectral) description of the wave field. We define the correlation function $n_{\mathbf{k}}$:

$$\langle a(\mathbf{k}) a^*(\mathbf{k}') \rangle = n_{\mathbf{k}} \delta(\mathbf{k} - \mathbf{k}'), \tag{2.35}$$

where "$\langle\rangle$" denotes the ensemble average. This definition of $n_{\mathbf{k}}$ is physically ambiguous. To obtain a better understanding, we first make connections of $n_{\mathbf{k}}$ with a wave elevation spectrum $I_\eta(\mathbf{k})$, where

$$\langle \widehat{\eta}(\mathbf{k}) \widehat{\eta}^*(\mathbf{k}') \rangle = I_\eta(\mathbf{k}) \delta(\mathbf{k} - \mathbf{k}'). \tag{2.36}$$

To this end, we expand $\langle \widehat{\eta}(\mathbf{k}) \widehat{\eta}^*(\mathbf{k}') \rangle$, using (2.21), as

$$\begin{aligned} \langle \widehat{\eta}(\mathbf{k}) \widehat{\eta}^*(\mathbf{k}') \rangle = & \frac{(kk')^{-1/4}}{2} [\langle a(\mathbf{k}) a^*(\mathbf{k}') \rangle + \langle a(\mathbf{k}) a(-\mathbf{k}') \rangle \\ & + \langle a^*(-\mathbf{k}) a^*(\mathbf{k}') \rangle + \langle a^*(-\mathbf{k}) a(-\mathbf{k}') \rangle] \end{aligned} \tag{2.37}$$

We make assumptions of random phase distribution (which also underlies (2.35)) and isotropic spectrum ($n(k) = n(\mathbf{k})$), under which (2.36) and (2.37) can be reduced to

$$n(\mathbf{k}) = k^{1/2} I_\eta(\mathbf{k}). \tag{2.38}$$

A straightforward and superficial understanding of $I_\eta(\mathbf{k})$ can be obtained by writing $I_\eta(\mathbf{k}) \sim \langle \widehat{\eta}(\mathbf{k})^2 \rangle$. This, in principle, can be used intuitively, but with great cautious, as it messes up the dimension of (2.36). Here we present a more rigourous understanding by connecting $I_\eta(\mathbf{k})$ with the energy density spectrum $\widetilde{I}_\eta(\mathbf{k})$ (e.g. Phillips, 1985), defined under the Wiener-Khinchin theorem:

$$\widetilde{I}_\eta(\mathbf{k}) = \frac{1}{4\pi^2} \int_{-\infty}^{\infty} \overline{\eta(\mathbf{x})\eta(\mathbf{x}+\mathbf{r})} e^{-i\mathbf{k}\cdot\mathbf{r}} d\mathbf{r}, \tag{2.39}$$

with the overline denoting spatial average. We claim that, under the assumptions of homogeneity and ergodicity, $I_\eta(\mathbf{k})$ is proportional to $\widetilde{I}_\eta(\mathbf{k})$, with

$$I_\eta(\mathbf{k}) = 4\pi^2 \widetilde{I}_\eta(\mathbf{k}). \tag{2.40}$$

The proof of (2.40) is shown in Appendix A. Equation (2.39) defines the energy density spectrum $\widetilde{I}_\eta(\mathbf{k})$ as the Fourier Transform of the autocorrelation $\overline{\eta(\mathbf{x})\eta(\mathbf{x}+\mathbf{r})}$. We note that the Fourier Transform here is differently normalized compared with (2.3), as this results in an expression of energy density with unity normalization. This can be obtained by the inverse Fourier Transform of (2.39) with $\mathbf{r} = 0$:

$$\overline{\eta(\mathbf{x})^2} = \int_{-\infty}^{\infty} \widetilde{I}_\eta(\mathbf{k}) d\mathbf{k}. \tag{2.41}$$

Analogously, the leading-order energy density of the wave field $\overline{E}_L = \overline{(\nabla\eta(\mathbf{x}))^2} = \int_{-\infty}^{\infty} k^2 \widetilde{I}_\eta(\mathbf{k}) d\mathbf{k}$ can be expressed in terms of $n(\mathbf{k})$. Invoking the dispersion relation

$$\omega(\mathbf{k}) = k^{3/2}, \tag{2.42}$$

we obtain

$$\overline{E}_L = \frac{1}{4\pi^2}\int_{-\infty}^{\infty} \omega_{\mathbf{k}} n_{\mathbf{k}} d\mathbf{k}. \tag{2.43}$$

We believe that the factor $1/(4\pi^2)$ in (2.43) is overlooked in the original derivation in Pushkarev & Zakharov (2000), which results in a later mis-representation of energy (density) flux P.

2.3 Derivation of the kinetic equation

In order to derive the evolution equation for $n(\mathbf{k})$, we multiply (2.34) by $a^*(\mathbf{k}')$,

$$\begin{aligned} & i a^*_{\mathbf{k}'}\frac{\partial a_{\mathbf{k}}}{\partial t} - \omega_{\mathbf{k}} a_{\mathbf{k}} a^*_{\mathbf{k}'} = \iint_{-\infty}^{\infty} [V(\mathbf{k},\mathbf{k}_1,\mathbf{k}_2) a^*_{\mathbf{k}'} a_{\mathbf{k}_1} a_{\mathbf{k}_2}\delta(\mathbf{k}-\mathbf{k}_1-\mathbf{k}_2) \\ & + V(\mathbf{k}_1,\mathbf{k},\mathbf{k}_2) a^*_{\mathbf{k}'} a_{\mathbf{k}_1} a^*_{\mathbf{k}_2}\delta(\mathbf{k}-\mathbf{k}_1+\mathbf{k}_2) + V(\mathbf{k}_2,\mathbf{k},\mathbf{k}_1) a^*_{\mathbf{k}'} a^*_{\mathbf{k}_1} a_{\mathbf{k}_2}\delta(\mathbf{k}+\mathbf{k}_1-\mathbf{k}_2) \\ & + \widetilde{V}(\mathbf{k},\mathbf{k}_1,\mathbf{k}_2) a^*_{\mathbf{k}'} a^*_{\mathbf{k}_1} a^*_{\mathbf{k}_2}\delta(\mathbf{k}+\mathbf{k}_1+\mathbf{k}_2)] d\mathbf{k}_1 d\mathbf{k}_2, \end{aligned} \tag{2.44}$$

and multiply the conjugate of (2.34) (with $\mathbf{k}$ replaced by $\mathbf{k}'$) by $a(\mathbf{k})$,

$$\begin{aligned} & - i a_{\mathbf{k}}\frac{\partial a^*_{\mathbf{k}'}}{\partial t} - \omega_{\mathbf{k}'} a^*_{\mathbf{k}'} a_{\mathbf{k}} = \iint_{-\infty}^{\infty} [V(\mathbf{k}',\mathbf{k}_1,\mathbf{k}_2) a_{\mathbf{k}} a^*_{\mathbf{k}_1} a^*_{\mathbf{k}_2}\delta(\mathbf{k}'-\mathbf{k}_1-\mathbf{k}_2) \\ & + V(\mathbf{k}_1,\mathbf{k}',\mathbf{k}_2) a_{\mathbf{k}} a^*_{\mathbf{k}_1} a_{\mathbf{k}_2}\delta(\mathbf{k}'-\mathbf{k}_1+\mathbf{k}_2) + V(\mathbf{k}_2,\mathbf{k}',\mathbf{k}_1) a_{\mathbf{k}} a_{\mathbf{k}_1} a^*_{\mathbf{k}_2}\delta(\mathbf{k}'+\mathbf{k}_1-\mathbf{k}_2) \\ & + \widetilde{V}(\mathbf{k}',\mathbf{k}_1,\mathbf{k}_2) a_{\mathbf{k}} a_{\mathbf{k}_1} a_{\mathbf{k}_2}\delta(\mathbf{k}'+\mathbf{k}_1+\mathbf{k}_2)] d\mathbf{k}_1 d\mathbf{k}_2. \end{aligned} \tag{2.45}$$

Averaging the equation obtained by subtraction of (2.45) from (2.44) gives

$$
\begin{aligned}
i\frac{\partial n_{\mathbf{k}}}{\partial t}\delta(\mathbf{k}-\mathbf{k}') + a^*_{\mathbf{k}'}a_{\mathbf{k}}(\omega_{\mathbf{k}'}-\omega_{\mathbf{k}}) = \iint_{-\infty}^{\infty} \Big\{ & \\
& [V(\mathbf{k},\mathbf{k}_1,\mathbf{k}_2)\langle a^*_{\mathbf{k}'}a_{\mathbf{k}_1}a_{\mathbf{k}_2}\rangle\delta(\mathbf{k}-\mathbf{k}_1-\mathbf{k}_2) - V(\mathbf{k}',\mathbf{k}_1,\mathbf{k}_2)\langle a_{\mathbf{k}}a^*_{\mathbf{k}_1}a^*_{\mathbf{k}_2}\rangle\delta(\mathbf{k}'-\mathbf{k}_1-\mathbf{k}_2)] \\
& + [V(\mathbf{k}_1,\mathbf{k},\mathbf{k}_2)\langle a^*_{\mathbf{k}'}a_{\mathbf{k}_1}a^*_{\mathbf{k}_2}\rangle\delta(\mathbf{k}-\mathbf{k}_1+\mathbf{k}_2) - V(\mathbf{k}_1,\mathbf{k}',\mathbf{k}_2)\langle a_{\mathbf{k}}a^*_{\mathbf{k}_1}a_{\mathbf{k}_2}\rangle\delta(\mathbf{k}'-\mathbf{k}_1+\mathbf{k}_2)] \\
& + [V(\mathbf{k}_2,\mathbf{k},\mathbf{k}_1)\langle a^*_{\mathbf{k}'}a^*_{\mathbf{k}_1}a_{\mathbf{k}_2}\rangle\delta(\mathbf{k}+\mathbf{k}_1-\mathbf{k}_2) - V(\mathbf{k}_2,\mathbf{k}',\mathbf{k}_1)\langle a_{\mathbf{k}}a_{\mathbf{k}_1}a^*_{\mathbf{k}_2}\rangle\delta(\mathbf{k}'+\mathbf{k}_1-\mathbf{k}_2)] \\
& + [\widetilde{V}(\mathbf{k},\mathbf{k}_1,\mathbf{k}_2)\langle a^*_{\mathbf{k}'}a^*_{\mathbf{k}_1}a^*_{\mathbf{k}_2}\rangle\delta(\mathbf{k}+\mathbf{k}_1+\mathbf{k}_2) - \widetilde{V}(\mathbf{k}',\mathbf{k}_1,\mathbf{k}_2)\langle a_{\mathbf{k}}a_{\mathbf{k}_1}a_{\mathbf{k}_2}\rangle\delta(\mathbf{k}'+\mathbf{k}_1+\mathbf{k}_2)] \\
& \Big\} d\mathbf{k}_1 d\mathbf{k}_2.
\end{aligned}
\tag{2.46}
$$

We define a third-order correlation function

$$
J_{k12}\delta(\mathbf{k}-\mathbf{k}_1-\mathbf{k}_2) = \langle a^*_{\mathbf{k}}a_{\mathbf{k}_1}a_{\mathbf{k}_2}\rangle. \tag{2.47}
$$

Apply an integral $\int_{-\infty}^{\infty} d\mathbf{k}$ on (2.46) and let $\mathbf{k}' = \mathbf{k}$, we obtain

$$
\begin{aligned}
\frac{\partial n_{\mathbf{k}}}{\partial t} =& 2Im \iint_{-\infty}^{\infty} \Big[V_{k12}J_{k12}\delta_{\mathbf{k}-\mathbf{k}_1-\mathbf{k}_2} - V_{1k2}J_{1k2}\delta_{\mathbf{k}-\mathbf{k}_1+\mathbf{k}_2} \\
& - V_{2k1}J_{2k1}\delta_{\mathbf{k}+\mathbf{k}_1-\mathbf{k}_2} - \widetilde{V}_{k12}\langle a_{\mathbf{k}_1}a_{\mathbf{k}_2}a_{\mathbf{k}}\rangle \Big] d\mathbf{k}_1 d\mathbf{k}_2,
\end{aligned}
\tag{2.48}
$$

where Im takes the imaginary part of the following integral, and we have extensively used the subscripts j for $\mathbf{k}_j$ as arguments of functions .

Equation (2.48) is the evolution equation for $n_{\mathbf{k}}$, which nevertheless involves the third-order statistics. To close (2.48), we need to find closure models for J_{k12}, J_{1k2}, J_{2k1} and $\langle a_{\mathbf{k}_1}a_{\mathbf{k}_2}a_{\mathbf{k}}\rangle$. While all these terms are zero in a linear wave field due to randomness of phases, they are nonzero in second-order perturbation theory as mode coupling is possible for triad resonant interactions. This argument also eliminates the term $\langle a_{\mathbf{k}_1}a_{\mathbf{k}_2}a_{\mathbf{k}}\rangle$ in (2.48), as $\mathbf{k}+\mathbf{k}_1+\mathbf{k}_2 = 0$ does not form a resonant triad, and $\langle a_{\mathbf{k}_1}a_{\mathbf{k}_2}a_{\mathbf{k}}\rangle = 0$ can be obtained in a linear consideration.

Theoretically, J_{k12}, J_{1k2} and J_{2k1} can all be obtained by deriving their evolution equations based on (2.34). Since all these derivations are similar, we present here with the example of $\langle a^*_{\mathbf{k}} a_{\mathbf{k}_1} a_{\mathbf{k}_2} \rangle$, which can be written as

$$\frac{\partial (a^*_{\mathbf{k}} a_{\mathbf{k}_1} a_{\mathbf{k}_2})}{\partial t} = a^*_{\mathbf{k}} a_{\mathbf{k}_1} \frac{\partial a_{\mathbf{k}_2}}{\partial t} + a^*_{\mathbf{k}} a_{\mathbf{k}_2} \frac{\partial a_{\mathbf{k}_1}}{\partial t} + a_{\mathbf{k}_1} a_{\mathbf{k}_2} \frac{\partial a^*_{\mathbf{k}}}{\partial t}, \tag{2.49}$$

We need the representations of all three terms on the RHS. These can be obtained by manipulations of (2.34),

$$\begin{aligned} a^*_{\mathbf{k}} a_{\mathbf{k}_1} \frac{\partial a_{\mathbf{k}_2}}{\partial t} =& - i\omega_{\mathbf{k}_2} a^*_{\mathbf{k}} a_{\mathbf{k}_1} a_{\mathbf{k}_2} - i \iint_{-\infty}^{\infty} \Big[V_{234} a^*_{\mathbf{k}} a_{\mathbf{k}_1} a_{\mathbf{k}_3} a_{\mathbf{k}_4} \delta_{\mathbf{k}_2 - \mathbf{k}_3 - \mathbf{k}_4} \\ &+ V_{324} a^*_{\mathbf{k}} a_{\mathbf{k}_1} a_{\mathbf{k}_3} a^*_{\mathbf{k}_4} \delta_{\mathbf{k}_2 - \mathbf{k}_3 + \mathbf{k}_4} + V_{423} a^*_{\mathbf{k}} a_{\mathbf{k}_1} a^*_{\mathbf{k}_3} a_{\mathbf{k}_4} \delta_{\mathbf{k}_2 + \mathbf{k}_3 - \mathbf{k}_4} \\ &+ \widetilde{V}_{234} a^*_{\mathbf{k}} a_{\mathbf{k}_1} a^*_{\mathbf{k}_3} a^*_{\mathbf{k}_4} \delta_{\mathbf{k}_2 + \mathbf{k}_3 + \mathbf{k}_4} \Big] d\mathbf{k}_3 d\mathbf{k}_4, \end{aligned} \tag{2.50}$$

$$\begin{aligned} a^*_{\mathbf{k}} a_{\mathbf{k}_2} \frac{\partial a_{\mathbf{k}_1}}{\partial t} =& - i\omega_{\mathbf{k}_1} a^*_{\mathbf{k}} a_{\mathbf{k}_1} a_{\mathbf{k}_2} - i \iint_{-\infty}^{\infty} \Big[V_{134} a^*_{\mathbf{k}} a_{\mathbf{k}_2} a_{\mathbf{k}_3} a_{\mathbf{k}_4} \delta_{\mathbf{k}_1 - \mathbf{k}_3 - \mathbf{k}_4} \\ &+ V_{314} a^*_{\mathbf{k}} a_{\mathbf{k}_2} a_{\mathbf{k}_3} a^*_{\mathbf{k}_4} \delta_{\mathbf{k}_1 - \mathbf{k}_3 + \mathbf{k}_4} + V_{413} a^*_{\mathbf{k}} a_{\mathbf{k}_2} a^*_{\mathbf{k}_3} a_{\mathbf{k}_4} \delta_{\mathbf{k}_1 + \mathbf{k}_3 - \mathbf{k}_4} \\ &+ \widetilde{V}_{134} a^*_{\mathbf{k}} a_{\mathbf{k}_2} a^*_{\mathbf{k}_3} a^*_{\mathbf{k}_4} \delta_{\mathbf{k}_1 + \mathbf{k}_3 + \mathbf{k}_4} \Big] d\mathbf{k}_3 d\mathbf{k}_4, \end{aligned} \tag{2.51}$$

$$\begin{aligned} a_{\mathbf{k}_1} a_{\mathbf{k}_2} \frac{\partial a^*_{\mathbf{k}}}{\partial t} =& i\omega_{\mathbf{k}} a^*_{\mathbf{k}} a_{\mathbf{k}_1} a_{\mathbf{k}_2} + i \iint_{-\infty}^{\infty} \Big[V_{k34} a_{\mathbf{k}_1} a_{\mathbf{k}_2} a^*_{\mathbf{k}_3} a^*_{\mathbf{k}_4} \delta_{\mathbf{k} - \mathbf{k}_3 - \mathbf{k}_4} \\ &+ V_{3k4} a_{\mathbf{k}_1} a_{\mathbf{k}_2} a^*_{\mathbf{k}_3} a_{\mathbf{k}_4} \delta_{\mathbf{k} - \mathbf{k}_3 + \mathbf{k}_4} + V_{4k3} a_{\mathbf{k}_1} a_{\mathbf{k}_2} a_{\mathbf{k}_3} a^*_{\mathbf{k}_4} \delta_{\mathbf{k} + \mathbf{k}_3 - \mathbf{k}_4} \\ &+ \widetilde{V}_{k34} a_{\mathbf{k}_1} a_{\mathbf{k}_2} a_{\mathbf{k}_3} a_{\mathbf{k}_4} \delta_{\mathbf{k} + \mathbf{k}_3 + \mathbf{k}_4} \Big] d\mathbf{k}_3 d\mathbf{k}_4, \end{aligned} \tag{2.52}$$

The average of these equations involves the fourth-order statistics, for which we need a model. Since the four-wave interaction is not considered (we have assumed that the three-wave interaction is dominant), there is no four-wave nonlinear coupling in the wave field, i.e., these statistics can be obtained from the consideration of a linear wave field:

$$< a^*_1 a^*_2 a_3 a_4 >= n_1 n_2 (\delta_{1-3}\delta_{2-4} + \delta_{1-4}\delta_{2-3}), \tag{2.53}$$

where we have extensively used j to denote $\mathbf{k}_j$, and $< a^*_1 a_2 a_3 a_4 >=< a^*_1 a^*_2 a^*_3 a_4 >=< a_1 a_2 a_3 a_4 >= 0$. Now, summing up (2.50), (2.51) and (2.52) and taking the average, we obtain

$$\begin{aligned}\frac{\partial\langle a^*_{\mathbf{k}}a_{\mathbf{k}_1}a_{\mathbf{k}_2}\rangle}{\partial t} &= i\langle a^*_{\mathbf{k}}a_{\mathbf{k}_1}a_{\mathbf{k}_2}\rangle(\omega_{\mathbf{k}}-\omega_{\mathbf{k}_1}-\omega_{\mathbf{k}_2}) - i\iint_{-\infty}^{\infty}\Big[\\ &\quad V_{324}n_{\mathbf{k}}n_4(\delta_{k-1}\delta_{4-3}+\delta_{k-3}\delta_{4-1})\delta_{2-3+4}+V_{423}n_{\mathbf{k}}n_3(\delta_{3-4}\delta_{k-1}+\delta_{3-1}\delta_{k-4})\delta_{2+3-4}\\ &+V_{314}n_{\mathbf{k}}n_4(\delta_{k-2}\delta_{4-3}+\delta_{k-3}\delta_{4-2})\delta_{1-3+4}+V_{413}n_{\mathbf{k}}n_3(\delta_{k-2}\delta_{3-4}+\delta_{k-4}\delta_{3-2})\delta_{1+3-4}\\ &-V_{k34}n_3n_4(\delta_{3-1}\delta_{4-2}+\delta_{3-2}\delta_{4-1})\delta_{k-3-4}\Big]d\mathbf{k}_3d\mathbf{k}_4.\end{aligned} \tag{2.54}$$

In (2.54), we can set $\delta_{k-1}=\delta_{k-2}=0$, as these possibilities are excluded by the fact that $a_{\mathbf{k}}$, $a_{\mathbf{k}_1}$ and $a_{\mathbf{k}_2}$ are coupled by triad resonant interactions. Working out the integral in (2.54), we obtain

$$\begin{aligned}\frac{\partial\langle a^*_{\mathbf{k}}a_{\mathbf{k}_1}a_{\mathbf{k}_2}\rangle}{\partial t} &= i\langle a^*_{\mathbf{k}}a_{\mathbf{k}_1}a_{\mathbf{k}_2}\rangle(\omega_{\mathbf{k}}-\omega_{\mathbf{k}_1}-\omega_{\mathbf{k}_2}) - i[V_{k21}n_{\mathbf{k}}n_1\delta_{2-k+1}\\ &\quad +V_{k21}n_{\mathbf{k}}n_1\delta_{2+1-k}+V_{k12}n_{\mathbf{k}}n_2\delta_{1-k+2}+V_{k12}n_{\mathbf{k}}n_2\delta_{1+2-k}\\ &\quad -V_{k12}n_1n_2\delta_{k-1-2}-V_{k21}n_2n_1\delta_{k-2-1}]\\ &= i\langle a^*_{\mathbf{k}}a_{\mathbf{k}_1}a_{\mathbf{k}_2}\rangle(\omega_{\mathbf{k}}-\omega_{\mathbf{k}_1}-\omega_{\mathbf{k}_2}) - 2iV_{k12}\delta_{k-1-2}(n_{\mathbf{k}}n_1+n_{\mathbf{k}}n_2-n_1n_2).\end{aligned} \tag{2.55}$$

⇒

$$\frac{\partial J_{k12}}{\partial t} - iJ_{k12}\Omega_{k12} + iA_{k12} = 0, \tag{2.56}$$

with $\Omega_{k12} \equiv \omega_{\mathbf{k}} - \omega_{\mathbf{k}_1} - \omega_{\mathbf{k}_2}$, and $A_{k12} \equiv 2V_{k12}(n_{\mathbf{k}}n_1 + n_{\mathbf{k}}n_2 - n_1n_2)$.

The solution of (2.56) provides the closure for J_{k12}. This can be obtained by two manners, respectively outlined in Zakharov *et al.* (1992) and Janssen (2003). Both methods yield the same closure of ImJ_{k12} under the assumptions of long term evolution ($t \to \infty$), slow spectral variation and infinite wave domain. Here we present following the procedure of Zakharov *et al.* (1992), and leave the counterpart of Janssen (2003) in Appendix B.

It is usually assumed that the evolution of the spectrum $n_{\mathbf{k}}$, and thus A_{k12}, is slower compared to that of J_{k12}. This can be understood from (2.56) that J_{k12} evolves on a time scale of $O(\epsilon^{-1})$, and from (2.48) that $n_{\mathbf{k}}$ evolves on $O(\epsilon^{-2})$. As a result, the term A_{k12} can be considered as a constant in solving (2.56). This leads to a solution in the form

$$J_{k12} = Bexp(i\Omega_{k12}t) + \frac{A_{k12}}{\Omega_{k12}}. \tag{2.57}$$

The term $Bexp(i\Omega_{k12}t)$ involves a fast oscillation with the change of Ω_{k12} for $t \to \infty$. As it is substituted into (2.48), this term can be neglected under the integration of $\mathbf{k}_1$ and $\mathbf{k}_2$ from $-\infty$ to ∞. This reduces (2.57) to $J_{k12} = A_{k12}/\Omega_{k12}$, which, upon substitution to (2.48), gives

$$\begin{aligned}\frac{\partial n_{\mathbf{k}}}{\partial t} =& 2Im \iint_{-\infty}^{\infty} \Big[\frac{A_{k12}}{\Omega_{k12}+i\epsilon} V_{k12}\delta_{\mathbf{k}-\mathbf{k}_1-\mathbf{k}_2} - \frac{A_{1k2}}{\Omega_{1k2}+i\epsilon} V_{1k2}\delta_{\mathbf{k}_1-\mathbf{k}-\mathbf{k}_2} \\ & - \frac{A_{2k1}}{\Omega_{2k1}+i\epsilon} V_{2k1}\delta_{\mathbf{k}_2-\mathbf{k}-\mathbf{k}_1}\Big] d\mathbf{k}_1 d\mathbf{k}_2.\end{aligned} \tag{2.58}$$

where we have added a small positive parameter $i\epsilon$ to the denominator to circumvent the pole, i.e., to eliminate the singularity of the integral. This procedure is mathematically similar as the limiting absorption principle (e.g. Ignatowsky, 1905). According to the Sokhotski-Plemelj theorem

$$\lim_{\epsilon\to 0^+} \int_{-\infty}^{\infty} \frac{f(x)}{x \pm i\epsilon} dx = \mp i\pi f(0) + \mathcal{P}\int_{-\infty}^{\infty} \frac{f(x)}{x} dx, \tag{2.59}$$

with $\mathcal{P}$ denoting the Cauchy principal value, (2.58) can be reduced to

$$\begin{aligned}\frac{\partial n_{\mathbf{k}}}{\partial t} =& -4\pi \iint_{-\infty}^{\infty} \Big[V_{k12}^2 (n_{\mathbf{k}}n_2 + n_{\mathbf{k}}n_1 - n_1 n_2)\delta(\mathbf{k}-\mathbf{k}_1-\mathbf{k}_2)\delta(\omega_{\mathbf{k}}-\omega_1-\omega_2) \\ & - V_{1k2}^2 (n_1 n_2 + n_1 n_{\mathbf{k}} - n_{\mathbf{k}} n_2)\delta(\mathbf{k}_1-\mathbf{k}-\mathbf{k}_2)\delta(\omega_1-\omega_{\mathbf{k}}-\omega_2) \\ & - V_{2k1}^2 (n_2 n_1 + n_2 n_{\mathbf{k}} - n_{\mathbf{k}} n_1)\delta(\mathbf{k}_2-\mathbf{k}-\mathbf{k}_1)\delta(\omega_2-\omega_{\mathbf{k}}-\omega_1)\Big] d\mathbf{k}_1 d\mathbf{k}_2.\end{aligned} \tag{2.60}$$

Equation (2.60) is the kinetic equation of capillary waves. After some algebraic manipulations, we summarize and write it in the following symmetric form:

$$\frac{\partial n_{\mathbf{k}}}{\partial t} = S(n_{\mathbf{k}}), \tag{2.61}$$

$$S(n_{\mathbf{k}}) = \iint_{-\infty}^{\infty} [R_{\mathbf{k}\mathbf{k}_1\mathbf{k}_2} - R_{\mathbf{k}_1\mathbf{k}\mathbf{k}_2} - R_{\mathbf{k}_2\mathbf{k}\mathbf{k}_1}] d\mathbf{k}_1 d\mathbf{k}_2, \tag{2.62}$$

$$R_{\mathbf{k}\mathbf{k}_1\mathbf{k}_2} = 4\pi|V_{\mathbf{k}\mathbf{k}_1\mathbf{k}_2}|^2\delta(\mathbf{k}-\mathbf{k}_1-\mathbf{k}_2)\delta(\omega_\mathbf{k}-\omega_{\mathbf{k}_1}-\omega_{\mathbf{k}_2})[n_{\mathbf{k}_1}n_{\mathbf{k}_2}-n_\mathbf{k}n_{\mathbf{k}_1}-n_\mathbf{k}n_{\mathbf{k}_2}], \quad (2.63)$$

$$V_{\mathbf{k}\mathbf{k}_1\mathbf{k}_2} = \frac{1}{8\pi\sqrt{2}}(\omega_\mathbf{k}\omega_{\mathbf{k}_1}\omega_{\mathbf{k}_2})^{1/2}[\frac{L_{\mathbf{k}_1,\mathbf{k}_2}}{(k_1k_2)^{1/2}k} - \frac{L_{\mathbf{k},-\mathbf{k}_1}}{(kk_1)^{1/2}k_2} - \frac{L_{\mathbf{k},-\mathbf{k}_2}}{(kk_2)^{1/2}k_1}], \quad (2.64)$$

$$L_{\mathbf{k}_1,\mathbf{k}_2} = \mathbf{k}_1\cdot\mathbf{k}_2 + k_1k_2. \quad (2.65)$$

For energy transfer to be possible in the framework of KE, i.e., $R_{\mathbf{k}\mathbf{k}_1\mathbf{k}_2} \neq 0$, we have mathematically assumed that the two arguments in the two delta functions in (2.63) can vanish simultaneously. This stems from (2.58) where we allow $\epsilon \to 0^+$, and physically corresponds to the exact triad resonance. Under the dispersion relation of capillary waves, this is not possible in a finite (rectangular) domain (Kartashova, 1990). Therefore, an inherent assumption involved in the KE is that the wave field evolves in an infinite domain.

2.4 Stationary solution of the kinetic equation

Consider the kinetic equation (KE) (2.61)∼(2.65). This set of equations can be simplified in an isotropic wavefield, by transforming the integral in (2.62) from Cartesian coordinates $\mathbf{k}$ to Polar coordinates (k,θ), with the purpose of eliminating the angle dependency in the KE. The result (after multiplication of $kdk/d\omega$ on both sides to keep the symmetry) can be written as

$$k\frac{dk}{d\omega}\frac{\partial n_k}{\partial t} = \int_0^{2\pi}\int_0^{2\pi}\int_0^{\infty}\int_0^{\infty}[R_{\mathbf{k}\mathbf{k}_1\mathbf{k}_2} - R_{\mathbf{k}_1\mathbf{k}\mathbf{k}_2} - R_{\mathbf{k}_2\mathbf{k}\mathbf{k}_1}]kk_1k_2\frac{dk}{d\omega}\frac{dk_1}{d\omega_1}\frac{dk_2}{d\omega_2}d\omega_1 d\omega_2 d\theta_1 d\theta_2. \quad (2.66)$$

where θ_i is the argument of the vector $\mathbf{k}_i$.

Consider the first term $R_{\mathbf{k}\mathbf{k}_1\mathbf{k}_2}$ as an example for the evaluation of this integral. Substitution of (2.63), (2.64), and separation of the angle dependent part of the integrand lead to

$$
\begin{aligned}
&\int_0^{2\pi}\int_0^{2\pi}\int_0^{\infty}\int_0^{\infty} R_{\mathbf{k}\mathbf{k}_1\mathbf{k}_2} k k_1 k_2 \frac{dk}{d\omega}\frac{dk_1}{d\omega_1}\frac{dk_2}{d\omega_2} d\omega_1 d\omega_2 d\theta_1 d\theta_2 = \\
&\frac{1}{108\pi}\int_0^{\infty}\int_0^{\infty} (\omega_k\omega_1\omega_2)^{4/3}\delta(\omega_k-\omega_1-\omega_2)(n_{\omega_1}n_{\omega_2}-n_\omega n_{\omega_1}-n_\omega n_{\omega_2}) \qquad (2.67)\\
&\int_0^{2\pi}\int_0^{2\pi}[\frac{L_{1,2}}{(k_1k_2)^{1/2}k}-\frac{L_{k,-1}}{(kk_1)^{1/2}k_2}-\frac{L_{k,-2}}{(kk_2)^{1/2}k_1}]^2\delta(\mathbf{k}-\mathbf{k}_1-\mathbf{k}_2)d\theta_1 d\theta_2 d\omega_1 d\omega_2,
\end{aligned}
$$

where $n_\omega \equiv n_k$ for $k = \omega^{2/3}$.

Equation (2.67) involves a key integral which appears in many wave turbulence derivations (for another example, gravity waves, Zakharov, 2010), in the form of

$$
I = \int_0^{2\pi}\int_0^{2\pi} f(Q)\delta(\mathbf{k}-\mathbf{k}_1-\mathbf{k}_2)d\theta_1 d\theta_2, \qquad (2.68)
$$

where $f(Q)$ is a general function depending on $Q = (k, k_1, k_2, \mathbf{k}_1\cdot\mathbf{k}_2, \mathbf{k}\cdot\mathbf{k}_1, \mathbf{k}\cdot\mathbf{k}_2)$. The argument of the delta function in (2.68) vanishes when θ_1 and θ_2 take values which make vectors $\mathbf{k}$, $\mathbf{k}_1$ and $\mathbf{k}_2$ form a triangle. Denoting variables on the triangle with a subscript "Δ", the integral can be evaluated as

$$
I = \int_0^{2\pi}\int_0^{2\pi} f(Q)\delta(k-k_1cos\theta_1-k_2cos\theta_2)\delta(k_1sin\theta_1+k_2sin\theta_2)d\theta_1 d\theta_2 = 2\cdot|\mathcal{J}_\Delta|^{-1}f(Q_\Delta) \qquad (2.69)
$$

where $\mathcal{J}_\Delta$ is the Jacobian determinant

$$
\mathcal{J}_\Delta = \left|\begin{matrix} \frac{\partial(k_1cos\theta_1+k_2cos\theta_2)}{\partial\theta_1} & \frac{\partial(k_1cos\theta_1+k_2cos\theta_2)}{\partial\theta_2} \\ \frac{\partial(k_1sin\theta_1+k_2sin\theta_2)}{\partial\theta_1} & \frac{\partial(k_1sin\theta_1+k_2sin\theta_2)}{\partial\theta_2} \end{matrix}\right|_\Delta \qquad (2.70)
$$

The factor "2" in (2.69) comes from the fact that, for given $\mathbf{k}$, k_1 and k_2 (the delta constraint on frequency ensures that $k > k_1$, $k > k_2$ and $k < k_1+k_2$), there are always two possible ways to choose θ_1 and θ_2 (along the integration path) in a 2D space to

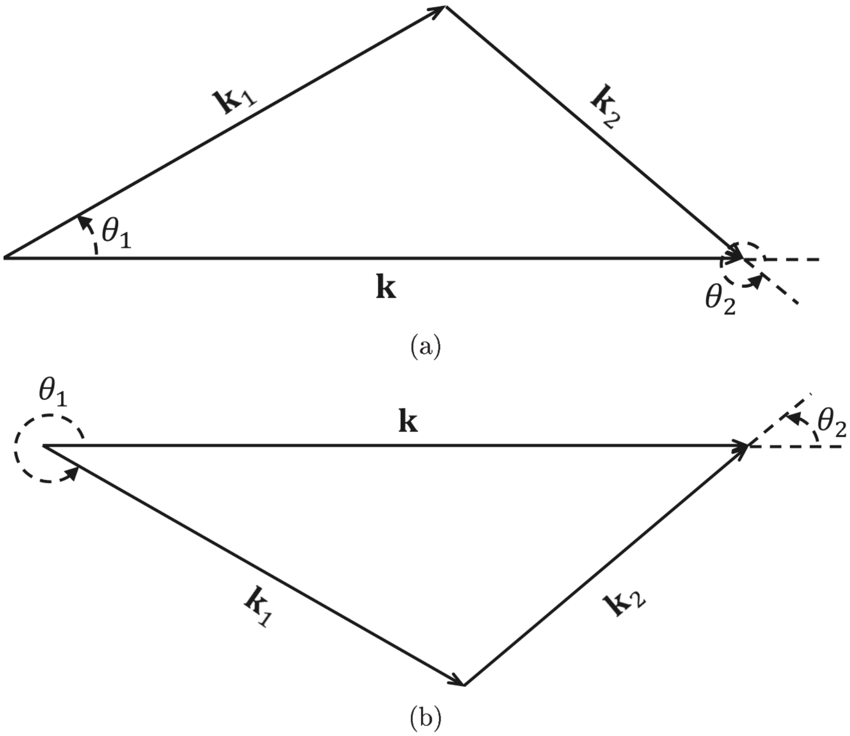

Figure 2-1: Two possible ways (a) and (b) to choose θ_1 and θ_2 in a 2D space to form a triangle ($\mathbf{k}_\Delta$, $\mathbf{k}_{1\Delta}$, $\mathbf{k}_{2\Delta}$), for given $\mathbf{k}$, k_1 and k_2.

form a triangle $\mathbf{k} - \mathbf{k}_1 - \mathbf{k}_2 = 0$), for which $f(Q)$ takes the same value, as shown in figure 2-1. This is missed in the original derivation in Pushkarev & Zakharov (2000). Substitution of (2.70) to (2.69) gives

$$I = f(Q_\Delta)/T_\Delta, \tag{2.71}$$

where T_Δ is the area of the triangle formed by k, k_1 and k_2, and $Q_\Delta \equiv Q(\mathbf{k}, \mathbf{k}_1, \mathbf{k}_2)$ for which $\mathbf{k} - \mathbf{k}_1 - \mathbf{k}_2 = 0$.

Note that $f(Q_\Delta)$ only depends on k, k_1 and k_2, as the angles between the vectors are uniquely determined given the triangle $\mathbf{k} - \mathbf{k}_1 - \mathbf{k}_2 = 0$. Therefore, substitution of (2.71) into (2.67) eliminates all the angle dependency in the integral. This procedure can next be applied on the second and third terms in (2.66), and we obtain the kinetic equation for an isotropic wave field:

$$
\begin{aligned}
k\frac{dk}{d\omega}\frac{\partial n_k}{\partial t} = \iint_0^\infty \Big[& S_{\omega\omega_1\omega_2}\delta(\omega-\omega_1-\omega_2)(n_{\omega_1}n_{\omega_2}-n_\omega n_{\omega_1}-n_\omega n_{\omega_2}) \\
& - S_{\omega_1\omega\omega_2}\delta(\omega_1-\omega-\omega_2)(n_\omega n_{\omega_2}-n_{\omega_1}n_\omega-n_{\omega_1}n_{\omega_2}) \\
& - S_{\omega_2\omega\omega_1}\delta(\omega_2-\omega-\omega_1)(n_\omega n_{\omega_1}-n_\omega n_{\omega_2}-n_{\omega_2}n_{\omega_1})\Big] d\omega_1 d\omega_2,
\end{aligned}
\tag{2.72}
$$

where

$$
S_{\omega_l\omega_m\omega_n} = \frac{1}{27\pi}(\omega_l\omega_m\omega_n)^{4/3}\frac{1}{k_l^2}\cdot \frac{[(1+\frac{1-\xi_1^{4/3}-\xi_2^{4/3}}{2\xi_1^{2/3}\xi_2^{2/3}})(\xi_1\xi_2)^{1/3}-(1-\frac{1+\xi_1^{4/3}-\xi_2^{4/3}}{2\xi_1^{2/3}})(\frac{\xi_1}{\xi_2^2})^{1/3}-(1-\frac{1+\xi_2^{4/3}-\xi_1^{4/3}}{2\xi_2^{2/3}})(\frac{\xi_2}{\xi_1^2})^{1/3}]^2}{\sqrt{4\xi_1^{4/3}\xi_2^{4/3}-(1-\xi_1^{4/3}-\xi_2^{4/3})^2}},
\tag{2.73}
$$

with $\xi_1 = \omega_m/\omega_l$ and $\xi_2 = \omega_n/\omega_l$. We note that in the derivation of (2.72), we have expressed the area of a triangle $T_\Delta = \sqrt{2(k^2k_1^2+k^2k_2^2+k_1^2k_2^2)-(k^4+k_1^4+k_2^4)}/4$. The right hand side of (2.72) is twice as that in Pushkarev & Zakharov (2000), due to the correction of the integral (2.68).

The following steps seek for a stationary power-law solution of (2.72). We first note two properties of function S:

- Homogeneous property of S:

$$
S(\varepsilon\omega,\varepsilon\omega_1,\varepsilon\omega_2) = \varepsilon^{8/3}S(\omega,\omega_1,\omega_2). \tag{2.74}
$$

- Symmetric property of S:

$$
S(\omega,\omega_1,\omega_2) = S(\omega,\omega_2,\omega_1). \tag{2.75}
$$

Suppose

$$
n_\omega = A\omega^x \tag{2.76}
$$

is a stationary solution of (2.72). We shall substitute (2.76) into the RHS of (2.72) with $\partial n_k/\partial t = 0$, solve for the exponent x, and relate A to the energy flux P. For this purpose, we need to make a (Zakharov) conformal transformation in the second term of RHS (2.72)

$$\omega_1 = \frac{\omega^2}{\omega_1'}, \quad \omega_2 = \frac{\omega\omega_2'}{\omega_1'}, \tag{2.77}$$

and in the third term

$$\omega_1 = \frac{\omega\omega_1'}{\omega_2'}, \quad \omega_2 = \frac{\omega^2}{\omega_2'}. \tag{2.78}$$

Now let us transform the terms in (2.72) one by one.

The first term:

$$\to \iint_0^\infty S(\omega,\omega_1,\omega_2)\delta(\omega-\omega_1-\omega_2)A^2\Big[(\omega_1\omega_2)^x-(\omega\omega_1)^x-(\omega\omega_2)^x\Big]d\omega_1 d\omega_2; \tag{2.79}$$

The second term:

$$\begin{aligned}\to -\iint_0^\infty & S(\frac{\omega^2}{\omega_1'},\omega,\frac{\omega\omega_2'}{\omega_1'})\delta(\frac{\omega^2}{\omega_1'}-\omega-\frac{\omega\omega_2'}{\omega_1'})A^2 \\ & \Big[(\omega\frac{\omega\omega_2'}{\omega_1'})^x-(\omega\frac{\omega^2}{\omega_1'})^x-(\frac{\omega^2}{\omega_1'}\frac{\omega\omega_2'}{\omega_1'})^x\Big]d(\frac{\omega^2}{\omega_1'})d(\frac{\omega\omega_2'}{\omega_1'}) \\ = -\iint_0^\infty & (\frac{\omega}{\omega_1})^{14/3+2x}S(\omega,\omega_1,\omega_2)\delta(\omega-\omega_1-\omega_2)A^2 \\ & \Big[(\omega_1\omega_2)^x-(\omega\omega_1)^x-(\omega\omega_2)^x\Big]d\omega_1 d\omega_2;\end{aligned} \tag{2.80}$$

The third term:

$$\to -\iint_0^\infty(\frac{\omega}{\omega_2})^{14/3+2x}S(\omega,\omega_1,\omega_2)\delta(\omega-\omega_1-\omega_2)A^2\Big[(\omega_1\omega_2)^x-(\omega\omega_1)^x-(\omega\omega_2)^x\Big]d\omega_1 d\omega_2. \tag{2.81}$$

These transform (2.72) to

$$\begin{aligned}k\frac{dk}{d\omega}\frac{\partial n_k}{\partial t} = \iint_0^\infty & S(\omega,\omega_1,\omega_2)\delta(\omega-\omega_1-\omega_2)A^2 \\ & \Big[(\omega_1\omega_2)^x-(\omega\omega_1)^x-(\omega\omega_2)^x\Big]\Big[1-(\frac{\omega}{\omega_1})^y-(\frac{\omega}{\omega_2})^y\Big]d\omega_1 d\omega_2,\end{aligned} \tag{2.82}$$

where $y = 14/3 + 2x$.

There are two stationary solutions of (2.82): $x = -1$ and $y = -1 (x = -17/6)$. The former represents a thermodynamically equilibrium distribution where energy flux is zero (as all three energy-transfer terms on the RHS of (2.72) vanish). This is not what we are physically interested. The latter corresponds to the Kolmogorv-Zakharov spectrum which is formed by the balance of energy transfer and carries a finite energy flux.

The remaining task is to relate A with the energy flux P so that we can find the scaling between n_ω and P. To determine P, we invoke the equation of balance of spectral energy:

$$\frac{\partial \epsilon_\omega}{\partial t} + \frac{\partial P}{\partial \omega} = 0, \tag{2.83}$$

where ϵ_ω is the spectral density of energy density. Transforming (2.43) to frequency integration, we obtain

$$\overline{E}_L = \frac{1}{4\pi^2} \int_0^\infty \omega_k n_k \cdot 2\pi k \frac{dk}{d\omega} d\omega. \tag{2.84}$$

Therefore, ϵ_ω can be expressed by $\epsilon_\omega = \omega N_\omega / (4\pi^2)$, where $N_\omega = 2\pi k n_k dk/d\omega$ (note that this is different with n_ω), such that $\overline{E}_L = \int_0^\infty \epsilon_\omega d\omega$.

Integrate (2.83) with respect to ω, we obtain

$$P = -\int_0^\omega \frac{\partial \epsilon_\omega}{\partial t} d\omega = -\frac{1}{4\pi^2} \int_0^\omega \omega \frac{\partial N_\omega}{\partial t} d\omega. \tag{2.85}$$

We note that the factor $1/(4\pi^2)$ is missed in Pushkarev & Zakharov (2000). Evaluation of (2.85) can be obtained by substituting (2.82), which, under the solution of

$y = -1$, yields

$$\begin{aligned} P =& -\frac{1}{2\pi}\int_0^\omega \omega k \frac{dk}{d\omega}\frac{\partial n_k}{\partial t}\Big|_{y=-1} d\omega \\ =& -\frac{1}{2\pi}\int_0^\omega \omega^y d\omega \iint_0^\infty S(1,\xi_1,\xi_2)\delta(1-\xi_1-\xi_2)A^2\Big[(\xi_1\xi_2)^x - \xi_1^x - \xi_2^x\Big] \\ & \qquad\qquad \Big[1-\xi_1^{-y}-\xi_2^{-y}\Big]d\xi_1 d\xi_2\Bigg|_{y=-1} \\ =& -\frac{A^2}{54\pi^2}\frac{\omega^{y+1}}{y+1}J(y)\Big|_{y=-1}, \end{aligned} \tag{2.86}$$

where

$$J(y) = \iint_0^\infty (\xi_1\xi_2)^{4/3}\delta(1-\xi_1-\xi_2)\Big[(\xi_1\xi_2)^x - \xi_1^x - \xi_2^x\Big]\Big[1-\xi_1^{-y}-\xi_2^{-y}\Big]$$
$$\frac{\Big[(1+\frac{1-\xi_1^{4/3}-\xi_2^{4/3}}{2\xi_1^{2/3}\xi_2^{2/3}})(\xi_1\xi_2)^{1/3} - (1-\frac{1+\xi_1^{4/3}-\xi_2^{4/3}}{2\xi_1^{2/3}})(\frac{\xi_1}{\xi_2^2})^{1/3} - (1-\frac{1+\xi_2^{4/3}-\xi_1^{4/3}}{2\xi_2^{2/3}})(\frac{\xi_2}{\xi_1^2})^{1/3}\Big]^2}{\sqrt{4\xi_1^{4/3}\xi_2^{4/3}-(1-\xi_1^{4/3}-\xi_2^{4/3})^2}} d\xi_1 d\xi_2. \tag{2.87}$$

Equation (2.86) involves 0/0 and can be evaluated by L'Hospital's Rule. This leads to

$$P = -\frac{A^2}{54\pi^2}\frac{\partial J(y)}{\partial y}\Big|_{y=-1}, \tag{2.88}$$

where

$$\frac{\partial J(y)}{\partial y}\Big|_{y=-1} = \iint_0^\infty (\xi_1\xi_2)^{4/3}\delta(1-\xi_1-\xi_2)\Big[(\xi_1\xi_2)^x - \xi_1^x - \xi_2^x\Big]\Big[\xi_1 log\xi_1 - \xi_2 log\xi_2\Big]$$
$$\frac{\Big[(1+\frac{1-\xi_1^{4/3}-\xi_2^{4/3}}{2\xi_1^{2/3}\xi_2^{2/3}})(\xi_1\xi_2)^{1/3} - (1-\frac{1+\xi_1^{4/3}-\xi_2^{4/3}}{2\xi_1^{2/3}})(\frac{\xi_1}{\xi_2^2})^{1/3} - (1-\frac{1+\xi_2^{4/3}-\xi_1^{4/3}}{2\xi_2^{2/3}})(\frac{\xi_2}{\xi_1^2})^{1/3}\Big]^2}{\sqrt{4\xi_1^{4/3}\xi_2^{4/3}-(1-\xi_1^{4/3}-\xi_2^{4/3})^2}} d\xi_1 d\xi_2. \tag{2.89}$$

The integral in (2.89) can be evaluated numerically to yield $\partial J/\partial y\Big|_{y=-1} = -0.28$. This establishes the relation of A and P and leads to the final solution:

$$n_\omega = 2\pi C P^{1/2}\omega^{-17/6}, \tag{2.90}$$

where the Kolmogorov Constant

$$C = 6.97. \tag{2.91}$$

Note that we have factored "2π" out in (2.90). This compensates for the missing of factor $1/(4\pi^2)$ in (2.85) in Pushkarev & Zakharov (2000). The final solution of C (2.91) is thus different as that in Pushkarev & Zakharov (2000) with a factor of $\sqrt{2}$, due to the corrected evaluation of the integral (2.68).

2.5 Summary of solutions

While (2.90) and (2.91) are the final solutions of WTT for capillary waves, we summarize here the solutions in different forms. Transforming (2.90) to wavenumber representation, we obtain

$$n_k = 2\pi C P^{1/2} k^{-17/4}. \tag{2.92}$$

This can also be expressed in terms of the wave elevation spectrum $I_\eta(k)$ by using (2.38):

$$I_\eta(k) = 2\pi C P^{1/2} k^{-19/4}. \tag{2.93}$$

Finally, we retrieve the parameters ρ and σ to the solution, and express the solution in dimensional form:

$$I_\eta(k) = 2\pi C \frac{P^{1/2}\rho^{1/4}}{\sigma^{3/4}} k^{-19/4}. \tag{2.94}$$

For sake of completeness, we repeat the dimensions of parameters here: $P(kg/s^3)$, $\sigma(kg/s^2)$, $\rho(kg/m^3)$ and $I_\eta(m^4)$.

2.6 Summary of assumptions

We list all inherent assumptions involved in the derivation. These include:

1. Weak nonlinearity;

2. Random phase distribution;

3. Infinite domain;
4. Dominance of three-wave interactions;
5. Homogeneity and ergodicity;
6. Long-time evolution;
7. Slow spectral variation.

We will show in later chapters that the assumption 3 is a most delicate one in numerical simulations or physical experiments, as these are usually obtained in finite computational domains or wave basins.

Chapter 3

Numerical formulation for primitive Euler equations

In this chapter, we present the numerical formulation for capillary-wave primitive Euler equations. We introduce two formulations for the surface tension term, which are developed in consistency with the frameworks of Dommermuth & Yue (1987) and West *et al.* (1987). The theoretical difference of these two methods are discussed, though they can be used interchangeably for numerical purposes. The developed method is benchmarked against an analytical solution of Crapper wave. We further present an Implicit 4th-order Runge-Kutta (IRK4) scheme, which are designed to alleviate the time step limitation due to capillarity. The linear and nonlinear stability of this scheme is analyzed. Finally, we introduce a spatial de-aliasing scheme, which can be considered as an improvement to the one used in Dommermuth & Yue (1987).

3.1 Basic numerical formulation

As introduced in Chapter 2, we consider capillary waves in two surface dimensions on the free surface of an ideal incompressible fluid. The system is described in the context of potential flow with governing equations (2.1) and (2.2) in terms of the surface elevation $\eta(\mathbf{x}, t)$ and surface potential $\phi^s(\mathbf{x}, t) \equiv \phi(\mathbf{x}, z = \eta, t)$. For initial conditions, $\phi^s(\mathbf{x}, 0)$ and $\eta(\mathbf{x}, 0)$ are prescribed.

3.1.1 Nonlinear expansion to determine ϕ_z

Equations (2.1) and (2.2) are numerically evolved in time from the initial conditions. Within each time step, the key element is to solve for the surface vertical velocity $\phi_z(\mathbf{x}, t)$ from a boundary value problem, with values of $\phi^s(\mathbf{x}, t)$ and $\eta(\mathbf{x}, t)$ defined on the free surface and the field (Laplace) equation

$$\nabla^2_{\mathbf{x}}\phi(\mathbf{x}, z, t) + \phi_{zz}(\mathbf{x}, z, t) = 0, \quad \text{for } z \leq \eta(\mathbf{x}, t). \tag{3.1}$$

The algorithm of this evaluation is described in Dommermuth & Yue (1987) and West *et al.* (1987). Both methods rely on an Taylor expansion of surface quantities based on their value at $z = 0$, but differ in detail regarding the nonlinearity order in representing ϕ_z. Generally, this problem can be considered as a Dirichlet-Neumann Operation (DNO), and this class of method is referred to as boundary perturbation method (Nicholls & Reitich, 2001). For completeness, we outline the procedures here, with an illustration of the difference between the two methods.

We assume that $\eta(\mathbf{x}, t)$ and $\phi^s(\mathbf{x}, t)$ are $O(\epsilon)$ quantities, where ϵ is a small parameter measuring the wave steepness. We consider a consistent approximation up to and including a given order M in ϵ, and write $\Phi(\mathbf{x}, t) \equiv \phi(\mathbf{x}, 0, t)$ as a perturbation series in ϵ:

$$\Phi(\mathbf{x}, t) = \sum_{m=1}^{M} [\Phi]^{(m)}(\mathbf{x}, t), \tag{3.2}$$

where $[\ ]^{(m)}$ denotes a quantity of $O(\epsilon^m)$. Consistently up to order M, an equation can be obtained which relates the surface potential ϕ^s with $[\Phi]^{(m)}$ using the Taylor expansion around $z = 0$:

$$\phi^s(\mathbf{x}, t) = \sum_{m=1}^{M} \sum_{l=0}^{M-m} \frac{\eta^l}{l!} \frac{\partial^l}{\partial z^l} [\Phi]^{(m)}(\mathbf{x}, t). \tag{3.3}$$

$[\Phi]^{(m)}$ can be solved by inverting (3.3) at each order, which gives

$$[\Phi]^{(m)}(\mathbf{x}, t) = [R]^{(m)}(\mathbf{x}, t), \quad m = 1, 2, ..., M, \tag{3.4}$$

where

$$[R]^{(1)}(\mathbf{x},t)=\phi^s(\mathbf{x},t), \tag{3.5}$$

and

$$[R]^{(m)}(\mathbf{x},t)=-\sum_{l=1}^{m-1}\frac{\eta^l}{l!}\frac{\partial^l}{\partial z^l}[\Phi]^{(m-l)}(\mathbf{x},t), \quad m=2,3,...M. \tag{3.6}$$

These equations can be solved successively at increasing orders for any prescribed ϕ^s and η.

Our ultimate goal is to determine the surface vertical velocity $\phi_z(\mathbf{x},t)$. To this end, we express $\phi(\mathbf{x},z,t)$ as a truncated eigenfunction expansion

$$\phi(\mathbf{x},z,t)=\sum_{m=1}^{M}\sum_{n=1}^{N}[\widehat{\Phi}_n]^{(m)}(t)\Psi_n(\mathbf{x},z), \tag{3.7}$$

where $\Psi_n(\mathbf{x},z)$ is an eigenfunction at mode n which satisfies (3.1). $\phi_z(\mathbf{x},t)$ can be determined by vertical derivative of (3.7), where $\Psi_n(\mathbf{x},z)$ is expressed as a Taylor expansion around $z=0$:

$$[\phi_z](\mathbf{x},t;M)=\sum_{m=1}^{M}[\phi_z]^{(m)}(\mathbf{x},t)=\sum_{m=1}^{M}\sum_{l=0}^{M-m}\frac{\eta^l}{l!}\sum_{n=1}^{N}[\widehat{\Phi}_n]^{(m)}(t)\frac{\partial^{l+1}}{\partial z^{l+1}}\Psi_n(\mathbf{x},z)|_{z=0}. \tag{3.8}$$

where $[\ ](\mathbf{x},t;M)=\sum_{m=1}^{M}[\ ]^{(m)}(\mathbf{x},t)$ represents a quantity up to order M. Equation (3.1) (with the deep-water boundary condition) indicates that the eigenfunction $\Psi_n(\mathbf{x},z)$ can be expressed in the form of

$$\Psi_n(\mathbf{x},z)\sim exp(i\mathbf{k}_n\cdot\mathbf{x}+k_nz), \tag{3.9}$$

where $k_n=|\mathbf{k}_n|$. This provides significant numerical convenience in evaluating (3.8), as the vertical derivative can be calculated by

$$\frac{\partial^{l+1}}{\partial z^{l+1}}\Psi_n(\mathbf{x},z)|_{z=0}=k_n^{l+1}\Psi_n(\mathbf{x},0), \tag{3.10}$$

and $[\widehat{\Phi}_n]^{(m)}(t)$ can be determined using the Fast Fourier Transform (FFT) of $[\Phi]^{(m)}(\mathbf{x},t)$

(by assuming horizontally periodic boundary condition).

The formulations in Dommermuth & Yue (1987) and West *et al.* (1987) (hereafter referred to as DY and WW) differ in the next step in truncating $\phi_z(\mathbf{x}, t)$ in (2.1) and (2.2). DY simply represents $\phi_z(\mathbf{x}, t)$ using $[\phi_z](\mathbf{x}, t; M)$, which results in the following evolution equations:

$$\eta_t + \nabla_{\mathbf{x}}\phi^s \cdot \nabla_{\mathbf{x}}\eta - (1 + \nabla_{\mathbf{x}}\eta \cdot \nabla_{\mathbf{x}}\eta)[\phi_z](\mathbf{x}, t; M) = 0, \tag{3.11}$$

$$\phi^s_t + \mathcal{T}_{DY}(\eta) + \frac{1}{2}\nabla_{\mathbf{x}}\phi^s \cdot \nabla_{\mathbf{x}}\phi^s - \frac{1}{2}(1 + \nabla_{\mathbf{x}}\eta \cdot \nabla_{\mathbf{x}}\eta)[\phi_z](\mathbf{x}, t; M)^2 = 0, \tag{3.12}$$

where $\mathcal{T}_{DY}(\eta)$ denotes the surface tension term that will be discussed in the next section. In viewing (3.11) and (3.12), we see that these two equations consistently include all terms within order M, but introduce some terms with higher orders (e.g., $\nabla_{\mathbf{x}}\eta \cdot \nabla_{\mathbf{x}}\eta\phi_z(\mathbf{x}, t; M)$ with order $M + 2$). In contrast, WW develops a completely order-consistent scheme, which truncates (2.1) and (2.2) exactly at order M:

$$\eta_t + \nabla_{\mathbf{x}}\phi^s \cdot \nabla_{\mathbf{x}}\eta - [\phi_z](\mathbf{x}, t; M) - \nabla_{\mathbf{x}}\eta \cdot \nabla_{\mathbf{x}}\eta[\phi_z](\mathbf{x}, t; M - 2) = 0, \tag{3.13}$$

$$\phi^s_t + \mathcal{T}_{WW}(\eta) + \frac{1}{2}\nabla_{\mathbf{x}}\phi^s \cdot \nabla_{\mathbf{x}}\phi^s - \frac{1}{2}[\phi_z^2](\mathbf{x}, t; M) - \frac{1}{2}\nabla_{\mathbf{x}}\eta \cdot \nabla_{\mathbf{x}}\eta[\phi_z^2](\mathbf{x}, t; M - 2), \tag{3.14}$$

where

$$[\phi_z^2](\mathbf{x}, t; M) = \sum_{m=1}^{M}\sum_{l=1}^{m}[\phi_z]^{(l)}[\phi_z]^{(m-l)}. \tag{3.15}$$

In terms of the numerical accuracy, the DY and WW formulations are equivalent: they both result in a truncation error of $O(\epsilon^{M+1})$ in η or ϕ^s, even though WW excludes all terms higher than M while DY retains some of them. As we have tested, the truncation error of these two formulations are case-dependent. Nevertheless, the WW formulation bears a slight theoretical advantage as it keeps an exact Hamiltonian structure of the truncated equations (see Milder, 1990). Upon proper truncation in terms of $\mathcal{T}_{WW}(\eta)$ and energy E^{WW}, exact energy conservation within order M can be obtained in the WW framework. This will be illustrated by an example after we introduce the formulations of $\mathcal{T}$ and E.

3.1.2 Formulation of the surface tension term $\mathcal{T}$

In the framework of DY, the term $\mathcal{T}_{DY}(\eta)$ can be represented by its fully nonlinear form

$$\mathcal{T}_{DY}(\eta) = -\nabla_{\mathbf{x}} \cdot \frac{\nabla_{\mathbf{x}}\eta}{\sqrt{1+\nabla_{\mathbf{x}}\eta \cdot \nabla_{\mathbf{x}}\eta}}. \tag{3.16}$$

This formulation, in principle of perturbation series, can be considered as equivalent to $\mathcal{T}_{DY}(\eta) = \sum_{m=1}^{\infty}[\mathcal{T}(\eta)]^{(m)}$. Indeed, this introduces nonlinear terms with order higher than M which are merged into the truncation error of $O(\epsilon^{M+1})$.

On the other hand, to develop the formulation of $\mathcal{T}_{WW}(\eta)$ consistent with the WW framework, we shall truncate (3.16) at order M. This can be obtained using Taylor expansion around $|\nabla_{\mathbf{x}}\eta|^2 = 0$:

$$\mathcal{T}_{WW}(\eta) = -\nabla_{\mathbf{x}} \cdot \Big\{\nabla_{\mathbf{x}}\eta\big(1 + \sum_{m=1}^{FL\left[\frac{M-1}{2}\right]} \frac{1}{m!}(-1)^m \frac{1\times 3\times ...\times(2m-1)}{2^m}|\nabla_{\mathbf{x}}\eta|^{2m}\big)\Big\}, \tag{3.17}$$

where $FL[a]$ calculates the nearest integer less than or equal to a. Substituting (3.17) into (3.14) leads to the evolution equations truncated exactly at nonlinearity order M.

3.1.3 Formulation of the energy E

The total energy in the wavefield can be decomposed into the kinetic energy and potential energy (due to surface tension):

$$E = E_{kin} + E_{pot}. \tag{3.18}$$

In the framework of DY, both E_{kin}^{DY} and E_{pot}^{DY} can be represented by their fully nonlinear forms

$$E_{kin}^{DY} = \frac{1}{2}\int \phi^s \eta_t d\mathbf{x}, \tag{3.19}$$

and

$$E_{pot}^{DY} = \frac{1}{2}\int (\sqrt{1+|\nabla\eta|^2} - 1)d\mathbf{x}. \tag{3.20}$$

The WW framework requires both E_{kin}^{WW} and E_{pot}^{WW} to be truncated at order $M+1$. Mathematically, E_{kin}^{WW} retains the same form as E_{kin}^{DY},

$$E_{kin}^{WW} = \frac{1}{2}\int \phi^s \eta_t d\mathbf{x}, \tag{3.21}$$

as the term η_t determined by (3.13) contains orders exactly up to M. The potential energy E_{pot}^{WW} can be evaluated by Taylor expansion around $|\nabla_{\mathbf{x}}\eta|^2 = 0$:

$$E_{pot}^{WW} = \frac{1}{2}\int \sum_{m=1}^{FL\left[\frac{M+1}{2}\right]} \frac{1}{m!}\frac{1\times(-1)\times ...\times(3-2m)}{2^m}|\nabla_{\mathbf{x}}\eta|^{2m} d\mathbf{x}. \tag{3.22}$$

The total energy E^{DY} and E^{WW} can be calculated correspondingly.

3.1.4 Time integration

Equations (3.11)/(3.13) and (3.12)/(3.14) are integrated in time using an explicit 4th-order Runge-Kutta scheme. Here we present a numerical test illustrating the difference between the DY and WW formulations. Numerically, we use $N_x = N_y = 512$ grid points in a $2\pi \times 2\pi$ domain to represent a wavefield (k from 1 to 256), and the nonlinearity order $M = 3$. We start the simulation from the initial condition represented by linear solution of an arbitrary JONSWAP spectrum (i.e., $\phi^s(\mathbf{x}, 0)$ and $\eta(\mathbf{x}, 0)$ are specified as modal summation of linear wave solution, see Appendix C for details), with peak wavenumber $k_p = 16$ and significant wave height $H_s = 0.025$. The wave field is evolved using respectively the DY and WW formulations.

The corresponding energies $E^{DY}(t)$ and $E^{WW}(t)$ are evaluated at each time step, and plotted in figure 3-1. While $E^{DY}(t)$ varies with time which magnifies the $O(\epsilon^{M+2})$ truncation error in energy, $E^{WW}(t)$ keeps a constant. This indicates complete energy conservation (other than those caused by the error of numerical integration) within order $O(\epsilon^{M+1})$, which is indeed the main objective of the WW formulation.

We remark that the WW formulation is not more accurate than the DY formulation, despite the complete energy conservation as described. In fact, this slight

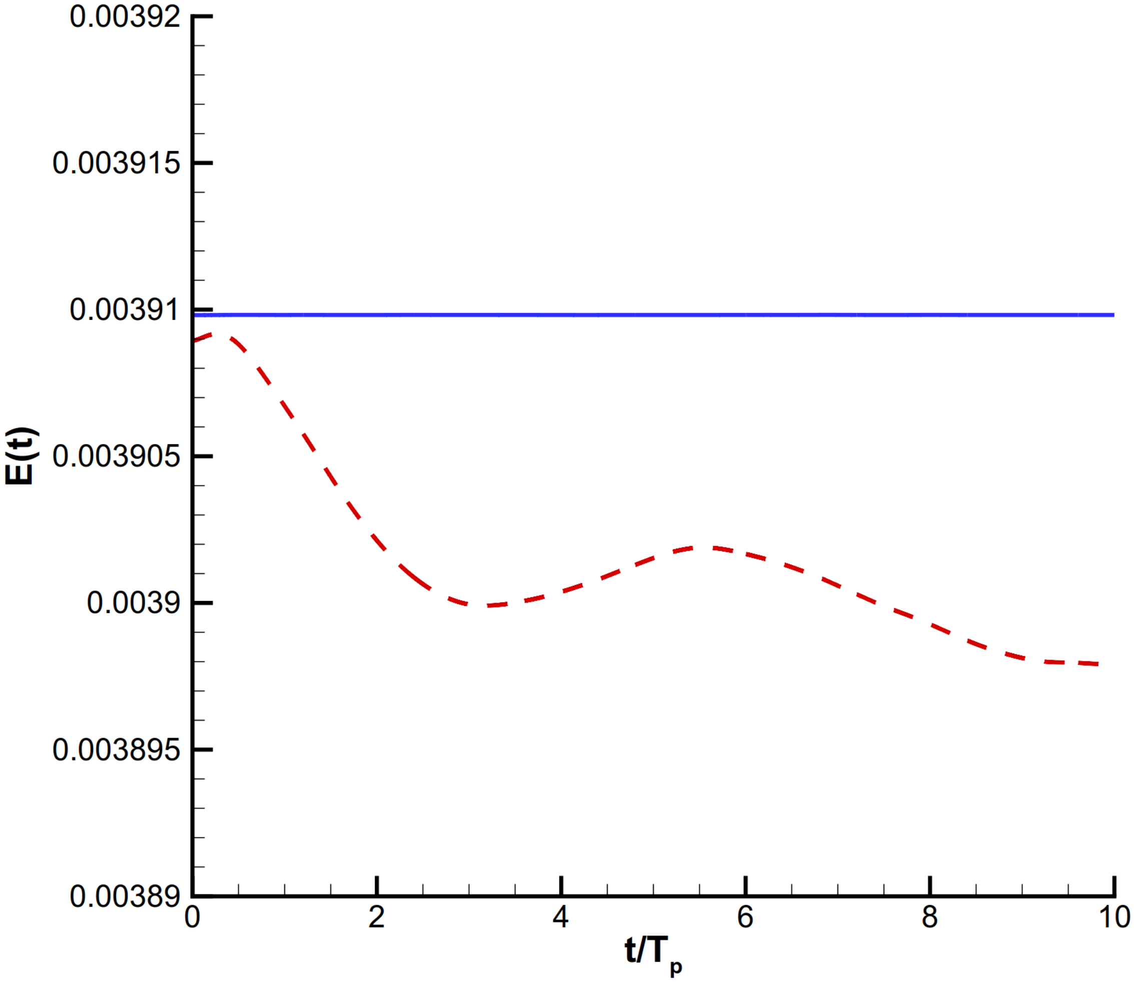

Figure 3-1: Evolution of energies $E^{DY}(t)$ (——) and $E^{WW}(t)$ (– – –) with time. The time t is non-dimensionalized by t/T_p, where T_p is the period of the peak wavenumber in the JONSWAP spectrum.

theoretical advantage of WW formulation is resulted from its consistent truncations of (3.13), (3.14) and energy E^{WW}. Numerically, we have not yet found any direct evidence of the superiority of WW formulation to DY formulation, as either method is associated with a truncation error of $O(\epsilon^{M+1})$ in η (or ϕ^s). The practical performance of these two formulations are case-dependent upon our tests. For general purposes, they can be interchangeably applied.

3.2 Benchmark with a Crapper wave solution

To verify the method's capability in modelling capillary waves, we use as a benchmark test the Crapper analytical solution for a 1D capillary wave of finite amplitude. As derived in Crapper (1957), the Crapper wave solution represents a progressive capillary wave with permanent form which satisfies (2.1) and (2.2). It can be written as

$$\frac{z_c}{\lambda} = \alpha - \frac{2i}{\pi}[1 + \frac{2\lambda}{\pi a}\{(1 + \frac{\pi^2 a^2}{4\lambda^2})^{1/2} - 1\}e^{2\pi i \alpha}]^{-1} + \frac{2i}{\pi} \tag{3.23}$$

where $z_c = x_c + iy_c$, with x_c being horizontal coordinate pointing left and y_c being vertical coordinate pointing downwards, a is the height of the wave, defined as the vertical height between trough and crest, $\alpha = (\phi + i\psi)/(c\lambda)$, with ϕ being the velocity potential, ψ being the stream function, λ being the wavelength, c being the phase speed and calculated as

$$c = (\frac{2\pi\sigma}{\lambda\rho})^{1/2}(\frac{1 - A^2}{1 + A^2})^{1/2} \tag{3.24}$$

where

$$A = \frac{2\lambda}{\pi a}\{(1 + \frac{\pi^2 a^2}{4\lambda^2})^{1/2} - 1\} \tag{3.25}$$

The solution (3.23) can be considered as obtained in a crest-fixed coordinate system with (ϕ, ψ) being the independent coordinates. Therefore, the solution of the free surface (x_c^s, y_c^s) in a period can be obtained with $\psi = 0$ and $0 \leq \phi \leq c\lambda$, i.e., $(x_c^s, y_c^s) = (x_c, y_c)|_{\psi=0, 0\leq\phi\leq c\lambda}$. A typical solution (x_c^s, y_c^s) of a Crapper wave with $a = 0.2$ and $\lambda = 2\pi$ is plotted in figure 3.23.

The analytical solution of $\phi_z|_\eta$ can be obtained by substituting the free surface

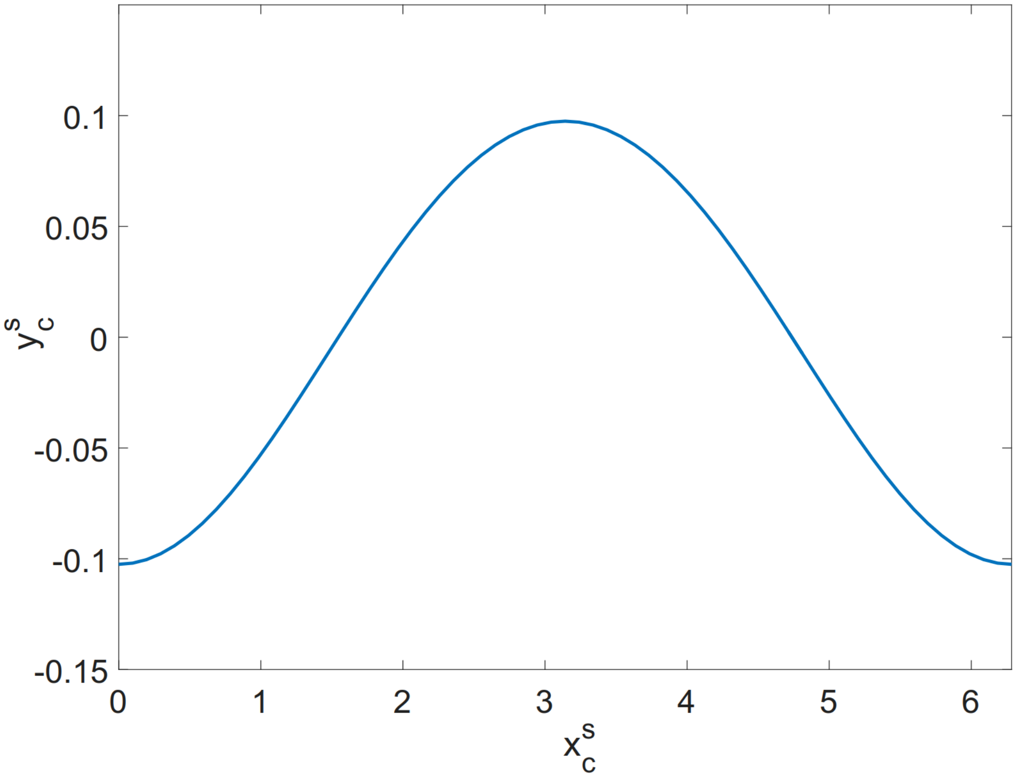

Figure 3-2: A typical Crapper wave solution with $a = 0.2$ and $\lambda = 2\pi$. For convenience, we have adjusted the directions of the coordinates to conventional definition, in contrast to that of (3.23).

		M				
ϵ	N	2	3	4	6	8
0.1	4	2.0×10^{-4}	1.1×10^{-5}	3.6×10^{-6}	2.6×10^{-6}	2.6×10^{-6}
	8	2.0×10^{-4}	1.1×10^{-5}	1.8×10^{-6}	1.7×10^{-8}	7.9×10^{-10}
	16	2.0×10^{-4}	1.1×10^{-5}	1.9×10^{-6}	1.8×10^{-8}	1.7×10^{-10}
0.2	4	1.6×10^{-3}	2.0×10^{-4}	1.1×10^{-4}	1.1×10^{-4}	1.1×10^{-4}
	8	1.6×10^{-3}	1.8×10^{-4}	6.1×10^{-5}	2.3×10^{-6}	7.3×10^{-7}
	16	1.6×10^{-3}	1.8×10^{-4}	6.1×10^{-5}	2.3×10^{-6}	9.0×10^{-8}
0.3	4	5.7×10^{-3}	1.2×10^{-3}	7.6×10^{-4}	9.4×10^{-4}	9.3×10^{-4}
	8	5.7×10^{-3}	9.6×10^{-4}	4.8×10^{-4}	4.4×10^{-5}	3.9×10^{-5}
	16	5.7×10^{-3}	9.6×10^{-4}	4.8×10^{-4}	4.2×10^{-5}	3.8×10^{-6}

Table 3.1: Maximum absolute error in surface vertical velocity $\phi_z|_\eta$ of a Crapper wave of steepness $\epsilon = \pi a/\lambda$ for varying nonlinearity order M and number of modes N.

	t/T				
ϵ	100	200	300	400	500
0.3	1.9×10^{-4}	4.1×10^{-4}	5.2×10^{-4}	6.0×10^{-4}	7.4×10^{-4}

Table 3.2: Modal error $\{\frac{1}{N}|||\widehat{\eta}_{k\mathcal{N}}|^2 - |\widehat{\eta}_{k\mathcal{A}}|^2||_1\}^{1/2}/a$ (where $\widehat{\eta}_{k\mathcal{N}}$ and $\widehat{\eta}_{k\mathcal{A}}$ are the numerical and analytical solutions of $\widehat{\eta}_k$, and a the wave amplitude) in long time simulation of Crapper wave with $M = 3$, $N = 16$, and up to t/T=500, where T is the fundamental period of the wave. DY formulation is applied.

solution to (2.1). This can be used to benchmark the boundary perturbation solution of the boundary value problem for $\phi_z|_\eta$. Table 3.1 shows the error of $\phi_z|_\eta$, as numerically determined from (3.8), compared to the analytical solution. It can be seen that the error decreases exponentially with both N and M as they increase (the exponential convergences of M and N are established after sufficient N and M respectively).

The performance of the method for long-time evolution of the wave field can also be tested against (3.23). Table 3.2 illustrates the accuracy of the method for up to $O(500)$ fundamental periods of a Crapper wave.

3.3 Linear numerical stability analysis

To understand the numerical behavior of time integration and develop a Courant condition in simulating (2.1) and (2.2), we conduct a linear numerical stability analysis, with a representative explicit 4th-order Runge-Kutta (ERK4) scheme.

3.3.1 For a single wave mode

We linearize (2.1) and (2.2) as follows:

$$\eta_t - \phi_z = 0, \tag{3.26}$$

$$\phi^s_t - \nabla_{\mathbf{x}} \cdot \nabla_{\mathbf{x}} \eta = 0. \tag{3.27}$$

These two equations can be re-written in matrix form in wavenumber domain:

$$\frac{\partial}{\partial t} \begin{bmatrix} \widehat{\eta}_k \\ \widehat{\phi^s}_k \end{bmatrix} = \begin{bmatrix} 0 & k \\ -k^2 & 0 \end{bmatrix} \begin{bmatrix} \widehat{\eta}_k \\ \widehat{\phi^s}_k \end{bmatrix} \tag{3.28}$$

where we have written $\widehat{\eta}_{\mathbf{k}}$ and $\widehat{\phi^s}_{\mathbf{k}}$ as $\widehat{\eta}_k$ and $\widehat{\phi^s}_k$ because (3.28) depends only on k. The numerical stability analysis of (3.28) is equivalent as that of a single equation

$$\frac{\partial v}{\partial t} = \lambda_m v, \tag{3.29}$$

where $\lambda_m = \pm i k^{3/2}$ is the eigenvalue(s) of the matrix $[0,\ k;\ -k^2,\ 0]$. Strictly speaking, (3.29) can be obtained by diagonalization of (3.28), which is later shown in section 3.4.1.

With the problem simplified to (3.29), we only need to compare λ_m with the stability diagram of a numerical scheme to determine the Courant condition. (As a reminder, the stability diagram of a numerical scheme refers to a region of $\lambda \Delta t$ which leads to stable result, as it is applied to solve $\partial v/\partial t = \lambda v$.) Since λ_m is purely imaginary, we need a numerical scheme whose stability diagram contains the imaginary axis. The ERK4 method is a scheme of such kind, whose stability diagram covers the imaginary axis up to $\lambda\Delta t \leq 2\sqrt{2}i$ (e.g. Moin, 2010). This gives the Courant condition of ERK4 as applied to (3.28):

$$\Delta t \leq (2/k)^{3/2}, \tag{3.30}$$

or

$$\frac{\Delta t}{T} \leq \frac{\sqrt{2}}{\pi}. \tag{3.31}$$

with $T = 2\pi/k^{3/2}$.

3.3.2 For a capillary wave spectrum

Consider a capillary wave spectrum peaked at k_p. We shall derive the Courant condition for simulation of this spectrum in terms of t/T_p. According to (3.30) (or (3.31)), the most severe stability requirement is applied on the highest wavenumber k_{max}, i.e., $\Delta t \leq (2/k_{max})^{3/2}$ or $\Delta t \leq \sqrt{2}T_{min}/\pi$. Using the dispersion relation (2.42), we obtain $T_p/T_{min} = (k_{max}/k)^{3/2}$. Therefore, the Courant condition can be written as

$$\frac{\Delta t}{T_p} \leq \frac{\sqrt{2}}{\pi}(\frac{k_p}{k_{max}})^{3/2}. \tag{3.32}$$

This imposes more limitation of the time step size Δt compared to its counterpart for gravity waves $\Delta t/T_p \leq (\sqrt{2}/\pi)(k_p/k_{max})^{1/2}$, especially for $k_p \ll k_{max}$. We are dedicated to develop a new time integration scheme which mitigates the stability requirement of (3.32).

3.4 Implicit 4th-order Runge-Kutta (IRK4) method

We combine the linear propagator method (Hou *et al.*, 1994) and the ERK4 method to develop an implicit 4th-order Runge-Kutta (IRK4) method. This method is supposed to be (unconditionally) linearly stable and exact.

3.4.1 Formulation

We split the linear and nonlinear parts of (2.1) and (2.2), and write them in wavenumber space:

$$\frac{\partial}{\partial t}\begin{bmatrix}\widehat{\eta}_{\mathbf{k}}\\ \widehat{\phi^s}_{\mathbf{k}}\end{bmatrix}=\begin{bmatrix}0 & k\\ -k^2 & 0\end{bmatrix}\begin{bmatrix}\widehat{\eta}_{\mathbf{k}}\\ \widehat{\phi^s}_{\mathbf{k}}\end{bmatrix}+\begin{bmatrix}\widehat{P}_{\mathbf{k}}\\ \widehat{Q}_{\mathbf{k}}\end{bmatrix} \tag{3.33}$$

where $\widehat{P}$ and $\widehat{Q}$ represent the nonlinear terms in (2.1) and (2.2).

Diagonalization of (3.33) gives

$$\frac{\partial}{\partial t}\begin{bmatrix}v_1\\ v_2\end{bmatrix}=\begin{bmatrix}\lambda_1 & 0\\ 0 & \lambda_2\end{bmatrix}\begin{bmatrix}v_1\\ v_2\end{bmatrix}+\begin{bmatrix}F_1\\ F_2\end{bmatrix} \tag{3.34}$$

where $\lambda_1 = ik^{3/2}$, $\lambda_2 = -ik^{3/2}$, and

$$\begin{bmatrix}v_1\\ v_2\end{bmatrix}=\Omega^{-1}\begin{bmatrix}\widehat{\eta}_{\mathbf{k}}\\ \widehat{\phi^s}_{\mathbf{k}}\end{bmatrix}, \tag{3.35}$$

$$\begin{bmatrix}F_1\\ F_2\end{bmatrix}=\Omega^{-1}\begin{bmatrix}\widehat{P}_{\mathbf{k}}\\ \widehat{Q}_{\mathbf{k}}\end{bmatrix}, \tag{3.36}$$

with

$$\Omega=\begin{bmatrix}ik^{-1/2} & ik^{-1/2}\\ -1 & 1\end{bmatrix}. \tag{3.37}$$

We define $\Psi_1 = exp(-\lambda_1 t)v_1$ and $\Psi_2 = exp(-\lambda_2 t)v_2$, with which (3.34) transforms to

$$\frac{\partial}{\partial t}\Psi_1 = exp(-\lambda_1 t)F_1 \tag{3.38}$$

$$\frac{\partial}{\partial t}\Psi_2 = exp(-\lambda_2 t)F_2 \tag{3.39}$$

The ERK4 scheme is then applied to (3.38) and (3.39). This completes the formulation of the IRK4 scheme. This scheme is (unconditionally) linearly stable and exact. This can be understood by setting $F_1 = F_2 = 0$ in (3.38) and (3.39), due to which the evolution equations can be written as

$$exp(-\lambda_1 t^{n+1})v_1^{n+1} = exp(-\lambda_1 t^n)v_1^n, \tag{3.40}$$

$$exp(-\lambda_2 t^{n+1})v_2^{n+1} = exp(-\lambda_2 t^n)v_2^n. \tag{3.41}$$

We can see that the solution of (3.40) and (3.41) corresponds to that of a linear wave field, independent of time step size Δt.

3.4.2 Numerical test

Despite the linear stability of IRK4, the presence of nonlinearity in the simulation ($F_1 \neq 0, F_2 \neq 0$) can still lead to numerical instability. We benchmark the stability and accuracy of IRK4 as applied to a Crapper wave evolution. This is conducted by starting the simulation with the exact Crapper wave solution, and measure the error in surface elevation at $t/T = 1$. Tables 3.3 and 3.4 show the maximum error, in simulating a Crapper wave of $\epsilon = \pi a/\lambda = 0.1$ and 0.2, incurred in IRK4, with the comparison to that in ERK4, for varying Δt and N. In general, smaller Δt is required for larger N and ϵ. By comparing the results from IRK4 and ERK4, we see that the allowable Δt by IRK4 is appreciably larger than that of ERK4, and the accuracy of IRK4 is significantly improved compared to that of ERK4 (in general O(10) times better).

To further understand the numerical behavior regarding the nonlinear stability of IRK4, we develop a more sophisticated criterion to evaluate the nonlinear stability of a simulation: A simulation is considered to be stable if the numerical error is confined within that of IRK4 for $t/T \leq 10$. Practically, a test based on this criterion can be realized in the following three steps:

1. We conduct simulations up to $t/T = 10$ by varying Δt, and obtain a function of $\epsilon(\Delta t)$, where ϵ is the maximum error in wave elevation at $t/T = 10$ (note that $\epsilon \sim (T/\Delta t)\Delta t^5 \sim \Delta t^4$ if the case is stable, since IRK4 is used).

2. For $\Delta t_s \to 0$, for which the simulation is meant to be stable, we evaluate ϵ_s. In

		$T/\Delta t$				
N	Method	20	40	60	80	100
8	ERK4	$\times$	$\times$	8.04×10^{-7}	2.53×10^{-7}	1.04×10^{-7}
	IRK4	$\times$	1.54×10^{-7}	3.04×10^{-8}	9.50×10^{-9}	3.87×10^{-9}
		200	300	400	500	600
	ERK4	6.64×10^{-9}	1.46×10^{-9}	5.82×10^{-10}	3.43×10^{-10}	5.57×10^{-10}
	IRK4	3.85×10^{-10}	2.19×10^{-10}	1.90×10^{-10}	1.83×10^{-10}	1.80×10^{-10}
16		20	40	60	80	100
	ERK4	$\times$	$\times$	$\times$	$\times$	$\times$
	IRK4	$\times$	1.55×10^{-7}	3.06×10^{-8}	9.67×10^{-9}	3.96×10^{-9}
		200	300	400	500	600
	ERK4	6.48×10^{-9}	1.28×10^{-9}	4.05×10^{-10}	1.66×10^{-10}	7.99×10^{-11}
	IRK4	2.47×10^{-10}	4.88×10^{-11}	1.55×10^{-11}	6.34×10^{-12}	3.06×10^{-12}
32		20	40	60	80	100
	ERK4	$\times$	$\times$	$\times$	$\times$	$\times$
	IRK4	$\times$	$\times$	$\times$	$\times$	$\times$
		200	300	400	500	600
	ERK4	$\times$	$\times$	$\times$	1.66×10^{-10}	7.99×10^{-11}
	IRK4	2.48×10^{-10}	4.88×10^{-11}	1.55×10^{-11}	6.34×10^{-12}	3.06×10^{-12}

Table 3.3: Maximum absolute error in surface elevation $|\eta_{num}(x) - \eta_{ana}(x)|$ of a Crapper wave of steepness $\epsilon = \pi a/\lambda = 0.1$, measured at $t/T = 1$, for varying time step size Δt and number of modes N. The unstable simulations are marked by $\times$.

		$T/\Delta t$				
N	Method	20	40	60	80	100
8	ERK4	×	×	2.21×10^{-6}	7.31×10^{-7}	3.34×10^{-7}
	IRK4	×	1.80×10^{-6}	2.93×10^{-7}	1.73×10^{-7}	1.52×10^{-7}
		200	300	400	500	600
	ERK4	1.55×10^{-7}	1.43×10^{-7}	1.39×10^{-7}	1.37×10^{-7}	1.37×10^{-7}
	IRK4	1.37×10^{-7}	1.36×10^{-7}	1.36×10^{-7}	1.36×10^{-7}	1.36×10^{-7}
16		20	40	60	80	100
	ERK4	×	×	×	×	×
	IRK4	×	×	×	7.17×10^{-8}	2.99×10^{-8}
		200	300	400	500	600
	ERK4	1.74×10^{-8}	3.42×10^{-9}	1.06×10^{-9}	4.19×10^{-10}	1.93×10^{-10}
	IRK4	1.90×10^{-9}	3.63×10^{-10}	1.02×10^{-10}	3.01×10^{-11}	1.52×10^{-11}
32		20	40	60	80	100
	ERK4	×	×	×	×	×
	IRK4	×	×	×	×	×
		200	300	400	500	600
	ERK4	×	×	×	4.22×10^{-10}	1.91×10^{-10}
	IRK4	×	3.59×10^{-10}	9.72×10^{-11}	2.56×10^{-11}	1.42×10^{-11}

Table 3.4: Maximum absolute error in surface elevation $|\eta_{num}(x) - \eta_{ana}(x)|$ of a Crapper wave of steepness $\epsilon = \pi a/\lambda = 0.2$, measured at $t/T = 1$, for varying time step size Δt and number of modes N. The unstable simulations are marked by ×.

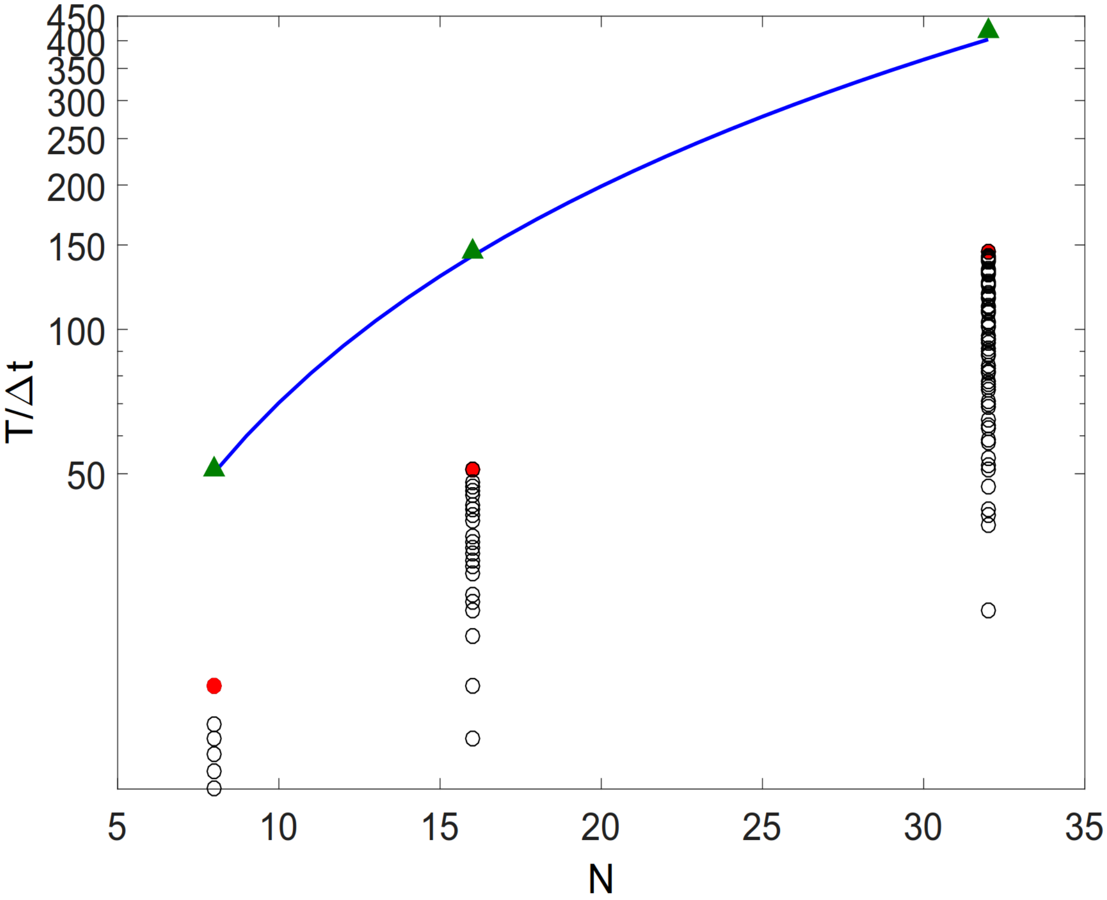

Figure 3-3: Stability analysis of IRK4 and ERK4: marginal time step Δt_{ME} for ERK4 (▲), graphically above which (meaning $\Delta t < \Delta t_{ME}$) all Δt give stable results; marginal time step Δt_{MI} for IRK4 (●); time step Δt (○) that is larger than Δt_{MI} but leads to stable results; linear Courant condition for ERK4 (——).

practice, we use a sufficiently small Δt to obtain ϵ_s.

3. IRK4 scheme is considered as stable for a certain Δt if $\epsilon(\Delta t) < C\epsilon_s(\Delta t/\Delta t_s)^4$, where C (say $C = 1.2$) is a relaxation factor.

Based on this criterion, we test the stability of IRK4 and ERK4 as they are applied to a Crapper wave of $\epsilon = 0.1$, with an increment of Δt as $\delta(T/\Delta t) = 1$. The results are plotted in figure (3-3), along with the linear Courant condition of ERK4. We see that the marginal time step Δt_{ME} (all $\Delta t < \Delta t_{ME}$ give stable results) for ERK4 is slightly smaller than that predicted from the Courant condition, reflecting the influence of nonlinearity on the stability. The marginal time step Δt_{MI} for IRK4 is significantly larger than Δt_{ME}, which is as expected. What remains unclear in figure 3-3 is that there exists discontinuous $\Delta t > \Delta t_{MI}$ which lead to stable results. We investigate the mechanism underlying this behavior in the following.

To obtain a better elucidation for these stable $\Delta t > \Delta t_{MI}$, we plot these Δt in figure 3-4 respectively for $N = 8$,16 and 32. It is evident that these Δt form "clusters" around some "attractor" of $\Delta t = T_n$, where $T_n = T/n^{3/2}$ is the period of mode n, especially for large N.

To understand this salient "clustered" behavior, we need to consider the energy transfer mechanism in a 1D capillary wave field, as an "unstable" simulation is generally caused by the accumulation of energy at high wave mode n. Physically, it has been shown that energy transfer can be caused by the triad resonant interaction among three modes satisfying (Mcgoldrick, 1965)

$$k_a + k_b = k_c, \tag{3.42}$$

and

$$\omega_a + \omega_b = \omega_c. \tag{3.43}$$

Equation (3.43) can be relaxed with a "$\approx$" for quasi-resonant interactions. It has been shown (Mcgoldrick, 1965) that (3.42) and (3.43) cannot be simultaneously satisfied in 1D with ω representing the physical frequency. However, the situation is different in numerical simulation. As Δt becomes larger, the sampling rate is possibly lower than the Nyquist frequency for some high-frequency mode. As a result, these modes manifest themselves with the aliasing frequency

$$\omega' = |\omega - \omega_s|, \tag{3.44}$$

with ω_s being the sampling frequency. A toy model problem to illustrate these concepts is sketched in figure 3-5. With ω replaced by ω' in (3.43), a "pseudo" triad resonant interaction is possible.

Since most energy are concentrated at the fundamental mode for Crapper wave,

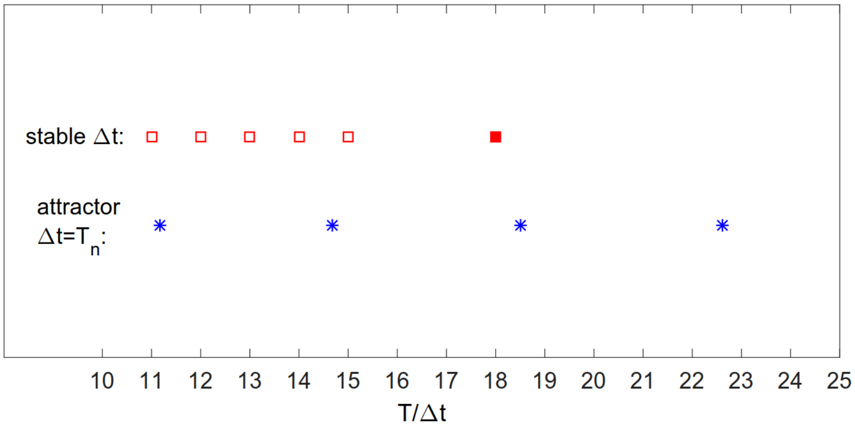

(a)

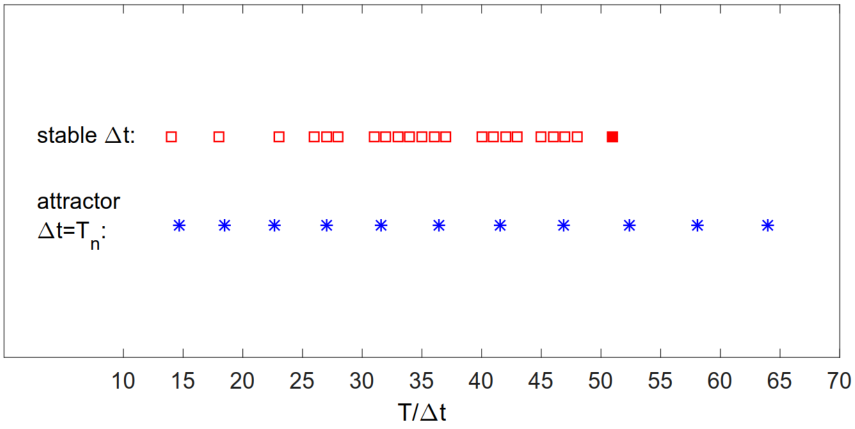

(b)

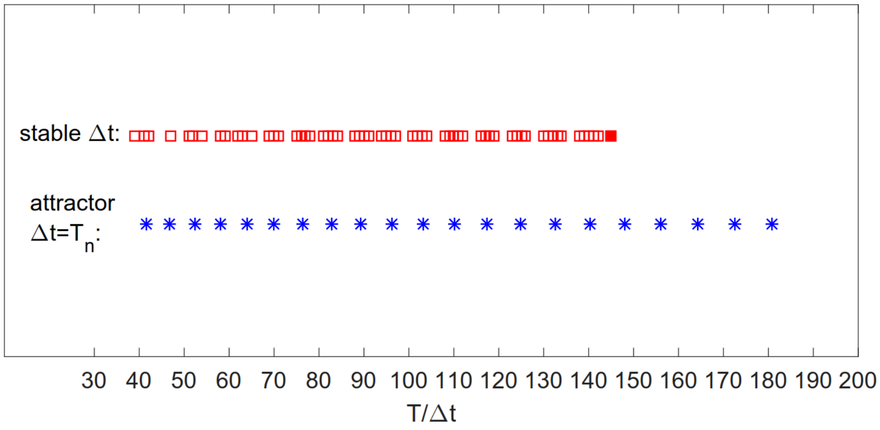

(c)

Figure 3-4: Stable time step $\Delta t > \Delta t_{MI}$ (□) for (a) $N = 8$, (b) $N = 16$ and (c) $N = 32$. The marginal time step Δt_{MI} (■) and the attractors ($*$) are indicated for each subfigure.

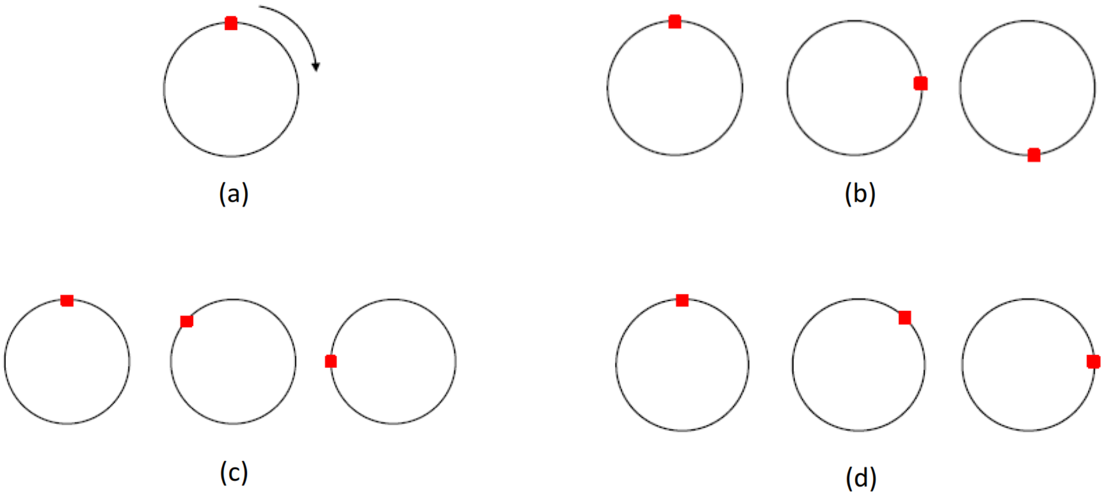

Figure 3-5: Sketch of a toy model problem to illustrate the Nyquist frequency and aliasing frequency. (a) A continuously rotating wheel with frequency f, and Nyquist frequency calculated as $f_N = 2f$; (b) Consecutive samples with sampling frequency $f_s = 4f(> f_N)$, the captured frequency $f_c = f$; (c) Consecutive samples with sampling frequency $f_s = 8f/7(< f_N)$, the captured frequency $f_c = f/7$; (d)Consecutive samples with sampling frequency $f_s = 8f/9(< f_N)$, the captured frequency $f_c = f/9$.

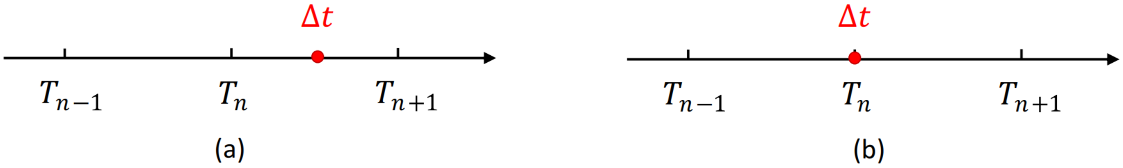

Figure 3-6: Sketch of the configurations of Δt: (a) a most "dangerous" situation, with Δt locating amid T_n and T_{n+1}; (b) a most "safe" situation, with Δt locating coincidentally on T_n.

the most possible "pseudo" triad that can be involved in energy transfer is among 1, n and $n+1$. In general (for Crapper wave), a case becomes unstable if the following condition is satisfied,

$$\omega_1 + \omega'_n \approx \omega'_{n+1}. \tag{3.45}$$

This places a direct restriction on the configuration of Δt. For the sake of explanation, we describe two situations. Figure 3-6(a) shows a most "dangerous" situation, with Δt located amid T_n and T_{n+1}. This leads to $\omega'_n \approx \omega'_{n+1}$ (see figure 3-5(c) and (d) for an illustration), which renders (3.45) most likely to be satisfied. On the contrary, figure 3-6(b) shows a most "safe" situation, with Δt locating coincidentally on T_n. In this configuration, $\omega'_n - \omega'_{n+1} = \omega_n - \omega_{n+1}$ (see (3.44)), and the "pseudo" resonance is not possible. As a result, the time step Δt that leads to stable results are "clustered" around $\Delta t = T_n$. In summary, the application of IRK4 does gain some advantage compared to ERK4, in terms of numerical stability. Nevertheless, this scheme should be used with great caution if accuracy is under consideration. As larger Δt is used, the accuracy regarding the high-frequency modes can be severely deteriorated, even though the results stay stable. In addition, the above analysis only considers the simulation with most energy concentrated in the fundamental modes. For the general simulation of a broadband spectrum, there could be much more possibilities leading to the "pseudo" resonance and the "clustered" behavior is less applicable.

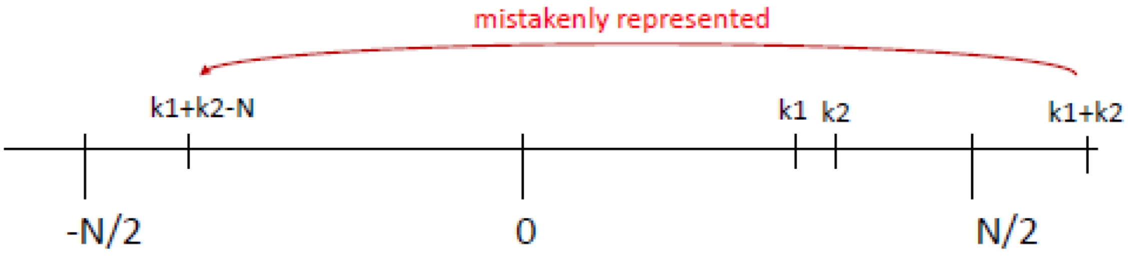

Figure 3-7: Sketch of the spatial aliasing: mode with wavenumber $k_1 + k_2$ mistakenly represented by $k_1 + k_2 - N$.

3.5 Spatial de-aliasing

We present the 2/3 spatial de-aliasing rule, which is widely applied and superior to the 1/2 de-aliasing rule used in Dommermuth & Yue (1987). We remark that the spatial aliasing considered here is different with the time aliasing in section 3.4.2. Instead, it is caused by the insufficient grid points to resolve high wavenumbers due to multiplication of functions. For example, say we have two functions $u_1(x) = cos(k_1 x)$ and $u_2(x) = cos(k_2 x)$ defined on a computational domain with $x \in [0, 1, ..., N] \times 2\pi/N$, i.e., $k \in [-N/2, -N/2+1, ..., N/2]$. If $k_1 + k_2 > N/2$, the multiplication result $u_1 u_2$ cannot be properly represented. It results in an aliasing mode which is mistakenly represented by wavenumber $k_1 + k_2 - N$ in the computational domain (see figure 3-7 for a sketch).

To avoid the aliasing error, we can use the zero-padding scheme in spatial domain, i.e., we set part of the amplitudes to zero always prior to and after multiplications, and keep the sub-range $[-K, K]$ free of aliasing. To determine the value of K, we consider a most severe situation, with $k_1 = k_2 = K$, which results in an aliasing wavenumber $2K - N$. For this mode to be out of the alias-free range, we need to set $2K - N \leq -K$, which gives

$$K \leq N/3. \tag{3.46}$$

Therefore, $K = N/3$ is the most computationally efficient choice, as maximum number of modes can be kept in the simulation. This scheme is called the 2/3 spatial de-aliasing rule as we keep 2/3 of the total modes (see figure 3-8 for a sketch). In contrast, the previous choice of 1/2 de-aliasing rule in Dommermuth & Yue (1987) is

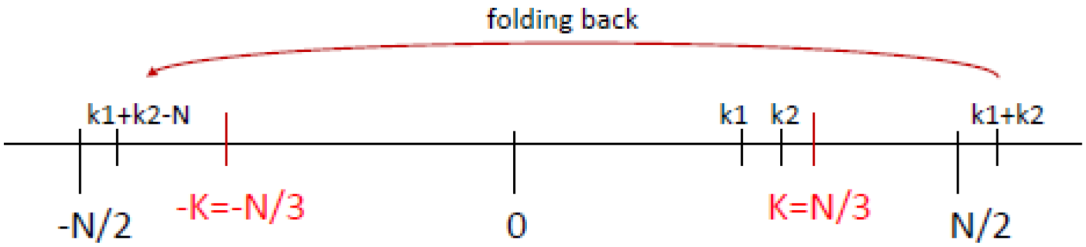

Figure 3-8: Sketch of the 2/3 de-aliasing rule.

sufficient but not necessary.

3.6 Summary

We have developed the formulation of high-order spectral method for the simulation of capillary waves. We present two ways to simulate the capillarity term, which are respectively consistent with the frameworks of DY (Dommermuth & Yue, 1987) and WW (West *et al.*, 1987) formulations, and should be used accordingly. While the WW formulation bears a slight theoretical advantage of achieving exact energy conservation, the two methods can be used interchangeably for general purposes. The accuracy of the developed scheme is benchmarked using an analytical Crapper wave solution. A linear numerical stability analysis is conducted with respect to the ERK4 scheme for time integration. It is found that capillarity imposes a more severe limitation on time step size Δt, compared to that for gravitation, for simulation of a wave spectrum. To mitigate this limitation, we have developed an IRK4 scheme for time integration, which is obtained by combining the ERK4 scheme and linear propagator method. The new IRK4 scheme is shown to be linearly stable and exact, and more accurate than the ERK4 scheme when applied to a Crapper wave. The stability of IRK4 under nonlinearity is numerically analyzed. It is shown that its marginal time step Δt_m (for all $\Delta t < \Delta t_m$ results are stable) is much larger than that of ERK4. We also find that there are many $\Delta t > \Delta t_m$ which leads to stable results. These Δt are observed to show a "clustered" behavior around $\Delta t = T_n$. This is explained in terms of the "pseudo" resonant interactions which result in energy transfer to high wavenumbers. We finally end the chapter by presenting the 2/3 de-aliasing rule, which obtains a computational improvement compared with the previous 1/2 de-aliasing rule used in Dommermuth & Yue (1987).

Chapter 4

Direct numerical investigation of capillary wave turbulence

In this chapter, our objective is to investigate isotropic turbulence of capillary waves, and evaluate the validity of WTT, by direct numerical simulation of the primitive Euler equations. The aim is to obtain a clean development of the wave spectrum not obscured by complexities associated with the mechanical forcing of the waves (Pushkarev & Zakharov, 1996, 2000; Falcon *et al.*, 2007; Xia *et al.*, 2010; Deike *et al.*, 2014*a*) and difficulties associated with the estimation of P (Falcon *et al.*, 2007; Xia *et al.*, 2010; Deike *et al.*, 2014*a*). Furthermore, we seek to uncover the physics at a substantially broader range of nonlinearity level relative to existing measurements (Falcon *et al.*, 2007; Xia *et al.*, 2010; Deike *et al.*, 2014*a*) and numerics (Pushkarev & Zakharov, 1996, 2000; Deike *et al.*, 2014*b*). To achieve this, we consider the free evolution of an arbitrary initial wavefield represented by a general isotropic spectrum. We then look for the development of a power-law spectrum in the process of the evolution from different initial nonlinearity levels. The energy flux P is evaluated, without ambiguity, by direct evaluation of the energy dissipation rate in the dissipation range.

We show the development of the WTT $k^{-19/4}$ power-law spectrum, at high enough nonlinearity, and $I_\eta \sim P^{1/2}$. The Kolmogorov constant C is for the first time found to be reasonably close to $C_0 = 6.97$ (see 2.91). With decreased nonlinearity on a fixed grid (or decreased mode number N for a given nonlinearity), our results illustrate the finite box effect (Pushkarev & Zakharov, 2000), i.e., nonlinear resonance broadening becomes insufficient to overcome the discreteness in k, which results in a reduced capability of energy transport. This is reflected in the reduction of energy flux P, larger and smaller values respectively of observed Kolmogorov Constant C and spectral slope α, relative to WTT. These results offers, for the first time, both a validation of and supplement to WTT in the description of capillary wave turbulence.

The main results of this chapter is also presented in Pan & Yue (2014).

4.1 Numerical formulation

We consider capillary waves in two surface dimensions on the free surface of an ideal incompressible fluid. For small Bond number, gravity is neglected. The system is described in the context of potential flow (velocity potential $\phi(x, y, z, t)$) in terms of nonlinear evolution equations (Zakharov, 1968) for surface elevation $\eta(x, y, t)$ and velocity potential at the surface $\phi^s(x, y, t) \equiv \phi(x, y, \eta, t)$:

$$\eta_t = -\nabla_{\mathbf{x}}\phi^s \cdot \nabla_{\mathbf{x}}\eta + (1 + \nabla_{\mathbf{x}}\eta \cdot \nabla_{\mathbf{x}}\eta)\phi_z + F^{-1}[\gamma_k \eta_{\vec{k}}], \tag{4.1}$$

$$\begin{aligned} \phi^s_t = -\frac{1}{2}\nabla_{\mathbf{x}}\phi^s \cdot \nabla_{\mathbf{x}}\phi^s + \frac{1}{2}(1 + \nabla_{\mathbf{x}}\eta \cdot \nabla_{\mathbf{x}}\eta)\phi_z^2 + \\ \frac{\sigma}{\rho}\nabla_{\mathbf{x}} \cdot \frac{\nabla_{\mathbf{x}}\eta}{\sqrt{1 + \nabla_{\mathbf{x}}\eta \cdot \nabla_{\mathbf{x}}\eta}} + F^{-1}[\gamma_k \phi^s_{\vec{k}}], \end{aligned} \tag{4.2}$$

where F^{-1} is the inverse Fourier transform, γ_k is the dissipation rate at small scales.

Equations (4.1) and (4.2) can be simulated using the schemes described in Chapter 3, other than the dissipation terms $F^{-1}[\gamma_k \eta_{\vec{k}}]$ and $F^{-1}[\gamma_k \phi^s_{\vec{k}}]$. These terms are introduced beyond k_γ to represent the physical (viscous) damping, with γ_k defined in the Fourier space with the following form (Pushkarev & Zakharov, 1996):

$$\gamma_k = \begin{cases} -\gamma_0(k - k_\gamma)^2, & k \geq k_\gamma \\ 0, & k < k_\gamma. \end{cases} \tag{4.3}$$

These two terms can be straightforwardly included in the simulation by multiplying both $\widehat{\eta}(k)$ and $\widehat{\phi}^s(k)$ with $exp(\gamma_k \Delta t)$ at each time step.

The energy (density) dissipation rate, and thus the energy (density) flux, due to (4.3), can be evaluated explicitly (cf. Pushkarev & Zakharov (1996)):

$$P = \frac{1}{4\pi^2} \iint_{k>k_\gamma} \gamma_k (k I_\phi(k) + \sigma k^2 I_\eta(k)) d\vec{k}, \tag{4.4}$$

where $I_\phi(k)$ is (proportional to) the energy density spectrum (see (2.40) for an analogy of $I_\eta(k)$) of ϕ^s. We note that this definition is equivalent to (2.85).

The simulation starts from an initial isotropic wavefield with a somewhat arbitrary spectral energy distribution. The wavefield is allowed to evolve freely, with total energy decreasing due to dissipation at high wavenumbers. In the presence of nonlinear wave interactions, after sufficient time $t > t_A$, a power-law spectrum develops in the inertial range. In this asymptotic phase, as the overall spectrum decays with time, its slope in the inertial range as well as scaling with P, and value of C remain quasi-stationary and are evaluated. Note that the general development of the power-law spectrum is independent of the details of the initial spectrum (which we verify numerically). For specificity, we choose initial wavefields described by a JONSWAP spectrum (see Appendix C for the specificity of $\eta(\mathbf{x}, 0)$ and $\phi^s(\mathbf{x}, 0)$). The nonlinearity of the initial spectrum is characterized by the effective wave steepness

$$\beta = k_p H_s / 2, \tag{4.5}$$

where k_p is the peak wavenumber and H_s is the significant wave height. To cover a broad range of P (and nonlinearity), we can conduct a single simulation (starting with a sufficiently large β) and follow the asymptotic spectrum as it decays. Alternatively, we can conduct different simulations with different initial spectral energies. The predicted results are effectively identical (figure 4-2).

HOS simulations are carried out using the DY formulation with $N_x = N_y = N = 128$ alias-free modes, with $k_p = 16k_0$ and $k_\gamma = 60k_0$, where k_0 is the fundamental wavenumber of the (doubly periodic) domain. For dissipation, we use

$$\widehat{\gamma}_0 \equiv \gamma_0 k_p^2/\omega_p = 5 \times 10^{-3}, \tag{4.6}$$

which leads to the asymptotic spectrum with a smooth development of and connection between the power-law and dissipation ranges (we verify that the realized spectra and evaluation of P are not sensitive to variation of γ_0 around this choice). For $\widehat{\gamma}_0 \gg 5 \times 10^{-3}$, a sharp transition develops between the power-law and dissipation ranges; For $\widehat{\gamma}_0 \ll 5 \times 10^{-3}$, the dissipation is not sufficient to damp the energy transferred from large scales.

HOS can handle arbitrary order, M, of nonlinear interactions. Although the nonlinear capillary wave evolution is expected to be dominated by the three-wave process (Zakharov & Filonenko, 1967), we follow Pushkarev & Zakharov (1996) to use $M = 3$ (corresponding to their H_2). The inclusion of four-wave processes is important for broadening the spectral tail where the nonlinearity level is low for triad resonance (cf. the discussions Xia *et al.* (2010); Pushkarev & Zakharov (1996, 2000)). Thus $M = 3$ significantly speeds up the spectral evolution relative to $M = 2$ (although the final predictions are little affected).

4.2 Results

4.2.1 Spectral evolution

Figure 4-1 shows a typical evolution of the spectrum starting with β=0.25. For this case, a power-law spectrum is fully developed at $t_A \sim O(500T_p)$, where $T_p = 2\pi(\rho/(\sigma k_p^3))^{1/2}$. Within a substantial range, the power-law spectrum follows closely the theoretical slope of $\alpha_0 = -19/4$. As the spectrum decays, the normalized energy flux

$$\widehat{P} \equiv P/(\sigma\omega_p) \tag{4.7}$$

also decreases, while the inertial range remains power-law.

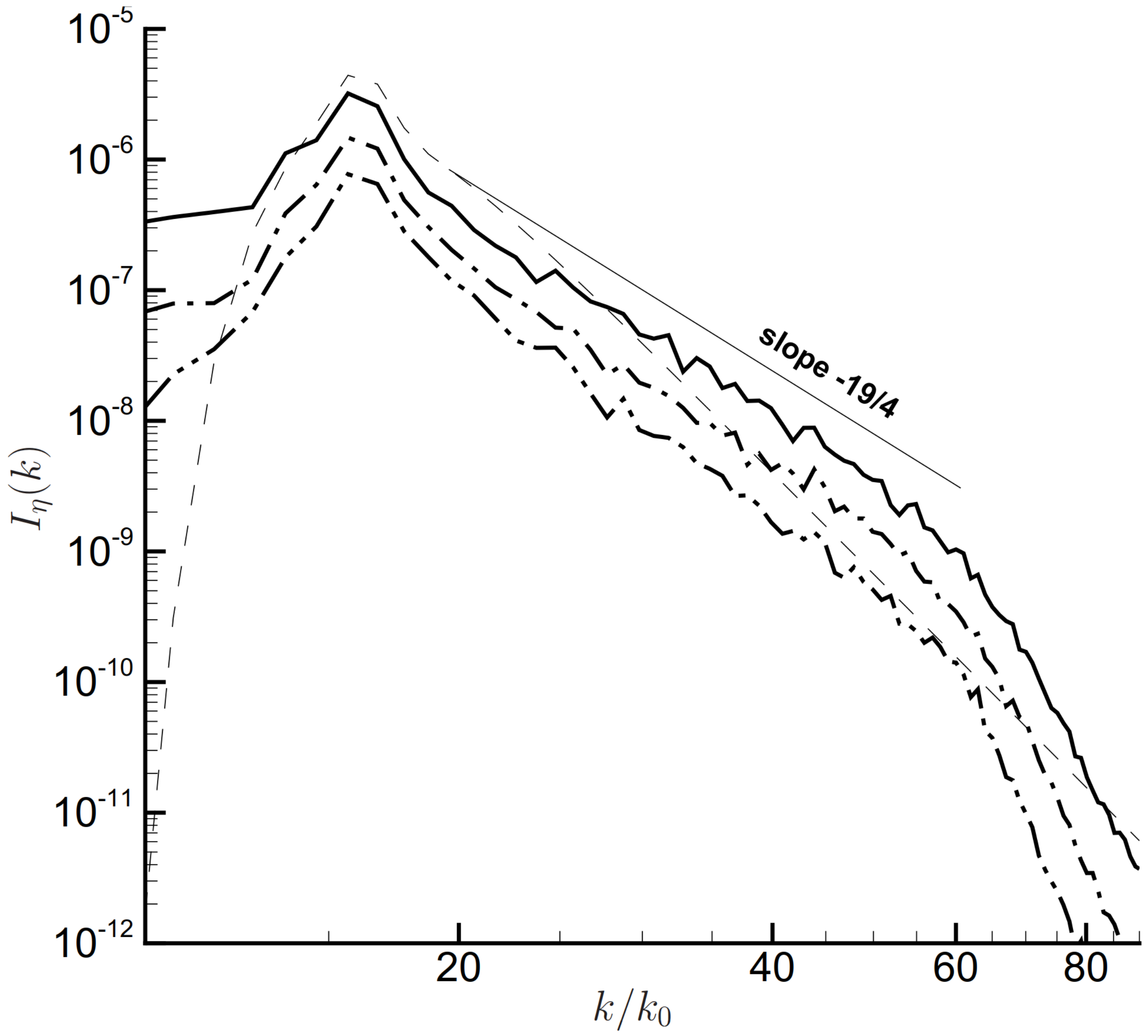

Figure 4-1: Typical development of spectrum with time. Initial spectrum at t/T_p=0 (– – –); fully-developed spectrum corresponding to $\widehat{P}$=9.6 × 10^{-7} (—–); decayed spectra corresponding to $\widehat{P}$=1.6 × 10^{-7} (- · -) and 3.2 × 10^{-8} (- · · -).

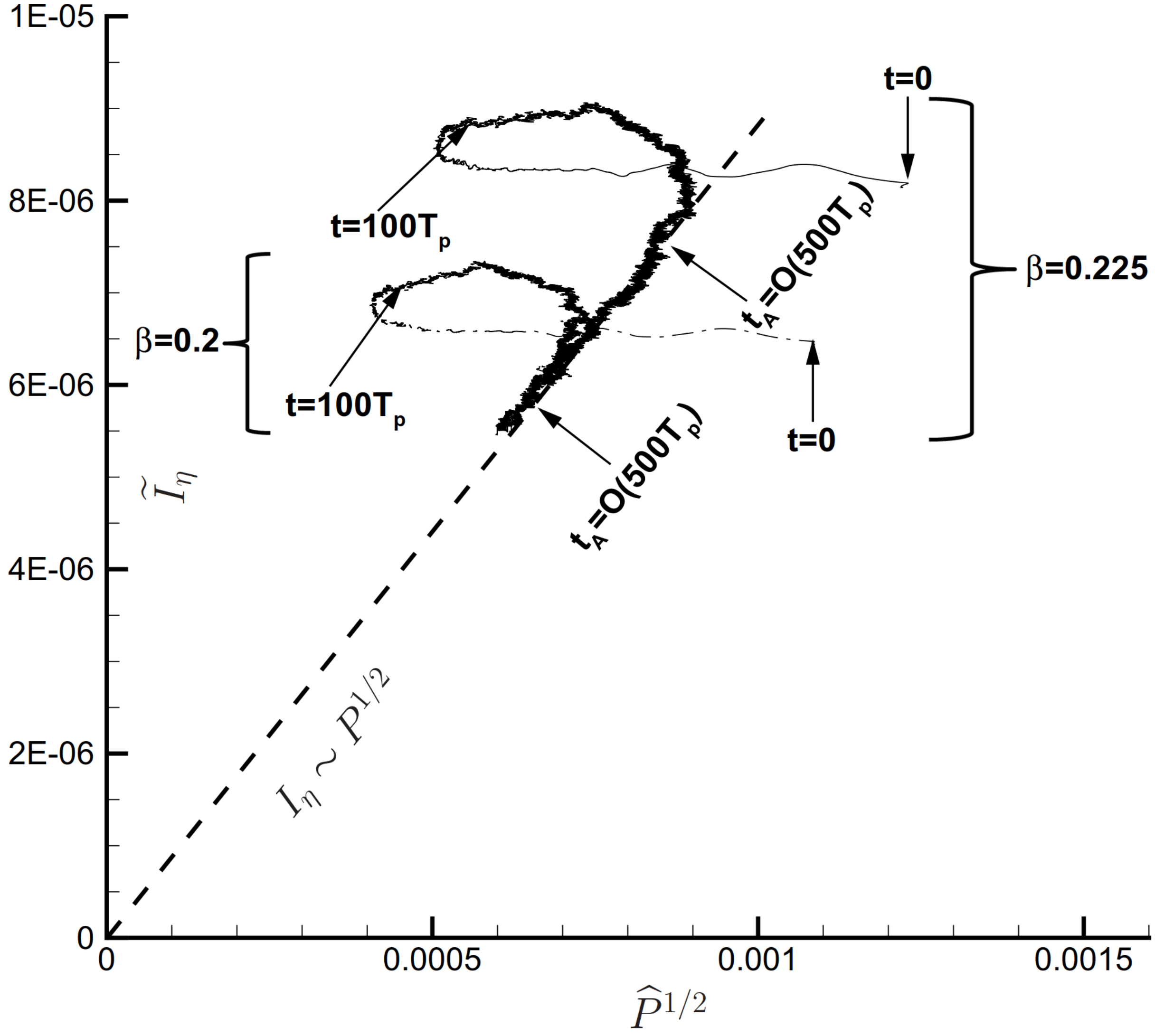

Figure 4-2: Time trajectories of $(\widehat{P}^{1/2}, \widetilde{I}_\eta)$ for two simulations with different initial effective wave slopes: β=0.225 (——) and β=0.2 (- · -). For reference, the WTT $I_\eta \sim P^{1/2}$ scaling (– – –) is indicated.

We define

$$\widetilde{I}_\eta \equiv \int_{k_p}^{k_\gamma} I_\eta(k)dk \tag{4.8}$$

as an integral measure of the amplitude of $I_\eta(k)$ within the inertial range. The time trajectories of $(\widehat{P}^{1/2}, \widetilde{I}_\eta)$, for two simulations with different initial values of β are plotted in figure 4-2. Indicated are the respective time t_A when the asymptotic phase is established for each case. For $t > t_A$, the slopes of the $(\widehat{P}^{1/2}, \widetilde{I}_\eta)$ trajectories follow closely the WTT $I_\eta \sim P^{1/2}$ scaling. We establish this scaling for a wide range of $\widehat{P}$ by repeating simulations such as those in figure 4-2 for many initial values of β or equivalently by following a long single evolution starting from large β.

4.2.2 Evaluation of P, C and α

Figure 4-3 plots $\widehat{P}^{1/2}$ versus $\widetilde{I}_\eta$ for $\widehat{P} \in [\widehat{P}_{min}, \widehat{P}_{max}]$ ranging over 1.5 decades. Our $\widehat{P}_{max}$ is limited by the capability of HOS, and $\widehat{P}_{min}$ is chosen to be sufficiently small to reveal the mechanism at low nonlinearity level. The WTT $P^{1/2}$ scaling is realized, with the deviation from the theoretical fit greater at lower values of $\widehat{P}$ (and $\widetilde{I}_\eta$). These deviations are due to the finite box effect (Pushkarev & Zakharov, 2000), i.e., nonlinear resonance is limited by the finite wavenumber spacing. As a result, fewer triads are active in transferring energy, resulting in a reduced $\widehat{P}$. For given N, as nonlinearity further decreases below some critical value, frozen turbulence (Pushkarev & Zakharov, 2000) obtains and $\widehat{P} \rightarrow 0$ with a finite $\widetilde{I}_\eta$. The present result provides a direct numerical confirmation of $I_\eta \sim P^{1/2}$ for the first time. They thus help support the recent clarification (Deike *et al.*, 2014*a*) of apparent inconsistencies in the experimental predictions (Falcon *et al.*, 2007; Xia *et al.*, 2010), and illustrate the finite box effect by substantially extending the range of $\widehat{P}$ realized in the measurements.

The Kolmogorov constant C can be evaluated directly from the simulation data. Specifically, at each value of $\widehat{P}$, we define

$$\kappa(\alpha) = [k_1, k_2]_\alpha \tag{4.9}$$

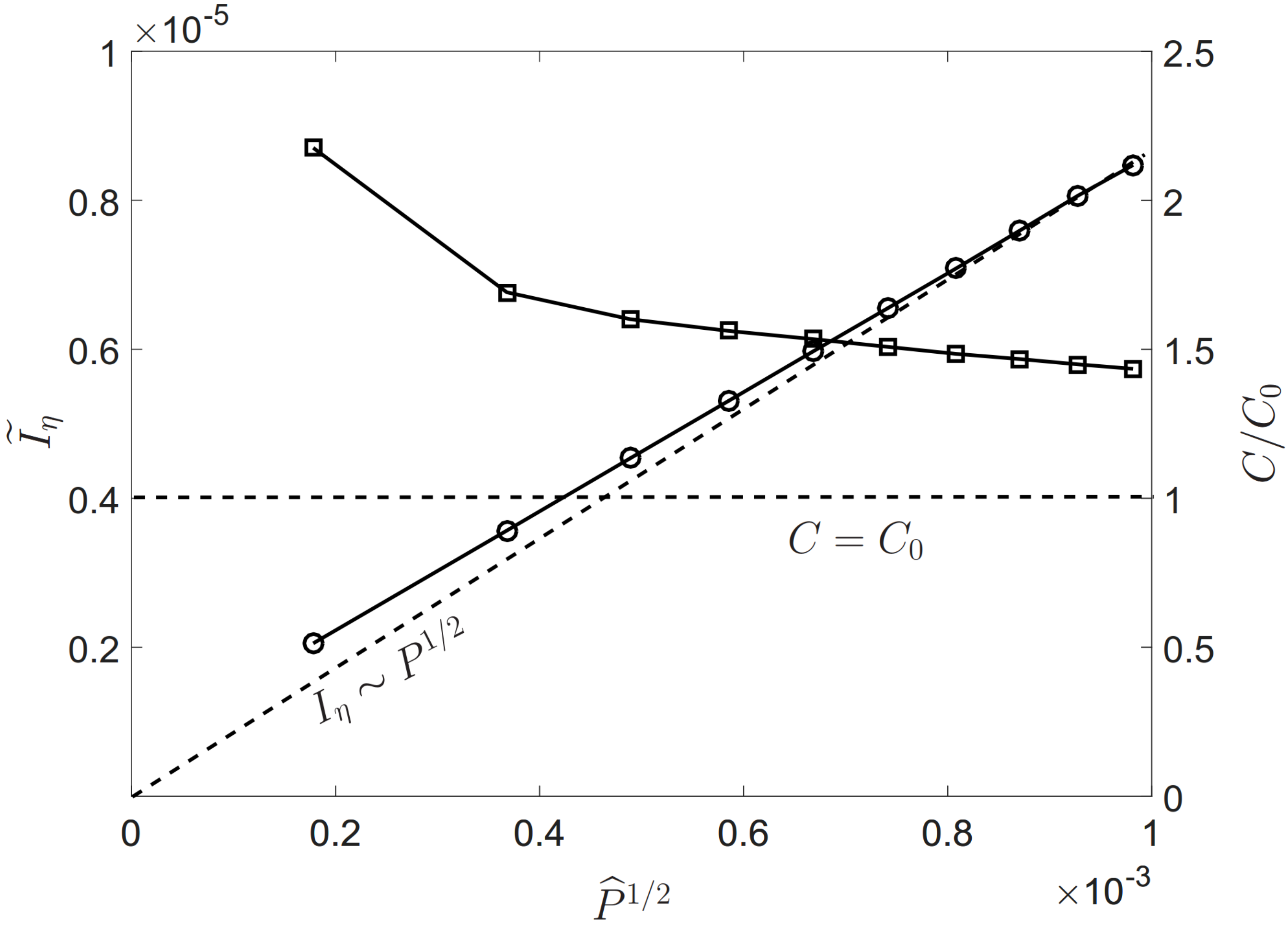

Figure 4-3: $\widetilde{I}_\eta$ (—o—) and C/C_0 (—□—) as functions of $\widehat{P}^{1/2}$, compared to WTT (− − −).

as the maximum spectral interval within which the linear fit $\log I_\eta(k) \sim \alpha \log k$ has $R^2 > 0.99$. $C(\widehat{P})$, plotted in figure 4-3, is then evaluated from (2.94) in the range $\kappa(\alpha_0{=}-19/4)$. The higher values of C at lower values of $\widehat{P}$ reflects the deviation from the WTT $I_\eta \sim P^{1/2}$ scaling in this range. With the increase of nonlinearity, $C(\widehat{P})$ approaches $C = 9.90$, with reasonable error compared to the theoretical $C_0{=}6.97$. Despite the discrepancy, this study regarding the value of C is much improved compared to previous ones (Pushkarev & Zakharov, 2000; Deike *et al.*, 2014*a*,*b*), from both theoretical and numerical considerations. The difference between $C(\widehat{P}_{max})$ and C_0 is resulted from the reduced nonlinearity with the increase of k, which becomes insufficient to sustain the energy flux needed to recover C_0. This point will be revisited and discussed in detail in Chapter 5.

In practice, the finite box effect, in limiting the nonlinear resonance, also results in a deviation of α from α_0. To show this effect, at each $\widehat{P}$, we calculate a best-fit α and the spectral range $\kappa(\alpha)$. The dependence of α on $\widehat{P}$ is shown in figure 4-4. Near $\widehat{P}_{max}$, $\alpha = -4.8$; and it decreases monotonically with decreasing $\widehat{P}$ to $\alpha = -5.8$ at $\widehat{P}_{min}$. Similar phenomenon of steepening of the spectrum at low nonlinearity has been reported in experiment for gravity waves (Denissenko *et al.*, 2007). Also reported in figure 4-4 are the widths of the spectral ranges $\kappa(\alpha)$ and $\kappa(\alpha_0)$ as functions of $\widehat{P}$. $\kappa(\alpha)$ is almost constant, while $\kappa(\alpha_0)$ decreases monotonically with decreasing $\widehat{P}$. In general $\kappa(\alpha) > \kappa(\alpha_0)$ except asymptotically at large $\widehat{P}$. These results are in contrast to the theoretical self-similar decay (Falkovich *et al.*, 1995), and are useful in the interpretation of observed deviations of α from α_0 in experiments (Xia *et al.*, 2010; Wright *et al.*, 1996; Brazhnikov *et al.*, 2007). The detailed mechanism leading to the steepening of the spectrum at lower nonlinearity level is discussed in Chapter 5.

For given nonlinearity, finite box effect can be mitigated by increasing N (or by increasing the physical dimension of the experimental tank). We show this by varying N with $N = 64$ and 256 from the preceding value of $N = 128$ (with k_p/k_0 and k_γ/k_0 scaled correspondingly). Figure 4-5 shows the calculated α and C with varying N. With the increase of N, α and C approach WTT values (despite the discrepancy of C) showing that earlier deviations from these asymptotic values are

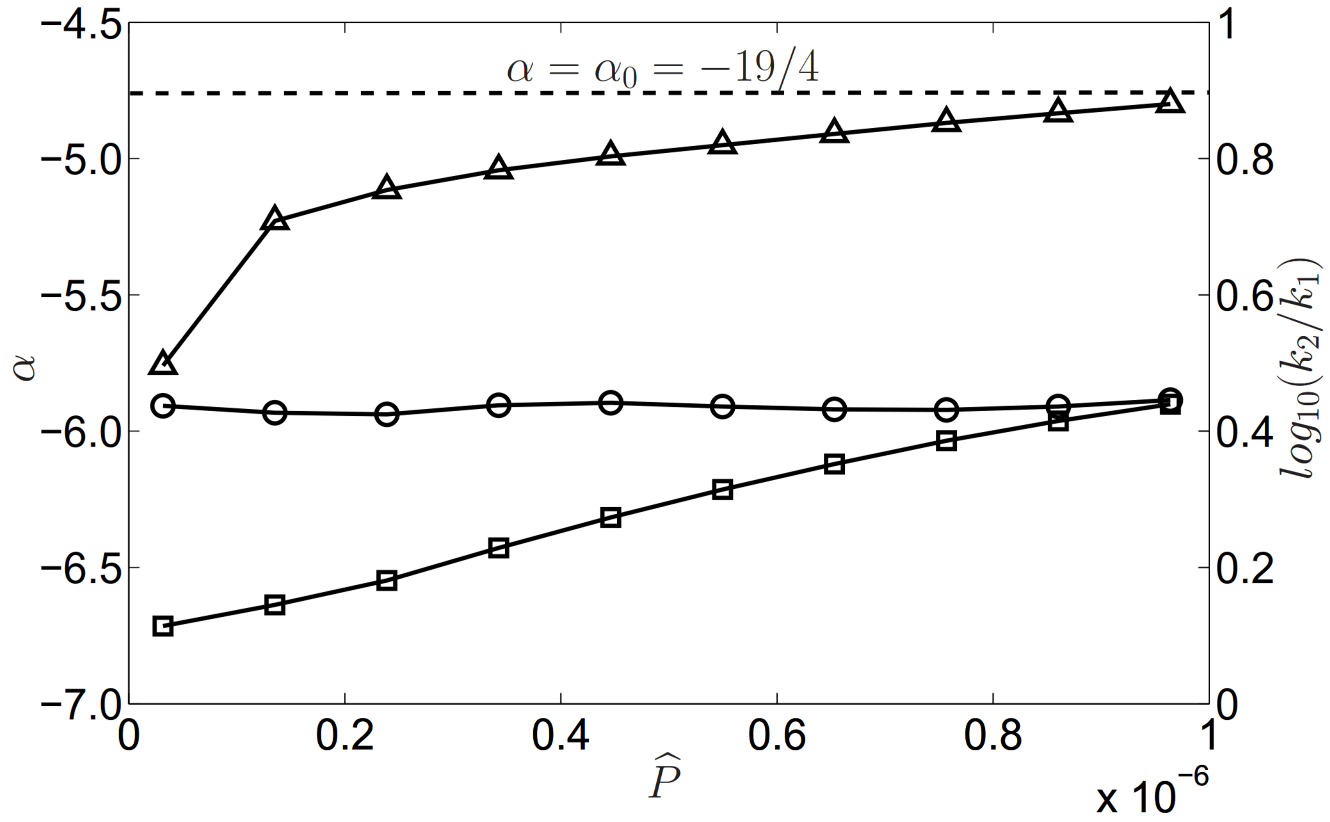

Figure 4-4: Evaluated α (—△—) compared to WTT (− − −), and $\log_{10}(k_2/k_1)_\alpha$ (—○—), $\log_{10}(k_2/k_1)_{\alpha_0}$ (—□—) as functions of $\widehat{P}$.

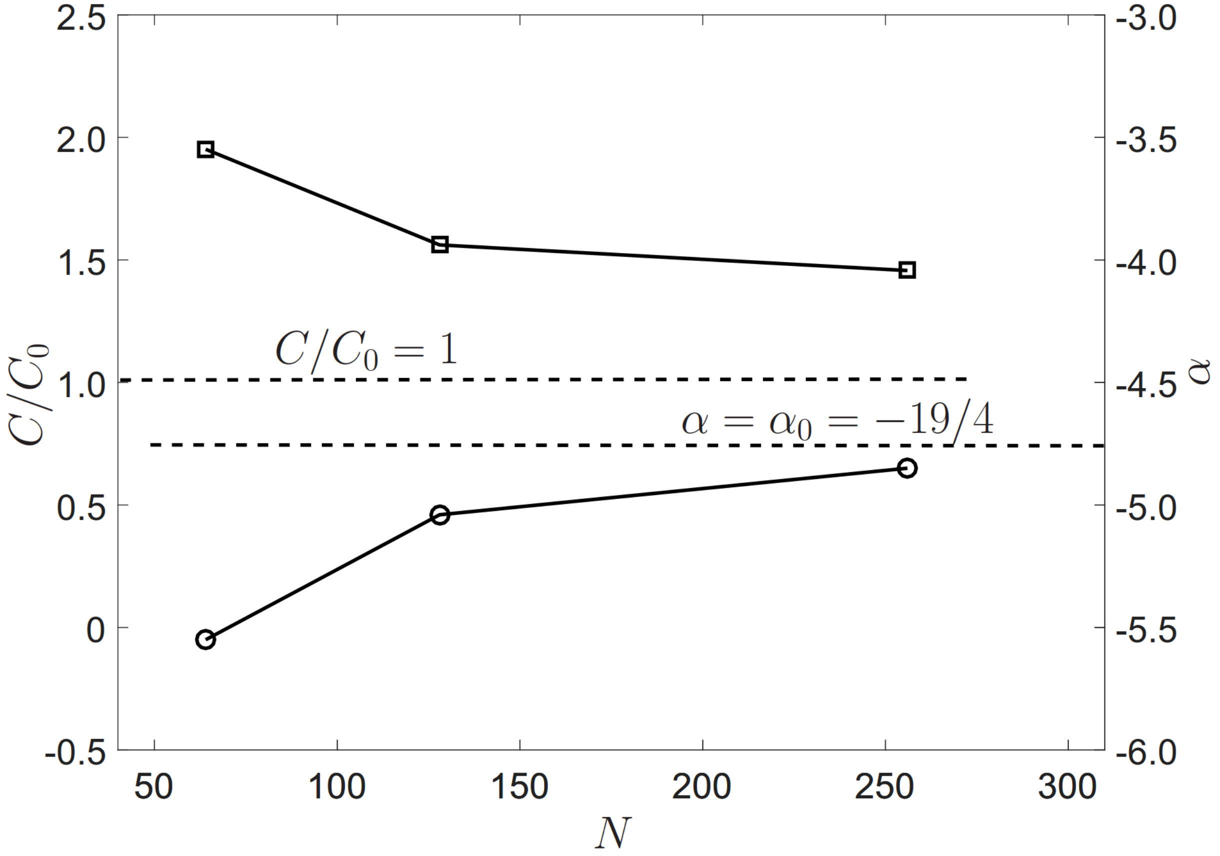

Figure 4-5: C/C_0 (—□—) and α (—○—) compared to WTT (– – –) with varying mode number N, for $\widehat{P} = 3.4 \times 10^{-7}$.

indeed manifestations of the finite box effect.

4.3 Summary

In this Chapter, we present results from direct numerical simulations of freely-evolutional capillary wave turbulence. With the precisely evaluated P from the energy dissipation rate, we are able to confirm the WTT $P^{1/2}$ scaling over a broad range of P. For sufficiently large P, the WTT $k^{-19/4}$ scaling is recovered to high accuracy, and the value of Kolmogorov Constant $C \approx 9.9$ is obtained with reasonable error compared to the theoretical value of $C_0 = 6.97$. At lower nonlinearity level, the deviations of the power-law spectral slope α and proportionality constant C from their asymptotic values at sufficient nonlinearity are obtained and shown to be a result of finite box effect. The current work reinforces the validity of WTT as a description of capillary wave turbulence over a broad range of energy fluxes, and quantifies the deviations from WTT due to finite box effect when grid resolution or tank size is limited. We have studied the special case of capillary wave turbulence, our main findings are expected to also hold for weak turbulence in other similar physical systems.

Chapter 5

Understanding discrete capillary wave turbulence using quasi-resonant kinetic equation (QRKE)

Investigations in Chapter 4 have shown that the power-law spectrum of weak turbulence, theoretically derived by assuming infinite domain with continuous wavenumber representation, is realizable in realistic finite domain with discrete wavenumbers. In this chapter, we seek to understand this phenomenon of discrete capillary wave turbulence, under the framework of the Kinetic Equation (KE). In cases of finite domain, the KE is not directly applicable, as the condition of exact triad resonant interaction does not hold, i.e., the frequency mismatch within a triad is restrained from being zero and energy transfer is governed by the quasi-resonant interactions with nonlinear resonance broadening. In order to develop appropriate modification of the KE, we conduct a study on the mechanism of nonlinear broadening using data from the simulation of the primitive Euler equations (Pan & Yue, 2014). It is elucidated that the nonlinear broadening increases with nonlinearity level (wave steepness), and reaches an upper limit at sufficient nonlinearity level in the regime of weak turbulence. Inspired by these findings, we develop a quasi-resonant kinetic equation (QRKE) for capillary waves, which takes into consideration the wavenumber discreteness and quasi-resonant triad interactions. An additional non-dimensional parameter κ is introduced in the equation, which exclusively governs the ratio between nonlinear broadening and wavenumber discreteness. The simulation of the QRKE shows that an arbitrary initial spectrum, subject to forcing at the fundamental wavenumber, evolves into a stationary power-law spectrum. At $\kappa = \kappa_0 = 0.02$, the theoretical values α_0 and C_0 are simultaneously recovered. This physically represents an upper limit that the energy flux by quasi-resonance approaching that of exact resonance in theoretically infinite domain. For $\kappa < \kappa_0$, physics of insufficient nonlinearity, namely the steepened power-law spectral slope and reduced energy flux, is replicated in the simulation results. We thus establish the physical connection of nonlinearity level, nonlinear broadening and features of the power-law spectrum. The method is further justified by showing that the key parameter κ is linearly correlated with nonlinear broadening obtained from the data of Euler equations.

5.1 On the Kinetic Equation and Resonance Condition

For completeness of this chapter, we re-write the kinetic equation (KE) derived in Chapter 2:

$$\frac{\partial n_{\mathbf{k}}}{\partial t} = S(n_{\mathbf{k}}), \tag{5.1}$$

$$S(n_{\mathbf{k}}) = \iint_{-\infty}^{\infty} [R_{\mathbf{k}\mathbf{k}_1\mathbf{k}_2} - R_{\mathbf{k}_1\mathbf{k}\mathbf{k}_2} - R_{\mathbf{k}_2\mathbf{k}\mathbf{k}_1}] d\mathbf{k}_1 d\mathbf{k}_2, \tag{5.2}$$

$$R_{\mathbf{k}\mathbf{k}_1\mathbf{k}_2} = 4\pi |V_{\mathbf{k}\mathbf{k}_1\mathbf{k}_2}|^2 \delta(\mathbf{k} - \mathbf{k}_1 - \mathbf{k}_2)\delta(\omega_{\mathbf{k}} - \omega_{\mathbf{k}_1} - \omega_{\mathbf{k}_2})[n_{\mathbf{k}_1} n_{\mathbf{k}_2} - n_{\mathbf{k}} n_{\mathbf{k}_1} - n_{\mathbf{k}} n_{\mathbf{k}_2}], \tag{5.3}$$

$$V_{\mathbf{k}\mathbf{k}_1\mathbf{k}_2} = \frac{1}{8\pi\sqrt{2}} (\omega_{\mathbf{k}} \omega_{\mathbf{k}_1} \omega_{\mathbf{k}_2})^{1/2} [\frac{L_{\mathbf{k}_1,\mathbf{k}_2}}{(k_1 k_2)^{1/2} k} - \frac{L_{\mathbf{k},-\mathbf{k}_1}}{(k k_1)^{1/2} k_2} - \frac{L_{\mathbf{k},-\mathbf{k}_2}}{(k k_2)^{1/2} k_1}], \tag{5.4}$$

$$L_{\mathbf{k}_1,\mathbf{k}_2} = \mathbf{k}_1 \cdot \mathbf{k}_2 + k_1 k_2. \tag{5.5}$$

For simplicity, the time and mass units are chosen so that the surface tension coefficient σ and the fluid density ρ are unity. In the KE, $n_{\mathbf{k}}$ is the spectral density of wave action (see Chapter 2 for the normalization) at wavenumber $\mathbf{k}$. $S(n_{\mathbf{k}})$ is the collision integral, representing the nonlinear spectral evolution due to triad resonant interactions. At a mode $k = |\mathbf{k}|$,

$$\omega_{\mathbf{k}} = |\mathbf{k}|^{3/2} \tag{5.6}$$

is the angular frequency determined from the linear dispersion relation.

In an isotropic wavefield, the analytical stationary solution (with large-scale forcing and small-scale dissipation) of the KE yields a power-law spectrum in the inertial range (see the derivation in Chapter 2),

$$n(k) = 2\pi C_0 P^{1/2} k^{-17/4}, \tag{5.7}$$

where P is the energy flux from large forcing scales to small dissipative scales, and $C_0 = 6.97$ is the Kolmogorov Constant. In obtaining (5.7), a key assumption is made, under which $S(n_{\mathbf{k}})$ can take non-zero value, that the wave domain contains triad $(\mathbf{k}, \mathbf{k}_1, \mathbf{k}_2)$ in exact triad resonance, satisfying

$$\mathbf{k} - \mathbf{k}_1 - \mathbf{k}_2 = 0, \tag{5.8}$$

$$\omega_{\mathbf{k}} - \omega_{\mathbf{k}_1} - \omega_{\mathbf{k}_2} = 0. \tag{5.9}$$

The existence of exact triad resonance is mathematically only possible as $\mathbf{k}$ varies continuously in a theoretically infinite wave tank/domain. In a finite domain with wavenumber discreteness, significant difference can be originated from the mathematical property of the (5.8) and (5.9): It is shown in Kartashova (1990) that there is no solution of exact triad resonance, as the frequency condition (5.9) turns into a particular case of Fermat's last theorem. Therefore, the KE is not directly applicable, as the integral $S(n_{\mathbf{k}})$ is rendered to be zero. It is, however, desirable to establish this framework, which is physically more tangible than that of the primitive Euler equations, in terms of its explicit mathematical description of energy transfer by triads (see (5.3)). We postulate that the influence of the nonlinearity level on the dynamics of energy transfer can be elucidated after the corresponding parameter is properly introduced.

5.2 Nonlinear Broadening in Discrete Wave Turbulence

In a $L \times L$ finite domain associated with wavenumber discreteness $\Delta k \sim 1/L$, the KE is not directly applicable, as the triad resonant condition for frequency (5.9) cannot be exactly satisfied. Physically under this constraint, the nonlinear broadening plays a key role in exciting the quasi-resonant interaction, allowing a small mismatch in (5.9). While it is argued (e.g. Pushkarev & Zakharov, 2000; Connaughton *et al.*, 2001) that the energy transfer is only possible under sufficient nonlinear broadening, a quantitative description of this mechanism is lacking. In order to develop an appropriate modification of KE for this scenario, we first conduct such a study using the results from the simulation of primitive Euler equations. With the data in analysis drawn from the fully-developed wavefield represented by power-law spectra, we provide a direct measure of nonlinear broadening and the corresponding spectral properties under different nonlinearity levels.

To construct a quantitative measure of the nonlinear broadening, we first define a bi-coherence

$$B_i(\mathbf{k}, \mathbf{k}_1) = \frac{|\langle \eta^*(\mathbf{k}) \eta(\mathbf{k}_1) \eta(\mathbf{k}_2 = \mathbf{k} - \mathbf{k}_1) \rangle|}{\langle |\eta(\mathbf{k})||\eta(\mathbf{k}_1)||\eta(\mathbf{k}_2 = \mathbf{k} - \mathbf{k}_1)| \rangle}, \tag{5.10}$$

with $\langle\rangle$ denoting the time average and $*$ the complex conjugate, $\eta(\mathbf{k})$ being the spatial Fourier component of the surface elevation at wavenumber $\mathbf{k}$. B_i measures the phase coupling of the three wave vectors $\mathbf{k}$, $\mathbf{k}_1$ and $\mathbf{k}_2 = \mathbf{k} - \mathbf{k}_1$. It ranges from 0 to 1 for zero and perfect coupling. In a wavefield with discrete wavenumber, B_i obtains high values for quasi-resonant triads, and low values for non-resonant triads.

Without loss of generality, we set $\mathbf{k} = (25, 0)$, and plot B_i as a function of $\mathbf{k}_1 = (k_{1x}, k_{1y})$. This is shown for two cases with higher and lower nonlinearity levels in figure 5-1(a) and (b) in the same finite domain, i.e., same Δk. The regions of high values of $B_i(\mathbf{k}_1)$ for both cases are concentrated around curves of $\mathbf{k}_1$ for which exact

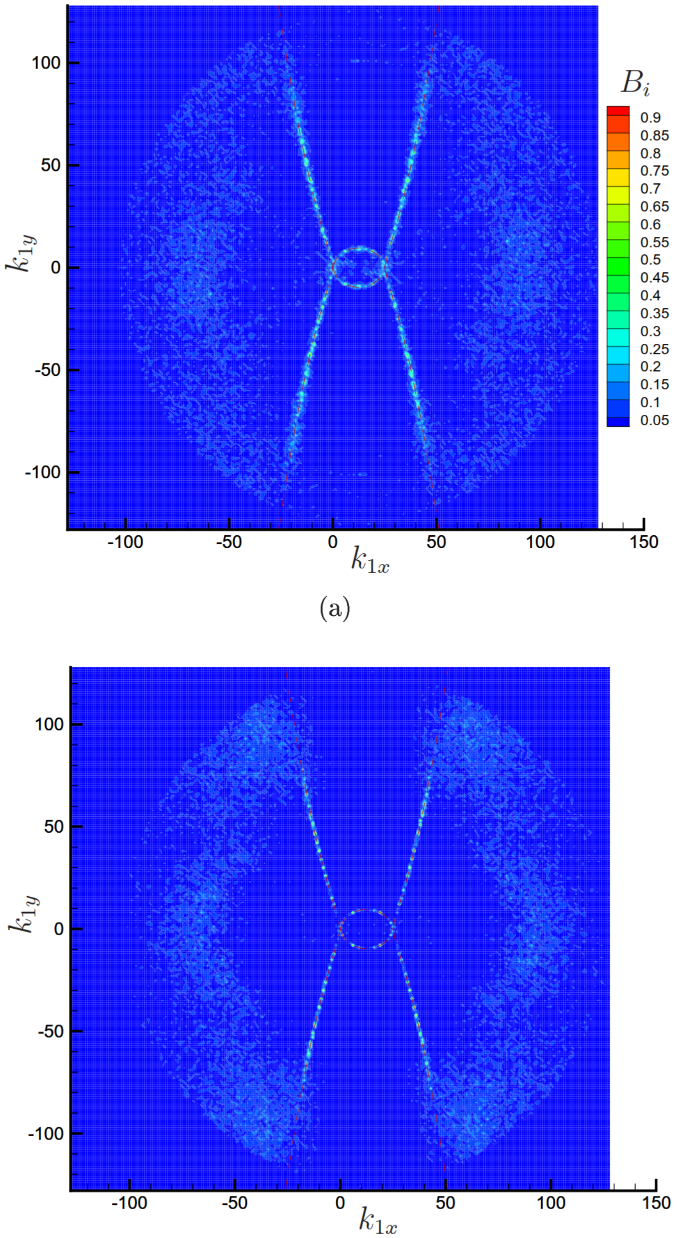

(a)

(b)

Figure 5-1: B_i for (a) high nonlinearity ($\alpha \approx -4.25$) and (b) low nonlinearity ($\alpha \approx -4.6$) wavefield. Time average are obtained over $200T_p$, where T_p is the modal period of wavenumber at the spectral peak. The vectors $\mathbf{k}_1$ for which exact resonance occurs are indicated by $---$. The middle ellipse represents the triads of $\langle \eta^*(\mathbf{k})\eta(\mathbf{k}_1)\eta(\mathbf{k}_2)\rangle$ ($\Omega_{k12} = 0$), and the left and right branches represent, due to conjugation, $\langle \eta^*(\mathbf{k})\eta^*(-\mathbf{k}_1)\eta(\mathbf{k}_2)\rangle$ ($\Omega_{2k1} = 0$) and $\langle \eta^*(\mathbf{k})\eta(\mathbf{k}_1)\eta^*(-\mathbf{k}_2)\rangle$ ($\Omega_{1k2} = 0$).

resonance condition is satisfied. These curves are mathematically characterized by

$$\Omega \equiv min(|\Omega_{k12}|, |\Omega_{1k2}|, |\Omega_{2k1}|) = 0, \tag{5.11}$$

where $\Omega_{ijl} \equiv \omega_i - \omega_j - \omega_l$. With the finite width of $B_i(\mathbf{k}_1)$ at the vicinity of the resonant curves measuring the nonlinear broadening, it is now visibly clear from figure 5-1 that the nonlinear broadening associated with higher nonlinearity level (and shallower spectral slope α) is appreciably wider than that of lower nonlinearity level (and steeper α). To further obtain a quantitative measure, we define

$$\hat{L}_b = \frac{\sum |\hat{\Omega}| B_i}{\sum B_i}, \tag{5.12}$$

with $\hat{\Omega} \equiv \Omega/(\Delta k k^{1/2})$ being a normalized frequency mismatch, i.e., distance of a point in the domain to the resonance curve measured by frequency, and the summation being for all grid points adjacent to the resonance curve (say $|\hat{\Omega}| < 2$). The parameter $\hat{L}_b$ thus measures the (non-dimensional) characteristic length of nonlinear broadening by first moment of $B_i(\mathbf{k}_1)$ centered at the resonance curve.

We plot in figure 5-2 the variation of L_b and the spectral slope α with the increase of nonlinearity level, measured here by the amount of (non-dimensionalized) energy flux $\hat{P}$ (see Chapter 4 for its calculation). The range of nonlinearity considered here corresponds to the weak turbulence regime, i.e., cases with relatively small wave steepness such that perturbation analysis in WTT/HOS is valid. It is shown that the approaching of α to the theoretical value α_0 is accompanied by that of $\hat{L}_b$ toward some constant. This is an illustration of the broadening approaching a limit with sufficiently large nonlinearity (in the considered range), for which the dynamics governed by quasi-resonance approximates that of exact resonance in theoretically infinite domain. While the dynamics above this limit remains elusive (e.g. Denissenko *et al.*, 2007) and is beyond the capability of HOS and KE, we focus our consideration on the range below it.

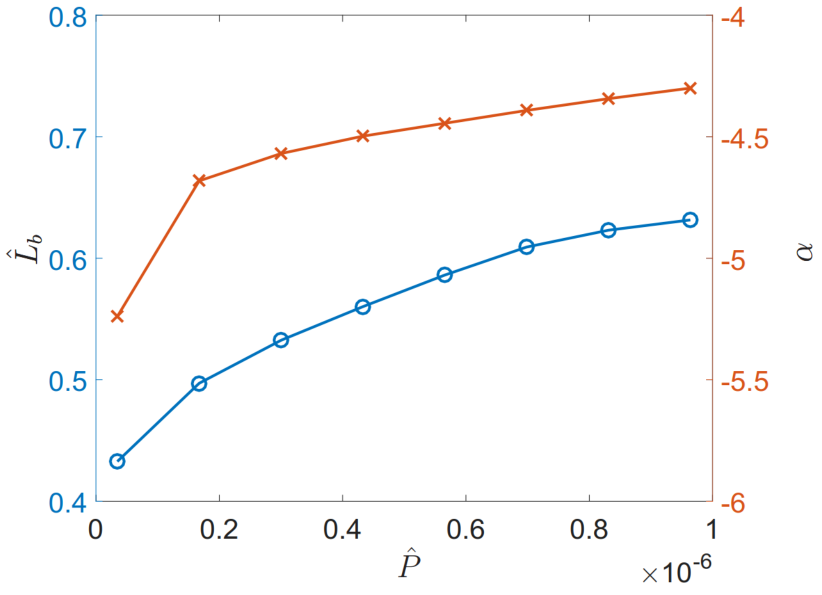

Figure 5-2: The spectral slope α (—×—) and the broadening $\hat{L}_b$ (—o—) as functions of the non-dimensionalized energy flux $\hat{P} \equiv P/(\sigma\omega_p)$, with ω_p being the angular frequency of the peak mode.

5.3 QRKE for Discrete Turbulence

In addition to elucidating the mechanism of nonlinear broadening, the analysis in section 5.2 inspires us to develop a simplified model in the framework of the KE. To represent the quasi-resonant interactions, we broaden the exact delta function $\delta(\Omega_{k12})$ in (5.3) (and the counterparts for other triads) as a finite-width delta function,

$$\delta(\Omega_{k12}) \sim \delta_g(\Omega_{k12}) = \frac{\beta}{\pi}\frac{1}{\beta^2 + \Omega_{k12}^2}, \tag{5.13}$$

where β is a small parameter introduced to characterize the nonlinear resonance broadening in frequency. The physical significance of using (5.13) can additionally be traced back in the derivation of KE. Rigourously speaking, the delta function in (5.3) is a result of the closure for third-order cumulant J_{k12} ($\sim$ ensemble average of multiplication of modal amplitudes at $\mathbf{k}$, $\mathbf{k}_1$ and $\mathbf{k}_2$), which renders J_{k12} to be nonzero only when $\Omega_{k12} = 0$. The treatment of (5.13) broadens the nonzero region of J_{k12}, and, in the framework of KE, effectively allows the triads in quasi-resonance to be excited for nonlinear energy transfer. The specific form (5.13) of the finite-width delta function is preferred as it is mathematically a direct result of relaxing the limit of zero-approaching small parameter (to account for the discrete wavenumber) in the application of the Sokhotski-Plemelj theorem in the derivation (cf. Zakharov *et al.*, 1992).

We further define the non-dimensional frequency broadening:

$$\kappa = \frac{\beta}{\Delta k k^{1/2}}, \tag{5.14}$$

where the denominator $\Delta k k^{1/2}$ is a measure of the frequency discreteness associated with Δk at wavenumber k. κ is thus a non-dimensional parameter characterizing the ratio between nonlinear broadening and grid spacing, i.e., a measure of the number of grid points underneath the broadening. Furthermore, it is the exclusive parameter in the modified KE by which the nonlinearity level is introduced, and is of significant role in the dynamics of energy transfer on a discrete grid. In a single simulation with a particular nonlinearity level, κ is set as a constant, and β is calculated accordingly as a function of k. This ensures that the frequency broadening scales with the frequency discreteness, and is thus evenly applied, at all wavenumbers.

The simulation domain is confined to be $(0, k_{max}]$, where k_{max} physically corresponds to the cut-off wavenumber of the inertial range. To model the small-scale energy sink, we assume that all the energy transferring across k_{max} is dissipated. This is equivalent to adding an additional term $\Gamma(n_k)$ in (5.1), in the form of

$$\Gamma(n_k) = -\iint_{k_{max}<k_1<k_d} 8\pi |V_{\mathbf{k}_1\mathbf{k}\mathbf{k}_2}|^2 \delta(\mathbf{k}_1 - \mathbf{k} - \mathbf{k}_2)\delta_g(\omega_{k_1} - \omega_k - \omega_{k_2}) n_k n_{k_2} d\mathbf{k}_1 d\mathbf{k}_2, \tag{5.15}$$

which selects all the triads transferring energy from $k \in (0, k_{max}]$ to $[k_{max}, k_d]$. While $n(k > k_{max})$ is set to be zero and not updated in the simulation, $[k_{max}, k_d]$ serves as an energy sink regime, which physically absorbs energy transferred from $(0, k_{max}]$. In theory, $k_d = 2k_{max}$ accounts for all such triads and (5.15) thus provides a parameter-free dissipation model with $\Gamma(n_k)$ representing the evolution of n_k due to these quasi-resonant triad interactions. The energy flux can be directly evaluated as the energy transfer across k_{max},

$$P = -\frac{1}{2\pi}\int_{k=0}^{k_{max}} k^{5/2}\Gamma(n_k)dk. \tag{5.16}$$

With these configurations, it is expected that the continuous case described by the original KE can be numerically represented with the parameter $\kappa \gg 1$ on a sufficiently fine grid. We have been able to verify this, by obtaining converged results of α and C to their theoretical values with the decrease of grid size for any large enough value of κ. This provides a direct confirmation of our newly evaluated value of C_0, and an alternative way by which different types of kinetic equation can be solved numerically for the theoretical solution (even prior to the lengthy theoretical derivation). These solutions, however, do not correspond to the cases of discrete turbulence (for example, it requires at least $O(10^5\times10^5)$ modes to obtain the theoretical results, which is much more than that for discrete turbulence ($O(100 \times 100)$, as in Chapter 4).

Our purpose is to study the discrete capillary wave turbulence in the framework of the QRKE, that is, to obtain the stationary spectrum on a coarse grid with small values of κ. To this end, we perform simulations with $O(10 \sim 100)$ modes and selected values of $\kappa < 1$. Starting from a somewhat arbitrary initial solution, chosen in present work as an exponential function $n(k) = exp(-k^2/5)$, we numerically evolve the spectrum in time according to the QRKE, (5.1)∼(5.5) and (5.13)∼(5.15), with a second-order Runge-Kutta scheme. To obtain a stationary spectrum, a large-scale forcing is required. Instead of adding an extra forcing term in the KE (e.g. Pushkarev *et al.*, 2003), we assume that the forcing exactly compensates for the decrease of n at large scales due to energy transfer to small scales, i.e., $n(k)$ within the forcing regime numerically keeps constant in the simulation. This approach is found to be very efficient in obtaining the converged stationary spectrum. Without loss of generality, we consider the forcing concentrated at the fundamental wavenumber $k = \Delta k$.

5.4 Results of the QRKE

We consider the evolutions of the spectra governed by the QRKE with prescribed values of κ. After sufficient time, the spectra evolve to stationary power-law solutions with different spectral slopes α for different values of κ. These are plotted in figure 5-3(a) with $k_{max} = 32$, $\Delta k = 1$ and selected values of κ. The evolutions of the total spectral energy E for these cases are plotted in figure 5-3(b), showing that the stationary state is reached as the power-law spectra are formed.

The evaluation of spectral slope α is straightforward at the stationary state. The Kolmogorov Constant C is evaluated, after the value of α is obtained, as $C = \langle n(k)/(2\pi P^{1/2}k^{\alpha})\rangle_k$, where P is calculated using (5.16) and $\langle\rangle_k$ denotes the average over range of k (This is in contrast to Chapter 4 where we can find an interval complying with α_0 slope amid the spectrum with overall but slowly-varying slope α). The value of C such evaluated is a measure of the capability of a spectrum to transfer energy: For two spectra with different values of C, the one associated with larger C has smaller energy flux scaled by the spectral amplitude at $k = 1$, i.e., weaker capability of transferring energy.

Guided by the analysis in section 5.2, we consider the range of κ (and Δk) corresponding to the physically realizable spectra in weak turbulence regime, i.e., those with $|\alpha| \geq |\alpha_0|$ and $C \geq C_0$, which otherwise covers broad range of α and C. These are plotted in figure 5-4 for $\Delta k = 1$. It is shown that the theoretical values of $\alpha_0 = -17/4$ and $C_0 = 6.97$ are simultaneously achieved at $\kappa = \kappa_0 = 0.02$. This thus physically corresponds an upper limit, in our consideration, of nonlinear broadening, for which the dynamics excited by the quasi-resonant interactions approximates that of the exact resonance in theoretically infinite domain. For $\kappa \leq \kappa_0$, the plots show that both $|\alpha|$ and C monotonically increase with the decrease of κ in the tested range. These results are clear manifestations of the physics with insufficient nonlinearity level, i.e., steepened spectral slope and reduced capability of energy transfer. These phenomena are also fundamentally observed in the direct simulation of the primitive Euler equations (Chapter 4) and experiments (e.g. Denissenko *et al.*, 2007; Deike *et al.*, 2013, 2015).

The influence of Δk on α and C is considered and plotted in the two insets of figure 5-4, using the case with $\kappa = \kappa_0$ as a representation. It is shown that both α and C can be considered as functions of κ only, even though C exhibits weak oscillations

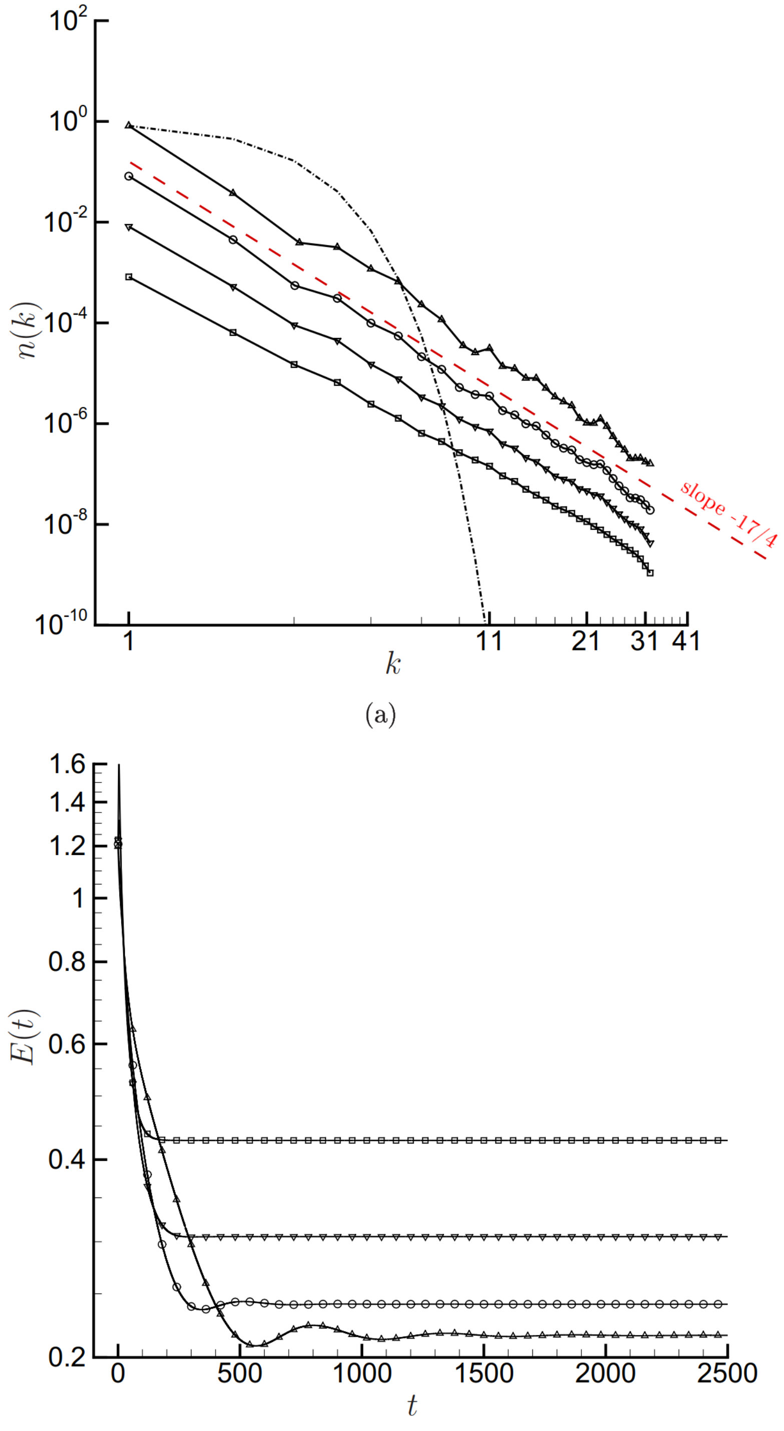

(a)

(b)

Figure 5-3: (a) Converged stationary power-law spectra at t=2500 and (b) variations of total energy E in the spectral evolutions for $\kappa = 0.01$ (—△—), $\kappa = 0.02$ (—○—), $\kappa = 0.04$ (—▽—) and $\kappa = 0.1$ (—□—). In (a), the initial spectrum (- · -) and the theoretical slope $-17/4$ (– – –) are indicated. Curves with different values of κ are shifted for clarity.

around the mean value. This can be mathematically understood from the scalability of the problem. The variation of Δk without modifying α and C is a direct result of the scale invariance of the KE (where, numerically for the QRKE, the summation of triads is obtained by sampling near $\hat{\Omega} = 0$ with shifts that are similarly distributed for different Δk). The physical implication of this independence on Δk is profound. It signifies that values of α and C, both reflections of dynamics of energy transfer on discrete grid, are solely determined by the ratio between nonlinear broadening and grid discreteness, i.e., the dynamics can be changed equivalently by varying the nonlinear broadening or grid discreteness.

As nonlinearity level is solely represented by κ in the QRKE, the steepened spectral slope and reduced energy flux at insufficient nonlinearity level can be directly explained through the decreased nonlinear broadening. To corroborate this point with the results of Euler equations in section 5.2, we plot in figure 5-5 κ as a function of the corresponding $\hat{L}_b$, associated with the same spectral slope α. It is clear that κ increases monotonically with $\hat{L}_b$, with the correlation being linear in this considered range, and $\kappa = \kappa_0 = 0.02$ corresponds to the largest value of $\hat{L}_b$ for which $\alpha = \alpha_0$ is obtained. This result confirms the established connection of nonlinear broadening with the spectral properties, and provides a direct justification of the formulation of κ in the modified KE.

We finally remark an important difference in the mechanism of nonlinear broadening between the Euler equations and the QRKE. Instead of the uniformly applied broadening (5.14) in k, nonlinearity decreases as k increases due to the decreased wave steepness for a realistic wavefield. This is illustrated in figure 5-1 by the diminished value of B_i with the increase of k, which vanishes for sufficiently large k. Dynamically, this results in a reduced energy flux, and to some extend, explains the discrepancy between C_0 and the obtained value of $C \approx 9.9$ in Chapter 4 from the primitive Euler equations.

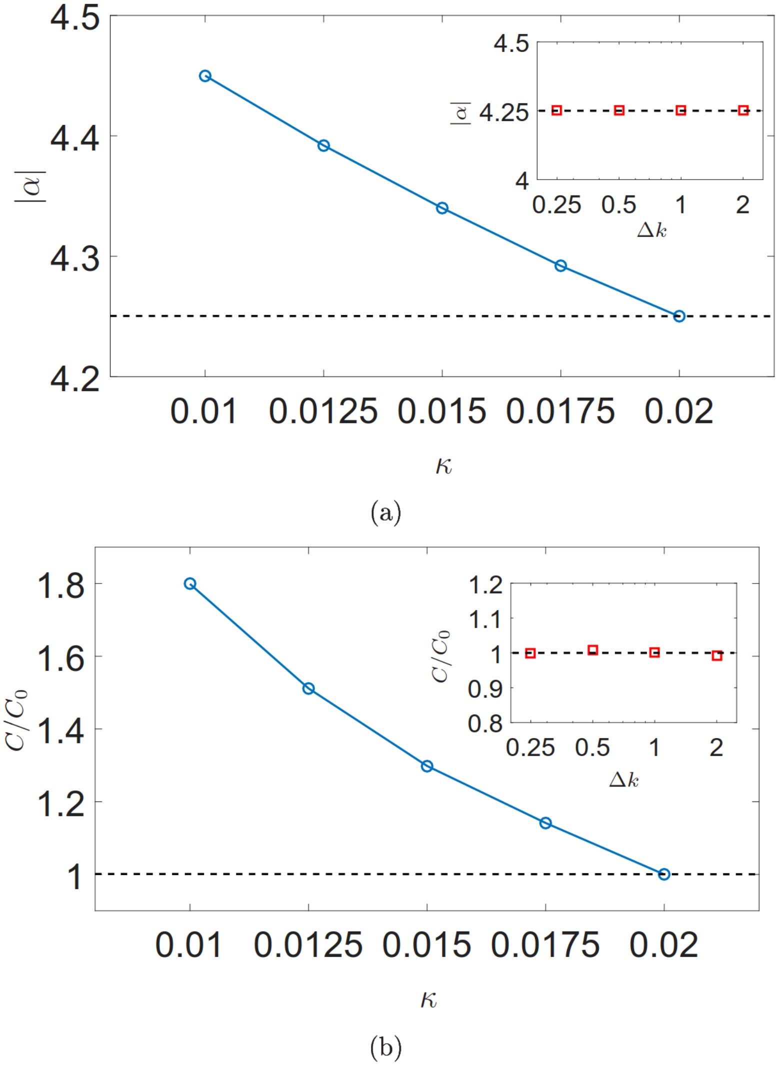

Figure 5-4: (a) $|\alpha|$ and (b) C/C_0 as functions of κ for $\Delta k = 1$. Insets: (a) $|\alpha|$ and (b) C/C_0 as functions of Δk for $\kappa = \kappa_0$. The theoretical values (– – –) of $|\alpha_0| = 17/4$ and $C/C_0 = 1$ are indicated in all figures.

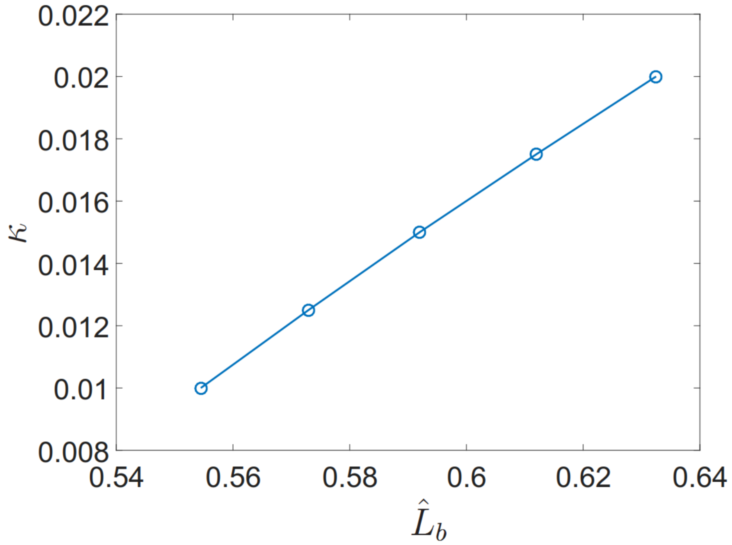

Figure 5-5: The parameter κ as a function of the corresponding $\hat{L}_b$ associated with the same spectral slope α. From left to right, the associated values of α are 4.45, 4.39, 4.34, 4.29 and α_0=4.25.

5.5 Summary

We present a study regarding discrete capillary wave turbulence in the framework of the Kinetic Equation (KE). Under the assumption of theoretically infinite domain, the original derivation of the stationary solution of the KE is expanded. With the correction of a key integral in the derivation process, we obtain the theoretical Kolmogorov Constant with an updated value of $C_0 = 6.97$. In cases of discrete turbulence in a finite domain where energy transfer is sustained by quasi-resonant interactions, the KE is not directly applicable, and further development requires a quantitative understanding of the mechanism of nonlinear broadening. This is obtained using data from the simulation of the primitive Euler equations. It is found that nonlinear broadening increases with the increase of nonlinearity level, and reaches an upper limit in the regime of weak turbulence. Guided by these findings, we develop a quasi-resonant kinetic equation (QRKE) for discrete capillary wave turbulence, by introducing a non-dimensional parameter κ governing the ratio of nonlinear broadening and wavenumber discreteness. In simulation of the QRKE, we find that the obtained values of α and C are functions of κ only. As $\kappa = \kappa_0 = 0.02$, the theoretical values of α_0 and C_0 are simultaneously recovered, indicating an upper limit of energy flux by quasi-resonance approaching that of exact resonance in theoretically infinite domain. For $\kappa < \kappa_0$, the simulation results replicate those with insufficient nonlinearity level, namely the steepened spectral slope and reduced capability of transferring energy. As a justification of the established QRKE, the key parameter κ is confirmed to be linearly correlated with the nonlinear broadening in Euler equations. The elucidation the role of nonlinear broadening in discrete turbulence and the methodology regarding the QRKE are expected to be valid for the weak turbulence in various physical contexts.

Chapter 6

Decaying capillary wave turbulence under broad-scale dissipation

In this chapter, we perform direct numerical simulation of decaying capillary wave turbulence implementing the nonlinear primitive Euler equations. We consider low Bond number such that the influence of gravity is neglected. The problem we solve is a substantial generalization of Chapter 4, or Pan & Yue (2014), where realistic broad-scale dissipation is included in the context of decaying turbulence. In contrast to Chapter 4, we also simulate the evolving spectrum for a long enough time scale to investigate the time-varying dynamics. Our results replicate those from experiments of a power-law spectrum with exponential modal decay, as well as monochromatic decrease of the cut-off wavenumber k_c and variation of α during the decay. Along with the evolution of the spectrum ($\partial I_\eta/\partial t \neq 0$), the broad-scale dissipation results in variation of the energy transfer, $\mathcal{J}(k,t)$, along k. This substantially complicates the evaluation of the energy flux P. We propose a novel and effective way to obtain P, by integrating the modal energy balance equation along k, thus incorporating both effects of unsteadiness and nonconstant inter-model energy transfer $\mathcal{J}$. The obtained results on P are shown to be consistent with the framework of Pushkarev & Zakharov (2000) and Pan & Yue (2014) in term of the scaling $I_\eta \sim P^{1/2}$. By considering energy dissipated at broad scales, we also show that the total energy dissipation rate Γ can be significantly higher than P, which settles the previous debate on the measurement of P by assuming the equivalence of the two (Falcon *et al.*, 2007; Xia *et al.*, 2010).

Based on our simulations, we are able to describe the time-dependent power-law spectrum within the inertial range $[k_b, k_c(t)]$ in an explicit general form:

$$\begin{gathered} I_\eta(k,t) = I^0 k^{\alpha^0 - A(t-t^0)} e^{-B(t-t^0)}, \\ \text{for } k_b < k < k_c(t) \text{ and } t > t^0 \end{gathered} \tag{6.1}$$

where I^0 and α^0 are respectively the spectral amplitude and slope of the spectrum at $t{=}t^0$. k_b is the (almost) constant wavenumber above which the power-law spectrum is established, and $k_c(t)$ is the spectral location where the spectrum departs from the power law (6.1). A and B are functions of γ_0 only.

Equation (6.1) is shown to fit our numerical data obtained over the ranges of dissipation magnitude, spectral amplitude (nonlinearity) and evolution time that can be obtained by our simulation. For sufficiently high initial nonlinearity, $\alpha^0 \approx -19/4$. While $A(\gamma_0)$ represents the time-varying rate of the spectral slope $\alpha(t) = \alpha^0 - A(t-t^0)$, we show that the value of α at a given t can be solely related to the nonlinearity level of the spectrum at that time, irrespective of γ_0. The evolution of energy $E_I(t)$ within the inertial range is shown to be well predicted by the analytical integration of (6.1).

The main results of this chapter is also presented in Pan & Yue (2015).

6.1 Numerical Formulation

We consider isotropic decaying capillary wave turbulence in the context of potential flow (velocity potential $\phi(x,y,z,t)$), in terms of the primitive Euler evolution equations (e.g. Zakharov, 1968) for the surface elevation $\eta(x,y,t)$ and surface velocity potential $\phi^s(x,y,t) \equiv \phi(x,y,\eta,t)$:

$$\eta_t = -\nabla_{\mathbf{x}}\phi^s \cdot \nabla_{\mathbf{x}}\eta + (1 + \nabla_{\mathbf{x}}\eta \cdot \nabla_{\mathbf{x}}\eta)\phi_z + F^{-1}[\gamma_k \eta_{\vec{k}}], \tag{6.2}$$

$$
\begin{aligned}
\phi_t^s = -\frac{1}{2}\nabla_{\mathbf{x}}\phi^s \cdot \nabla_{\mathbf{x}}\phi^s + \frac{1}{2}(1 + \nabla_{\mathbf{x}}\eta \cdot \nabla_{\mathbf{x}}\eta)\phi_z^2 + \\
\frac{\sigma}{\rho}\nabla_{\mathbf{x}} \cdot \frac{\nabla_{\mathbf{x}}\eta}{\sqrt{1 + \nabla_{\mathbf{x}}\eta \cdot \nabla_{\mathbf{x}}\eta}} + F^{-1}[\gamma_k \phi_{\vec{k}}^s],
\end{aligned}
\tag{6.3}
$$

where F^{-1} is the inverse Fourier transform, and $\gamma_k \equiv \gamma(k) = -\gamma_0 k^2$ is applied on all k, modeling the broad-scale viscous dissipation at the free surface (e.g. Deike *et al.*, 2014*a*).

We numerically integrate (6.2) and (6.3) in time with the WW formulation of the HOS method (refer to Chapter 3 for a validation of the method), with the dissipation term modelled as exponentially decayed wave modes (see Chapter 4). The simulation starts from an initial isotropic wave field with arbitrary spectral energy distribution. After sufficient time, an inertial-range power-law spectrum forms due to nonlinear wave interactions. Our objective is to study the decay of this spectrum until the physics reaches purely dissipative regime, i.e., we focus on the spectrum with an inertial range longer than a critical value (in practice, $\gtrsim$0.3 decade). To obtain a broad range of energy variation, we choose an initial state specified by a JONSWAP spectrum (the inertial-range results are not sensitive to the specific choice of the initial spectrum), with effective steepness $\beta = k_p H_s/2 = 0.25$ (with k_p being the peak wave number and H_s the significant wave height), which is the highest nonlinearity that can be modelled by HOS.

Simulations are carried out on a periodic domain with 256×256 grid points (k_{max}=256) with a 2/3 de-aliasing rule. The peak wavenumber $k_p = 10k_0$, with k_0 being the fundamental wavenumber of the domain. Up to third-order nonlinearity is included to allow interactions of both three and four waves (cf. Pushkarev & Zakharov, 1996; Pan & Yue, 2014). We define normalized dissipation coefficient $\widehat{\gamma}_0 \equiv \gamma_0 k_p^2/\omega_p$, where $\omega_p = \sqrt{\sigma k_p^3/\rho}$ is the angular frequency corresponding to k_p. Power-law spectrum can be obtained in our simulation for $\widehat{\gamma}_0 \in (0.5 \times 10^{-5}, 3.0 \times 10^{-5})$. This range is limited above by the dominance of dissipation over nonlinear interaction, and below by the inherent numerical instability associated with the growth of short waves. Results from selected values of $\widehat{\gamma}_0 = 0.8 \times 10^{-5}$, 1.6×10^{-5} and 2.4×10^{-5} are presented.

6.2 Results

6.2.1 Spectral decay

Figure 6-1 shows a typical decay of spectrum I_η after the power-law inertial range is established. This plot is a representative of all our results, where the evolving spectrum features a power-law range within $[k_b, k_c(t)]$ (with $k_b \approx 1.5k_p$) and an exponential range within $[k_c(t), k_{max}]$. In practice (with sufficiently wide $[k_b, k_c]$), k_c is obtained from the intersection of the power-law $I_\eta \sim k^\alpha$ and exponential $I_\eta \sim exp(\beta k)$ fits of the numerical data. Physically, k_c corresponds to the spectral location at which the time scales of nonlinear interaction and viscous dissipation are balanced (Kolmakov *et al.*, 2004; Deike *et al.*, 2014*b*). As the spectrum decays, k_c decreases monotonically (cf. Kolmakov *et al.*, 2004). This decrease is found to be approximately linear with t for all our cases (see figure 6-1 inset). Within the power-law range, it is clear that $I_\eta \sim k^\alpha$ where $\alpha = \alpha(t)$. As spectrum evolves, α decreases as the negative power-law spectral slope steepens. This phenomenon, also observed in the simulation without dissipation in the inertial range (Chapter 4), is concluded to be due to the finite box effect. This is a phenomenon where nonlinear wave interactions are suppressed due to the discreteness in k (and nonlinear resonance broadening is insufficient to overcome it) (e.g. Pushkarev & Zakharov, 2000). It results in steeper spectrum at lower nonlinearity, as evidenced also from gravity wave turbulence (e.g. Denissenko *et al.*, 2007).

Figure 6-2 plots $I_\eta(k_j, t)$ as functions of time for different values of $k_j \in [k_b, k_{max}]$. Regardless of whether k_j is in the power-law range, $I_\eta(t; k_j)$ decays exponentially (cf. Deike *et al.*, 2012, 2013) with $I_\eta(k, t) \sim \exp(-\xi t)$, where $\xi{=}\xi(k)$. As a fixed k_j goes from below to above $k_c(t)$ (due to the time-variation of $k_c(t)$), ξ slightly decreases, as evidenced by the change of slope of $I_\eta(t; k_j)$ beyond t when $k_c(t)$ becomes smaller than k_j (for example the $k_j/k_0{=}24$, 32 curves in the figure; whilst ξ are constants for $k_j = 16k_0 < k_c(t)$ and $k_j = 45k_0 > k_c(t)$ for the time range plotted).

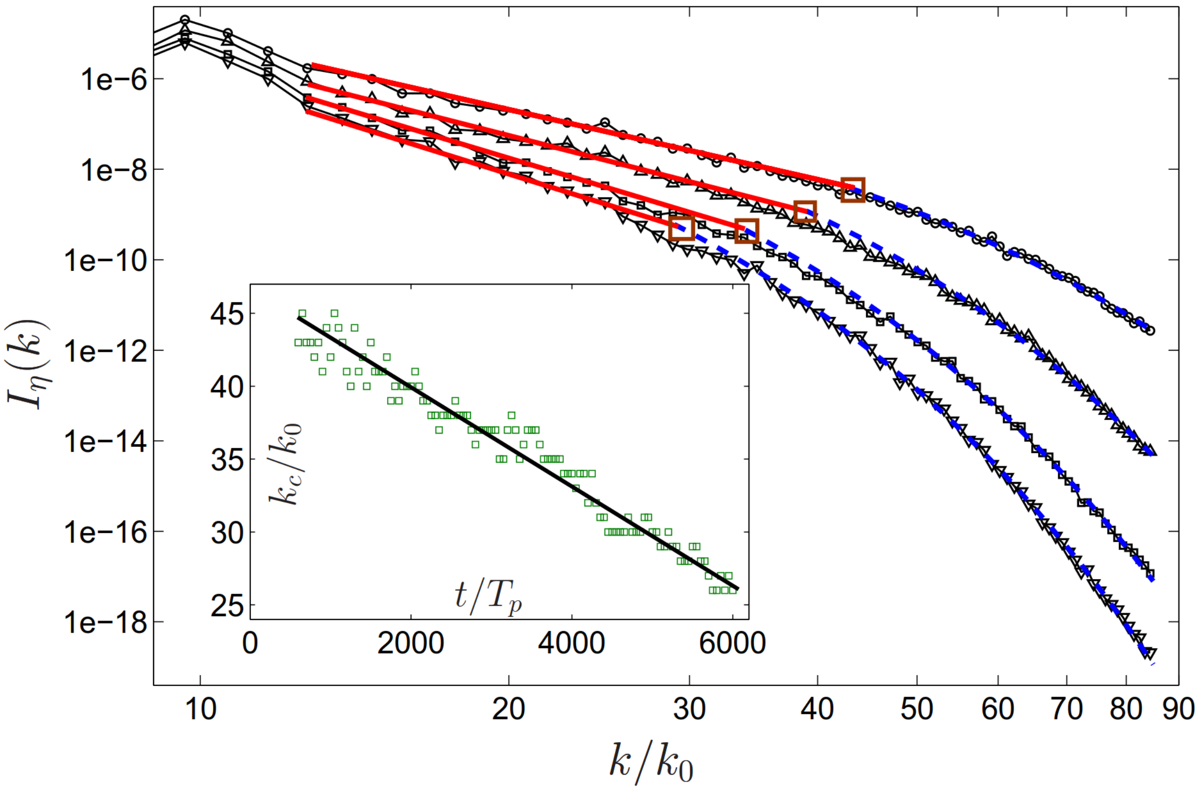

Figure 6-1: A typical decay of the power-law spectrum for $\widehat{\gamma}_0$=1.6×10^{-5}. The spectra from top to bottom are realized at respectively t/T_p = 600 (—○—) with α=-4.8; t/T_p = 2100 (—△—) with α=-5.7; t/T_p = 3600 (—□—) with α=-6.7; t/T_p = 5100 (—▽—) with α=-7.5, where T_p=$2\pi/\omega_p$. For reference, the power-law (——) and exponential (– – –) fits of the spectra respectively within [k_b,k_c] and [k_c,k_{max}], as well as values of k_c (□) are indicated. Inset: Variation of k_c (□) with t, and the linear fit (——) with R^2=0.96.

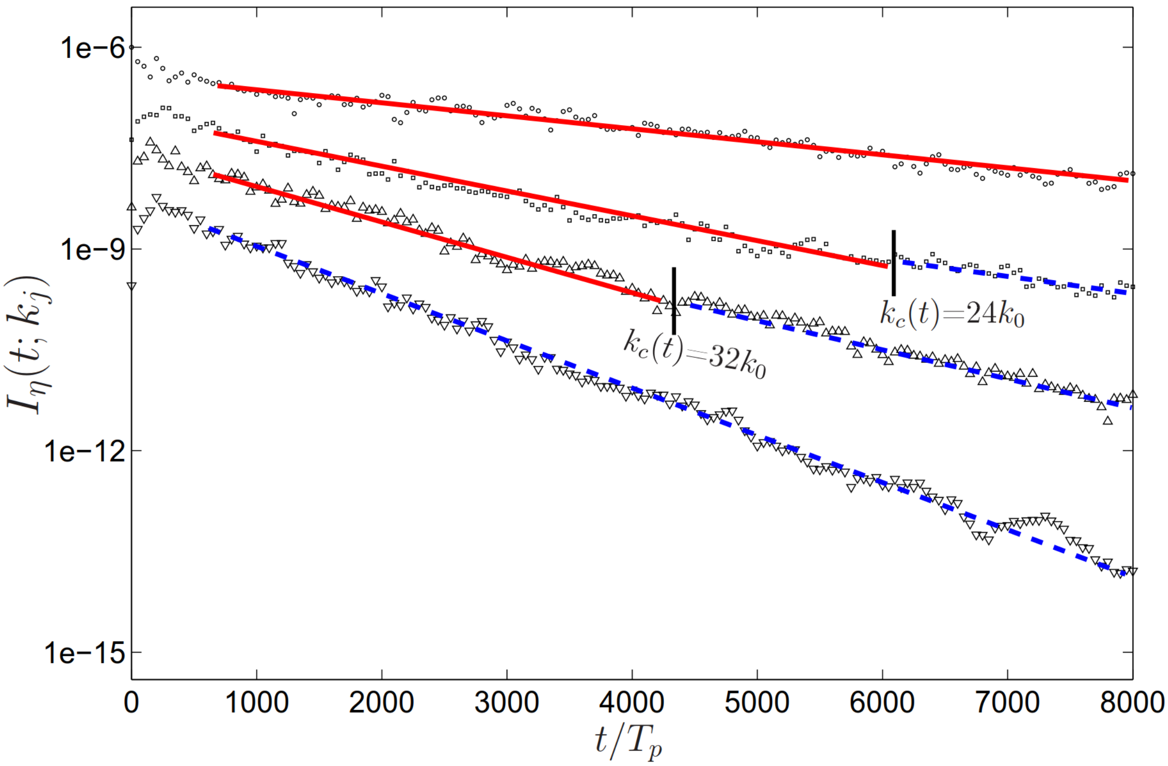

Figure 6-2: Evolution of $I_\eta(t;k_j)$ for four select modes k_j/k_0=16 (○), 24 (□), 32 (Δ) and 45 (∇). For reference, linear curve fits for k_j less (——) or greater (– – –) than $k_c(t)$ are plotted.

6.2.2 Evaluation of P

The modal decay rate $\xi(k)$ as a function of k is plotted in fig. 6-3. For comparison, the modal dissipation rate $\gamma_\nu(k) = 2|\gamma(k)|$ is also shown. In general, $\xi(k) \neq \gamma_\nu(k)$ due to the inter-modal energy transfer. For a given γ_0, there is a wavenumber k_γ above which $\xi(k) < \gamma_\nu(k)$, indicating a transition to a regime where more energy is dissipated by γ_0 than that can be explained by the decrease in I_η. This can be elucidated by considering the modal energy balance:

$$\frac{\partial \mathscr{E}}{\partial t} + \frac{\partial \mathcal{J}}{\partial k} = -\gamma_\nu \mathscr{E} \ , \tag{6.4}$$

where $\mathscr{E}(k,t) = \sigma k^3 I_\eta(k)/(2\pi)$ is the modal energy density. As $\partial\mathscr{E}/\partial t = -\xi\mathscr{E}$, $\partial\mathcal{J}/\partial k$ can be explicitly evaluated as $\partial\mathcal{J}/\partial k = (\xi - \gamma_\nu)\mathscr{E}$. In the sub-regime $k < k_\gamma$, we have $\xi \approx \gamma_\nu$ and $\partial\mathcal{J}/\partial k \approx 0$ (see fig.6-3); and the energy flux can be approximated by a constant, say, $P_\gamma \equiv \mathcal{J}|_{k=k_\gamma}$. In this wavenumber regime, the framework of WTT is recovered with (constant) energy flux $P = P_\gamma$. For $k > k_\gamma$, $\xi < \gamma_\nu$ and $\partial\mathcal{J}/\partial k < 0$, showing that the energy transferred by P_γ is absorbed in this regime. Using this physical argument, P_γ can be evaluated by

$$P_\gamma = \int_{k_\gamma}^{k_{max}} (\gamma_\nu - \xi)\mathscr{E}(k)dk. \tag{6.5}$$

Figure 6-4 shows the variation of ${P_\gamma}^{1/2}$ as a function of the spectral evolution characterized by the spectral amplitude at the reference wavenumber k_b, $I_\eta(t;k_b)/I_\eta(t^0;k_b)$. We observe that the dependence of $I_\eta \sim {P_\gamma}^{1/2}$ resembles closely that obtained in Chapter 4 for P in the context of WTT. The deviations from the WTT theoretical scaling for decreasing amplitude in both cases reflect the presence of finite box effect. Since $I_\eta(t;k_b) \sim \exp(-\xi t)$, we obtain $P_\gamma \sim \exp(-2\xi t)$. The total energy dissipation rate, calculated as

$$\Gamma = \int_0^{k_{max}} \gamma_\nu \mathscr{E} dk, \tag{6.6}$$

is also plotted in fig. 6-4, showing that in general $\Gamma > P_\gamma$. This explains the significant over-prediction of P using Γ (or equivalently by using energy input in forcing turbulence) in previous work (Falcon *et al.*, 2007; Xia *et al.*, 2010).

The impact of the unsteady effect on the evaluation of P_γ can be seen from (6.5), which tends to reduce P_γ. The relative importance of the unsteady effect can be characterized by a parameter $\mathcal{Z}$

$$\mathcal{Z} \equiv \frac{\int_{k>k_\gamma} \xi \mathscr{E} dk}{\int_{k>k_\gamma} \gamma_\nu \mathscr{E} dk}. \tag{6.7}$$

The parameter $\mathcal{Z}$ is plotted in fig.6-4 showing that $\mathcal{Z} = 0.6 \sim 0.7$ (in general also a function of γ_0). This illustrates the significant unsteady effect for this problem, in contrast to our previous work for quasi-stationary turbulence (Chapter 4) where, in theory, $\mathcal{Z} = 0$ (in the actual numerics, $\mathcal{Z} = 0.1 \sim 0.2$ (Chapter 4)).

6.2.3 General form of the time-dependent power-law spectrum

Equation (6.1) is equivalent to

$$I = I^0 k^{\alpha^0} exp(-\xi(k)(t - t^0)), \tag{6.8}$$

where $\xi = A \ln k + B$, which describes the exponential modal decay with rate $\xi(k)$ from an initial power-law spectrum $I^0 k^{\alpha^0}$, as evidenced from fig.6-1 and 6-2. The linear dependence of ξ and $\ln k$ is confirmed in fig.6-3. Indeed, this is an algebraic requirement for the spectrum to maintain power-law form in the evolution. Since ξ is not a function of time in the power-law range (cf. fig.6-2), A and B are constants (and functions of γ_0 only).

The explicit time dependence of the spectral slope $\alpha(t)$ can be factored out in (6.1) to obtain:

$$\alpha = \frac{1}{lnk + R}(ln\frac{I_\eta(k)}{I^0} + R\alpha^0)\ , \quad R \equiv B/A. \tag{6.9}$$

While A and B are functions of γ_0, we find that the value of R (see fig.6-3 inset) remains almost constant over the range of γ_0 we consider. Equation (6.9) thus shows that, even though the evolutional rates of $\alpha(t)$ and $I_\eta(t;k)$ depend on the magnitude of dissipation, the instantaneous α is uniquely related to the spectral magnitude

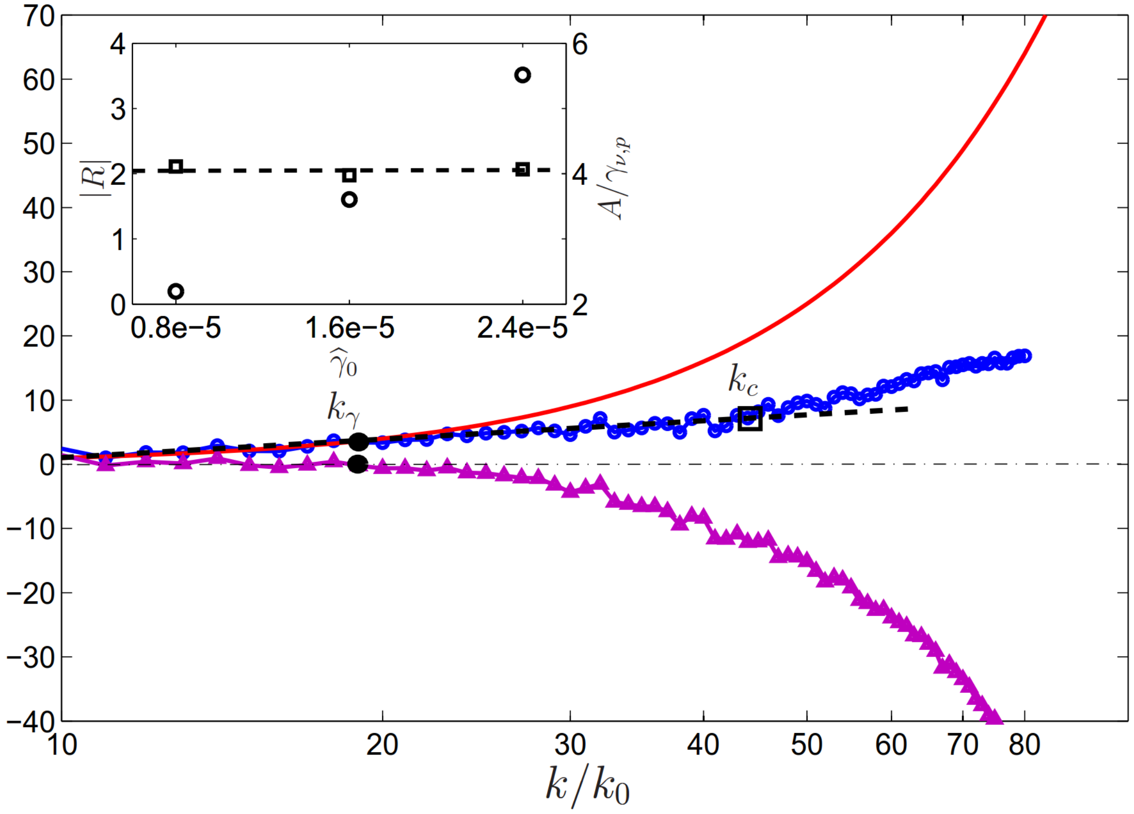

Figure 6-3: Normalized modal decay rate $\hat{\xi}(k)\equiv \xi(k)/\gamma_{\nu,p}$ (—○—), modal dissipation rate $\hat{\gamma}_\nu(k)= 2|\gamma(k)|/\gamma_{\nu,p}$ (——), and variation of energy transfer $\frac{\partial \mathcal{J}}{\partial k}/(\mathscr{E}\gamma_{\nu,p})$ (—△—) as functions of k at a certain time $t/T_p = 2100$, where $\gamma_{\nu,p}\equiv\gamma_\nu(k_p)$. The linear fit within the inertial range $\xi = A\ln k + B$ (− − −), and locations of k_γ (●) and k_c (☐) are indicated. Inset: Values of $|R| = |B/A|$ (☐) and $A/\gamma_{\nu,p}$ (○) for different values of $\widehat{\gamma}_0$.

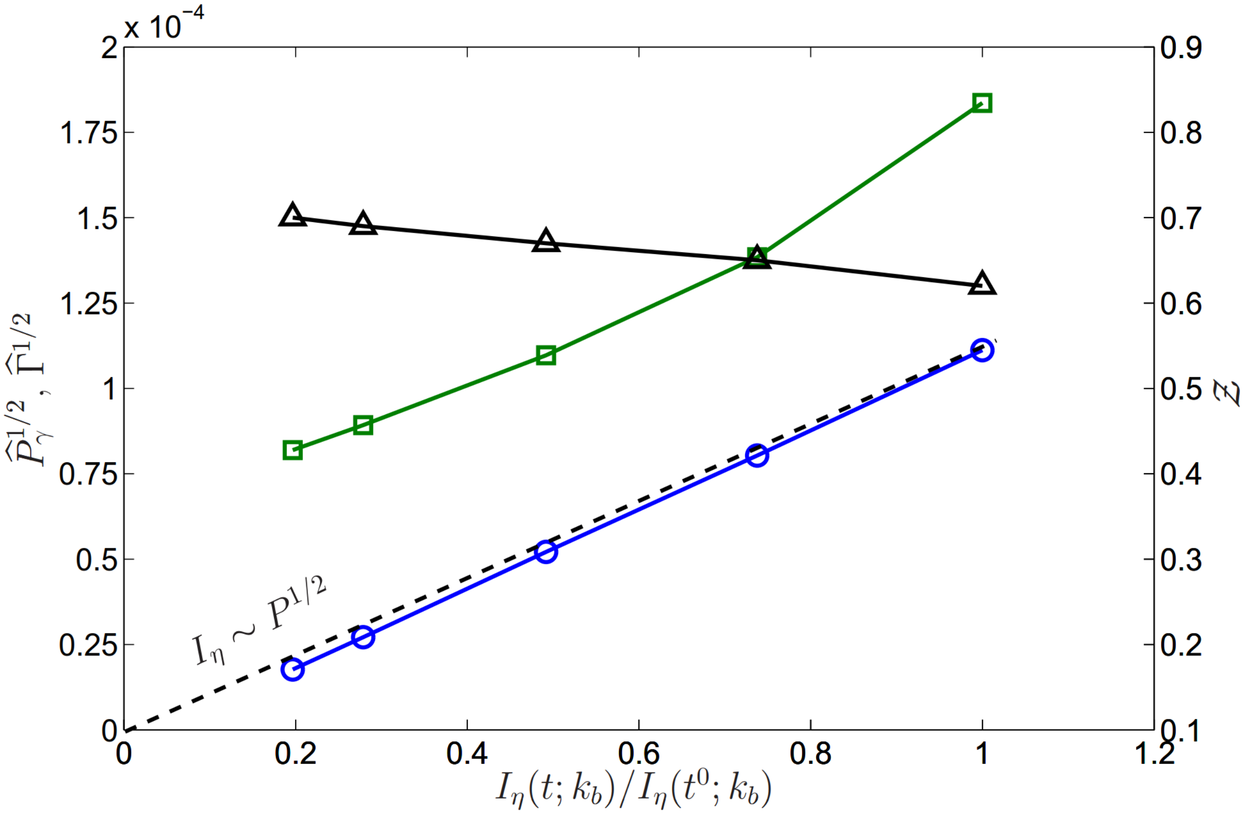

Figure 6-4: Normalized energy flux $\widehat{P}_\gamma \equiv P_\gamma/(\sigma\omega_p)$ (—○—), total energy dissipation rate $\widehat{\Gamma} \equiv \Gamma/(\sigma\omega_p)$ (—□—), and unsteady parameter $\mathcal{Z}$ (—△—) as functions of spectral decay characterized by $I_\eta(t;k_b)/I_\eta(t^0;k_b)$. The WTT scaling $I_\eta \sim P^{1/2}$ is indicated (− − −)

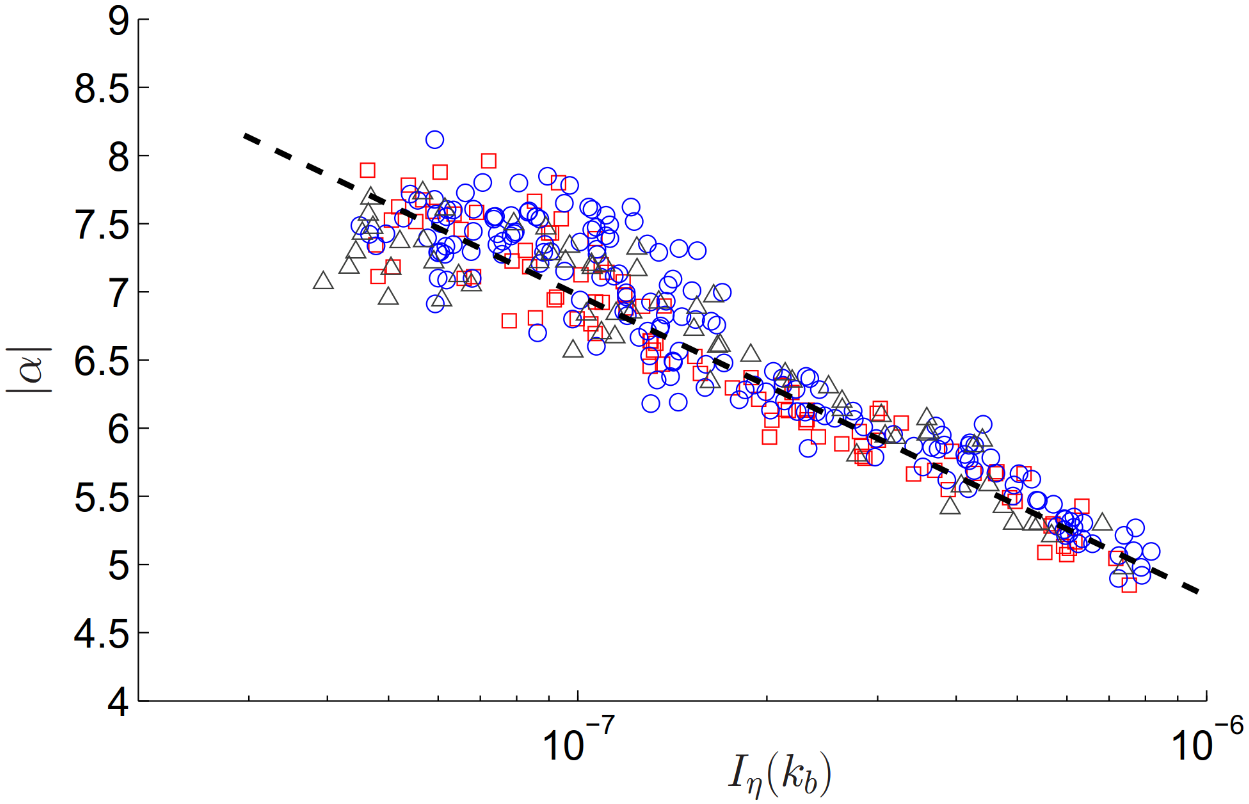

Figure 6-5: Spectral slope $|\alpha|$ as a function of $I_\eta(k_b)$ for $\gamma_0 = 0.8\times10^{-5}$ (○), 1.6×10^{-5} (□) and 2.4×10^{-5} (Δ). Scatter of the data is caused by the fluctuations of the spectra. Equation (6.9) is indicated (– – –).

(nonlinearity), independent of γ_0. Physically, this states that the development of the spectral slope within the inertial range is governed by nonlinear wave interactions (only), i.e., local effects of dissipation are removed by faster nonlinear interactions.

To further validate this, we plot in fig.6-5 the spectral slope α as a function of $I_\eta(k_b)$ for all the values of γ_0 we consider. Indeed, all the data collapse to the curve described by (6.9). The value of $\alpha \approx -19/4$, corresponding to WTT (see (2.94)), is achieved at highest nonlinearity ($I_\eta(k_b)$) that can be modelled in HOS. In recent experiment with much broader range of dissipation magnitude (varying over a factor of 100) (Deike *et al.*, 2014*a*), α is found to be different between the regimes of high and low dissipation. The result may also depend on the specific form of dissipation considered (cf. Deike *et al.*, 2012; Miquel *et al.*, 2014). The underlying physics for broader ranges of dissipation magnitude and nonlinearity level requires further investigation.

6.2.4 Decay of energy

If dissipation is absent in the power-law range (and $\mathcal{Z} \to 0$), the decay of the total energy E can be related to the (constant) nonlinear energy flux P to obtain $E \sim t^{-1}$ (Falkovich *et al.*, 1995). Indeed, This relation can be derived by direct integration of the equation $dE/dt = -\Gamma = -P \sim -E^2$ (since $I_\eta \sim P^{1/2}$), where the assumption of $P = \Gamma$ is needed. In the present context of broad-scale dissipation, $\Gamma > P_\gamma \sim P$ and the t^{-1} scaling does not hold. We focus on the power-law range and define

$$E_I \sim \iint_{k_b}^{k_c} k^2 I_\eta(k) d\vec{k}. \tag{6.10}$$

Substitution of (6.1) (or equivalently (6.8)) gives

$$E_I(t) \sim \frac{exp(-B(t-t^0))}{4+\alpha(t)} (k_c(t)^{4+\alpha(t)} - k_b^{4+\alpha(t)}) \ . \tag{6.11}$$

Figure 6-6 plots the evolution of E_I with time, comparing the numerical data with (6.11). Agreements are achieved over two decades of E_I for the range of γ_0 we consider. This consolidates the effectiveness of (6.1) in representing the decaying spectrum, and provides a simple form in approximating $E_I(t)$.

6.3 Summary

We present a direct numerical investigation of freely decaying capillary wave turbulence with broad-scale dissipation of magnitude γ_0. The problem we consider is an extension of WTT (Zakharov & Filonenko, 1967; Falkovich *et al.*, 1995) where the turbulence is allowed to evolve freely in the presence of physically realistic dissipation and finite box effect. Our simulation results are consistent with evidences from physical experiments, in terms of the shortening of power-law range and steepening of spectral slope α during the decay (e.g. Deike *et al.*, 2012, 2013; Kolmakov *et al.*, 2004; Miquel & Mordant, 2011). Based on our numerical findings, we obtain a simple model, (6.1), describing the evolution of the power-law spectrum in the form of

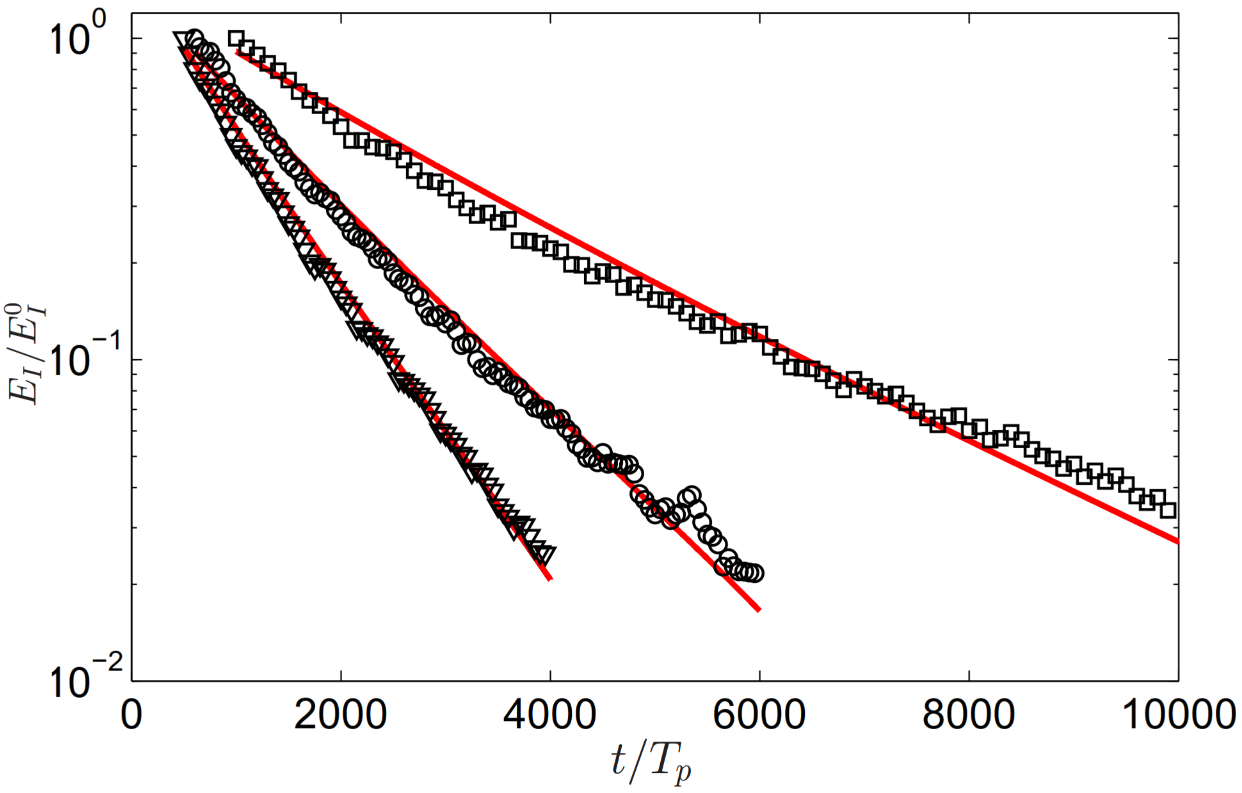

Figure 6-6: Variations of energy E_I/E_I^0 (where E_I^0 is the inertial-range spectral energy at $t = t^0$) with time from predictions of (6.11) (——) and numerical data for $\gamma_0 = 0.8 \times 10^{-5}$ (□), 1.6×10^{-5} (○) and 2.4×10^{-5} (∇).

exponential modal decay from an initial spectrum. The rate of modal decrease in time, $\xi(k)$, is shown to be given by $\xi(k) = A \ln k + B$, with A and B depending only on γ_0. Over the range of dissipation magnitude that can be obtained using our direct simulation, the instantaneous spectral slope α during the evolution is found to depend only on the nonlinearity of the spectrum at that time, irrespective of γ_0. The decay of energy within the inertial range obtained from (6.1) is also shown to approximate well those obtained from simulations. These findings are in contrast to the theoretical result (Falkovich *et al.*, 1995) without broad-scale dissipation and finite box effect, underscoring the importance of these effects in the actual physical problem. Relative to WTT, broad-scale dissipation and unsteadiness here result in a nonconstant inter-modal energy transfer $\mathcal{J}$ in the inertial range, which requires an alternative quantification of the energy flux P. Within a subrange $k < k_\gamma$ of our inertial range, we find that $\partial \mathcal{J} / \partial k \approx 0$, so that the energy flux can be approximated by a constant $P = P_\gamma = \mathcal{J}|_{k=k_\gamma}$. In this subrange, the framework of (stationary) WTT obtains, and we recover the WTT scaling $I_\eta \sim P_\gamma^{1/2}$ (e.g. Pan & Yue, 2014; Pushkarev & Zakharov, 2000). The present results describing decaying capillary wave turbulence are expected to hold in other weak turbulence systems with broad-scale dissipation.

Chapter 7

Simulation of long-short wave interaction

Having extensively studied the capillary wave turbulence in Chapters 2,4, 5 and 6, our next task in understanding the upper ocean dynamics is to investigate the interaction of these short waves with long waves. This requires the HOS simulation of a multi-scale wave field with significantly disparate wavelengths. Unfortunately, the boundary perturbation method in calculating ϕ_z is known to be numerically ill-conditioned for this multi-scale simulation. In this Chapter, we illustrate this ill-conditioning, which is related to the presence of large "divergent" terms, proportional to the product of long-wave amplitude and short-wave wavenumber raised to power $m-1$, in the Taylor expansion to calculate $[\phi_z]^{(m)}$. Although these terms are subject to analytical cancellations at arbitrary order m, for which we provide the first general proof, they numerically amounts to the calculation of small numbers as the differences of large numbers. This results in diverged results for large m, and largely limits the capability of HOS in multi-scale simulations. A detailed error analysis is performed which reveals this mechanism of error generation, where we also show that higher precision arithmetic can mitigate this divergence. As a fundamental remedy, we develop a method based on a mapping scheme, which eliminates this numerical ill-conditioning, at the cost of increased computational complexity due to the additional discretization in vertical direction. We present a relatively efficient way to solve the mapped equation based on a Fourier-Chebyshev collocation method, accelerated by Richardson iteration and pre-conditioning. The validity of this new scheme to remove the numerical instability is verified in solving a prescribed boundary value problem, and its possible physical application in studying the long-short wave interactions are discussed.

For simplicity, we use formulation under one-dimensional surface in this chapter, though all the schemes and analysis presented are straightforwardly extended to two-dimensional surface. The variable definitions in Chapter 3 are retained, with newly-defined variables only and wherever necessary.

7.1 Problem definition

7.1.1 Governing equations

The governing equations of general gravity-capillary waves on a one-dimensional free surface $\eta(x)$, in the context of potential flow (surface velocity potential $\phi^s(x) \equiv \phi(x, z = \eta(x))$), can be written as

$$\eta_t + \phi^s_x \eta_x - (1 + \eta_x^2)\phi_z = 0, \tag{7.1}$$

$$\phi^s_t + g\eta - \frac{\sigma}{\rho}\frac{\eta_{xx}}{(1 + \eta_x^2)^{3/2}} + \frac{1}{2}\phi^s_x\phi^s_x - \frac{1}{2}(1 + \eta_x^2)\phi_z^2 = 0, \tag{7.2}$$

We consider a wave field with $k_i a_i \sim O(\epsilon)$ for $i = 1, 2, ..., N$, where k_i and a_i are the wavenumber and elevation amplitude for mode i, and N is the total number of modes in consideration. The maximum wavelength ratio of this problem is defined by $\gamma = k_N/k_1$. For simulation of long-short wave interaction with widely separated wavelengths, we consider $\gamma \gg 1$.

7.1.2 Boundary value problem (BVP)

The key procedure in HOS to march (7.1) and (7.2) in time is to express the surface vertical velocity ϕ_z in terms of ϕ^s and η. This requires the solution of $\phi(x, z)$ from a boundary value problem (for simplicity, we neglect the t dependence of the variables and assume deep water):

$$\frac{\partial^2\phi}{\partial x^2}+\frac{\partial^2\phi}{\partial z^2}=0,\ \text{for } z\le\eta(x), \tag{7.3}$$

subject to

$$\phi=\phi^s,\ \text{on } z=\eta(x), \tag{7.4}$$

$$\nabla\phi\to 0,\ \text{on } z\to-\infty, \tag{7.5}$$

and horizontally periodic boundary condition.

Since only $\phi_z=\partial\phi/\partial z|_{z=\eta}$ at $z=\eta(x)$ is needed, the boundary value problem can be conveniently cast into a Dirichlet-Neumann Operator (DNO) $\hat{D}$, which produces vertical derivatives from boundary values. Our task can be considered as establishing the formulation of $\hat{D}\phi^s$.

7.1.3 Formulation of boundary perturbation method

The boundary value problem (BVP) (7.3), (7.4) and (7.5) are solved using the boundary perturbation method in HOS (Dommermuth & Yue, 1987; West *et al.*, 1987). We briefly review the procedures discussed in Chapter 3, with some newly-defined variables.

By expressing the surface potential ϕ^s as Taylor expansion around $\Phi(x)=\phi(x,z=0)$ and solving the inversion problem, we obtain (3.4),(3.5) and (3.6). These equations can be written in orders:

$$\begin{aligned}
&[\Phi]^{(1)}=\phi^s,\\
&[\Phi]^{(2)}=-\eta\kappa[\Phi]^{(1)},\\
&[\Phi]^{(3)}=-\eta\kappa[\Phi]^{(2)}-\frac{1}{2}\eta^2\kappa^2[\Phi]^{(1)},\\
&[\Phi]^{(4)}=-\eta\kappa[\Phi]^{(3)}-\frac{1}{2}\eta^2\kappa^2[\Phi]^{(2)}-\frac{1}{6}\eta^3\kappa^3[\Phi]^{(1)},\\
&\ldots\ldots
\end{aligned} \tag{7.6}$$

In (7.6) we have used an operator κ, where $\kappa\Phi$ multiplies each Fourier coefficient of Φ by its corresponding wavenumber magnitude $|k|$. This definition of κ is due to the BVP ((7.3), (7.4) and (7.5)), which renders the wave field representable by eigenfunctions $\phi(x,z) = \sum_k \widehat{\Phi}(k) exp(ikx + |k|z)$. As a result, $\partial\phi/\partial z|_{z=0}$ is equivalent as $\kappa\Phi$. The introduction of the operator κ offers convenient mathematical expressions in the following analysis.

By writing $\phi_z = \sum_n \eta^n/n! \cdot \kappa^{n+1}\Phi$, we obtain

$$\begin{aligned}
&[\phi_z]^{(1)} = \kappa[\Phi]^{(1)}, \\
&[\phi_z]^{(2)} = \kappa[\Phi]^{(2)} + \eta\kappa^2[\Phi]^{(1)}, \\
&[\phi_z]^{(3)} = \kappa[\Phi]^{(3)} + \eta\kappa^2[\Phi]^{(2)} + \frac{1}{2}\eta^2\kappa^3[\Phi]^{(1)}, \\
&[\phi_z]^{(4)} = \kappa[\Phi]^{(4)} + \eta\kappa^2[\Phi]^{(3)} + \frac{1}{2}\eta^2\kappa^3[\Phi]^{(2)} + \frac{1}{6}\eta^3\kappa^4[\Phi]^{(1)}, \\
&\ldots\ldots
\end{aligned} \tag{7.7}$$

The surface vertical velocity ϕ_z can then be expressed in terms of surface potential ϕ by combining (7.6) and (7.7). Upon using an operator expansion of the DNO,

$$\hat{D}\phi^s = \sum_{i=1}^{\infty} \hat{D}_i\phi^s, \tag{7.8}$$

the final expression can be written as

$$\begin{aligned}
&[\phi_z]^{(1)} = \hat{D}_1\phi^s = \kappa\phi^s, \\
&[\phi_z]^{(2)} = \hat{D}_2\phi^s = -\kappa\eta\kappa\phi^s + \eta\kappa^2\phi^s, \\
&[\phi_z]^{(3)} = \hat{D}_3\phi^s = \kappa\eta\kappa\eta\kappa\phi^s - \eta\kappa^2\eta\kappa\phi^s + \frac{1}{2}(\eta^2\kappa^3\phi^s - \kappa\eta^2\kappa^2\phi^s) \\
&\ldots\ldots
\end{aligned} \tag{7.9}$$

7.1.4 Ill-conditioning of boundary perturbation method

We show that the boundary perturbation method is ill-conditioned in calculating high-order surface vertical velocity ($[\phi_z]^{(m)}$ with $m \gg 1$) for a wave field with $\gamma \gg 1$. For simplicity, we consider two modes with respectively k_S, a_S and k_L, a_L, for which

$\gamma = k_S/k_L \gg 1$ and $k_S a_S \sim k_L a_L \sim O(\epsilon)$. By this definition, $k_S a_L \sim \gamma\epsilon$ is a large number which increases with γ.

By substituting these two modes in (7.9), we can see that large terms involving $O(k_S a_L)$ are present in $[\phi_z]^{(m)}$ for $m > 1$. This is shown by using the first term in $[\phi_z]^{(2)}$ as an example:

$$\begin{aligned} & \kappa\eta\kappa\phi^s \\ \sim & \kappa(\eta_L + \eta_S)\kappa(\phi^s_L + \phi^s_S) \\ \sim & \kappa(\eta_L + \eta_S)(k_L\phi^s_L + k_S\phi^s_S) \\ \sim & \kappa\eta_L k_L\phi^s_L + \kappa\eta_L k_S\phi^s_S + \kappa\eta_S k_L\phi^s_L + \kappa\eta_S k_S\phi^s_S. \end{aligned} \tag{7.10}$$

All terms in (7.10) are of $O(\epsilon^2)$, except for the second one, for which $\kappa\eta_L k_S\phi^s_S \sim O(\gamma\epsilon^2)$. And this is the term involving the large quantity produced by $k_S a_L$. Applying this analysis to higher orders of ϕ_z, we can generally conclude that terms of $O(\gamma^{m-1}\epsilon^m) = O((k_S a_L)^{m-1}\epsilon)$ are present in $[\phi_z]^{(m)}$. For $m \gg 1$ (and $\gamma \gg 1$), these terms can be "divergently" large.

This seemingly ill-posed expansion (7.9) has historically roused criticism, where it is postulated that the boundary perturbation method is incapable of solving problems involving long-short wave interactions with widely separated wavelengths. The criticism is rested in Brueckner & West (1988), where the authors argue that the "divergent" terms involving $k_S a_L$ are analytically cancelled against one another at each order. This cancellation is explicitly shown in Brueckner & West (1988) for $[\phi_z]^{(2)}$, with the higher-order cancellation briefly argued through the similarity in formulations regarding a commutation operation. We shall provide a general proof for the cancellation of "divergent" terms for $[\phi_z]^{(m)}$ in section 7.2.

Despite the vindication for boundary perturbation method in analytical consideration, the "divergent" terms do cause ill-conditioned configuration in numerical simulation. In calculation of $[\phi_z]^{(m)}$ ($m \gg 1$), the presence of these terms result in two issues of significant error accumulation:

1. Calculating $[\phi_z]^{(m)}$ from (7.9) amounts to the calculation of a small term ($\sim \epsilon^m$)

as the difference of large terms ($\sim (\gamma^{m-1}\epsilon^m)$. This operation results in absolute error of $\mathcal{P}G$, where $\mathcal{P}$ is the machine epsilon (relative machine error), with $\mathcal{P} \sim O(10^{-7})$, $O(10^{-16})$ and $O(10^{-34})$ for single, double and quadruple precisions, and G is the largest number involved in (7.9).

2. Calculation of $[\phi_z]^{(m)}$ from (7.9) involves successive multiplication and de-aliasing. This results in the error accumulation near the de-aliasing boundary as the elimination of the modes by zero padding affects the modes near the boundary in the next multiplication.

With respect to the second issue, a strategy that can largely fix the problem is to use a filter near the de-aliasing boundary. Specifically, after each term in $[\phi_z]^{(m)}$ is calculated, we zero N_F (say $N_F = 150$) modes near the de-aliasing boundary. This is found to be effective in removing the error near the de-aliasing boundary caused by successive multiplication. The first issue, however, is inherent in, and directly limits the accuracy of boundary perturbation method as long as floating numbers are used in computation. A detailed error analysis is provided in section 7.3, where we explicitly reveal the numerical divergence due to this issue, and show that this divergence with increase of m can be procrastinated by using higher precision arithmetic. Complete circumvention of this numerically ill-conditioned expansion requires us to develop an alternative scheme to solve the BVP ((7.3), (7.4) and (7.5)), which ensures the implicit cancellation of the "divergent" terms. This is discussed in section 7.4.

7.2 Analytical cancellation of the "divergent" terms

We first show the cancellation of terms proportional to $k_S a_L$ in $[\phi_z]^{(2)}$, following a similar procedure as in Brueckner & West (1988). (Note that $[\phi_z]^{(1)}$, by definition, is free of terms involving $k_S a_L$.)

We write η and ϕ^s as summations of their Fourier components:

$$\eta = \sum_{q=-\infty}^{\infty} a_q e^{iqx}, \tag{7.11}$$

and

$$\phi^s = \sum_{r=-\infty}^{\infty} a_r e^{irx}. \tag{7.12}$$

where, for simplicity, we have omitted the factor ω_q/k_q (in linear consideration) in the coefficients of ϕ^s. This simplification does not have any influence on our analysis since our goal is to find terms proportional to $k_S a_L$, for which the factor ω_q/k_q does not play a role. We consider $qa_q \sim O(\epsilon)$, for all q.

A typical Fourier component of $[\phi_z]^{(2)}$ (composed of mode q in η and mode r in ϕ^s) can be written as

$$[\phi_z]^{(2)} \sim -a_r a_q \kappa e^{iqx} \kappa e^{irx} + a_r a_q e^{iqx} \kappa^2 e^{irx} = a_r a_q (|r|^2 - |r||q+r|) e^{i(r+q)x}. \tag{7.13}$$

Here and hereafter in this section, we use "$\sim$", wherever necessary, to denote a particular Fourier component of a variable, with its coefficient exactly represented. For terms proportional to $k_S a_L$ to be present in the calculation of $[\phi_z]^{(2)}$, we need $|r| > |q|$ (or $|r| \gg |q|$), for which $|r|^2 - |r||r+q| = -rq$. Therefore, (7.13) can be written as

$$[\phi_z]^{(2)} \sim -(ra_r)(qa_q) e^{i(r+q)x}. \tag{7.14}$$

We see that the expression (7.14) is free of terms proportional to $k_S a_L$ after cancellation. It is of $O(\epsilon^2)$, consistent with the definition of $[\phi_z]^{(2)}$.

This analysis can be continued to $[\phi_z]^{(m)}$ for $m > 2$ for a general proof. However, the formulation involved for $m \gg 1$ is dauntingly formidable, and the continuation of the analysis has to be ceased. We instead provide a proof by induction, based on a re-group of terms in ϕ_z.

It is shown in Milder (1990) that the DNO operator can be expanded as

$$\hat{D}_m = \frac{1}{m-1} \sum_{n=1}^{m-1} [\eta, \hat{D}_n] \hat{D}_{m-n}, \tag{7.15}$$

where $[\eta, \hat{D}_n]$ is a commutator which equals to $\eta \hat{D}_n - \hat{D}_n \eta$.

A useful property of this formulation is that the operator $\hat{D}_m$ is expressed in terms of $\hat{D}$ at orders smaller than m. This inspires us to prove the cancelation at all orders by induction. Having proved that $\hat{D}_1\phi^s$ and $\hat{D}_2\phi^s$ are both free of divergent terms, the only lemma we need to prove is as follows:

Lemma *If $\hat{D}_n\phi^s \sim O(\epsilon^n)$ and $\hat{D}_j\phi^s \sim O(\epsilon^j)$ are free of terms involving $k_S a_L$, then $[\eta, \hat{D}_j]\hat{D}_n\phi^s$ is free of terms involving $k_S a_L$ and $[\eta, \hat{D}_j]\hat{D}_n\phi^s \sim O(\epsilon^{j+n})$.*

Proof. Since $\hat{D}_n\phi^s$ is free of terms involving $k_S a_L$, it can be written as

$$\hat{D}_n\phi^s \sim \alpha_p^{(n)} e^{ipx}, \tag{7.16}$$

where $\alpha_p^{(n)}$, by definition, is of $O(\epsilon^n)$.

We then express $\hat{D}_j\phi^s$ in an alternative form. Since $\hat{D}_j\phi^s$ can be considered as multiplication of $j-1$ terms regarding η, and 1 term of ϕ^s, it can be written as (cf. (7.14))

$$\hat{D}_j\phi^s \sim \sum_p \mathcal{E}_{q-p}^{(j-1)}(pa_p)e^{iqx}, \tag{7.17}$$

where we have considered the component $\phi^s \sim a_p e^{ipx}$, and $\mathcal{E}_{q-p}^{(j-1)} p e^{i(q-p)x}$ given by the multiplication of the rest terms. $\mathcal{E}_{q-p}^{(j-1)}$, of $O(\epsilon^{j-1})$, depends only on the operator $\hat{D}_j$ and value of $q-p$.

Now we consider $\eta \sim a_R e^{iRx}$. In order to prove the Lemma, we only need to prove: For each R, the "divergent" terms in $\eta\hat{D}_j\hat{D}_n\phi^s$ are exactly cancelled by those in $\hat{D}_j\eta\hat{D}_n\phi^s$. Applying $\hat{D}_j$ on $\hat{D}_n\phi^s$ (replacing ϕ^s in (7.17) with $\hat{D}_n\phi^s$, in the form of (7.16)), we obtain

$$\hat{D}_j(\hat{D}_n\phi^s) \sim \sum_p \mathcal{E}_{q-p}^{(j-1)}(p\alpha_p^{(n)})e^{iqx}, \tag{7.18}$$

and in turn

$$\eta\hat{D}_j\hat{D}_n\phi^s \sim \sum_p \mathcal{E}_{q-p}^{(j-1)} a_R p \alpha_p^{(n)} e^{i(q+R)x}. \tag{7.19}$$

Similarly, by multiplying η with (7.16), we have

$$\eta\hat{D}_n\phi^s \sim \alpha_p^{(n)} a_R e^{i(p+R)x}. \tag{7.20}$$

Applying $\hat{D}_j$ on (7.20), we obtain (mode $p+R$ from $\eta \hat{D}_n \phi^s$ and mode $q-p$ from $\hat{D}_j$)

$$\hat{D}_j(\eta \hat{D}_n \phi^s) \sim \sum_p \mathcal{E}_{q-p}^{(j-1)}(p+R)\alpha_p^{(n)} a_R e^{i(q+R)x}. \tag{7.21}$$

Finally, we reach

$$[\eta, \hat{D}_j]\hat{D}_n\phi^s = \eta \hat{D}_j \hat{D}_n \phi^s - \hat{D}_j \eta \hat{D}_n \phi^s \sim -\sum_p \mathcal{E}_{q-p}^{(j-1)} \alpha_p^{(n)} R a_R e^{i(q+R)x}. \tag{7.22}$$

This is independent of "divergent" terms, and $[\eta, \hat{D}_j]\hat{D}_n\phi^s \sim O(\epsilon^{j+n})$. $\square$

As a direct result of Lemma 1 and (7.15), $\hat{D}_m\phi^s$ is free of "divergent" terms for all integer m. Even though (7.9) is derived by assuming η and ϕ^s to be small parameters, it is in essence a series only with respect to the small parameter of modal wave steepness. Since the proof is obtainable for arbitrary modes, it is valid for a broadband spectrum.

7.3 Error analysis in numerical implementation

In order to understand the numerical error accumulation and convergence property of the series (7.9), we consider the BVP (7.3), (7.4) and (7.5), with prescribed $\eta(x)$ and $\phi^s(x)$:

$$\eta(x) = a_S cos(k_S x) + a_L cos(k_L x), \tag{7.23}$$

$$\phi^s(x) = a_S sin(k_S x) exp(k_S \eta(x)) + a_L sin(k_L x) exp(k_L \eta(x)), \tag{7.24}$$

for which an analytical solution of ϕ_z is known:

$$\phi_z^e(x) = a_S k_S sin(k_S x) exp(k_S \eta(x)) + a_L k_L sin(k_L x) exp(k_L \eta(x)). \tag{7.25}$$

This BVP is solved using boundary perturbation method with $N_x = 4098$ (with 2/3 de-aliasing rule and $N_F = 150$). We consider two cases: (i) $a_L k_L = 0.2$, $a_S = 0$, and (ii) $\epsilon = a_L k_L = a_S k_S = 0.2$, $\gamma = k_S/k_L = 100$. The solutions, which can be expressed by the series (7.9), are obtained by respectively single, double and quadruple

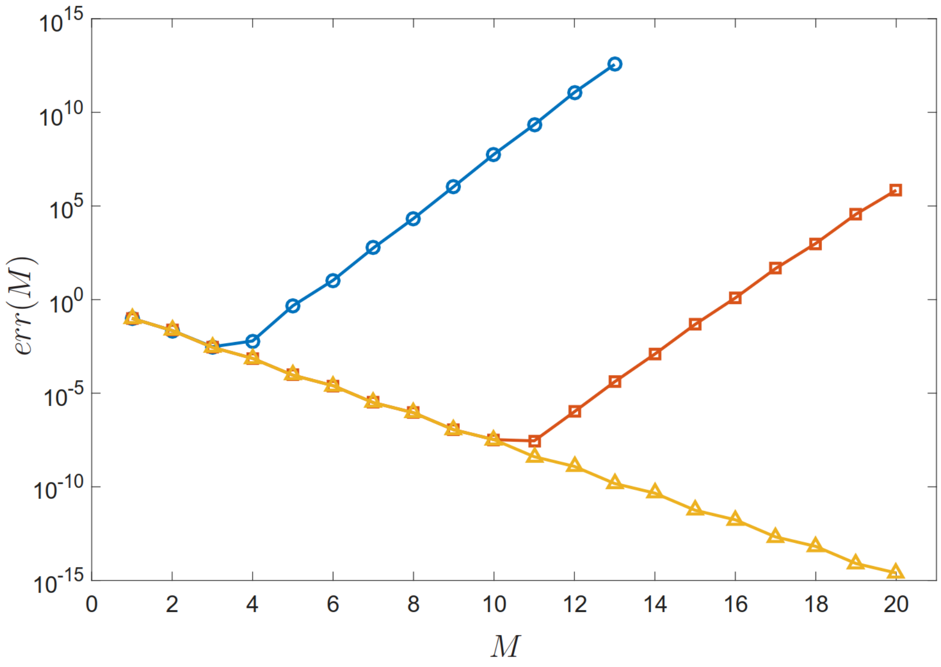

Figure 7-1: The relative L^2-norm error $err(M)$ with increase of nonlinearity order M, with respectively single (—○—), double (—□—) and quadruple (—△—) precisions. The plot is for case (i): $a_L k_L = 0.2$, $a_S = 0$, with $N_x = 4098$, 2/3 de-aliasing rule and $N_F = 150$.

precisions. The error of a numerical solution $[\phi_z](x; M) \equiv \sum_{m=1}^{M} [\phi_z]^{(m)}$ is defined as

$$err(M) = \frac{||\phi_z^e(x) - [\phi_z](x; M)||_2}{||\phi_z^e(x)||_2}. \tag{7.26}$$

Figure 7-1 plots the error $err(M)$ for case (i), with (7.9) calculated with respectively single, double and quadruple precisions. It is shown that $[\phi_z](x; M)$ converges exponentially with the increase of M before numerical divergence occurs at M_d (with $M_d = 4$ and 11 for single and double precisions, and M_d not present for quadruple precision). This is consistent with the analysis in section 7.2 that (7.9) is a power series with respect to the small parameter of wave steepness.

As discussed in section 7.1.4, the origin of this numerical divergence is the calculation of a small term as the difference of large terms. We note that large terms are present in case (i) even though the assigned modal energy is narrow-banded on the low-wavenumber modes. This is due to the existence of small machine errors (say

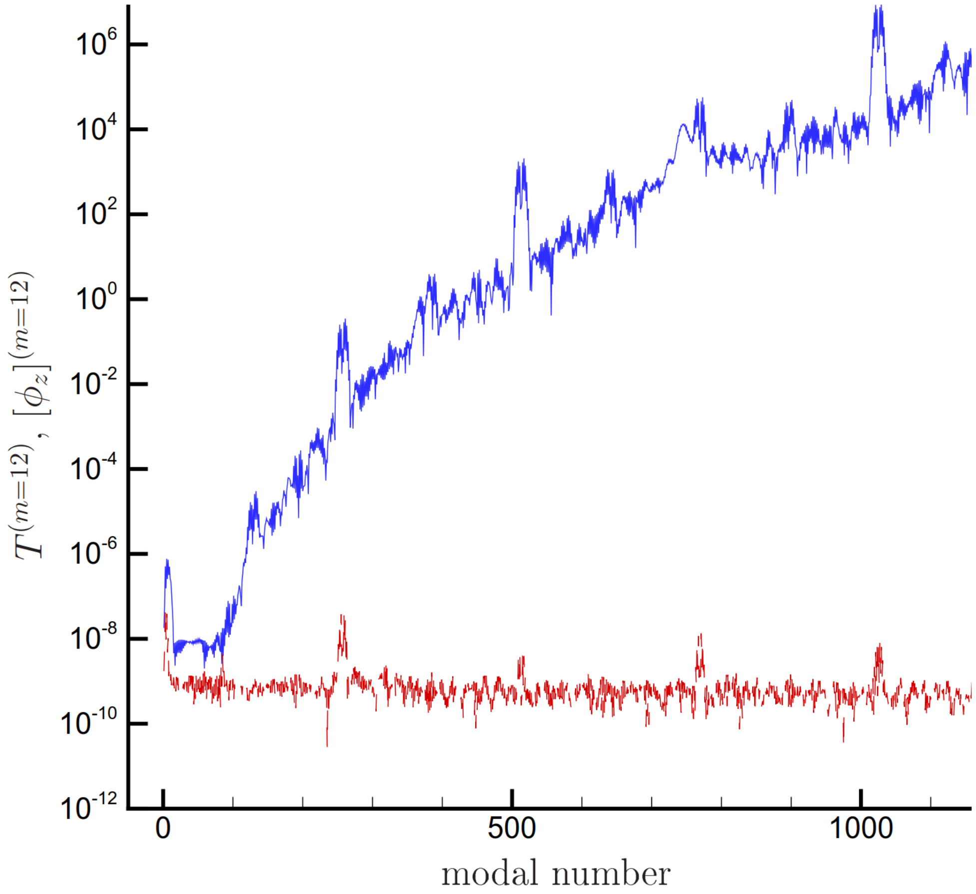

Figure 7-2: Amplitudes of $[\phi_z]^{(m)}$ (– – –) and $T^{(m)}$ (——) in wavenumber domain for $m = 12$ with double precision. The modes prior to filtering and de-aliasing zone are plotted. The plot is for case (i): $a_L k_L = 0.2$, $a_S = 0$, with $N_x = 4098$, 2/3 de-aliasing rule and $N_F = 150$.

$e \sim O(10^{-16})$ for double precision) on the high-wavenumber modes whose associated modal amplitudes are theoretically zero. In theory, the impact of these errors on $[\phi_z]^{(m)}$ is negligibly small ($\sim (k_L a_L)^{m-1}e$); In numerics, however, they are subject to the amplification of ($(k_S a_L)^{m-1}e$) in calculation of each single term in (7.9). To reveal the effect of this calculation, we plot in figure 7-2 the amplitudes of $[\phi_z]^{(m)}$ and $T^{(m)}$ in wavenumber domain for $m = 12$ with double precision, where $T^{(m)}$ is the single large term (with maximum element) in calculation of $[\phi_z]^{(m)}$. It is clear that the largest number involved in the calculation $G = ||T^{(12)}||_\infty \sim O(10^7)$, which results in the error in $[\phi_z]^{(12)}$ of $\mathcal{P}G \sim O(10^{-9})$. This limits the lower bound of number representation in $[\phi_z]^{(12)}$, i.e., all the numbers smaller than $O(10^{-9})$ are represented at the level of $O(10^{-9})$.

This analysis allows us to establish a quantitative criterion for the numerical divergence of the series (7.9), which is characterized by

$$\mathcal{P}||T^{(m)}||_\infty \sim ||[\phi_z^e]^{(m)}||_\infty, \tag{7.27}$$

where $[\phi_z^e]^{(m)}$ is the accurately calculated (or exact) vertical velocity ϕ_z at order m. As described by (7.27), the numerical divergence occurs with the increase of m as the error due to the existence of large number exceeds the level of the largest mode in $[\phi_z^e]^{(m)}$. In figure 7-3, we plot $\mathcal{F} \equiv \mathcal{P}||T^{(M)}||_\infty / ||[\phi_z^e]^{(M)}||_\infty$ and $err(M)$ with the increase of M, for both single and double precisions, where $[\phi_z^e]^{(M)}$ is obtained from the numerical solution using quadruple precision. Indeed, it can be seen that the increase of $err(M)$ occurs where $\mathcal{F} \sim O(1)$, which corroborates (7.27) in quantitatively characterizing the numerical divergence.

The same analysis is also performed for case (ii), where modal energy is present at both low and high wavenumbers. The error curves $err(M)$ with respectively single, double and quadruple precisions are plotted in figure 7-4. Similar as that for case (i), the boundary perturbation method achieves exponential convergence for $M < M_d$, and application of higher precision arithmetic procrastinates the occurrence of M_d, with $M_d = 4$, 9 and 18 for the three precisions considered.

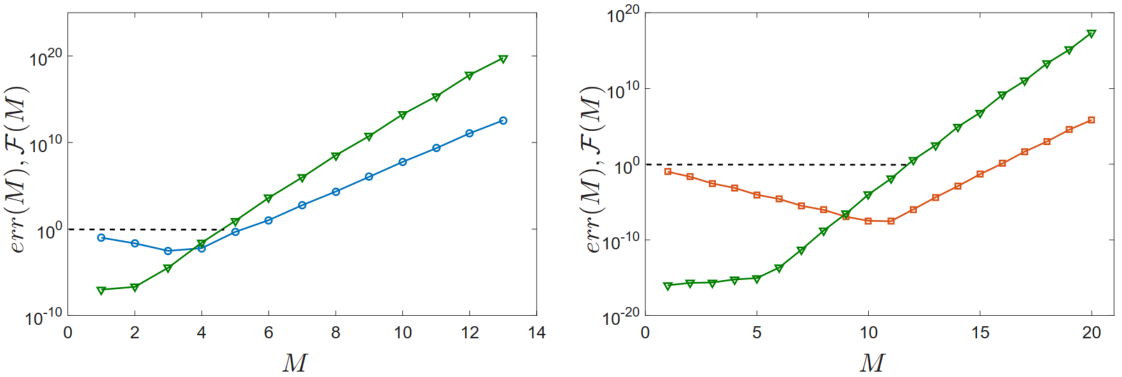

(a) (b)

Figure 7-3: $\mathcal{F} \equiv \mathcal{P}||T^{(M)}||_\infty/||[\phi_z^e]^{(M)}||_\infty$ (—▽—) and $err(M)$ (—○—, —□—) with the increase of M, for both (a) single and (b) double precisions, where $[\phi_z^e]^{(M)}$ is obtained from the numerical solution using quadruple precision. The position of $\mathcal{F} = 1$ is indicated by $---$. The plots are for case (i): $a_L k_L = 0.2$, $a_S = 0$, with $N_x = 4098$, 2/3 de-aliasing rule and $N_F = 150$.

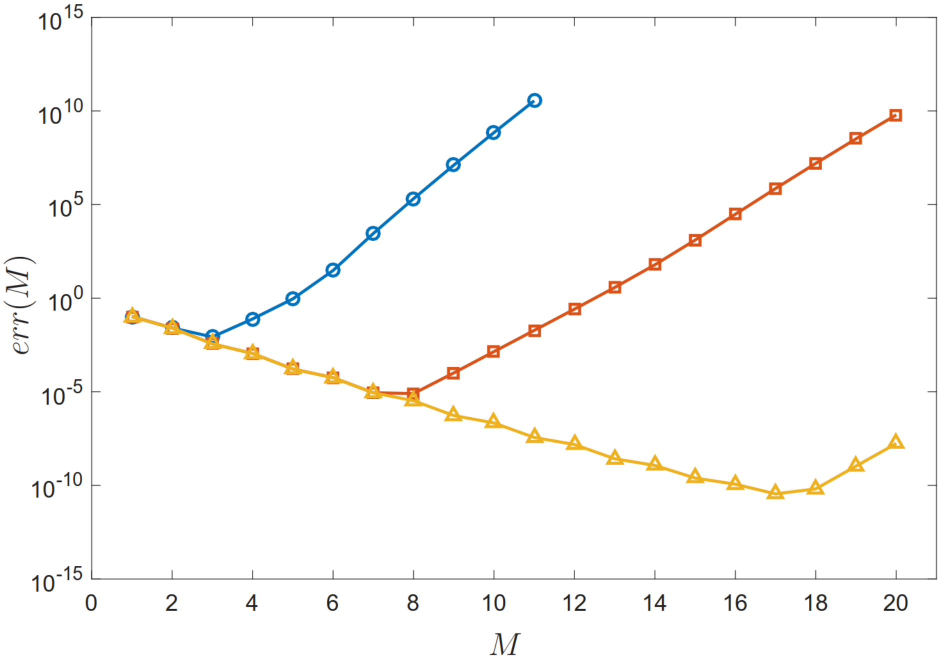

Figure 7-4: The relative L^2-norm error $err(M)$ with increase of nonlinearity order M, with respectively single (—○—), double (—□—) and quadruple (—△—) precisions. The plot is for case (ii): $\epsilon = a_L k_L = a_S k_S = 0.2$, $\gamma = k_S/k_L = 100$, with $N_x = 4098$, 2/3 de-aliasing rule and $N_F = 150$.

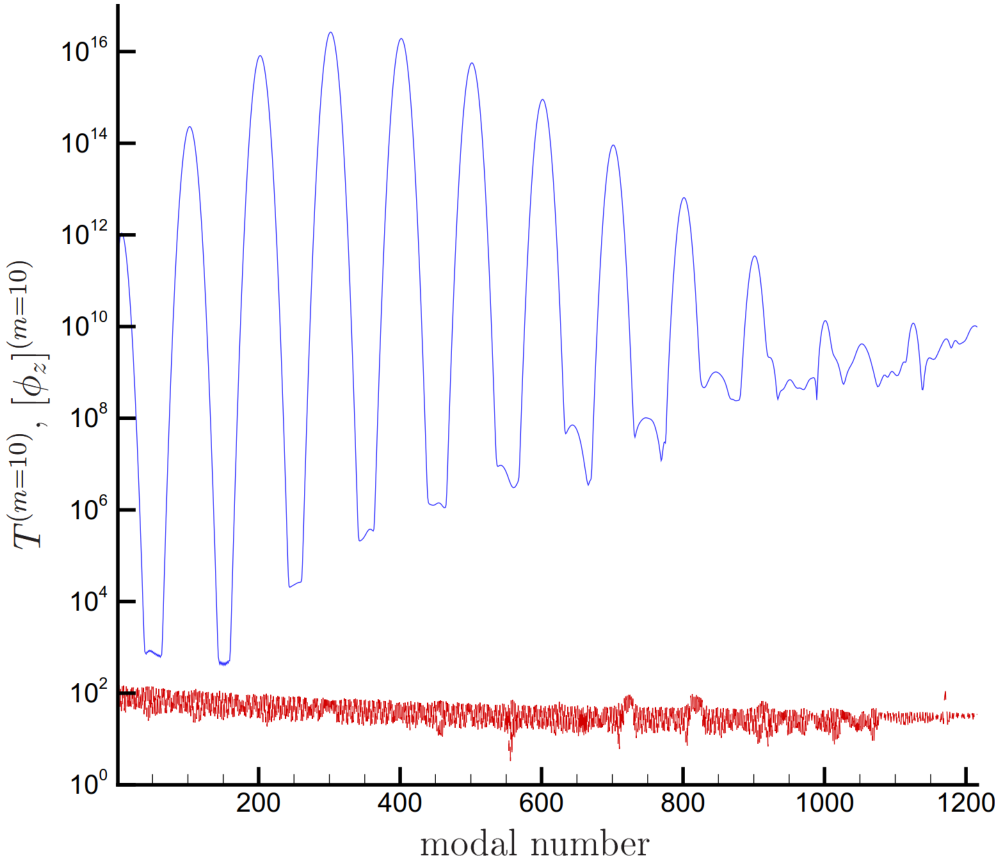

Figure 7-5: Amplitudes of $[\phi_z]^{(m)}$ (– – –) and $T^{(m)}$ (——) in wavenumber domain for $m = 10$ with double precision. The modes prior to filtering and de-aliasing zone are plotted. The plot is for case (ii): $\epsilon = a_L k_L = a_S k_S = 0.2$, $\gamma = k_S/k_L = 100$, with $N_x = 4098$, 2/3 de-aliasing rule and $N_F = 150$.

In addition to the machine error at high-wavenumber modes, the existence of large terms in calculation of $[\phi_z]^{(m)}$ using (7.9) for case (ii) is largely due to the finite modal amplitude at $k_L = 100$. In order to elaborate its impact on the error in $[\phi_z]^{(m)}$, we again plot in figure 7-5 the amplitudes of $[\phi_z]^{(m)}$ and $T^{(m)}$ in wavenumber domain for $m = 10$ with double precision. It is shown that the largest number involved in the calculation $||T||_\infty \sim O(10^{17})$ limits the lower bound of number representation in $[\phi_z]^{(10)}$ to be $\mathcal{P}||T||_\infty \sim O(10^1)$. We finally show that the numerical divergence for case (ii) is also characterized by (7.27) in figure 7-6.

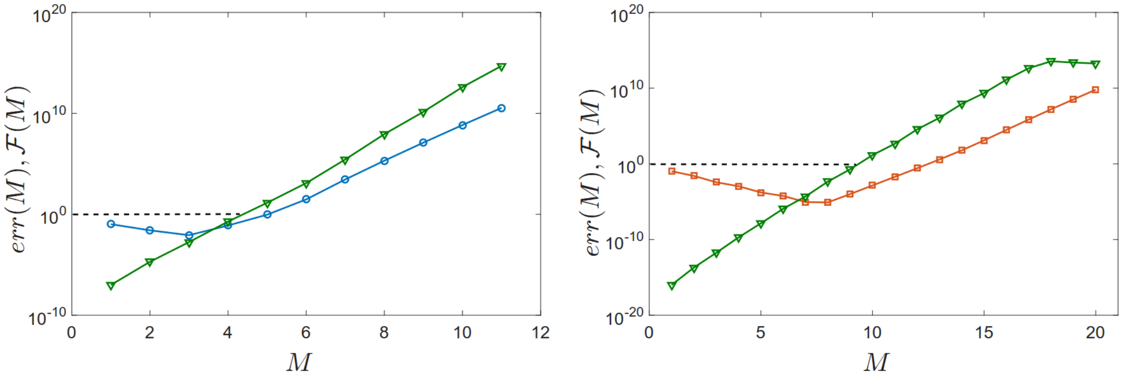

(a) (b)

Figure 7-6: $\mathcal{F} \equiv \mathcal{P}||T^{(M)}||_\infty/||[\phi_z^e]^{(M)}||_\infty$ (—▽—) and $err(M)$ (—○—, —□—) with the increase of M, for both (a) single and (b) double precisions, where $[\phi_z^e]^{(M)}$ is obtained from the numerical solution using quadruple precision. The position of $\mathcal{F} = 1$ is indicated by $---$. The plot is for case (ii): $\epsilon = a_L k_L = a_S k_S = 0.2$, $\gamma = k_S/k_L = 100$, with $N_x = 4098$, 2/3 de-aliasing rule and $N_F = 150$.

7.4 A new numerical approach

7.4.1 Mapping scheme

The numerical divergence described above does place an limitation on the accuracy and stability of the boundary perturbation method. Although this limitation can be mitigated by using higher precision arithmetic, a fundamental remedy for the problem is still desirable. This requires us to develop a scheme which is free of the large numbers involved in boundary perturbation method. We present in this section such a new approach to solve the BVP ((7.3), (7.4) and (7.5)), based on a mapping scheme (cf. Nicholls & Reitich, 2001).

We first transform the governing equation (7.3) and boundary conditions (7.4) and (7.5) from (x, z) to $(\hat{x}, \hat{z})$, where

$$\hat{x} = x, \tag{7.28}$$

$$\hat{z} = h(\frac{z - \eta(x)}{h + \eta(x)}), \tag{7.29}$$

where $h > 0$ is an arbitrary depth. The main objective of (7.28) and (7.29) is to deform the free surface $z = \eta(x)$ to a flat surface ($z = \eta \rightarrow \hat{z} = 0$), and $z = -h$ to $\hat{z} = -h$ (see figure 7-7 for the deformation of the computational domain).

Subject to (7.28) and (7.29), the derivative operations in the governing equation (7.3) can be transformed to:

$$
\begin{aligned}
\frac{\partial}{\partial x} &= \frac{\partial}{\partial \hat{x}}\frac{\partial \hat{x}}{\partial x} + \frac{\partial}{\partial \hat{z}}\frac{\partial \hat{z}}{\partial x} = \frac{\partial}{\partial \hat{x}} + \frac{\partial}{\partial \hat{z}} \cdot \frac{-\eta_{\hat{x}}(h+\hat{z})}{h+\eta}, \\
\frac{\partial^2}{\partial x^2} &= \frac{\partial^2}{\partial \hat{x}^2} + \frac{\partial^2}{\partial \hat{x}\partial \hat{z}}\frac{-\eta_{\hat{x}}(h+\hat{z})}{h+\eta} + \frac{\partial}{\partial \hat{z}}(h+\hat{z})\frac{-\eta_{\hat{x}\hat{x}}(h+\eta)+\eta_{\hat{x}}^2}{(h+\eta)^2} \\
&\quad + [\frac{\partial^2}{\partial \hat{x}\partial \hat{z}} + \frac{\partial^2}{\partial z^2}\frac{-\eta_{\hat{x}}(h+\hat{z})}{h+\eta} + \frac{\partial}{\partial \hat{z}}\frac{-\eta_{\hat{x}}}{h+\eta}] \cdot \frac{-\eta_{\hat{x}}(h+\hat{z})}{h+\eta}, \\
\frac{\partial}{\partial z} &= \frac{\partial}{\partial \hat{x}}\frac{\partial \hat{x}}{\partial z} + \frac{\partial}{\partial \hat{z}}\frac{\partial \hat{z}}{\partial z} = \frac{\partial}{\partial \hat{z}} \cdot \frac{h}{h+\eta}, \\
\frac{\partial^2}{\partial z^2} &= \frac{\partial^2}{\partial \hat{z}^2} \cdot (\frac{h}{h+\eta})^2.
\end{aligned}
\tag{7.30}
$$

Substituting (7.30) to (7.3), we obtain the governing equation in variables $(\hat{x}, \hat{z})$:

$$
\begin{aligned}
\nabla^2\phi(\hat{x},\hat{z}) = -(\frac{2\eta}{h} + \frac{\eta^2}{h^2})\frac{\partial^2\phi}{\partial \hat{x}^2} + \frac{2\eta_{\hat{x}}(h+\hat{z})(h+\eta)}{h^2}\frac{\partial^2\phi}{\partial \hat{x}\partial \hat{z}} \\
+ \frac{h+\hat{z}}{h^2}[\eta_{\hat{x}\hat{x}}(h+\eta) - 2\eta_{\hat{x}}^2]\frac{\partial\phi}{\partial \hat{z}} - \eta_{\hat{x}}^2(\frac{h+\hat{z}}{h})^2\frac{\partial^2\phi}{\partial \hat{z}^2}.
\end{aligned}
\tag{7.31}
$$

The deep-water bottom boundary condition (7.5) can be re-written as

$$
\frac{\partial\phi(x,z)}{\partial z}|_{z=-h} = \kappa\phi(x,-h),
\tag{7.32}
$$

due to the form of eigenfunction $exp(ikx + |k|z)$ imposed by (7.3). Upon the transformations (7.28) and (7.29), equation (7.32) becomes

$$
\frac{\partial\phi(x,z)}{\partial \hat{z}}|_{z=-h} - \kappa\phi(x,-h) = \frac{\eta}{h}\kappa\phi(x,-h).
\tag{7.33}
$$

In summary, by dropping the hat symbol on $\hat{x}$ and $\hat{z}$, we have a new BVP to be

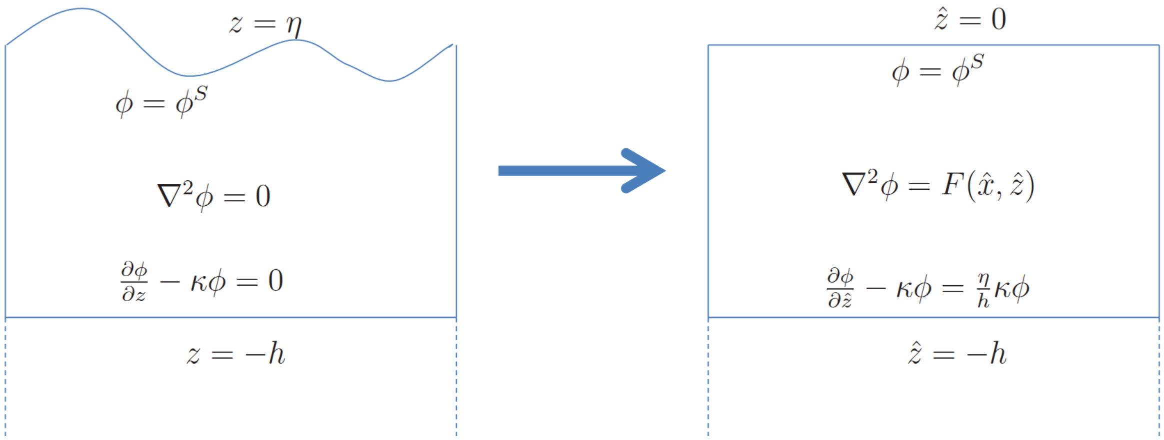

Figure 7-7: Sketch of the mapping scheme.

solved:

$$\begin{aligned}\nabla^2\phi(x,z) = F(x,z) = -\left(\frac{2\eta}{h}+\frac{\eta^2}{h^2}\right)\frac{\partial^2\phi}{\partial x^2} + \frac{2\eta_x(h+z)(h+\eta)}{h^2}\frac{\partial^2\phi}{\partial x\partial z}\\ + \frac{h+z}{h^2}[\eta_{xx}(h+\eta)-2\eta_x^2]\frac{\partial\phi}{\partial z} - \eta_x^2\left(\frac{h+z}{h}\right)^2\frac{\partial^2\phi}{\partial z^2}, \text{ for } -h\le z\le 0,\end{aligned} \tag{7.34}$$

subject to

$$\phi(x,z) = \phi^s(x), \text{ at } z=0, \tag{7.35}$$

$$\frac{\partial\phi(x,z)}{\partial z} - \kappa\phi(x,-h) = \frac{\eta}{h}\kappa\phi(x,-h), \text{ at } z=-h, \tag{7.36}$$

and periodic boundary condition horizontally. The transformation from (7.3), (7.4) and (7.5) to (7.34), (7.35) and (7.36) is sketched in figure 7-7.

7.4.2 Perturbation expansion

We now expand $\phi(x,z)$ as a perturbation series in ϵ

$$\phi(x,z) = \sum_m [\phi(x,z)]^{(m)}, \tag{7.37}$$

where $[\phi(x,z)]^{(m)} \sim O(\epsilon^m)$. Considering $\eta/h \sim O(\epsilon)$ and $\eta_x \sim O(\epsilon)$, equation (7.34) can then be successively written in orders:

$$\begin{aligned}
\nabla^2[\phi(x,z)]^{(1)} &= [F(x,z)]^{(1)} = 0,\\
\nabla^2[\phi(x,z)]^{(2)} &= [F(x,z)]^{(2)} = -\frac{2\eta}{h}\frac{\partial^2[\phi]^{(1)}}{\partial x^2} + \frac{2\eta_x(h+z)}{h}\frac{\partial^2[\phi]^{(1)}}{\partial x \partial z} + \frac{h+z}{h}\eta_{xx}\frac{\partial[\phi]^{(1)}}{\partial z},\\
\nabla^2[\phi(x,z)]^{(3)} &= [F(x,z)]^{(3)} = -\frac{2\eta}{h}\frac{\partial^2[\phi]^{(2)}}{\partial x^2} - \frac{\eta^2}{h^2}\frac{\partial^2[\phi]^{(1)}}{\partial x^2} + \frac{2\eta_x(h+z)}{h}\frac{\partial^2[\phi]^{(2)}}{\partial x \partial z}\\
&\qquad + \frac{2\eta_x(h+z)\eta}{h^2}\frac{\partial^2[\phi]^{(1)}}{\partial x \partial z} + \frac{h+z}{h}\eta_{xx}\frac{\partial[\phi]^{(2)}}{\partial z}\\
&\qquad + \frac{h+z}{h^2}(\eta\eta_{xx} - 2\eta_x^2)\frac{\partial[\phi]^{(1)}}{\partial z} - \eta_x^2(\frac{h+z}{h})^2\frac{\partial^2[\phi]^{(1)}}{\partial z^2},\\
\nabla^2[\phi(x,z)]^{(4)} &= [F(x,z)]^{(4)} = \ldots\ldots
\end{aligned} \tag{7.38}$$

In general, for $m \geq 3$, we have

$$\begin{aligned}
[F(x,z)]^{(m)} = &-\frac{2\eta}{h}\frac{\partial^2[\phi]^{(m-1)}}{\partial x^2} - \frac{\eta^2}{h^2}\frac{\partial^2[\phi]^{(m-2)}}{\partial x^2} + \frac{2\eta_x(h+z)}{h}\frac{\partial^2[\phi]^{(m-1)}}{\partial x \partial z}\\
&+ \frac{2\eta_x(h+z)\eta}{h^2}\frac{\partial^2[\phi]^{(m-2)}}{\partial x \partial z} + \frac{h+z}{h}\eta_{xx}\frac{\partial[\phi]^{(m-1)}}{\partial z}\\
&+ \frac{h+z}{h^2}(\eta\eta_{xx} - 2\eta_x^2)\frac{\partial[\phi]^{(m-2)}}{\partial z} - \eta_x^2(\frac{h+z}{h})^2\frac{\partial^2[\phi]^{(m-2)}}{\partial z^2}.
\end{aligned} \tag{7.39}$$

From (7.38) and (7.39) we see that $[F(x,z)]^{(m)}$ depends only on $[\phi]^{(n)}$ where $n < m$, and thus can be considered known at order m. Consequently, the BVP ((7.34),(7.35) and (7.36)) can be successively solved in orders. In each order m, we have a Poisson equation as the field equation, subject to a Dirichlet boundary condition on top, a Robin boundary condition at bottom, and periodic boundary condition horizontally, summarized as follows:

$$\nabla^2[\phi(x,z)]^{(m)} = [F(x,z)]^{(m)}, \text{ for } -h \leq z \leq 0, \tag{7.40}$$

subject to

$$[\phi(x,z)]^{(m)} = [\phi^U(x)]^{(m)} \equiv \begin{cases} \phi^s(x), & m=1 \\ 0, & m>1. \end{cases}, \quad \text{on } z=0, \tag{7.41}$$

$$\begin{aligned} \frac{\partial[\phi(x,z)]^{(m)}}{\partial z} - \kappa[\phi(x,-h)]^{(m)} &= [\phi^B(x)]^{(m)} \\ &\equiv \begin{cases} 0, & m=1 \\ \frac{\eta}{h}\kappa[\phi(x,-h)]^{(m-1)}, & m>1. \end{cases}, \quad \text{on } z=-h, \end{aligned} \tag{7.42}$$

$$[\phi(x,z)]^{(m)} = [\phi(x+\Lambda,z)]^{(m)}, \tag{7.43}$$

with Λ being the horizontal period.

In this newly-defined BVP at order m, the most intense multiplication involves only three variables. This thus effectively eliminates the accuracy (and stability) barrier imposed in the boundary perturbation method regarding $k_S a_L$. With the increase of m, the solution of (7.40), (7.41), (7.42) and (7.43) gives a successively accurate approximation of ϕ_z, even though the solution at each order m differs in nuance from that in the boundary perturbation method.

7.4.3 Fourier-Chebyshev collocation method

We use a Fourier-Chebyshev collocation method (e.g. Boyd, 2001) to solve (7.40), (7.41), (7.42) and (7.43). For each variable, to this end, we implement Fourier decomposition in x direction and discretize in z direction on the Gauss-Lobatto-Chebyshev collocation points:

$$[\phi(x,z_j)]^{(m)} = \sum_{k=-N_x/2}^{N_x/2} [\widehat{\phi}(k,z_j)]^{(m)} e^{ikx}, \tag{7.44}$$

$$[F(x,z_j)]^{(m)} = \sum_{k=-N_x/2}^{N_x/2} [\widehat{F}(k,z_j)]^{(m)} e^{ikx}, \tag{7.45}$$

$$[\phi^U(x)]^{(m)} = \sum_{k=-N_x/2}^{N_x/2} [\widehat{\phi^U}(k)]^{(m)} e^{ikx}, \tag{7.46}$$

$$[\phi^B(x)]^{(m)} = \sum_{k=-N_x/2}^{N_x/2} [\widehat{\phi^B}(k)]^{(m)} e^{ikx}, \tag{7.47}$$

where

$$z_j = \frac{h}{2}\big[\hat{z}_j - 1\big],\ j = 0, ..., N_z \tag{7.48}$$

with

$$\hat{z}_j = cos(\frac{j\pi}{N_z}),\ j = 0, ..., N_z \tag{7.49}$$

are the $N_z + 1$ Gauss-Lobatto-Chebyshev collocation points mapped from $[-1, 1]$ to $[-h, 0]$.

Substituting (7.44),(7.45),(7.46) and (7.47) to (7.40), (7.41) and (7.42), we obtain, at each order m and wavenumber k, a discretized 1D Helmholtz equation:

$$-k^2[\widehat{\phi}(k, z_j)]^{(m)} + \frac{\partial^2[\widehat{\phi}(k, z_j)]^{(m)}}{\partial z^2} = [\widehat{F}(k, z_j)]^{(m)},\ \text{for } j = 1, 2, ..., N_z - 1 \tag{7.50}$$

subject to

$$[\widehat{\phi}(k, z_j)]^{(m)} = [\widehat{\phi^U}(k)]^{(m)},\ \text{on } z_j = 0, \tag{7.51}$$

$$\frac{\partial[\widehat{\phi}(k, z_j)]^{(m)}}{\partial z} - |k|[\widehat{\phi}(k, z_j)]^{(m)} = [\widehat{\phi^B}(k)]^{(m)},\ \text{on } z_j = -h. \tag{7.52}$$

Using Chebyshev collocation method, the derivative operation $\partial/\partial z$ can be written in matrix form

$$\frac{\partial[\widehat{\phi}(k, z_j)]^{(m)}}{\partial z} = \sum_{l=0}^{N_z} \mathcal{D}_{jl}[\widehat{\phi}(k, z_l)]^{(m)}, \tag{7.53}$$

where

$$\mathcal{D}_{jl} = \frac{2}{h} \cdot \begin{cases} \frac{\bar{c}_j}{\bar{c}_l}\frac{(-1)^{j+l}}{\hat{z}_j - \hat{z}_l}, & j \neq l \\ -\frac{\hat{z}_j}{2(1-\hat{z}_j^2)}, & 1 \leq j = l \leq N_z - 1 \\ \frac{2N_z^2+1}{6}, & j = l = 0 \\ -\frac{2N_z^2+1}{6}, & j = l = N_z \end{cases}, \tag{7.54}$$

with

$$\hat{c}_j = \begin{cases} 2, & j = 0, N \\ 1, & 1 \leq j \leq N-1 \end{cases}. \tag{7.55}$$

Therefore, equations (7.50), (7.51) and (7.52) can be written in matrix form

$$\sum_{l=0}^{N_z} \mathcal{A}_{jl}[\widehat{\phi}(k, z_l)]^{(m)} = \mathcal{B}_j, \tag{7.56}$$

where

$$\mathcal{A}_{jl} = \begin{cases} (\mathcal{D}\mathcal{D})_{jl}, & 1 \leq j \leq N_z - 1, 0 \leq l \leq N_z, j \neq l \\ (\mathcal{D}\mathcal{D})_{jl} - k^2, & 1 \leq j \leq N_z - 1, 0 \leq l \leq N_z, j = l \\ 1, & j = l = 0 \\ 0, & j = 0, 1 \leq l \leq N_z \\ \mathcal{D}_{jl}, & j = N_z, 1 \leq l \leq N_z \\ \mathcal{D}_{jl} - |k|, & j = l = N_z \end{cases}, \tag{7.57}$$

and

$$\mathcal{B}_j = \begin{cases} [\widehat{\phi^U}(k)]^{(m)}, & j = 0 \\ [\widehat{F}(k, z_j)]^{(m)}, & 1 \leq j \leq N_z - 1 \cdot \\ [\widehat{\phi^B}(k)]^{(m)}, & j = N_z \end{cases} \tag{7.58}$$

7.4.4 Richardson Iterative method for solving (7.56)

Once (7.56) is solved for each m and k, we can obtain the solution $\phi(x, z)$ for (7.34), (7.35) and (7.36) by applying (7.37) and (7.44). However, the Chebyshev collocation method results in a full matrix $\mathcal{A}$, for which a direct inversion is particularly time-consuming for large N_z ($O(N_z^3)$ operations required if, say, Gaussian elimination is used). Moreover, the matrix $\mathcal{A}$ becomes increasingly ill-conditioned with the increase of N_z, with its spectral condition number (Canuto *et al.*, 2012)

$$\mathcal{K} = \frac{\lambda_{max}}{\lambda_{min}} \sim O(N_z^2), \tag{7.59}$$

where λ_{max} and λ_{min} are the largest and smallest eigenvalues of the positive definite matrix $\mathcal{A}$. This urges us to seek an efficient way to solve (7.56) for large N_z. We hereby present a Richardson iteration method combined with preconditioning scheme, which leads to a computational complexity of $O(N_z log N_z)$.

The Richardson iteration method to solve (7.56) (for simplicity, we use $\mathcal{V}_j$ for $[\widehat{\phi}(k, z_j)]^{(m)}$, $v(z)$ for $[\widehat{\phi}(k, z)]^{(m)}$, and consider solving $\mathcal{A}\mathcal{V} = \mathcal{B}$) can be considered to integrate the pseudo time-dependent equation

$$\mathcal{V}_t = -\mathcal{A}\mathcal{V} + \mathcal{B}, \tag{7.60}$$

with an initial guess $\mathcal{V}^0$ to $\mathcal{V}$. The subsequent approximation are obtained via

$$\mathcal{V}^{n+1} = \mathcal{V}^n + \tau(\mathcal{B} - \mathcal{A}\mathcal{V}^n), \tag{7.61}$$

where τ can be considered as a pseudo time step. For sufficient iteration, $\mathcal{V}^n$ approaches the final solution $\mathcal{V}$.

The efficiency of this iteration can be analyzed by defining the n-th iteration error

$$\mathcal{E}^n = \mathcal{V} - \mathcal{V}^n. \tag{7.62}$$

By substituting (7.62) to (7.61), we obtain

$$\mathcal{E}^{n+1} = \mathcal{G}\mathcal{E}^n, \tag{7.63}$$

where

$$\mathcal{G} = \mathcal{I} - \tau\mathcal{A}, \tag{7.64}$$

with $\mathcal{I}$ being the identity matrix. Defining the spectral radius $\rho(\mathcal{G})$ as the maximum in the magnitudes of eigenvalues of $\mathcal{G}$, the iteration scheme is then convergent for $\rho(\mathcal{G}) < 1$. This is equivalent to

$$|1 - \tau\lambda| < 1, \tag{7.65}$$

for all eigenvalues λ of $\mathcal{A}$. This places an limitation on the size of the pseudo time step

$$\tau < 2/\lambda_{max}. \tag{7.66}$$

The optimal choice of τ is that which minimizes $\rho(\mathcal{G})$. It can be obtained from the relation

$$1 - \tau\lambda_{max} = -(1 - \tau\lambda_{min}), \tag{7.67}$$

which gives the optimal τ as

$$\tau_{opt} = \frac{2}{\lambda_{max} + \lambda_{min}}, \tag{7.68}$$

and the spectral radius

$$\rho(\mathcal{G}) = \frac{\lambda_{max} - \lambda_{min}}{\lambda_{max} + \lambda_{min}}. \tag{7.69}$$

We define the rate of convergence R to be

$$R = -log(\rho), \tag{7.70}$$

whose reciprocal R^{-1} measures the number of iterations required for a significant decrease of the error (by a factor of e). Substituting (7.59) and (7.69) to (7.70), we obtain

$$R^{-1} \sim O(N_z^2). \tag{7.71}$$

This means that $O(N_z^2)$ iterations are required to obtain even moderate accuracy. For large N_z, this convergence rate becomes increasingly lamentable $(\lambda_{max}/\lambda_{min} \gg 1)$, and we are obliged to develop supplement to the Richardson iteration which can alleviate the limitation on convergence rate. Fortunately, It has been shown that the efficiency of the Richardson method can generally be tremendously improved through three supplements: (i) Chebyshev acceleration; (ii) Preconditioning and (iii) multigrid. We apply in current work a finite-difference preconditioning scheme, as presented below.

7.4.5 Finite-difference preconditioning

By using preconditioning, we consider solving a modification of (7.56):

$$\mathcal{H}^{-1}\mathcal{A}\mathcal{V} = \mathcal{H}^{-1}\mathcal{B}. \tag{7.72}$$

A preconditioned version of (7.61) is

$$\mathcal{V}^{n+1} = \mathcal{V}^n + \tau\mathcal{H}^{-1}(\mathcal{B} - \mathcal{A}\mathcal{V}^n). \tag{7.73}$$

In practice, the inverse of the preconditioning matrix $\mathcal{H}$ is never explicitly required. Instead we solve

$$\mathcal{H}(\mathcal{V}^{n+1} - \mathcal{V}^n) = \tau(\mathcal{B} - \mathcal{A}\mathcal{V}^n). \tag{7.74}$$

This places the first requirement for $\mathcal{H}$ that (7.74) can be solved inexpensively.

The effective iteration matrix associated with the error equation (7.63) is now

$$\mathcal{G} = \mathcal{I} - \tau \mathcal{H}^{-1} \mathcal{A}. \tag{7.75}$$

We then have the second requirement for $\mathcal{H}$ that $\mathcal{H}^{-1}$ is a good approximation to $\mathcal{A}^{-1}$, i.e., the spectral condition number $\mathcal{K}$ of $\mathcal{H}^{-1}\mathcal{A}$ is small.

A convenient choice of $\mathcal{H}$ under these two requirements is the finite-difference matrix, which approximates the derivative $\partial^2/\partial z^2$ as

$$\frac{\partial^2 v}{\partial z^2}(z_j) = \frac{2}{h_{j-1}(h_j + h_{j-1})}\mathcal{V}_{j-1} - \frac{2}{h_j h_{j-1}}\mathcal{V}_j + \frac{2}{h_j(h_j + h_{j-1})}\mathcal{V}_{j+1}, \tag{7.76}$$

where $h_j = z_j - z_{j+1}$. Taking consideration of the boundary conditions (7.51) and (7.52), $\mathcal{H}$ can be explicitly formulated as

$$\mathcal{H}_{jl} = \begin{cases} 1, & j = l = 0 \\ -\frac{2}{h_{j-1}h_j} - k^2, & 1 \le j = l \le N_z - 1 \\ \frac{2}{h_j(h_{j-1}+h_j)}, & 1 \le j \le N_z - 1, l = j+1 \\ \frac{2}{h_{j-1}(h_{j-1}+h_j)}, & 1 \le j \le N_z - 1, l = j-1 \\ \frac{1}{h_{j-1}}, & j = N_z, l = N_z - 1 \\ -\frac{1}{h_{j-1}} - |k|, & j = l = N_z \\ 0, & else \end{cases}. \tag{7.77}$$

It has been shown (Haldenwang *et al.*, 1984) that the convergence behavior by using this preconditioned Helmholtz operator with Dirichlet and Robin boundary conditions is practically similar as that with purely Dirichlet boundary conditions, where the eigenvalues (of $\mathcal{H}^{-1}\mathcal{A}$) of the latter are confined within $[1, \pi^2/4]$. This brings a spectral radius $\rho(\mathcal{G})$ and convergence rate R independent of N_z ($\rho \sim O(1)$,

$R \sim O(1)$), i.e., the iteration is efficient independent of N_z.

In each iteration, we need to solve (7.74). As $\mathcal{H}$ is a tridiagonal matrix, the solution regarding the (implicit) inversion of $\mathcal{H}$ takes only $O(N_z)$ operations. The most heavy operations in solving (7.74) lie in the multiplication of $\mathcal{A}\mathcal{V}^n$. For small N_z, this can be obtained by direct matrix-vector multiplication, which takes $O(N_z^2)$ operations. For large N_z, an algorithm making use of Fast Fourier Transform (FFT) can be used to retain the computational complexity with $O(N_z log N_z)$ operations (Don & Solomonoff, 1995).

In summary, by applying the Richardson iteration and finite-difference preconditioning, the solution of (7.56) can be obtained in $O(1)$ iterations with $O(N_z log N_z)$ operations required per iteration. The solution to the original problem (7.1) and (7.2) takes $O(MN_x log N_x N_z log N_z)$ operations per time step. As a trade-off for this increased computational cost compared with the boundary perturbation method, the current method obtains numerical stability and accuracy for $M \gg 1$, especially for the calculation of a wave field with $\gamma \gg 1$. This is validated in 7.4.6.

7.4.6 Numerical validation

Equations (7.3), (7.4) and (7.5) with (7.23) and (7.24) are solved respectively by using the boundary perturbation method and the current method associated with mapping scheme (hereafter we name it MAP). For both methods, we use $N_x = 2048$ (with 2/3 de-aliasing and $N_F = 0$) and double precision. For MAP, we additionally use $h = 0.5$ (As a rule of thumb, h should be chosen as a smallest possible value, as long as $\eta/h \sim O(\epsilon)$) and $N_z = 40$. The L^2-norm error in the solutions of these two methods are obtained by comparing with the exact solution (7.25). We consider cases with $a_S k_S = a_L k_L = 0.2$, and different wavelength ratio $\lambda \equiv k_S/k_L$ (for convenience, we fix $k_L = 1$). The results for $\lambda = 1$, $\lambda = 10$ and $\lambda = 100$, with increasing nonlinearity order M up to $M = 30$, are shown in figure 7-8.

We see that, even for $\gamma = 1$ ($a_L = 0$), the error of boundary perturbation method starts to increase with M for $M \geq 10$. The mechanism of error generation in this case of modal energy assigned narrow-banded at low wavenumbers is described in

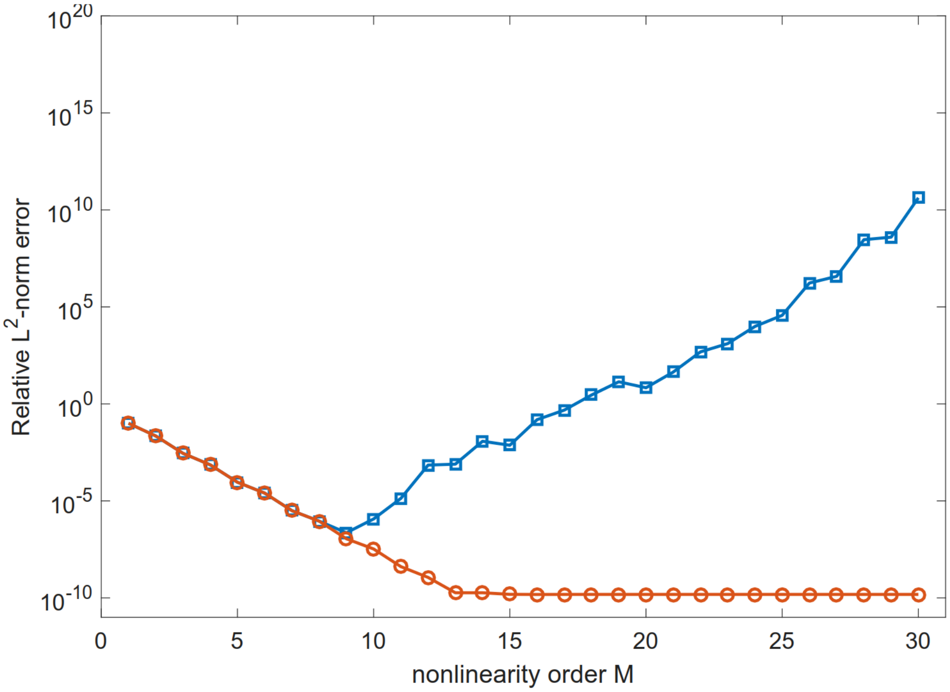
Relative L^2-norm error
10^20
10^15
10^10
10^5
10^0
10^-5
10^-10
0
5
10
15
20
25
30
nonlinearity order M

(a)

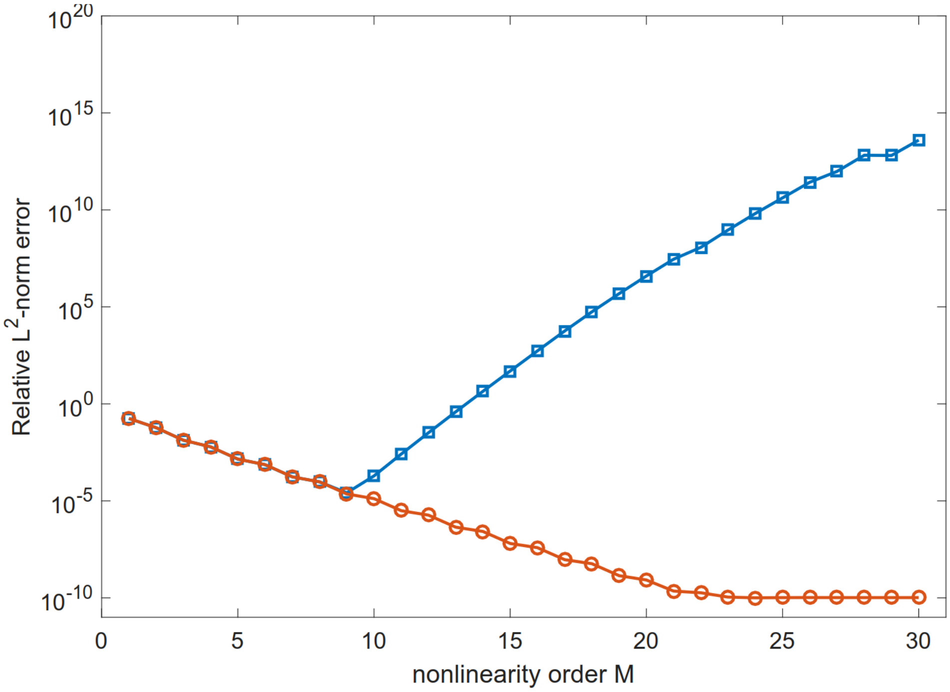
Relative L^2-norm error
10^20
10^15
10^10
10^5
10^0
10^-5
10^-10
0
5
10
15
20
25
30
nonlinearity order M

(b)

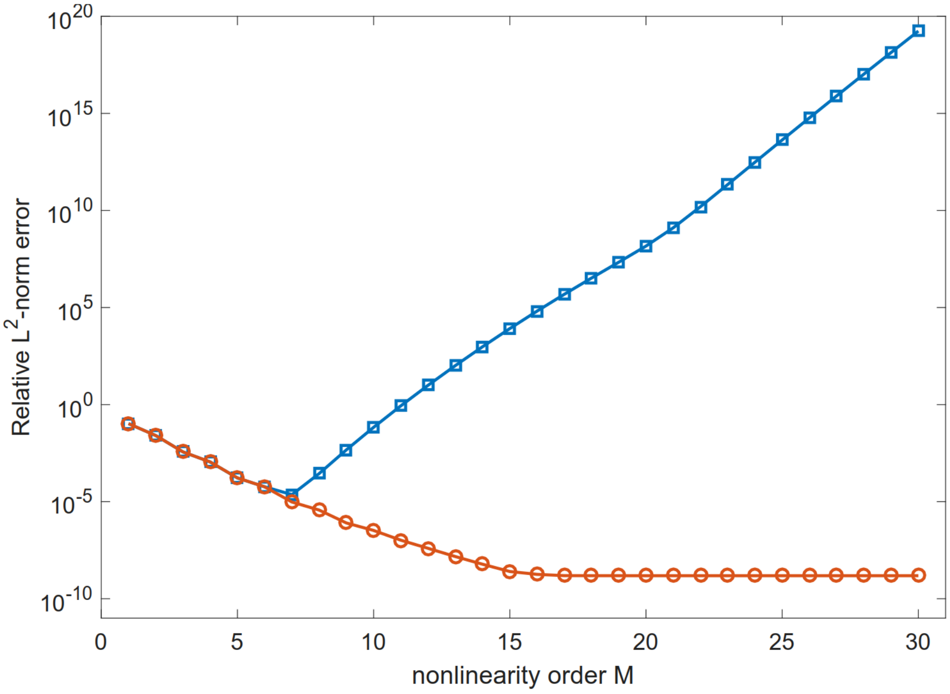

(c)

Figure 7-8: The relative L^2-norm error in the solution ϕ_z with increase of nonlinearity order M by boundary perturbation method (—□—) and MAP (—○—), for (a) $\gamma = 1$ ($a_L = 0$), (b) $\gamma = 10$ and (c) $\gamma = 100$.

section 7.3. This is clearly remedied by the MAP scheme, which is robust with converged results of $O(10^{-10})$ error for $M \geq 13$. With the increase of γ (figure 7.62(b) and (c)), the boundary perturbation method behaves increasingly poorly, with results starting to diverge at smaller value of M ($M = 10$ for $\gamma = 10$ and $M = 8$ for $\gamma = 100$). This reflects the increasing severity of the numerical instability caused by the long-short mode interaction. In contrast, the MAP scheme removes this instability, with converged results for all γ in the tested range. The accuracy of the converged results, on the other hand, should depend on the parameterization of the MAP scheme, including the choice of N_x, N_z and h. This is indeed the focus of our next investigation.

For this purpose, we evaluate the effect of N_x, N_z and h on the performance of the MAP scheme for the case of $\gamma = 100$ and $a_S k_S = a_L k_L = 0.2$. The variation of error in the MAP scheme with increasing M is plotted in figure 7-9 for varying values of N_z. For sufficient M, the result converges with the increase of N_z, illustrating the grid convergence in solving the boundary value problem. Figure 7-10 plots the error for different values of h (To avoid the influence of grid resolution on results, we keep $h/N_z = 0.0125$ as a constant). It is shown practically that larger value of h leads to smaller error, and the result converges with increase of h for sufficient M. Figure 7-11 shows the same error curve for different values of N_x. In principle, N_x affects the error due to the truncation in Fourier series. This is reflected in figure 7-11 that the error decreases with the increase of N_x (the convergence is yet to be shown as $N_x = 4096$ is forbidden by current machine memory).

7.5 Future work - physical application

The developed method significantly enhances our capability of simulating a wave field with $\gamma \gg 1$. It thus should be applied, with extension to two surface dimensions if necessary, to investigate physical problems involving long-short wave interactions. A brief literature review and possible future applications are described below.

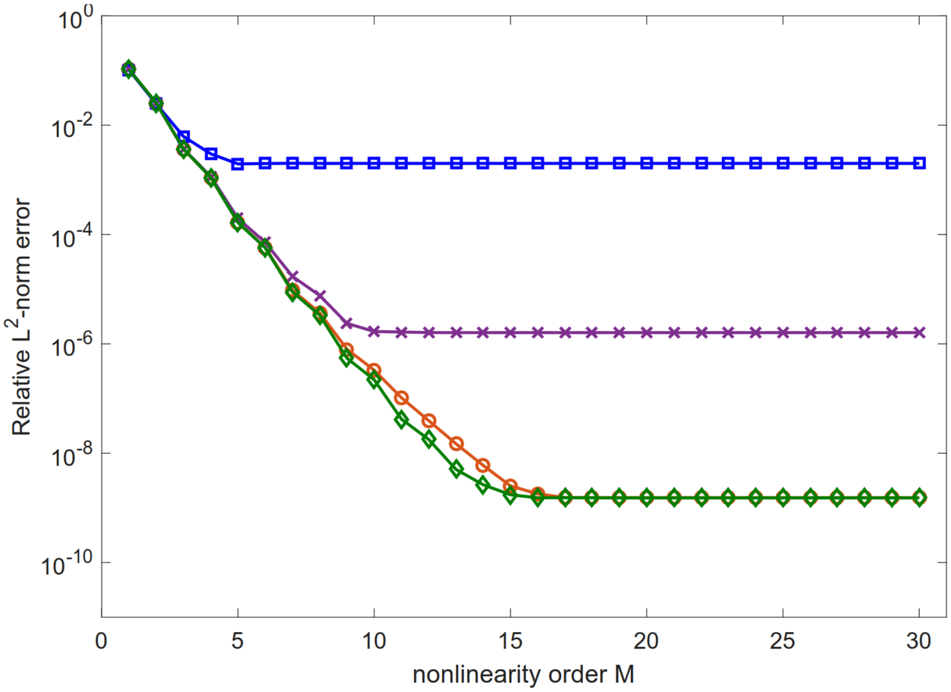

Figure 7-9: The relative L^2-norm error in the solution ϕ_z with increase of nonlinearity order M by MAP scheme, for $N_z = 20$ (—□—), 30 (—×—), 40 (—○—) and 50 (—◇—), with fixed $h = 0.5$ and $N_x = 2048$.

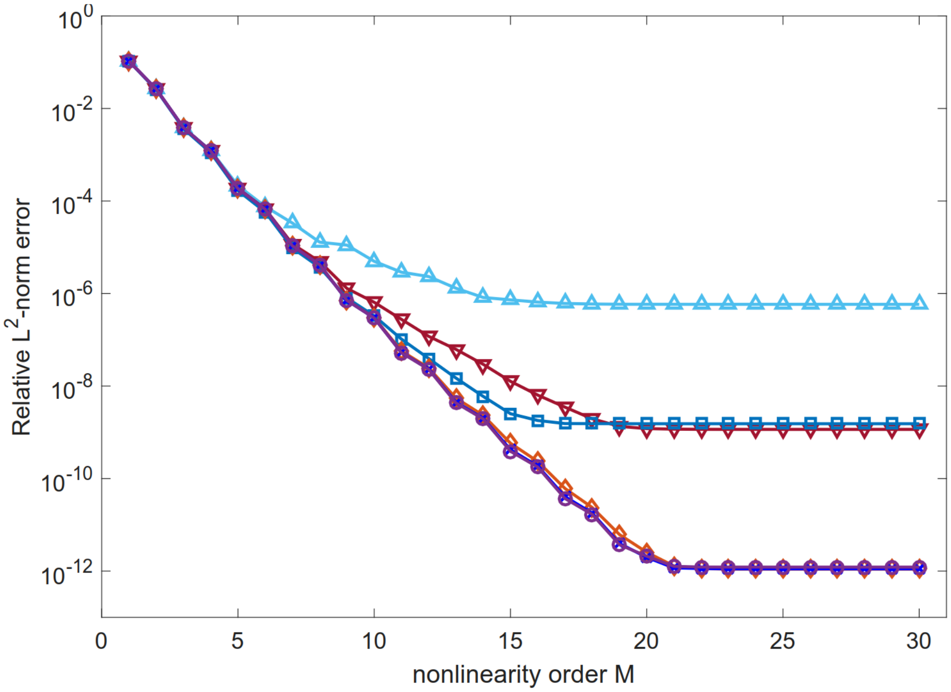

Figure 7-10: The relative L^2-norm error in the solution ϕ_z with increase of nonlinearity order M by MAP scheme, for $h = 0.3$ (—△—), 0.4 (—▽—), 0.5 (—□—), 0.6 (—◇—), 0.7 (—×—) and 0.8 (—○—), with fixed $h/N_z = 0.0125$ and $N_x = 2048$.

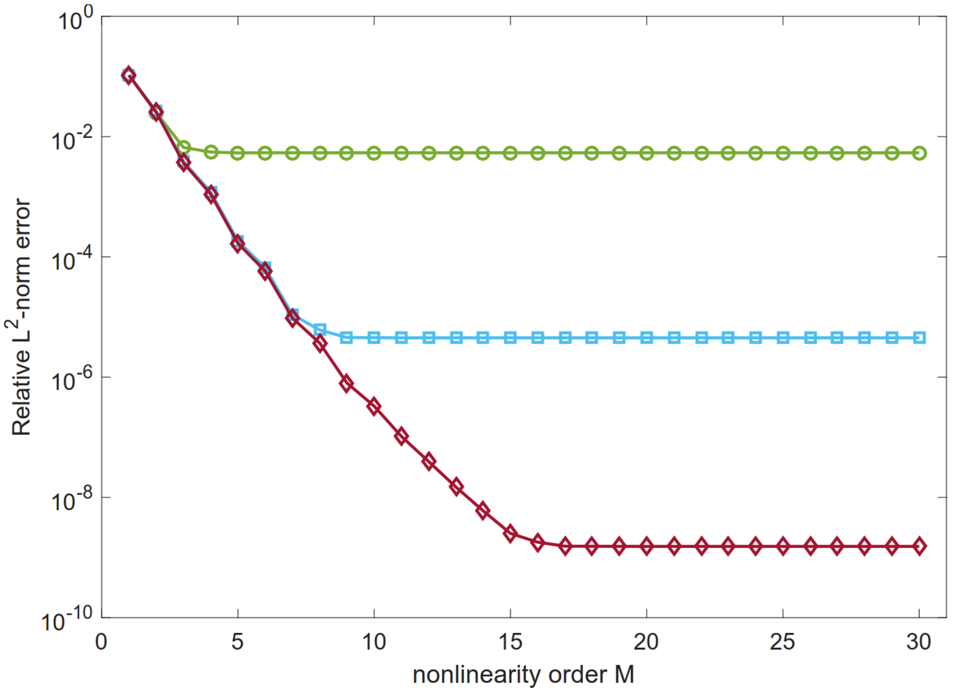

Figure 7-11: The relative L^2-norm error in the solution ϕ_z with increase of nonlinearity order M by MAP scheme, for $N_x = 512$ (—○—), 1024 (—□—) and 2048 (—◇—), with fixed $N_z = 40$ and $h = 0.5$.

7.5.1 Modulation of short waves by long waves

Short waves riding on long waves can interact with, and are modulated by the long wave. This study is an important component in remote sensing, where the back scattering from the sea surface involves waves with much smaller wavelength compared to the dominant wavelengths of ocean surface waves. The first investigation starts from Longuet-Higgins & Stewart (1960), who considers the modulation of a linear short wave by a weakly nonlinear long wave. Under the condition of $ka << O(1)$ (where k and a applies generally for long or short waves), the formulae for the modulation of short-wave wavenumber and amplitude are derived. Longuet-Higgins (1987) further extends the study and obtains the numerical solution of the modulation of a linear short wave on a finite-amplitude long wave. By expanding the short wave on the unperturbed long wave surface, Zhang & Melville (1990) remove the limitation of linearity of short wave and investigate the effect of short wave nonlinearity on the modulation. The instability of this solution is investigated in Zhang & Melville (1992), where it is found that in addition to the conventional sideband instability, the solution is also unstable for a wide range of perturbation wavenumber. Similar conclusions are found in Naciri & Mei (1992), by using Lagrangian formulation and Gerster's solution for the long wave.

Despite these theoretical/numerical analysis, this problem has never been studied through a direct numerical simulation of the wave field. Equipped with our developed MAP scheme, a simulation of (7.1) and (7.2), for the purpose of understanding short wave modulation by long waves (with $\gamma \gg 1$), can be obtained with high accuracy. We are prepared to establish the quantitative modification of a nonlinear short wave by a nonlinear long wave, with varying steepness for both waves. These results are expected to provide a validation and extension to Longuet-Higgins & Stewart (1960); Longuet-Higgins (1987); Zhang & Melville (1990), and investigate the unsteady effect which is ignored in all above analysis.

7.5.2 Nonlinear interaction of short waves in the presence of a long wave

In addition to the modulation of short wave field, the long wave also has impact on the energy transfer rate among short wave components. This is studied in Ölmez & Milgram (1995*a*), where they show both numerically and experimentally that the presence of the long wave reduces the energy transfer rate among short waves. However, their numerical simulations are limited to the initial growth of the tertiary wave component (code crashes for longer time), probably due to the numerical instability associated with the $k_S a_L$ issue. Their investigation is also limited to one particular case, i.e. all wave components are specially chosen and fixed. With our newly-developed approach, we can (i) do a long-time simulation of the interaction among short wave components in the presence of a long wave, thus give a comprehensive description of the phenomenon, probably including the Fermi-Pasta-Ulam recurrence behavior (Fermi *et al.*, 1955); (ii) investigate the effect of the long wave as a function of long wave direction, long-to-short wavelength ratio, etc.

7.5.3 Short wave spectrum under long wave background

Given the influence of long wave on the nonlinear interactions of short waves, it is not unreasonable to expect that a long wave background can affect the evolution of short wave spectrum. The study of this problem is in general lacking, with the only exception in awareness being Gramstad & Trulsen (2010), where the authors derive a modified nonlinear Schrodinger equation with a long wave background. This equation is applied to understand the influence of a swell background on the probability of rogue waves developed in a narrow-banded spectrum.

This study can be extended to broadband short-wave spectrum by our developed approach. The analysis of rogue wave probability by this direct numerical simulation can be obtained as an analogy of Xiao *et al.* (2013). The results should be supplemented by a theoretical derivation of Benjamin-Feir instability modulated by a long wave. Another application in this direction is the impact of a long wave on the WTT of the short wave field. Specifically, the spectral slope and energy flux of a capillary wave spectrum under long wave background are yet to be studied.

7.5.4 Parasitic capillary wave

Parasitic capillary wave generation on steep gravity or gravity-capillary waves has received much attention because of remote-sensing applications. Historical observation of this phenomenon starts from Russel (1838). While it is hypothesized (Munk, 1955) that the parasitic capillary waves are generated due to some (unknown) disturbance near the crest of the gravity waves, this phenomenon is later observed in experiment Cox (1958) even when wind is not present. Over the years it has been extensively studied, in experiments (Fedorov *et al.*, 1998; Chang *et al.*, 1978; Zhang, 1995; Perlin *et al.*, 1993), theory (Longuet-Higgins, 1963; Fedorov *et al.*, 1998; Longuet-Higgins, 1995) and numerics (Jiang *et al.*, 1999; Dommermuth, 1994; Hung & Tsai, 2009; Watson & Buchsbaum, 1996; Watson, 1999; Watson & Mcbride, 1993; Ceniceros & Hou, 1999). In spite of these great advances over the years, there are still some unsolved problems, and we list a few issues that can possibly be investigated using our direct numerical simulation.

1. Steadiness of the parasitic ripples: Most theoretical formulation assumes that the ripples are steady with respect to the phase of the long wave. This assumption is found not completely valid in both numerical and experimental work. The investigation in this direction can be carried on regarding two considerations. (i) Fedorov *et al.* (1998) shows experimentally that the capillary ripples become irregular (unstable) with respect to the phase of the long wave, for large long wave steepness ($ak = 0.3$). (ii) Both Perlin *et al.* (1993) and Hung & Tsai (2009) show that the ripple steepness varies periodically with time. Convincing explanations for these phenomenon have not yet been given.

2. Blockage of capillary wave: Phillips (1981) shows that the short capillary wave can be blocked to some phase point of the long wave. Longuet-Higgins (1995) further shows that due to this effect there exists a critical wave steepness above which the ripple steepness reduces with the increase of long wave steepness. However, this critical wavelength (as well as blockage) is not observed in numerical and experimental work (Jiang *et al.*, 1999). It is argued that unsteadiness may reduce ripple blocking, though a more detailed explanation is certainly desired.

3. Enhanced dissipation of gravity or gravity-capillary wave due to ripple generation: There have already been numerical (Tsai & Hung, 2010; Melville & Fedorov, 2015) and experimental (Zhang, 2002; Caulliez, 2013) evidences that the dissipation rate of the long wave is enhanced by the generation of ripples (energy transferred to ripples and then dissipated by viscosity). To develop an accurate model for this phenomenon, we may need include viscosity/vorticity in the HOS simulation. This is possibly obtainable in two ways: (i) Since we use vertical grid for the MAP scheme, we can take advantage of these grids and solve the vortex equation in the sub-layer of the surface. (ii) We may consider using a quasi-potential surface boundary condition (Dommermuth, 1994; Jiang *et al.*, 1999).

7.6 Summary

We have illustrated an ill-conditioning in the boundary perturbation method in solving the BVP involved in the HOS simulation of long-short wave interaction with largely disparate wavelength ratio ($\gamma \gg 1$). This is shown to be associated with large "divergent" terms proportional to $O((k_S a_L)^{m-1})$ in calculation of mth order vertical velocity $[\phi_z]^{(m)}$. Analytically, the boundary perturbation method behaves robustly as all these large terms cancel one another at each order m, for which we have provided the first general proof. Numerically, however, these cancelations are ill-conditioned, as it amounts to calculating relatively small numbers as differences of very large numbers. A detailed error analysis is performed, which quantitatively reveals the mechanism of numerical error generation in boundary perturbation method. We further show that this numerical ill-conditioning can be mitigated by using higher precision arithmetic. To fundamentally circumvent this difficulty, we have developed a mapping scheme, which transforms the original rough free surface to a flat surface, and the original BVP to a Poisson field equation subject to Dirichlet/Robin boundary conditions at top/bottom boundaries. This approach effectively removes the numerical instability inherent in the boundary perturbation method, as the most intense multiplications at arbitrary order M involve only three variables. As a trade-off to solve the new BVP, vertical grids are needed, which increases the computational cost. We present a relatively efficient way to solve the problem by a Fourier-Chebyshev collocation method, which, upon using Richardson iteration and finite-difference preconditioning, results in a computational complexity of $O(MN_x logN_x N_z logN_z)$. The validity of the developed MAP approach is benchmarked by solving a prescribed BVP involving long-short mode interactions, where it is shown that significant improvement in performance is obtained compared with the boundary perturbation method. Future extensions of the method and its possible physical explanations involving long-short wave interactions are discussed.

Chapter 8

Simulation of wave-current interaction

In this chapter, we develop the framework for numerical study of wave-current interactions. We first derive the governing equations for waves superposed on a prescribed steady and slowly-varying current. The derivation, which assumes negligible vorticity of the current field, is reformulated from that in Wu (2004). We further give the Hamiltonian formulation of the governed equations, which shows that the total (coupled) energy of wave and current is conserved by the equations. In addition, we provide a derivation which deals with generally rotational current field. Numerically, we consider waves passing a following/opposing current field, where it is shown that the former stretches and lowers the waves, while the latter behaves oppositely. Physical interpretations for these phenomenon, as well as possible future development and applications are discussed.

For simplicity, we assume one-dimensional surface in the derivation, and generalize the results to two surface dimensions after they are obtained. Without loss of generality, the time and mass units are assumed to be properly chosen so that the gravity acceleration g and fluid density ρ are unity.

8.1 Theoretical and numerical formulation

8.1.1 Derivation of the governing equations

In this section, we consider the derivation of the governing equations of a wave field superposed on a background steady current. For simplicity, the derivation is performed by assuming a one-dimensional surface. The derived governing equations are then generalized for a two-dimensional surface. This derivation is different from that in Wu (2004), as we do not assume a flat surface ($\bar{\eta} = 0$ as defined in (8.6)) due to current field. Instead, we allow the horizontal variation of $\bar{\eta}$, and use Taylor expansion based on the current surface $\bar{\eta}$. To start, we consider the total velocity field $\mathbf{V}_{TOT}$, decomposed as

$$\mathbf{V}_{TOT}(x, z, t) = \nabla\phi(x, z, t) + (U, W)(x, z), \tag{8.1}$$

where $\nabla\phi(x, z, t)$ is the velocity due to irrotational wave motion, $U(x, z)$ and $W(x, z)$ are the horizontal and vertical steady current velocity. We make the following assumptions on the current.

1. $\partial U/\partial x + \partial W/\partial z = 0$, i.e., the flow is incompressible.

2. Analytical continuation is valid near the surface, i.e., quantity on the wave surface can be obtained by Taylor expansion.

3. The horizontal length scale of current is much larger than that of the wave, i.e., $L_c \gg L_w$

4. The vorticity component $\partial U/\partial z \sim \partial W/\partial x \sim O(\epsilon^{M+1})$, and thus can be neglected in the derivation. The consideration of a general (rotational) current field significantly complicates the derivation, which is presented in Appendix E.

The kinematic boundary condition can be obtained by considering a particle remaining on the free surface, i.e., $D(z - \eta(x))/Dt = 0$, where D denotes the material derivative. This gives

$$\frac{\partial\eta}{\partial t}+\frac{\partial\eta}{\partial x}(\frac{\partial\phi}{\partial x}+U)-W-\frac{\partial\phi}{\partial z}=0. \tag{8.2}$$

The dynamic boundary condition can be obtained from the Bernoulli's equation, i.e., $\partial\phi/\partial t+V_{TOT}^2/2+\eta=0$, which gives

$$\frac{\partial\phi}{\partial t}+U\phi_x+W\phi_z+\frac{1}{2}(\phi_x^2+\phi_z^2)+\frac{1}{2}(U^2+W^2)+\eta=0. \tag{8.3}$$

By substituting the surface potential $\phi^s(x,t)=\phi(x,\eta(x,t),t)$ in (8.2) and (8.3), we obtain the governing equations in Zakharov form:

$$\eta_t+\eta_x\phi_x^s-(1+\eta_x^2)\phi_z+U\eta_x-W=0. \tag{8.4}$$

$$\phi_t^s+U\phi_x^s+\frac{1}{2}\phi_x^s\phi_x^s-\frac{1}{2}(1+\eta_x^2)\phi_z^2+\eta+\frac{1}{2}(U^2+W^2)=0. \tag{8.5}$$

Now let

$$\eta=\bar{\eta}+\eta^w, \tag{8.6}$$

where $\bar{\eta}$ and η^w are the surface elevations respectively due to current and wave. Considering a waveless flow motion, we have the kinematic and dynamic boundary conditions on the surface $z=\bar{\eta}$, determined by the current field

$$U\bar{\eta}_x=W, \text{ on } z=\bar{\eta}, \tag{8.7}$$

$$\bar{\eta}+\frac{1}{2}(U^2+W^2)=0, \text{ on } z=\bar{\eta}. \tag{8.8}$$

Due to assumption 3 (and the weak assumption that the current velocity is not terribly larger than the velocity due to wave motion), the variation of $\bar{\eta}$ can be considered negligible in a wavelength ($\bar{\eta}_x \ll \eta_x^w \sim O(\epsilon)$). As a result, expanding the surface quantity based on $z=\bar{\eta}$, we have

$$(U\eta_x-W)|_{z=\eta}=(U\eta_x-W)|_{z=\bar{\eta}}+\eta^w\frac{\partial}{\partial z}(U\eta_x-W)|_{z=\bar{\eta}}=(U\eta_x^w-\eta^wW_z)|_{z=\bar{\eta}}, \tag{8.9}$$

where we have used the assumptions 1, 2 and 4. Similarly

$$\begin{aligned}\frac{1}{2}(U^2+W^2)|_{z=\eta}+\eta &= \frac{1}{2}(U^2+W^2)|_{z=\bar{\eta}}+\eta^w\frac{\partial}{\partial z}\Big[\frac{1}{2}(U^2+W^2)\Big]\Big|_{z=\bar{\eta}}+\bar{\eta}+\eta^w \\ &= \eta^w+\eta^w(WW_z)|_{z=\bar{\eta}}=\eta^w.\end{aligned} \tag{8.10}$$

where the last equal sign is due to the fact of $WW_z \sim UU_x\bar{\eta}_x \sim \bar{\eta}_x^2 \ll 1$.

By substituting (8.9) and (8.10) to (8.4) and (8.5), and applying $\bar{\eta}_x \ll \eta_x^w$, we obtain the governing equations in terms of ϕ^s and η^w. The superscript "w" can further be dropped by considering a x-axis ($z=0$) coinciding with the surface of $\bar{\eta}$. This gives

$$\eta_t+\eta_x\phi_x^s-(1+\eta_x^2)\phi_z+\eta_x U|_{z=0}+\eta U_x|_{z=0}=0, \tag{8.11}$$

$$\phi_t^s+\eta+\frac{1}{2}\phi_x^s\phi_x^s-\frac{1}{2}(1+\eta_x^2)\phi_z^2+\phi_x^s U|_{z=0}=0. \tag{8.12}$$

This derivation can be straightforwardly generalized to two surface dimensions with a current field $(\mathbf{U},W)(\mathbf{x},z)$, where $\mathbf{U}\equiv(U,V)$,

$$\eta_t+\nabla_{\mathbf{x}}\eta\nabla_{\mathbf{x}}\phi^s-(1+\nabla_{\mathbf{x}}\eta\cdot\nabla_{\mathbf{x}}\eta)\phi_z+\nabla_{\mathbf{x}}\eta\cdot\mathbf{U}|_{z=0}+\eta\nabla_{\mathbf{x}}\cdot\mathbf{U}|_{z=0}=0, \tag{8.13}$$

$$\phi_t^s+\eta+\frac{1}{2}\nabla_{\mathbf{x}}\phi^s\cdot\nabla_{\mathbf{x}}\phi^s-\frac{1}{2}(1+\nabla_{\mathbf{x}}\eta\cdot\nabla_{\mathbf{x}}\eta)\phi_z^2+\nabla_{\mathbf{x}}\phi^s\cdot\mathbf{U}|_{z=0}=0. \tag{8.14}$$

We shall proceed with equations (8.13) and (8.14) hereafter.

8.1.2 Hamiltonian formulation

There is no guarantee that, after the above manipulation of including the current field, the governing equations (8.13) and (8.14) can retain a Hamiltonian structure. This is however desired, as energy conservation principle should not be degraded by the current field. Hence, we show the Hamiltonian formulation of (8.13) and (8.14) in this section, and prove that the quantity conserved by them is the total (coupled) energy of wave and current.

We first re-write (8.13) and (8.14):

$$\eta_t = \underbrace{-\nabla_{\mathbf{x}}\eta\nabla_{\mathbf{x}}\phi^s + (1+\nabla_{\mathbf{x}}\eta\cdot\nabla_{\mathbf{x}}\eta)\phi_z}_{①}\underbrace{-\nabla_{\mathbf{x}}\eta\cdot\mathbf{U}|_{z=0} - \eta\nabla_{\mathbf{x}}\cdot\mathbf{U}|_{z=0}}_{②}, \tag{8.15}$$

$$\phi^s_t = \underbrace{-\eta - \frac{1}{2}\nabla_{\mathbf{x}}\phi^s\cdot\nabla_{\mathbf{x}}\phi^s + \frac{1}{2}(1+\nabla_{\mathbf{x}}\eta\cdot\nabla_{\mathbf{x}}\eta)\phi_z^2}_{①}\underbrace{-\nabla_{\mathbf{x}}\phi^s\cdot\mathbf{U}|_{z=0}}_{②}. \tag{8.16}$$

We next show that (8.15) and (8.16) can be written as a Hamiltonian system,

$$\frac{\partial\eta}{\partial t} = \frac{\delta H}{\delta\phi^s}, \quad \frac{\partial\phi^s}{\partial t} = -\frac{\delta H}{\delta\eta}, \tag{8.17}$$

where δ denotes the variational derivative, and the Hamiltonian H can be decomposed as

$$H = H_w + H_c. \tag{8.18}$$

In (8.18), H_w is the part due to wave motion, corresponding to the terms marked by ① in (8.15) and (8.16). This has been well understood (e.g. Zakharov, 1968), which is equal to the summation of the wave-like potential energy and kinetic energy:

$$H_w = \frac{1}{2}\int\eta^2 d\mathbf{x} + \frac{1}{2}\int_{-\infty}^{\eta}\int\left[\nabla_{\mathbf{x}}\phi\cdot\nabla_{\mathbf{x}}\phi + (\frac{\partial\phi}{\partial z})^2\right]d\mathbf{x}dz. \tag{8.19}$$

This can be shown, by involving the Green's theorem $\int(\phi\nabla^2\phi + \nabla\phi\cdot\nabla\phi)dV = \oint\phi(\nabla\phi\cdot\mathbf{n})dS$ (where $\nabla\equiv(\nabla_{\mathbf{x}}, \partial/\partial z)$) and (8.15), to be

$$H_w = \frac{1}{2}\int\eta^2 d\mathbf{x} + \frac{1}{2}\int\phi^s\eta_t|_{\mathbf{U}=0}d\mathbf{x}, \tag{8.20}$$

where $\eta_t|_{\mathbf{U}=0}$ is obtained from (8.15) with $\mathbf{U}=0$, and we have assumed horizontally periodic boundary condition.

We now claim that H_c, which corresponds to the terms marked by ② in (8.15) and (8.16), can be expressed as

$$H_c = -\int\phi^s(\mathbf{U}|_{z=0}\cdot\nabla_{\mathbf{x}}\eta - \eta W_z|_{z=0})d\mathbf{x}. \tag{8.21}$$

Let's prove this by substituting (8.21) to (8.17) (refer to Zakharov *et al.* (1992) for the rule of variational derivative):

$$
\begin{aligned}
\frac{\delta H_c}{\delta \phi^s} &= -\int \delta(\mathbf{r}-\mathbf{r}_1)\big[\mathbf{U}(\mathbf{r}_1)|_{z=0}\cdot\nabla_{\mathbf{x}}\eta(\mathbf{r}_1)-\eta(\mathbf{r}_1)W_z(\mathbf{r}_1)|_{z=0}\big]d\mathbf{r}_1 \\
&= -\mathbf{U}|_{z=0}\cdot\nabla_{\mathbf{x}}\eta-\eta\nabla_{\mathbf{x}}\cdot\mathbf{U}|_{z=0}.
\end{aligned}
\tag{8.22}
$$

$$
\begin{aligned}
\frac{\delta H_c}{\delta \eta} &= -\frac{\delta}{\delta\eta}\int\big[\nabla_{\mathbf{x}}\cdot(\phi^s\eta\mathbf{U}|_{z=0})-\eta\nabla_{\mathbf{x}}\cdot(\phi^s\mathbf{U}|_{z=0})-\phi^s\eta W_z|_{z=0}\big]d\mathbf{x} \\
&= \nabla_{\mathbf{x}}\cdot(\phi^s\mathbf{U}|_{z=0})+\phi^s W_z|_{z=0} \\
&= \mathbf{U}|_{z=0}\cdot\nabla_{\mathbf{x}}\phi^s,
\end{aligned}
\tag{8.23}
$$

where we have used the horizontally periodic condition for the second equal sign. These are exactly the terms marked by ② in (8.15) and (8.16), and we have thus proved that the Hamiltonian H is in the form of (8.18), (8.20) and (8.21).

We next consider the physical meaning of $H_c=-\int\phi^s(\mathbf{U}|_{z=0}\cdot\nabla_{\mathbf{x}}\eta-\eta W_z|_{z=0})d\mathbf{x}$. We will show that it corresponds to the wave-current cross terms in the evaluation of the total (wave and current) kinetic energy. This can be obtained by subtracting the wave-only and current-only parts of the kinetic energy from the total kinetic energy:

$$
KE_{T-C-W}=\frac{1}{2}\int_{-\infty}^{\eta}\int\big[(\mathbf{U}+\nabla_{\mathbf{x}}\phi)\cdot(\mathbf{U}+\nabla_{\mathbf{x}}\phi)+(W+\frac{\partial\phi}{\partial z})^2\big]d\mathbf{x}dz-KE_C-KE_W,
\tag{8.24}
$$

where

$$
KE_C+KE_W=\frac{1}{2}\int_{-\infty}^{\eta}\int\big[\mathbf{U}\cdot\mathbf{U}+W^2+\nabla_{\mathbf{x}}\phi\cdot\nabla_{\mathbf{x}}\phi+(\frac{\partial\phi}{\partial z})^2\big]d\mathbf{x}dz.
\tag{8.25}
$$

We thus have

$$
KE_{T-C-W}=\int_{-\infty}^{\eta}\int(\mathbf{U}\cdot\nabla_{\mathbf{x}}\phi+W\frac{\partial\phi}{\partial z})d\mathbf{x}dz=\int_{-\infty}^{\eta}\int\nabla\cdot(\phi\mathbf{U}_T)d\mathbf{x}dz,
\tag{8.26}
$$

where $\nabla\equiv(\nabla_{\mathbf{x}},\partial/\partial z)$, $\mathbf{U}_T=(\mathbf{U},W)$, and we have used the continuity of the current field (assumption 1). Due to the divergence theorem, we have

$$KE_{T-C-W} = \int \phi^s \mathbf{U}_T|_{z=\eta} \cdot \mathbf{n} d\mathbf{s}, \tag{8.27}$$

where $d\mathbf{s}$ is an element on the free surface $z = \eta$, and $\mathbf{n}$ is the outward unit normal vector

$$\mathbf{n} = \frac{(-\eta_x, -\eta_y, 1)}{\sqrt{1 + \eta_x^2 + \eta_y^2}}. \tag{8.28}$$

Substituting (8.28) to (8.27), we obtain

$$KE_{T-C-W} = -\int \phi^s \mathbf{U}|_{z=\eta} \cdot \nabla_{\mathbf{x}} \eta d\mathbf{x} + \int W|_{z=\eta} \phi^s d\mathbf{x}. \tag{8.29}$$

Substituting (8.9) (the corresponding version for two-dimensional surface) to (8.29), and considering the surface-coinciding x-axis, we obtain

$$KE_{T-C-W} = -\int \phi^s (\mathbf{U}|_{z=0} \cdot \nabla_{\mathbf{x}} \eta - \eta W_z|_{z=0}) d\mathbf{x}. \tag{8.30}$$

Therefore, we have shown that

$$KE_{T-C-W} = H_c, \tag{8.31}$$

and the quantity conserved by (8.13) and (8.14) (or (8.15) and (8.16)) is the total (wave-current coupled) energy.

8.1.3 Numerical time integration

Equations (8.15) and (8.16) can be integrated in time, once ϕ_z is solved by boundary perturbation method in HOS at each time step. We conduct in this section a linear stability analysis, assuming ERK4 is used in the time integration.

We consider the decomposition

$$\mathbf{U} = \overline{\mathbf{U}} + \mathbf{u}, \tag{8.32}$$

where $\overline{\mathbf{U}}$ is the mean current field, and $\mathbf{u}$ is the fluctuation with zero mean (considered to be $O(\epsilon)$). The linear part of (8.15) and (8.16) can be separated, which, in wavenumber space, reads

$$\frac{\partial}{\partial t}\begin{bmatrix} \widehat{\eta}_{\mathbf{k}} \\ \widehat{\phi^s}_{\mathbf{k}} \end{bmatrix} = \mathcal{T}\begin{bmatrix} \widehat{\eta}_{\mathbf{k}} \\ \widehat{\phi^s}_{\mathbf{k}} \end{bmatrix}, \tag{8.33}$$

where

$$\mathcal{T} = \begin{bmatrix} -i\mathbf{k}\cdot\overline{\mathbf{U}} & k \\ -1 & -i\mathbf{k}\cdot\overline{\mathbf{U}} \end{bmatrix} \tag{8.34}$$

with $\mathbf{k} = (k_x, k_y)$ and $k = |\mathbf{k}|$.

As discussed in Chapter 3, the eigenvalues of the matrix $\mathcal{T}$ dictate the property of linear stability of the problem. This can be solved to be

$$\lambda_{\mathcal{T}} = \pm i\sqrt{k} - i\mathbf{k}\cdot\overline{\mathbf{U}}. \tag{8.35}$$

Defining $\beta = max(|\sqrt{k} - \mathbf{k}\cdot\overline{\mathbf{U}}|, |\sqrt{k} + \mathbf{k}\cdot\overline{\mathbf{U}}|)$, we obtain the linear stability criterion for using ERK4 to solve (8.33),

$$\Delta t \leq \frac{2\sqrt{2}}{\beta}. \tag{8.36}$$

From (8.36), we see that the time step Δt can be severely limited for large $|\overline{\mathbf{U}}|$. This problem can be remedied, if necessary, by using the IRK4 scheme presented in Chapter 3.

8.2 Numerical simulation

We consider gravity waves, on a two-dimensional surface, passing a prescribed realistic current field. The current field, applied on a $4km \times 4km$ region, is obtained from a MSEAS (http://mseas.mit.edu) analysis of ocean surface centered around $39^\circ\ 30'N,\ 72^\circ\ 30'W$. To manifest the effect of current on waves, we use a totally $10km \times 10km$ computational domain, centered by the $4km \times 4km$ patch with current, whose surroundings gradually diminishing to quiescence. This is shown in figure 8-

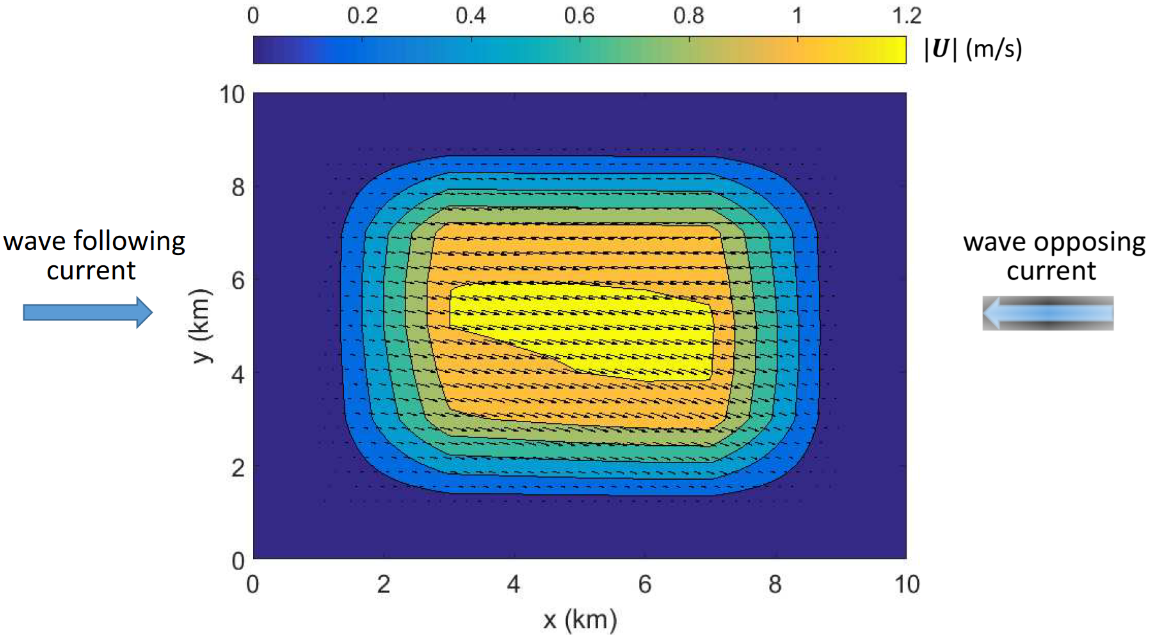

Figure 8-1: The current field, with a contour of current velocity magnitude and arrows indicating directions of velocity. The region with non-zero current velocity is centered in a $4km \times 4km$ patch, whose surroundings gradually diminishing to quiescence, within a totally $10km \times 10km$ computational domain. The data is obtained from a MSEAS (http://mseas.mit.edu) analysis of ocean surface centered around 39° 30'N, 72° 30'W.

1, with a contour of current velocity magnitude and arrows indicating directions of velocity.

We further consider a superposed wave field, whose initial condition is specified from a JONSWAP spectrum with peak period $T_p = 14s$, significant wave height $H_s = 12m$, effective steepness $\beta = k_p H_s/2 = 0.12$, and spreading angle of 30°. This spectrum is plotted in figure 8-2. Equations (8.13) and (8.14) are simulated by HOS with nonlinearity order $M = 3$, starting from this initial condition and the prescribed steady current field.

We consider three cases of simulation: (1) wave without current; (2) wave following current; and (3) wave opposing current. Cases (2) and (3) are indicated in figure 8-1 where these two scenarios are indeed realized in an approximate sense (since the current velocity is not exactly pointing rightward). Typical snapshots of the wave fields at $t = 75T_p$ for the three cases are shown in figure 8-3. Compared with case (1),

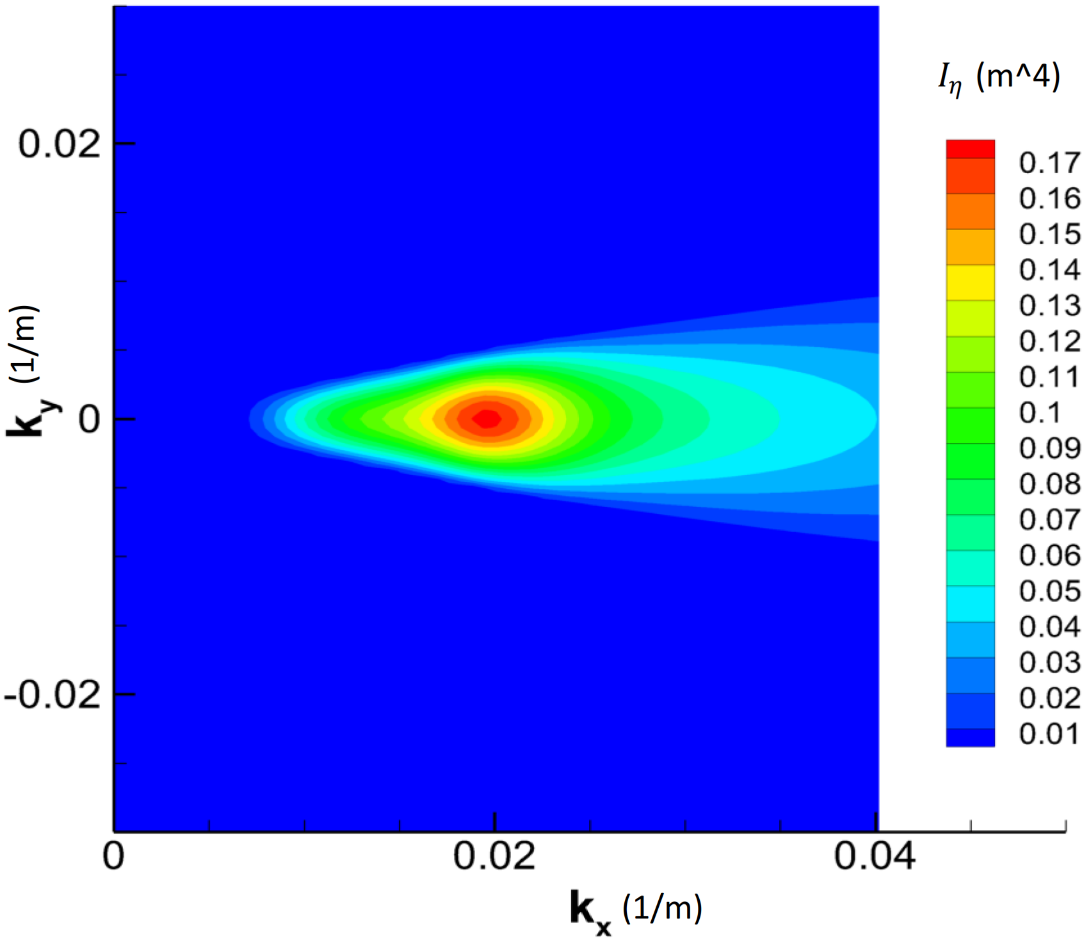

Figure 8-2: The initial JONSWAP wave spectrum, with peak period $T_p = 14s$, significant wave height $H_s = 12m$, effective steepness $\beta = k_p H_s/2 = 0.12$, and spreading angle of 30°.

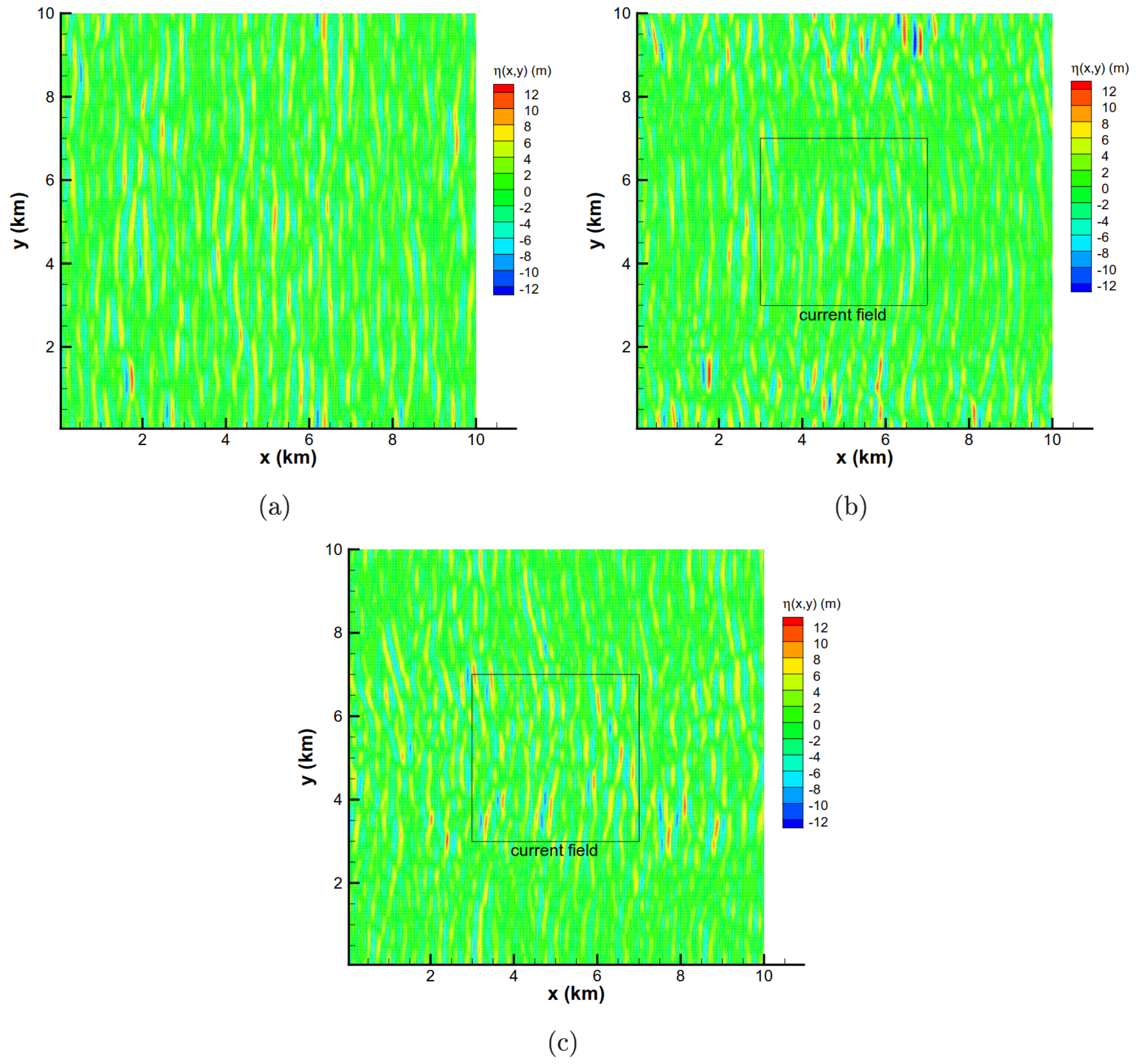

(a)

(b)

(c)

Figure 8-3: Typical snapshots of the wave fields at $t = 75T_p$ for the three cases: (a) wave without current; (b) wave following current; and (c) wave opposing current. The field with significant current velocity is indicated by a box in (b) and (c).

it is apparent that waves become longer and lower, i.e., suppressed, when following current (case 2), and behaves oppositely when opposing current (case 3).

For a more detailed elucidation, we define a variable ζ as a representation of surface roughness

$$\zeta(S) = \langle|\nabla\eta(x, y)|^2\rangle_S, \tag{8.37}$$

which computes the spatial average in the region S of the quantity $|\nabla\eta(x, y)|^2$. We plot, in figure 8-4, $\zeta(S)$ with S being the centered $4km \times 4km$ region. Compared to the case without current, we see that $\zeta(S)$ becomes respectively larger and smaller than normal when wave is opposing and following current.

The effect of following/opposing current on waves can be physically interpreted. This is first discussed in Longuet-Higgins & Stewart (1961). We summarize the key results here. For simplicity, we consider the steady wave field formed on a slowly-varying collinear current. (For general wave-current interaction on two-dimensional surface, ray theory can be used (Mei *et al.*, 2005).) The wavenumber modulation by current can be obtained by considering the conservation of apparent wave frequency (relative to a fixed point in space):

$$k(c+U)=k_0(c_0+U_0), \tag{8.38}$$

where $c=\sqrt{1/k}$ is the phase velocity of waves, and the subscript "0" denotes a reference position (say wave without current, for which $U_0=0$). Equation (8.38) can be considered as a quadratic equation in c/c_0, and can be solved as

$$\frac{k}{k_0}=(\frac{c}{c_0})^{-2}=[\frac{2(1+\gamma)}{1+\sqrt{1+4(1+\gamma)U/c_0}}]^2, \tag{8.39}$$

with $\gamma=U_0/c_0$.

As discussed in Longuet-Higgins & Stewart (1961), the energy conservation is not a valid assumption for waves on a varying current background. Instead, the modulation of wave amplitude by current should be determined by the conservation of wave action:

$$(c_g+U)\frac{E}{\omega}=(c_{g0}+U_0)\frac{E_0}{\omega_0}, \tag{8.40}$$

where $c_g=c/2$ is the group velocity of waves, and $E\sim a^2$ with a being the wave amplitude, $\omega=1/c$ is the intrinsic frequency of waves (in a frame of reference moving with U). The solution of (8.40) gives

$$\frac{a}{a_0}=[\frac{c_0(c_0+2U_0)}{c(c+2U)}]^{1/2}. \tag{8.41}$$

The effect of following/opposing current on waves can be obtained by setting

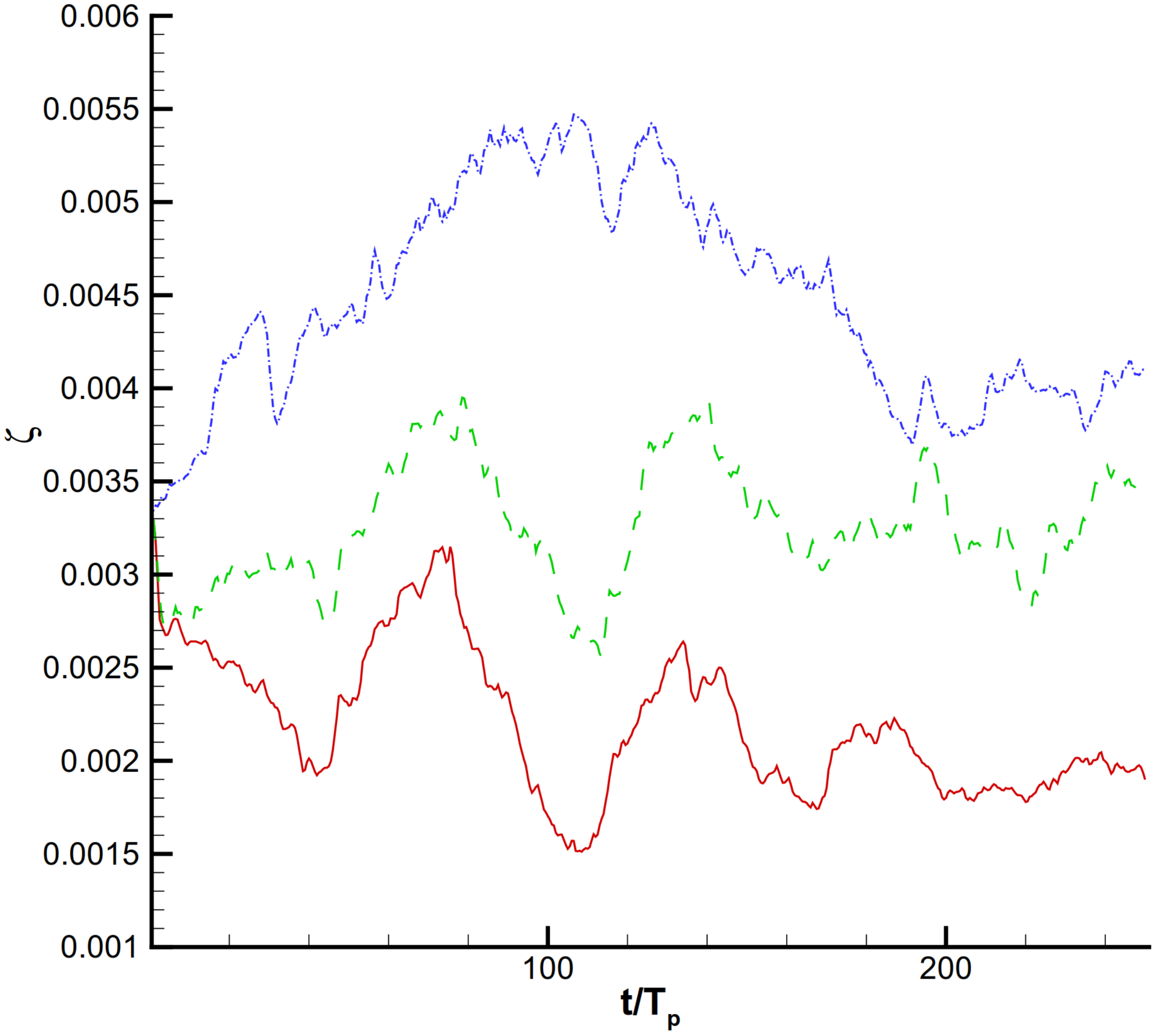

Figure 8-4: $\zeta(S)$ with S being the centered $4km \times 4km$ region for cases of (1) wave without current (– – –); (2) wave following current (——); and (3) wave opposing current (- · -).

$U_0 = 0$ in (8.39) and (8.41). It can be shown that for $U > 0$ (following current), we have $k < k_0$ and $a < a_0$, which means waves being stretched and lowered; for $U < 0$, we have $k > k_0$ and $a > a_0$, meaning a shortened and amplified wave field. These physical insights are consistent with our simulation results, and (8.39) and (8.41) are quantitatively verified by 2D linear HOS simulation in Wu (2004).

8.3 Future work

8.3.1 Influence of current field on wave attenuation

The study in section 8.2 elucidates the apparent effect of current field on wave steepness, which implies that the wave dissipation can also be affected by currents. Indeed, this has been shown experimentally in An & Shibayama (1994); Simons *et al.* (1988), that rate of wave attenuation increases in the opposing current and decreases in the following current. Besides these qualitative description, a quantitative relation is yet to be established. The influence on wave dissipation by a turbulent background flow is considered theoretically (Phillips, 1959) and experimentally (Green *et al.*, 1972; Gutiérrez & Aumaître, 2016), where it is shown that the background turbulence in general enhances wave dissipation. A numerical study of this phenomenon can be obtained by simulating the governing equations derived in appendix E, for which the influence of vorticity on the wave field is accounted.

8.3.2 Influence of current field on wave spectral evolution

It is expected that the nonlinear wave interaction, and thus spectral evolution, can be affected by a background current field. We are not aware of many studies on this subject, with the exception of Trulsen *et al.* (1990); Lamy *et al.* (2004), where the problem is studied in terms of the wave action balance equation (a kinetic-type equation). A direct numerical simulation of the wave field is desired in order to elucidate the mechanism involved in energy transfer modulated by current.

8.3.3 Influence of current field on rogue wave probability

It has been well understood that wave focusing by an opposing current can be an important factor for rogue wave occurrence (Dysthe *et al.*, 2008; Wu & Yao, 2004; Merkoune *et al.*, 2013; White & Fornberg, 1998; Lavrenov & Porubov, 2006; Lavrenov, 1998; Smith, 1976), and the incidences happening at the Agulhas current (Mallory, 1974) are largely attributed to this effect. In addition, the nonlinear focusing by Benjamin-Feir instability has also been shown to significantly contribute to rogue wave occurrence (Dysthe *et al.*, 2008; Xiao *et al.*, 2013). Notwithstanding, studies combing these two effects are rare, with the exception of Onorato *et al.* (2011); Hjelmervik & Trulsen (2009), which consider the nonlinear generation of rogue waves on an opposing current in the context of a Schrödinger equation. In spite of several physical findings, the validity of Schrödinger equation is limited for a narrow-banded spectrum, which can be violated for significant modulation of wavenumber by current. It is expected that the numerical simulation described in this chapter is especially useful to consider this problem involving both current-modulated Benjamin-Feir instability and current-focused wave groups.

8.3.4 wave-current interaction

Instead of a prescribed steady current field, it is desirable to develop a method which incorporates fully nonlinear wave-current interactions. This can be obtained by coupling the HOS solver for surface dynamics and a Navier-Stokes solver for underlying current field (see Appendix F for the detailed coupling algorithm). The developed approach can be used to understand the generated flow/vortex pattern beneath surface waves (e.g. Punzmann *et al.*, 2014; Constantin, 2015; Filatov *et al.*, 2016). In particular, the phenomenon, described in Punzmann *et al.* (2014), of wave-driven surface flows is worthwhile for a detailed study, which may enable us to engineer a new device for generation of inward and outward surface jets.

8.4 Summary

We have developed the framework for the simulation of a wave field superposed on a prescribed steady slowly-varying current field. The governing equations for waves are derived respectively for a current field with negligible vorticity and a generally rotational current field. The obtained equations for the former are converted to the Hamiltonian formulation, from which we show the quantity conserved in the equations is total (coupled) energy of wave and current. Numerical simulation is conducted with respect to a realistic current field obtained from a MSEAS simulation of ocean surface. We consider three cases: (1) wave without current; (2) wave following current; and (3) wave opposing current. From the results of these simulations, we observe that waves passing a following current field are stretched and lowered, while waves passing an opposing current field behave oppositely. Physical interpretations for these phenomena are discussed in terms of simplified collinear wave and current, from the principle of conservation of apparent frequency and wave action. Other possible physical applications of the developed approach are discussed, and numerical formulation for a method incorporating fully nonlinear wave-current interactions is proposed.

Chapter 9

Conclusions and future work

9.1 Conclusion

The major topic of this thesis is the study of weak turbulence theory (WTT) of capillary waves. On the theoretical aspect, we re-formulate the derivation of the stationary solution of the inertial-range capillary wave spectrum, starting from the primitive Euler equations. This leads to a theoretical surface elevation spectrum $I_\eta = 2\pi C P^{1/2} k^\alpha$, with theoretical values of $\alpha = \alpha_0 = -19/4$ and Kolmogorov Constant $C = C_0 = 6.97$. In particular, the value of C_0 is updated, due to our correction of two inconsistencies in the original derivation (Pushkarev & Zakharov, 2000), respectively regarding the normalization of energy flux P and the evaluation of a key integral.

In order to conduct direct numerical investigation of this problem, we develop an efficient solver for the primitive Euler equations based on a High-Order Spectral (HOS) method, with a modification for capillarity. Two different numerical formulations of the capillarity term are developed, which are respectively consistent with the framework of Dommermuth & Yue (1987) and West *et al.* (1987) for the rest part of the equations, and are expected to be used accordingly. While these two formulations can be used interchangeably for general purposes, their practical difference is discussed. The validity and accuracy of the developed approach is benchmarked with an analytical Crapper wave solution. The Courant condition for the simulation is obtained through a linear stability analysis, where it is shown that capillarity appreciably limits the time step size in simulation of a wave spectrum. To alleviate this situation, we develop an implicit 4th-order Runge-Kutta scheme (IRK4) for time integration, which combines the explicit Runge-Kutta scheme and a linear propagator method. The newly-developed IRK4 method is shown to be linearly stable and exact, and its efficacy when applied to nonlinear equations is demonstrated in the Crapper wave simulation, with the limitations illustrated. We end the numerical formulation by presenting the 2/3 spatial de-aliasing rule, which is more efficient than the previous 1/2 de-aliasing rule used in Dommermuth & Yue (1987).

The developed numerical method for the primitive Euler equations is then applied to study the capillary wave turbulence. The objective of this simulation is to obtain a clear development of the power-law spectrum and unambiguous evaluation of energy flux, for which a direct comparison to the WTT theory can be performed. To this end, we consider the free-evolution of a capillary wave spectrum, starting from a somewhat arbitrary isotropic spectrum. As the evolution reaches the quasi-stationary state, we measure the spectral slope α of the power-law spectrum, and the energy flux P directly from the energy dissipation rate. We also seek to uncover the physics for a long range of P to establish the scaling between I_η and P. This can be accomplished by starting the simulations from different nonlinearity levels (wave steepness), and measuring α and P as the power-law spectrum manifests itself in the simulation. This methodology allows us to confirm the WTT $I_\eta \sim P^{1/2}$ scaling over a broad range of P. For sufficiently large P, i.e., nonlinearity level, we find that $\alpha = \alpha_0 = -19/4$ is recovered with high accuracy, and the Kolmogorov constant is evaluated to be $C = 9.9$, with reasonable error, to be explained, compared to the theoretical value of $C_0 = 6.97$. As P decreases, i.e., lower nonlinearity level, deviations of α and C from there theoretical values are observed, and shown to be a direct result of finite box effect. The current results reinforce WTT as an effective model for stationary inertial-range capillary wave spectrum, and illustrate the limitation of the theory for the spectrum developed in a finite domain.

We further present a study regarding discrete capillary wave turbulence in the framework of the Kinetic Equation (KE). In cases of discrete turbulence in a finite domain where energy transfer is sustained by quasi-resonant interactions, the KE is not directly applicable, and further development requires a quantitative understanding of the mechanism of nonlinear broadening. This is obtained using data from the simulation of the primitive Euler equations. It is found that higher nonlinearity level is associated with larger nonlinear broadening, which reaches an upper limit with the increase of nonlinearity level in the weak turbulence regime. Guided by these findings, we develop a quasi-resonant kinetic equation (QRKE) for discrete capillary wave turbulence, by introducing a non-dimensional parameter κ governing the ratio of nonlinear broadening and wavenumber discreteness. In simulation of the QRKE, we find that the obtained values of α and C are functions of κ only. As $\kappa = \kappa_0 = 0.02$, the theoretical values of α_0 and C_0 are simultaneously recovered, indicating an upper limit of energy flux by quasi-resonance approaching that of exact resonance in theoretically infinite domain. For $\kappa < \kappa_0$, the simulation results replicate those with insufficient nonlinearity level, namely the steepened spectral slope and reduced energy flux. As a justification of the established QRKE, the parameter κ is confirmed to be linearly correlated with the nonlinear broadening in Euler equations. A key difference between the two is, however, also revealed. It is shown that the nonlinear broadening obtained in the Euler equations is increasingly weakened as the wavenumber k increases. This effectively limits the energy transfer even for the highest nonlinearity that can be simulated in HOS, and provides an explanation of the deviation of obtained value of C from C_0 in the simulation of the Euler equations.

The last topic in the field of weak turbulence is on the decaying capillary wave turbulence. This can be considered as an extension of WTT, where the turbulence is allowed to evolve freely in the presence of physically broad-scale dissipation and finite box effect. Our simulation through the primitive Euler equations replicates many experimental observations, including the variation of spectral slope α, and decreasing of the cut-off wavenumber k_c with the decay. Based on our numerical data, we obtain a generalized equation which describes the free decay of a capillary wave spectrum under different dissipation magnitudes γ_0. Over the range of γ_0 that we consider, we further show that the inertial-range spectral slope depends only on the nonlinearity of the spectrum, irrespective of γ_0, i.e., γ_0 determines only the magnitude of the modal decay rate. The decay of spectral energy is shown to be consistent with the prediction from our generalized spectral equation. These results provide a substantial generalization to the theory of Falkovich *et al.* (1995), where the role of finite box effect and broad-scale dissipation to the actual physics is highlighted.

The last two chapters of this thesis are devoted to the simulation of long-short wave and wave-current interactions. For long-short wave interactions, we illustrate the ill-conditioning of the boundary perturbation method used in HOS to solve the boundary value problem (BVP) regarding the field potential ϕ. This is shown to result from the divergent terms proportional to the multiplication of the short-wave wavenumber and long-wave amplitude ($k_S a_L$), especially for simulation of a wave field with largely disparate wavelength ratio ($\gamma \equiv k_S/k_L \gg 1$). Although these terms are shown to cancel one another theoretically (for which we provide the first general proof), they amount to calculation of small number as difference of very large numbers in numerical simulation. This is demonstrated in detail in numerical analysis, along with a proposition of a criterion for the numerical ill-conditioning. We further propose a mapping scheme which effectively remedies this ill-conditioning, with the cost of increased computational complexity. The effectiveness of the developed approach is illustrated by solving a prescribed BVP relevant to long-short wave interactions, where it is shown that the performance in solving a wave field with $\gamma \gg 1$ is much improved compared with the boundary perturbation method.

For wave-current interactions, we develop the framework for simulation of the evolution of nonlinear waves superposed on a prescribed steady slowly-varying current. The formulation is obtained for both a rotational and irrotational current field. We derive the Hamiltonian formulation for the former, where we show that the total coupled wave-current energy is conserved. We demonstrate the simulation by studying the evolution of a wave field superposed on a realistic current field obtained from the MSEAS analysis. It is observed that waves passing a following current are stretched and suppressed, while waves passing an opposing current behave oppositely. The physical explanation for these phenomena are provided, in terms of the conservation of apparent frequency and wave action.

9.2 Future work

There are much remaining to be done in the field of wave turbulence. We list a few in the followings.

9.2.1 Quantitative criterion for the cut-off wavenumber

The mechanism for the formation of cut-off wavenumber k_c is discussed in Kolmakov *et al.* (2004), which is shown to be a result of balance between viscous dissipation and nonlinear energy transfer. Despite the qualitative description, the quantitative criterion is yet to be established, which is possibly derivable from the principle of balance. This should then be confirmed by our numerical simulation. It serves as the counterpart for Kolmogorov scale in the field of weak turbulence.

9.2.2 MMT spectrum

It is shown in Majda *et al.* (1997); Cai *et al.* (1999, 2001) that the Majda-McLaughlin-Tabak (MMT) spectrum can form in a one-dimensional model of wave turbulence with a prescribed dynamical equation. The MMT spectrum can be derived by replacing the closure model for high-order cumulant (counterpart of (2.57)) by a MMT closure (Majda *et al.*, 1997). It is shown that spectral bifurcation exists for the prescribed dynamical equation. In particular, for de-focusing nonlinearity with random forcing, MMT spectrum is obtained as the stationary solution. While for focusing nonlinearity, WTT spectrum forms in the stationary state, with MMT spectrum present as a transient state. In spite of these numerically observed behavior, the theory that leads to the bifurcation is not clear (It is proposed that the coherent structures in the wave field can be a cause of the MMT spectrum (Zakharov *et al.*, 2004)). In addition, the MMT spectrum has not been observed and discussed in any realistic wave field. It is worthwhile to study the presence of MMT spectrum for, say, capillary waves.

9.2.3 Gravity wave turbulence

The framework of gravity wave turbulence is established in Zakharov & Filonenko (1966), where it is shown that the gravity wave spectrum exhibits a stationary solution of $I_\eta \sim CP^{1/3}k^{-7/2}$ for the direct cascade. This solution, in terms of the $k^{-7/2}$ scaling, has been extensively studied both numerically (Onorato *et al.*, 2002; Dyachenko *et al.*, 2003; Pushkarev *et al.*, 2003) and experimentally (Falcon *et al.*, 2007; Denissenko *et al.*, 2007; Deike *et al.*, 2015). The Kolmogorov Constant C (as well as the $P^{1/3}$), however, is much less understood. Theoretical and experimental studies regarding the value of C are only recently conducted in Zakharov (2010) and Deike *et al.* (2015). While they do not reach consistency, it is desirable to re-formulate the theoretical derivation and perform numerical study on the problem. A preliminary study which includes the procedure on theoretical evaluation of C is presented in Appendix G.

9.2.4 WTT spectrum vs. Phillips spectrum

The WTT spectrum and Phillips spectrum (Phillips, 1985) are derived based on different physical assumptions. While the former is based on an inertial-range consideration free of external forcing, the latter considers a spectrum where the energy transfer from large scales are balanced by the energy dissipation due to wave breaking. As a result, the Phillips spectrum, with a wavenumber scaling of $I_\eta \sim k^{-4}$, behaves differently from the WTT spectrum. Detailed numerical studies on understanding the physical mechanisms of these spectra are still lacking. An exception is Korotkevich (2008), which, in the framework of primitive Euler equations, shows that the WTT spectrum can transform to Phillips spectrum as the wave steepness increases. Nevertheless, more convincing numerical evidences are still desirable, and this may ultimately require the simulation using the Navier-Stokes equations.

9.2.5 Wave turbulence in the strong turbulence regime

The studies in this thesis are confined to wave turbulence under weak turbulence regime. This allows perturbation analysis to be used in derivation and numerics, and serves as the key for the validity of WTT and HOS. As nonlinearity level further goes up, dynamics reaching the strong turbulence regime remains elusive. The weak nonlinearity assumption and random phasing assumption assumed in WTT can be violated, as coherent structures (non-Gaussian statistics, such as wave breaking, rogue wave, etc) emerge in the wave field. In theory, the spectrum under this regime remains unsolved (the Phillips spectrum can be a typically simplified model for gravity waves). In numerics, this requires the simulation of the Navier-Stokes equations. The elucidation of these dynamics is, however, particularly desirable as it improves the understanding of wave turbulence, and may further shed light on the clarification of the intermittency phenomenon in general flow turbulence.

9.2.6 Wave turbulence under the background of current/long wave

Understanding the capillary wave spectrum in the real ocean requires the study of wave turbulence superposed on the background of current or long waves. The addition of the background flow to this dynamical system introduces two elements of difficulty in analysis. (1) A current or long wave can effectively modulate the nonlinear wave interactions (e.g. Ölmez & Milgram, 1995*b*; Gerber, 1987). (2) The directionality of the background flow breaks the assumption of isotropy of the wave turbulence spectrum. Extending the theory requires incorporating both mechanisms in the derivation.

9.2.7 Spectrum of gravity-capillary waves

There is no general theory for the spectrum of gravity-capillary waves. Connaughton *et al.* (2003) suggest that two sub-regions respectively corresponding to gravity and capillary wave power-law solution exist in the spectrum, and the two sub-regions can connect for sufficiently large forcing. This is experimentally confirmed in Falcon *et al.* (2007), where it is shown that the spectral slope of the capillary region agrees with the theory, while the spectral slope of the gravity region only approaches theoretical result with the increase of the forcing. A numerical study with consideration of both gravity and surface tension is useful in elucidating the physics regarding the forcing, spectral slopes and the connection of the gravity and capillary sub-regions.

Finally, future work for long-short wave interaction and wave-current interaction is respectively discussed in sections 7.5 and 8.3.

Appendix A

Proof of (2.40)

We first express $< \widehat{\eta}(\mathbf{k})\widehat{\eta}^*(\mathbf{k}') >$ in its Fourier transforms:

$$\begin{aligned} < \widehat{\eta}(\mathbf{k})\widehat{\eta}^*(\mathbf{k}') > &= \frac{1}{4\pi^2} < \int_{-\infty}^{\infty} \eta(\mathbf{x}) exp(-i\mathbf{k}\cdot\mathbf{x}) d\mathbf{x} \int_{-\infty}^{\infty} \eta(\mathbf{x}') exp(i\mathbf{k}'\cdot\mathbf{x}') d\mathbf{x}' > \\ &= \frac{1}{4\pi^2} \iint_{-\infty}^{\infty} exp(-i\mathbf{k}\cdot\mathbf{x} + i\mathbf{k}'\cdot\mathbf{x}') < \eta(\mathbf{x})\eta(\mathbf{x}') > d\mathbf{x}d\mathbf{x}' \end{aligned} \tag{A.1}$$

Let

$$\mathbf{X} = \mathbf{x} - \mathbf{x}', \qquad \mathbf{x}_0 = \frac{\mathbf{x} + \mathbf{x}'}{2}. \tag{A.2}$$

Substituting (A.2) into (A.1), which involves

$$\begin{aligned} &\mathbf{x} = \frac{\mathbf{X} + 2\mathbf{x}_0}{2}, \qquad \mathbf{x}' = \frac{2\mathbf{x}_0 - \mathbf{X}}{2}, \\ &-i\mathbf{k}\cdot\mathbf{x} + i\mathbf{k}'\cdot\mathbf{x}' = -i(\mathbf{k}+\mathbf{k}')\cdot\frac{\mathbf{X}}{2} + i(\mathbf{k}'-\mathbf{k})\cdot\mathbf{x}_0, \\ &d\mathbf{x}d\mathbf{x}' = d\mathbf{x}_0 d\mathbf{X}, \end{aligned}$$

and assuming homogeneity, we obtain

$$\begin{aligned} < \widehat{\eta}(\mathbf{k})\widehat{\eta}^*(\mathbf{k}') >= &\frac{1}{4\pi^2} \int_{-\infty}^{\infty} exp[-i(\mathbf{k}-\mathbf{k}')\cdot\mathbf{x}_0] d\mathbf{x}_0 \\ &\cdot \int_{-\infty}^{\infty} exp[-i(\mathbf{k}+\mathbf{k}')\cdot\frac{\mathbf{X}}{2}] < \eta(\mathbf{x}+\mathbf{X})\eta(\mathbf{x}) > d\mathbf{X}. \end{aligned} \tag{A.3}$$

Invoking (2.4) and (2.36), we obtain

$$I_\eta(\mathbf{k}) = \int_{-\infty}^{\infty} exp(-i\mathbf{k}\cdot\mathbf{X}) < \eta(\mathbf{x}+\mathbf{X})\eta(\mathbf{x}) > d\mathbf{X}. \tag{A.4}$$

Under the assumption of ergodicity, equation (A.4) can be re-written as

$$I_\eta(\mathbf{k}) = \int_{-\infty}^{\infty} exp(-i\mathbf{k}\cdot\mathbf{X})\overline{\eta(\mathbf{x}+\mathbf{X})\eta(\mathbf{x})}d\mathbf{X}. \tag{A.5}$$

Comparing (A.5) and (2.39), we obtain (2.40).

Appendix B

Solution of (2.56) following Janssen (2003)

The equation (2.56), as a first-order Ordinary Differential Equation with respect to t, can be solved directly:

$$J_{k12} = J^0 e^{i\Omega_{k12}t} - i\int_0^t A_{k12}(\tau)e^{-i\Omega_{k12}(\tau - t)}d\tau. \tag{B.1}$$

where J^0 depends on the initial solution at $t = 0$. Under the assumptions of long-term evolution ($t \to \infty$) and slow spectral evolution ($A \approx$ constant), equation (B.1) can be reduced to

$$J_{k12} = A_{k12}\frac{1 - e^{i\Omega_{k12}t}}{\Omega_{k12}}. \tag{B.2}$$

Equation (B.2) is then substituted into (2.56), which yields

$$\begin{aligned}\frac{\partial n_{\mathbf{k}}}{\partial t} =& -2\iint_{-\infty}^{\infty}\Big[A_{k12}V_{k12}R_i(\Omega_{k12},t)\delta_{\mathbf{k}-\mathbf{k}_1-\mathbf{k}_2} - A_{1k2}V_{1k2}R_i(\Omega_{1k2},t)\delta_{\mathbf{k}_1-\mathbf{k}-\mathbf{k}_2} \\ & - A_{2k1}V_{2k1}R_i(\Omega_{2k1},t)\delta_{\mathbf{k}_2-\mathbf{k}-\mathbf{k}_1}\Big]d\mathbf{k}_1 d\mathbf{k}_2.\end{aligned} \tag{B.3}$$

where

$$R_i(\Omega,t) = \frac{sin(\Omega t)}{\Omega}. \tag{B.4}$$

For $t \to \infty$,

$$\lim_{t\to\infty} R_i(\Omega, t) = \pi\delta(\Omega), \tag{B.5}$$

and (B.3) reduces to (2.60).

Appendix C

Determination of linear solution of $\widehat{\eta}$ and $\widehat{\phi}^s$ from a capillary wave spectrum $\widetilde{I}_\eta(\omega, \theta)$

We consider a general capillary wave spectrum $\widetilde{I}_\eta(\omega, \theta)$, say, in the JONSWAP form

$$\widetilde{I} = \frac{\alpha g^2}{\omega^5} exp\big[- \frac{5}{4}(\frac{\omega_p}{\omega})^4\big]\gamma^{exp\left[-\frac{(\omega-\omega_p^2)}{2\sigma^2\omega_p^2}\right]}\frac{2}{\pi}cos^2\theta, \quad -\frac{\pi}{2} \leq \theta < \frac{\pi}{2} \tag{C.1}$$

where θ is the spreading angle. For isotropic spectrum, the factor $cos^2\theta$ can be set to be a constant.

We first convert the spectrum from frequency-angle domain to wavenumber domain. Using the relation

$$(k_x, k_y) = \omega^{2/3}(cos\theta, sin\theta), \tag{C.2}$$

we obtain

$$dk_x dk_y = \begin{bmatrix} \frac{\partial k_x}{\partial \omega} & \frac{\partial k_x}{\partial \theta} \\ \frac{\partial k_y}{\partial \omega} & \frac{\partial k_y}{\partial \theta} \end{bmatrix} d\omega d\theta = \begin{bmatrix} \frac{2}{3}\omega^{-1/3}cos\theta & -\omega^{2/3}sin\theta \\ \frac{2}{3}\omega^{-1/3}sin\theta & \omega^{2/3}cos\theta \end{bmatrix} d\omega d\theta = \frac{2}{3}\omega^{1/3}d\omega d\theta. \tag{C.3}$$

Then, according to $\widetilde{I}_\eta(\omega,\theta)d\omega d\theta = \widetilde{I}_\eta(k_x,k_y)dk_x dk_y$, we have

$$\widetilde{I}_\eta(k_x,k_y) = \frac{3}{2}\omega^{-1/3}\widetilde{I}_\eta(\omega,\theta) \tag{C.4}$$

Invoking the definition of wave spectrum $\widehat{\eta}(k_x,k_y)^2/2 = \widetilde{I}_\eta(k_x,k_y)\Delta k_x \Delta k_y$, we obtain

$$\widehat{\eta}(k_x,k_y) = \sqrt{3\omega^{-1/3}\widetilde{I}_\eta(k_x,k_y)\Delta k_x \Delta k_y}. \tag{C.5}$$

Equation C.5 is applied to all wavenumbers k_x, k_y in the computational domain, with the phases obtained from a uniform random distribution in $[0, 2\pi)$. With $\widehat{\eta}(k_x,k_y)$ specified for each wave mode, the corresponding surface potential $\widehat{\phi}^s$ can be obtained from the linear solution:

$$\widehat{\phi}^s(k_x,k_y) = -\frac{i\omega}{k}\widehat{\eta}(k_x,k_y). \tag{C.6}$$

Appendix D

Scale invariance of the quasi-resonant kinetic equation (QRKE)

While the continuous kinetic equation (KE) is shown to be scale-invariant under power-law form solutions (Pushkarev & Zakharov, 2000), it is not clear if the quasi-resonant KE (QRKE) remains this property. For this purpose of investigation, we re-write the QRKE (only the first term is maintained for illustration), by eliminating the delta function on wavenumber:

$$\begin{aligned}\frac{\partial n_{\mathbf{k}}}{\partial t} &\sim \int_{\mathbf{k}_1} \delta_g(\Omega \equiv \omega_k - \omega_1 - \omega_{k-1}) F(\mathbf{k}, \mathbf{k}_1, \mathbf{k}-\mathbf{k}_1, n_{\mathbf{k}}) d\mathbf{k}_1 \\ &\sim \sum_{\mathbf{k}_1} \frac{\beta}{\pi} \frac{1}{\beta^2 + \Omega^2} F(\mathbf{k}, \mathbf{k}_1, \mathbf{k}-\mathbf{k}_1, n_{\mathbf{k}}) \Delta\mathbf{k}_1,\end{aligned} \tag{D.1}$$

where $\beta = \kappa \Delta k k^{1/2}$. Defining $\Omega = \hat{\Omega} \Delta k k^{1/2}$, we obtain

$$\frac{\partial n_{\mathbf{k}}}{\partial t} \sim \sum_{\mathbf{k}_1} \frac{\kappa}{\pi} \frac{1}{\kappa^2 + \hat{\Omega}^2} F(\mathbf{k}, \mathbf{k}_1, \mathbf{k}-\mathbf{k}_1, n_{\mathbf{k}}) k^{-1/2} \Delta k^{-1} \Delta\mathbf{k}_1. \tag{D.2}$$

It has been shown that the function $F(\mathbf{k}, \mathbf{k}_1, \mathbf{k}-\mathbf{k}_1, n_{\mathbf{k}})$ is homogeneous under isotropic power-law solutions of $n_{\mathbf{k}}$. Therefore, the key for determining whether (D.2) is scale-invariant is the parameter $\hat{\Omega}$. With sufficient number of the grid in summation, it is only relevant to consider the Probability Distribution Function (PDF) of $\hat{\Omega}$

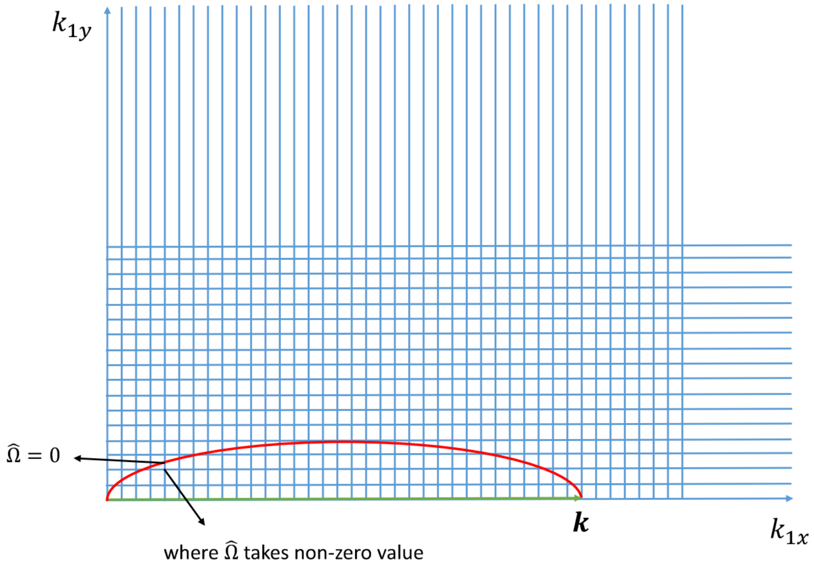

Figure D-1: resonance curve $\hat{\Omega}=0$ in the grid for a particular $\mathbf{k}$.

adjacent to the resonance curve (see the sketch of figure D-1), which dominates (D.2). We shall numerically show that $\hat{\Omega}$ is similarly distributed for different $\mathbf{k}$, and thus (D.2) is scale-invariant upon summation of sufficient grid points.

For this purpose, we set $k_{max}=32$ and $\Delta k=0.05$ (we use relatively smaller Δk to calculate the PDF of Ω more accurately). We plot the PDF (histogram) of $\hat{\Omega}$ (for the grid adjacent to $\hat{\Omega}=0$) in figure D-2 for respectively k =10, 15, 20, 25 and 30. It can be seen that they resemble one another. This means that a single value of κ works for any k, i.e., the whole spectrum. It also means that the PDF is independent of the grid size, because by scaling, doubling the grid number for $k=5$ is equivalent to evaluating the PDF for $k=10$ on the same grid. This explains the scale invariance of the QRKE on power-law spectrum, and the independence of the solution to the grid size.

We further verify the (continuous) theoretical scaling of $\partial n/\partial t \sim k^{-7/2}$ using (D.2) with $\kappa=\kappa_0$, as this is the key for the theoretical power-law spectrum to be realized for a range of k. We plot the value of $\partial n/\partial t$ obtained from (D.2) with the theoretical scaling in figure D-3. Indeed, the $k^{-7/2}$ is realized, which justifies the validity for

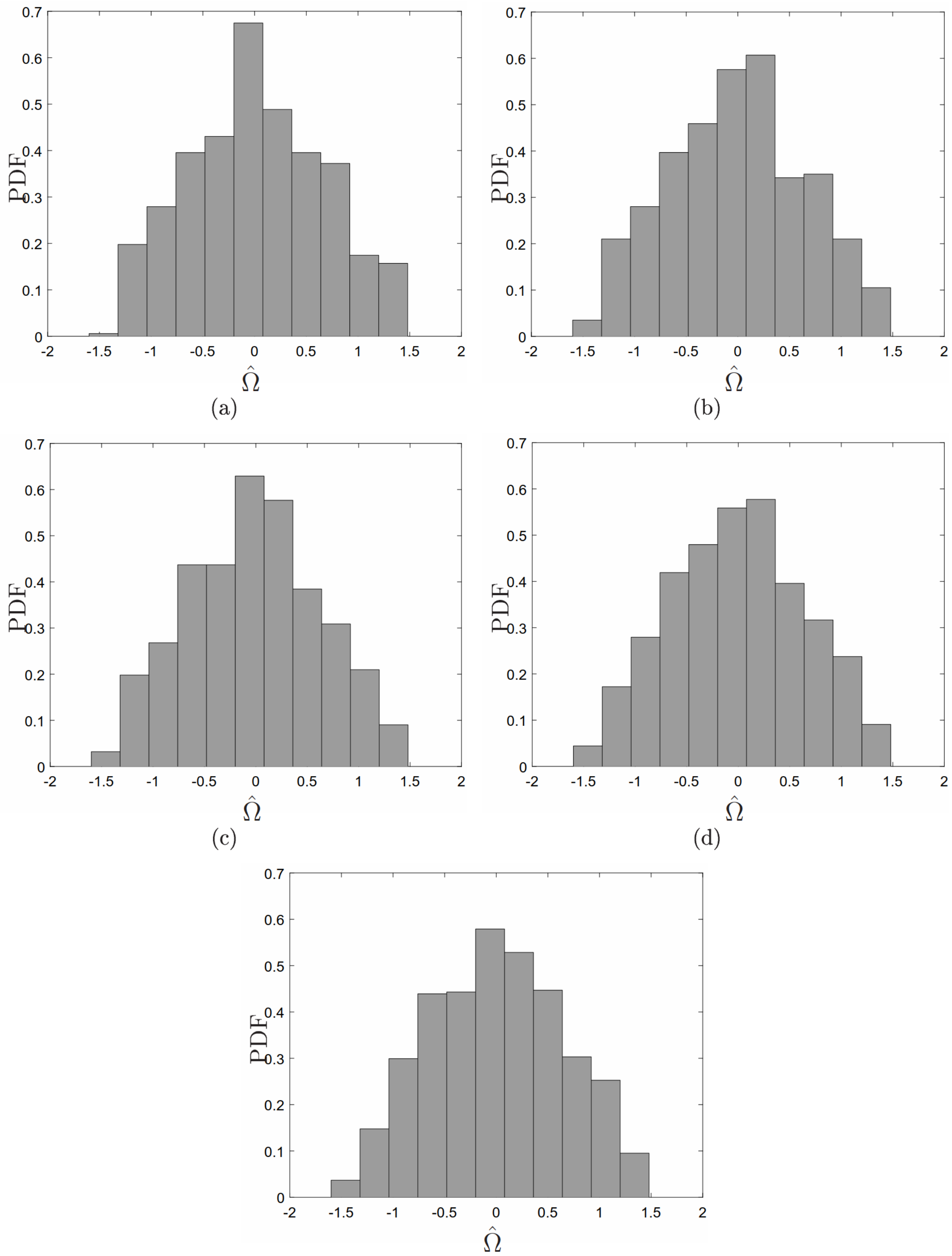

(a) (b) (c) (d) (e)

Figure D-2: PDF (histogram) of $\hat{\Omega}$ (for the grid adjacent to $\hat{\Omega} = 0$) for respectively $k =$ (a) 10, (b) 15, (c) 20, (d) 25 and (e) 30.

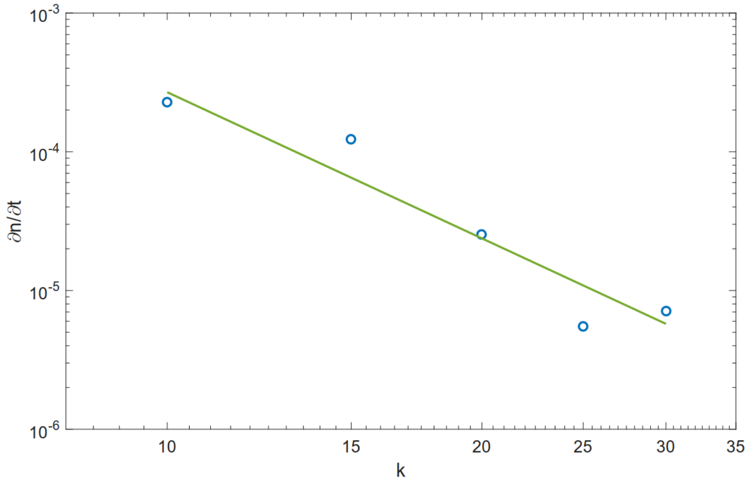

Figure D-3: Value of $\partial n/\partial t$ obtained from (D.2) ($\circ$) with the theoretical scaling of $\partial n/\partial t \sim k^{-7/2}$ (——).

formation of the power-law spectrum using the QRKE.

We finally mention that the fluctuations in figure D-3 are due to two sources: (1) The similarity of PDF of $\hat{\Omega}$ is only approximate, as we have finite number of points for all k. (2) The fact that $\partial n/\partial t \sim \int F(\mathbf{k}_1)\delta_g(\hat{\Omega})d\mathbf{k}_1$ disturbs the PDF of $\hat{\Omega}$. Rigourously, we should look at the PDF of $F(\mathbf{k}_1)\delta_g(\hat{\Omega})$. The factor $F(\mathbf{k}_1)$ modifies the similarity of PDF of $\delta_g(\hat{\Omega})$ at each k, resulting in fluctuations of the final scaling. These issues can potentially cause the fluctuation of the power-law spectrum, and requires further investigation.

Appendix E

Derivation of governing equations of waves superposed on a general (rotational) current field

In this appendix, we derive the governing equations, in Zakharov form, of gravity waves superposed on a general (rotational) current field. The derivation is in essence similar as that in Nwogu (2009), but obtained from a different path.

We consider the decomposition of the total velocity field:

$$\mathbf{V}_{TOT}(x,z,t) = \nabla\phi(x,z,t) + (U,W)(x,z), \tag{E.1}$$

Assumptions are placed on the current field $(U,W)(x,z)$:

1. $\partial U/\partial x + \partial W/\partial z = 0$, i.e., the flow is incompressible.
2. Analytical continuation is valid near the surface, i.e., quantity on the wave surface can be obtained by Taylor expansion.
3. The horizontal length scale of current is much larger than that of the wave, i.e., $L_c \gg L_w$

Instead of assumption 4 in Chapter 8, we allow general rotational flow motion in $(U,W)(x,z)$.

The kinematic boundary condition can be obtained similar as that in Chapter 8:

$$\frac{\partial \eta}{\partial t} + \frac{\partial \eta}{\partial x}\left(\frac{\partial \phi}{\partial x}|^s + U|^s\right) - W|^s - \frac{\partial \phi}{\partial z}|^s = 0. \tag{E.2}$$

where $|^s \equiv |_{z=\eta}$ denotes the evaluation of the preceding term on the free surface.

For the dynamic boundary condition, we cannot use the unsteady Bernoulli's equation as in Chapter 8, as the flow is rotational. Instead, we need to start from the Euler's equation, evaluated on the free surface:

$$\frac{\partial(\nabla\phi)}{\partial t}|^s = -\overline{\nabla\left[\frac{1}{2}(U + \frac{\partial \phi}{\partial x})^2 + \frac{1}{2}(W + \frac{\partial \phi}{\partial z})^2\right]}^s - \nabla(z) - \overline{\nabla(\frac{p}{\rho})}^s + \overline{\mathbf{V}_{TOT} \times \boldsymbol{\omega}}^s, \tag{E.3}$$

where $\overline{F}^s$ denotes a formulation F evaluated on the surface. This is used wherever necessary to avoid the confusion that can be caused by $|^s$. In (E.3), $\nabla \equiv (\partial/\partial x, \partial/\partial z)$, and

$$\boldsymbol{\omega} = \nabla \times \mathbf{V}_{TOT}, \tag{E.4}$$

is the vorticity.

Multiplying (E.3) by the unit tangential vector on free surface

$$\mathbf{l} \equiv (l_x, l_y) = \left(\frac{1}{\sqrt{1+\eta_x^2}}, \frac{\eta_x}{\sqrt{1+\eta_x^2}}\right), \tag{E.5}$$

we obtain

$$\frac{\partial(\nabla\phi \cdot \mathbf{l})}{\partial t}|^s - \overline{\nabla\phi}^s \cdot \frac{\partial \mathbf{l}}{\partial t} = -\overline{\nabla\left[\frac{1}{2}(U + \frac{\partial \phi}{\partial x})^2 + \frac{1}{2}(W + \frac{\partial \phi}{\partial z})^2\right]}^s \cdot \mathbf{l} - l_z + \overline{\mathbf{V}_{TOT} \times \boldsymbol{\omega}}^s \cdot \mathbf{l}, \tag{E.6}$$

We now seek to express (E.2) and (E.6) in surface variables. The connection of field and surface variables can be established via

$$\phi^s(x,t) = \phi(x, \eta(x,t), t) = \phi(x,z,t)|_{z=\eta}, \tag{E.7}$$

and

$$\phi_z|^s(x,t) = \phi_z(x, \eta(x,t), t) = \phi_z(x,z,t)|_{z=\eta}. \tag{E.8}$$

Other necessary transformations are derived as follows:

$$\phi_x^s = \phi_x|^s + \phi_z|^s\eta_x \Rightarrow \phi_x|^s = \phi_x^s - \phi_z|^s\eta_x; \tag{E.9}$$

$$\phi_z|_x^s = \phi_{zx}|^s + \phi_{zz}|^s\eta_x \Rightarrow \phi_{zx}|^s = \phi_z|_x^s - \phi_{zz}|^s\eta_x; \tag{E.10}$$

$$\begin{aligned} \phi_{xx}^s &= \phi_{xx}|^s + \phi_{xz}|^s\eta_x + \phi_z|_x^s\eta_x + \phi_z|^s\eta_{xx} \\ \Rightarrow \phi_{xx}|^s &= \phi_{xx}^s - 2\eta_x\phi_z|_x^s + \eta_x^2\phi_{zz}|^s - \eta_{xx}\phi_z|^s; \end{aligned} \tag{E.11}$$

$$\begin{aligned} \frac{\partial\overline{(\nabla\phi\cdot\mathbf{1})}^s}{\partial t} &= \frac{\partial(\nabla\phi\cdot\mathbf{1})}{\partial t}|^s + \eta_t\overline{\frac{\partial}{\partial z}(\nabla\phi\cdot\mathbf{1})}^s \\ &= \frac{\partial(\nabla\phi\cdot\mathbf{1})}{\partial t}|^s + \eta_t(\phi_{xz}|^s l_x + \phi_{zz}|^s l_z) \\ &= \frac{\partial(\nabla\phi\cdot\mathbf{1})}{\partial t}|^s + \eta_t l_x\phi_z|_x^s; \end{aligned} \tag{E.12}$$

$$\overline{\nabla\phi\cdot\mathbf{1}}^s = \phi_x|^s l_x + \phi_z|^s l_z = l_x\phi_x^s; \tag{E.13}$$

(E.12),(E.13) ⇒

$$\frac{\partial(\nabla\phi\cdot\mathbf{1})}{\partial t}|^s = \frac{\partial(\phi_x^s l_x)}{\partial t} - \eta_t l_x\phi_z|_x^s. \tag{E.14}$$

Substituting (E.9), (E.10), (E.11) and (E.14) to (E.2) and (E.6), we obtain

$$\eta_t = -U^s\eta_x - \phi_x^s\eta_x + \eta_x^2\phi_z|^s + \phi_z|^s + W^s, \tag{E.15}$$

and

$$\frac{\partial(\phi_x^s l_x)}{\partial t} = \eta_t l_x\phi_z|_x^s + \overline{\nabla\phi}^s\cdot\frac{\partial\mathbf{l}}{\partial t} - \overline{\nabla\Big[\frac{1}{2}(U+\phi_x)^2 + \frac{1}{2}(W+\phi_z)^2\Big]}^s\cdot\mathbf{1} - l_z + \overline{\mathbf{V}_{TOT}\times\boldsymbol{\omega}}^s\cdot\mathbf{1}. \tag{E.16}$$

Now let's transform (E.16) term by term:

$$\begin{aligned} \eta_t l_x\phi_z|_x^s &= l_x\phi_z|_x^s(-U^s\eta_x - \phi_x^s\eta_x + \eta_x^2\phi_z|^s + \phi_z|^s + W^s) \\ &= l_x(-U^s\eta_x\phi_z|_x^s - \phi_z|_x^s\phi_x^s\eta_x + \eta_x^2\phi_z|^s\phi_z|_x^s + \phi_z|^s\phi_z|_x^s + W^s\phi_z|_x^s); \end{aligned} \tag{E.17}$$

$$
\begin{aligned}
&\overline{\nabla\phi}^{s}\cdot\frac{\partial \mathbf{l}}{\partial t}=\phi_x|^s l_{xt}+\phi_z|^s l_{zt}\\
=&-l_x\phi_x^s\eta_x\eta_{xt}(1+\eta_x^2)^{-1}+l_x\big(-U_x|^s\eta_x\phi_z|^s+\phi_z|^sU_z|^s\eta_x^2-U^s\eta_{xx}\phi_z|^s-\phi_{xx}^s\eta_x\phi_z|^s\\
&-\phi_z|^s\phi_x^s\eta_{xx}+2\eta_x\eta_{xx}\phi_z|^s\phi_z|^s+\eta_x^2\phi_z|_x^s\phi_z|^s+\phi_z|^s\phi_z|_x^s+W_x|^s\phi_z^s+W_z|^s\eta_x\phi_z|^s\big);
\end{aligned}
\tag{E.18}
$$

$$
\begin{aligned}
&-\overline{\nabla\Big[\frac{1}{2}(U+\phi_x)^2+\frac{1}{2}(W+\phi_z)^2\Big]}^{s}\cdot\mathbf{1}\\
=&l_x\frac{\partial}{\partial x}\Big[\frac{1}{2}(U^s+\phi_x^s-\phi_z|^s\eta_x)^2+\frac{1}{2}(W^s+\phi_z|^s)^2\Big]\\
=&l_x\big(U^sU_x|^s+U^sU_z|^s\eta_x+U^s\phi_{xx}^s-U^s\eta_{xx}\phi_z|^s-U^s\eta_x\phi_z|_x^s+U_x|^s\phi_x^s+U_z|^s\eta_x\phi_x^s\\
&+\phi_x^s\phi_{xx}^s-\eta_{xx}\phi_z|^s\phi_x^s-\eta_x\phi_x^s\phi_z|_x^s-U_x|^s\phi_z|^s\eta_x-U_z|^s\eta_x^2\phi_z|^s-\phi_z|^s\eta_x\phi_{xx}^s\\
&+\eta_x\eta_{xx}\phi_z|^s\phi_z|^s+\eta_x^2\phi_z|^s\phi_z|_x^s+W^sW_x|^s+W^sW_z|^s\eta_x+W^s\phi_z|_x^s\\
&+\phi_z|^sW_x|^s+\phi_z|^sW_z|^s\eta_x+\phi_z|^s\phi_z|_x^s\big);
\end{aligned}
\tag{E.19}
$$

$$
\begin{aligned}
&\overline{\mathbf{V}_{TOT}\times\boldsymbol{\omega}}^{s}\cdot\mathbf{1}=\overline{(U+\phi_x,W+\phi_z,0)\times(0,0,W_x-U_z)}^{s}\cdot\mathbf{1}\\
=&\Big[\overline{(W+\phi_z)(W_x-U_z)}^{s},-\overline{(U+\phi_x)(W_x-U_z)}^{s}\Big]\cdot\mathbf{1}\\
=&l_x(W^sW_x|^s+\eta_xU^sU_z|^s+\eta_xU_z^s\phi_x^s-W^sU_z|^s+W_x|^s\phi_z|^s-U_z|^s\phi_z|^s\\
&-\eta_xU^sW_x|^s-\eta_xW_x|^s\phi_x^s+\eta_x^2W_x|^s\phi_z|^s-\eta_x^2U_z|^s\phi_z|^s);
\end{aligned}
\tag{E.20}
$$

$$
\frac{\partial}{\partial t}(\phi_x^sl_x)=l_x\frac{\partial\phi_x^s}{\partial t}-\phi_x^s\eta_x\eta_{xt}l_x(1+\eta_x^2)^{-1}.
\tag{E.21}
$$

Substituting (E.17), (E.18), (E.19), (E.20) and (E.21) to (E.16), we obtain

$$
\begin{aligned}
\frac{\partial\phi_x^s}{\partial t}=&-\eta_x+\eta_x\eta_{xx}\phi_z|^s\phi_z|^s+(1+\eta_x^2)\phi_z|^s(\phi_z|_x^s+W_x|^s-U_z|^s)\\
&-(U^s+\phi_x^s)(U_x|^s+\phi_{xx}^s+\eta_xW_x|^s)-W^s(U_z|^s-U_x|^s\eta_x).
\end{aligned}
\tag{E.22}
$$

This can be shown equivalent to

$$\begin{aligned}\frac{\partial \phi_x^s}{\partial t} =& \frac{\partial}{\partial x}\big[-\eta - \frac{1}{2}(U^sU^s + W^sW^s) - U^s\phi_x^s - \frac{1}{2}\phi_x^s\phi_x^s + \frac{1}{2}(1+\eta_x^2)\phi_z|^s\phi_z|^s\big] \\ &+ (1+\eta_x^2)\phi_z|^s(W_x|^s - U_z|^s) - U^s\eta_x(W_x|^s - U_z|^s) - \eta_x\phi_x^s(W_x|^s - U_z|^s) \\ &+ W^s(W_x|^s - U_z|^s).\end{aligned} \tag{E.23}$$

To summarize, we have the following governing equations, in Zackharov form:

$$\eta_t = -U^s\eta_x - \phi_x^s\eta_x + \eta_x^2\phi_z|^s + \phi_z|^s + W^s, \tag{E.24}$$

$$\begin{aligned}\frac{\partial \phi_x^s}{\partial t} =& \frac{\partial}{\partial x}\big[-\eta - \frac{1}{2}(U^sU^s + W^sW^s) - U^s\phi_x^s - \frac{1}{2}\phi_x^s\phi_x^s + \frac{1}{2}(1+\eta_x^2)\phi_z|^s\phi_z|^s\big] \\ &+ \big[(1+\eta_x^2)\phi_z|^s - U^s\eta_x - \eta_x\phi_x^s + W^s\big]\omega^s,\end{aligned} \tag{E.25}$$

where

$$\omega^s = W_x|^s - U_z|^s. \tag{E.26}$$

The first part of (E.25) is the same as the x-derivative of (8.5), and the influence of vorticity on waves is reflected by terms involving ω^s. To proceed, we can expand U^s, W^s and ω^s by Taylor series based on $z = 0$. The procedure is similar as that in Chapter 8, and is not repeated here.

Appendix F

Algorithm for simulation of fully nonlinear wave-current interactions

In this appendix, we develop the framework for the simulation incorporating the fully nonlinear wave-current interactions. This is obtained by coupling the HOS solver for surface dynamics and a Navier-Stokes solver for underlying current field, and requires the decomposition of the total velocity field into a potential flow field and a rotational flow field. We consider a 3D flow field vertically from $z = -h$ to $z = \eta$, with horizontally periodic boundary condition, for the following formulation. Two cases are discussed: (i) A general approach with a unique decomposition of the total velocity field, which is similar as that in Dommermuth (1993); (ii) A modification of the decomposition in (i) which is particularly suitable for wave-current interaction where the length scale of wave is much smaller than that of the current.

F.1 Governing equations

We first present the governing equations of the problem.

In the limit of high Reynolds number, the flow field is governed by the (non-dimensionalized) Euler equation

$$\frac{\partial \mathbf{u}}{\partial t} + \mathbf{u} \cdot \nabla \mathbf{u} = -\nabla p - \frac{1}{Fr^2} \hat{z}, \tag{F.1}$$

where $\mathbf{u}$ is the total velocity, normalized by a characteristic velocity U_c. p is the total pressure normalized by ρU_c^2. $Fr = U_c/\sqrt{gL_c}$ is the Froude number with L_c being the characteristic length. $\hat{z} = (0, 0, 1)$ denotes that the term $1/Fr^2$ applies only on the vertical direction.

On the surface $z = \eta$, we apply the pressure boundary condition

$$p = P_a, \tag{F.2}$$

where P_a is the atmospheric pressure. On the bottom $z = -h$, we apply the slip boundary condition

$$\mathbf{u} \cdot \hat{z} = 0. \tag{F.3}$$

F.2 The general approach

F.2.1 Decomposition of the field equations

We start by applying the Helmholtz decomposition to the total velocity:

$$\mathbf{u} = \nabla\phi + \boldsymbol{\mathcal{U}}, \tag{F.4}$$

where $\phi(x, y, z, t)$ is a velocity potential which describes the irrotational flow and $\boldsymbol{\mathcal{U}}$ is a solenoidal field which describes the vortical flow such that

$$\nabla^2\phi = 0, \tag{F.5}$$

$$\nabla \cdot \boldsymbol{\mathcal{U}} = 0. \tag{F.6}$$

Note that $\boldsymbol{\mathcal{U}}$ may contain a portion of irrotational field depending on the boundary conditions, described in section F.2.2. This is a freedom of the current approach, use of which is also made when dealing with the particular wave-current interaction problem (see section F.3).

Depending on the Helmholtz decomposition of the velocity field, we decompose the pressure field accordingly:

$$p = P_R + P_I, \tag{F.7}$$

where P_R is the rotational pressure, and

$$P_I = -\frac{\partial \phi}{\partial t} - \frac{1}{2}\nabla\phi \cdot \nabla\phi - \frac{1}{Fr^2}z, \tag{F.8}$$

is the irrotational pressure.

Substituting (F.4) and (F.7) into (F.1) gives

$$\frac{\partial \boldsymbol{\mathcal{U}}}{\partial t} + ((\boldsymbol{\mathcal{U}} + \nabla\phi) \cdot \nabla)\boldsymbol{\mathcal{U}} + (\boldsymbol{\mathcal{U}} \cdot \nabla)\nabla\phi = -\nabla P_R. \tag{F.9}$$

Divergence of (F.9), with the substitution of (F.5) and (F.6), gives the governing equation for P_R, written in the form of a Poisson equation (for clarity, Einstein notation is used.)

$$\nabla^2 P_R = -\frac{\partial U_j}{\partial x_i}\frac{\partial U_i}{\partial x_j} - 2\frac{\partial U_j}{\partial x_i}\frac{\partial^2 \phi}{\partial x_j \partial x_i}. \tag{F.10}$$

Equation (F.10) is subject to, due to the divergence theorem, a solvability condition:

$$\int_S \frac{\partial P_R}{\partial n} = -\int_V \left(\frac{\partial U_j}{\partial x_i}\frac{\partial U_i}{\partial x_j} + 2\frac{\partial U_j}{\partial x_i}\frac{\partial^2 \phi}{\partial x_j \partial x_i}\right), \tag{F.11}$$

which places a restriction in specifying the boundary conditions. In (F.11), V is the volume of fluid, S is the surface bounding the volume, and $\mathbf{n}$ is the outward-pointing normal vector on the surface.

F.2.2 Boundary conditions

For the Helmholtz decomposition (F.4) to be unique, an additional boundary condition is required. An expedient choice that can be specified, for which the evolution equation of surface elevation is most simplified, is that the normal component of the rotational velocity is zero on the free surface:

$$\boldsymbol{\mathcal{U}} \cdot \mathbf{n} = \frac{-U\eta_x - V\eta_y + W}{(\eta_x^2 + \eta_y^2 + 1)^{1/2}} = 0. \tag{F.12}$$

We note that only one component of $\boldsymbol{\mathcal{U}}$ can be specified as boundary condition, otherwise the decomposition of an arbitrary flow field (F.4) results in two boundary conditions for ϕ on the free surface in solving (F.5). For example, $\boldsymbol{\mathcal{U}} = 0$ cannot be specified here. The choice of other forms of boundary condition for $\boldsymbol{\mathcal{U}}$ results in different evolution equation for η (cf. (F.13)). In particular, (F.12) means that the evolution of free surface is entirely determined by the irrotational velocity, specified by potential ϕ, as follows:

$$\frac{\partial \eta}{\partial t} + \frac{\partial \eta}{\partial x}\frac{\partial \phi}{\partial x} + \frac{\partial \eta}{\partial y}\frac{\partial \phi}{\partial y} - \frac{\partial \phi}{\partial z} = 0. \tag{F.13}$$

The evolution of potential ϕ can be obtained from (F.8), as

$$\frac{\partial \phi}{\partial t} + \frac{1}{2}\nabla\phi \cdot \nabla\phi + \frac{1}{Fr^2} z = P_R - P_a, \tag{F.14}$$

with P_a being the atmospheric pressure. Evaluation of (F.14) on the free surface $z = \eta$, and specifying $P_a = 0$, gives

$$\frac{\partial \phi}{\partial t} + \frac{1}{2}\nabla\phi \cdot \nabla\phi + \frac{1}{Fr^2}\eta = P_R. \tag{F.15}$$

We now write (F.13) and (F.15) in Zakharov form ($\phi^s(x, y, t) = \phi(x, y, \eta(x, y, t), t)$):

$$\eta_t + \nabla_{\mathbf{x}}\phi^s \cdot \nabla_{\mathbf{x}}\eta - (1 + \nabla_{\mathbf{x}}\eta \cdot \nabla_{\mathbf{x}}\eta)\phi_z = 0, \tag{F.16}$$

$$\phi^s_t + \frac{1}{Fr^2}\eta + \frac{1}{2}\nabla_{\mathbf{x}}\phi^s \cdot \nabla_{\mathbf{x}}\phi^s - \frac{1}{2}(1 + \nabla_{\mathbf{x}}\eta \cdot \nabla_{\mathbf{x}}\eta)\phi_z^2 = P_R, \tag{F.17}$$

where $\nabla_{\mathbf{x}} \equiv (\partial/\partial x, \partial/\partial y)$.

The Poisson equation (F.10) for rotational pressure requires a boundary condition on the free surface. This can be specified by evaluating the momentum equation (F.9) on the free surface and then multiplying $\mathbf{n}$, which gives

$$\frac{\partial P_R}{\partial n} = -\mathbf{n} \cdot \frac{\partial \boldsymbol{\mathcal{U}}}{\partial t} - \mathbf{n} \cdot \left((\boldsymbol{\mathcal{U}} + \nabla\phi) \cdot \nabla\right)\boldsymbol{\mathcal{U}} - \mathbf{n} \cdot (\boldsymbol{\mathcal{U}} \cdot \nabla)\nabla\phi. \tag{F.18}$$

The first term on the right hand side of (F.18) can be simplified as

$$\begin{aligned} -\mathbf{n}\cdot\frac{\partial\boldsymbol{\mathcal{U}}}{\partial t} &= -\frac{\partial(\mathbf{n}\cdot\boldsymbol{\mathcal{U}})}{\partial t}+\boldsymbol{\mathcal{U}}\cdot\frac{\partial\mathbf{n}}{\partial t} = -\frac{d(\mathbf{n}\cdot\boldsymbol{\mathcal{U}})}{dt}+\eta_t\frac{\partial(\mathbf{n}\cdot\boldsymbol{\mathcal{U}})}{\partial z}+\boldsymbol{\mathcal{U}}\cdot\frac{\partial\mathbf{n}}{\partial t} \\ &= \eta_t\mathbf{n}\cdot\frac{\partial\boldsymbol{\mathcal{U}}}{\partial z}+\boldsymbol{\mathcal{U}}\cdot\frac{\partial\mathbf{n}}{\partial t}, \end{aligned} \tag{F.19}$$

where we have applied (F.12) and d/dt is the total derivative following the free surface. Substituting (F.19) into (F.18) gives

$$\frac{\partial P_R}{\partial n} = \eta_t\mathbf{n}\cdot\frac{\partial\boldsymbol{\mathcal{U}}}{\partial z}+\boldsymbol{\mathcal{U}}\cdot\frac{\partial\mathbf{n}}{\partial t}-\mathbf{n}\cdot\big((\boldsymbol{\mathcal{U}}+\nabla\phi)\cdot\nabla\big)\boldsymbol{\mathcal{U}}-\mathbf{n}\cdot(\boldsymbol{\mathcal{U}}\cdot\nabla)\nabla\phi, \tag{F.20}$$

where

$$\frac{\partial\mathbf{n}}{\partial t} = \frac{(-\eta_{xt}\eta_y^2-\eta_{xt}+\eta_x\eta_y\eta_{yt},-\eta_{yt}\eta_x^2-\eta_{yt}+\eta_x\eta_y\eta_{xt},-\eta_x\eta_{xt}-\eta_y\eta_{yt})}{(\eta_x^2+\eta_y^2+1)^{3/2}}. \tag{F.21}$$

With η_t specified by (F.16), equation (F.20) defines a Neumann boundary condition for (F.10). We note that (F.20) also guarantees that (F.12) is satisfied as the velocity field is updated by (F.9), i.e., the role of (F.20) to (F.12) is the same as (F.10) to continuity.

Up to now we have not specified the bottom boundary condition. A convenient choice for current problem is the slip boundary condition for both the potential and rotational flow components. We can thus specify

$$\partial\phi/\partial z = 0, \tag{F.22}$$

and

$$\boldsymbol{\mathcal{U}}\cdot\hat{z} = 0, \tag{F.23}$$

on $z=-h$.

The specification of boundary conditions for this problem is now complete.

F.2.3 Initial conditions

With (F.9), (F.16) and (F.17) being the evolution equation, we need to specify $\boldsymbol{\mathcal{U}}_0(x,y,z) \equiv \boldsymbol{\mathcal{U}}(x,y,z,t=0)$, $\eta_0(x,y) \equiv \eta(x,y,t=0)$ and $\phi_0^s(x,y) \equiv \phi^s(x,y,t=0)$ as initial conditions. We consider this specification in the case that we are given a general initial flow field with known $\eta_0(x,y)$ and $\mathbf{u}_0(x,y,z)$. Our task is thus to decompose $\mathbf{u}_0(x,y,z)$ into $\phi_0(x,y,z)$ and $\boldsymbol{\mathcal{U}}_0(x,y,z)$ that satisfies (F.12). This can be obtained by solving (F.5) subject to (F.22) on the bottom and

$$\frac{\partial \phi_0}{\partial n} = \mathbf{u}_0(x,y,z) \cdot \mathbf{n}, \tag{F.24}$$

on the free surface. $\boldsymbol{\mathcal{U}}_0(x,y,z)$ can then be obtained as the difference of $\nabla\phi_0(x,y,z)$ from $\mathbf{u}_0(x,y,z)$ and $\phi_0^s(x,y)$ specified as $\phi_0(x,y,\eta_0(x,y))$.

F.2.4 Solution procedure

Given $\boldsymbol{\mathcal{U}}_0(x,y,z)$, $\phi_0^s(x,y)$ and $\eta_0(x,y)$, the solution procedure is as follows:

1. Solve (F.5) with prescribed $\phi^s(x,y)$ and (F.22) at $z=-h$. The solution can be obtained by using the boundary perturbation method in HOS.

2. With ϕ_z determined, update η by (F.16).

3. Solve (F.10) subject to (F.20) at $z=\eta$ and a bottom pressure boundary condition obtainable from (F.23). The solution can be obtained by a mapping scheme which maps the free surface to a flat surface (see Dommermuth, 1993).

4. Update ϕ^s by (F.17).

5. Update $\boldsymbol{\mathcal{U}}$ by (F.9). We note that this should also be conducted in the mapped domain (with (F.9) transformed to the mapped domain), such that $\partial\boldsymbol{\mathcal{U}}/\partial t$ on the surface of the mapped domain corresponds to $d\boldsymbol{\mathcal{U}}/dt$ in the original physical domain.

6. Repeat steps 1$\sim$ 5.

F.3 Modification for wave-current interaction

We consider a simplification for a particular wave-current interaction problem, where the length scale of wave is much smaller than that of current. We further assume that the small-scale flow feature is completely governed by the potential-flow wave motion, and keeps irrotational in the time-dependent solution. As a result, the total velocity field can be decomposed into two components: the small-scale potential-flow wave motion and the large-scale rotational current motion, which are simulated respectively on a fine and coarse grid.

Suppose we are given an initial solution specified by separated current and wave fields. In the initial velocity decomposition, we need to make sure that all small-scale flow features are contained in $\nabla\phi_0$, with an arbitrary addition, as needed, of the large-scale irrotational flow field. The remaining large-scale flow features are specified by $\boldsymbol{\mathcal{U}}_0$. For this purpose, the boundary condition (F.12) has to be abandoned, as it results in a unique decomposition which may violate this required rule. Indeed, the most straightforward decomposition in this case is to assign directly the wave field to $\nabla\phi_0$ and the current field to $\boldsymbol{\mathcal{U}}_0$.

As (F.12) is abandoned, we need an alternative pressure boundary condition on $z = \eta$, instead of (F.20). This can be conveniently assigned as

$$P_R = 0. \tag{F.25}$$

In fact, arbitrary value of P_R can be specified, as (F.9) and (F.15) ensure that the addition $p = P_R + P_I = P_a$ at the free surface. This means that the addition $\boldsymbol{\mathcal{U}} + \nabla\phi$ keeps the same for different specifications of P_R, with a different partition between $\boldsymbol{\mathcal{U}}$ and $\nabla\phi$. Since P_R contains only large-scale flow features, the variation of P_R does not affect small-scale flow feature, i.e., variation of P_R only assigns different part of large-scale flow features to $\nabla\phi$, with $\boldsymbol{\mathcal{U}} + \nabla\phi$ unchanged. Furthermore, equation (F.13) should be modified to include the effect of $\boldsymbol{\mathcal{U}}$, which results in a different evolution equation for η, instead of (F.16),

$$\eta_t + \nabla_{\mathbf{x}}\phi^s \cdot \nabla_{\mathbf{x}}\eta - (1 + \nabla_{\mathbf{x}}\eta \cdot \nabla_{\mathbf{x}}\eta)\phi_z + U\eta_x + V\eta_y - W = 0. \tag{F.26}$$

With (F.26) being the evolution equation for η, the evolution equation for ϕ^s should be modified accordingly to maintain the Hamiltonian structure for wave motion. Physically, this guarantees that the energy of wave motion is conserved, though modulated by the current. To this end, we should start by modifying (F.8). Following the formulation in section 8.1.1, this is modified as

$$P_I = -\frac{\partial \phi}{\partial t} - \frac{1}{2}\nabla\phi \cdot \nabla\phi - \frac{1}{Fr^2}z - \frac{1}{2}\boldsymbol{\mathcal{U}} \cdot \boldsymbol{\mathcal{U}} - \boldsymbol{\mathcal{U}} \cdot \nabla\phi. \tag{F.27}$$

Note that the role of P_I within the computational domain is to ensure the continuity of the potential-flow field (F.5). The formulation (F.27) leaves the remaining part of (F.1), governing the rotational current field, as

$$\frac{\partial \boldsymbol{\mathcal{U}}}{\partial t} - \boldsymbol{\mathcal{U}} \times (\nabla \times \boldsymbol{\mathcal{U}}) + (\nabla\phi \cdot \nabla)\boldsymbol{\mathcal{U}} - \nabla(\boldsymbol{\mathcal{U}} \cdot \nabla)\phi = -\nabla P_R. \tag{F.28}$$

with the Poisson equation for the rotational pressure field, as

$$\nabla^2 P_R = -\frac{\partial U_j}{\partial x_i}\frac{\partial U_i}{\partial x_j} + \frac{1}{2}\nabla^2(\boldsymbol{\mathcal{U}} \cdot \boldsymbol{\mathcal{U}}) - \frac{\partial U_j}{\partial x_i}\frac{\partial^2 \phi}{\partial x_j \partial x_i} + \frac{\partial^2 U_j}{\partial x_i \partial x_i}\frac{\partial \phi}{\partial x_j} + \frac{\partial U_j}{\partial x_i}\frac{\partial \phi}{\partial x_i \partial x_j}. \tag{F.29}$$

Finally, the evolution equation for ϕ^s can be written as

$$\phi^s_t + \frac{1}{Fr^2}\eta + \frac{1}{2}\nabla_{\mathbf{x}}\phi^s \cdot \nabla_{\mathbf{x}}\phi^s - \frac{1}{2}(1 + \nabla_{\mathbf{x}}\eta \cdot \nabla_{\mathbf{x}}\eta)\phi_z^2 + (U, V) \cdot \nabla_{\mathbf{x}}\phi^s + \frac{1}{2}(\boldsymbol{\mathcal{U}} \cdot \boldsymbol{\mathcal{U}}) = P_R. \tag{F.30}$$

The specific solution procedure is similar as that described in section F.2.4, with (F.20), (F.16), (F.8), (F.9), (F.10) and (F.17) respectively replaced by (F.25), (F.26), (F.27), (F.28), (F.29) and (F.30).

Appendix G

Derivation of weak turbulence of gravity waves

We start from the kinetic equation for gravity waves (refer to Chapter 2 for variable definitions):

$$\begin{aligned}\frac{dn(\mathbf{k},t)}{dt} =& 4\pi \iiint d\mathbf{k}_1 d\mathbf{k}_2 d\mathbf{k}_3 |T_{k123}|^2 \delta(\mathbf{k}+\mathbf{k}_1-\mathbf{k}_2-\mathbf{k}_3) \\ & \delta(\omega+\omega_1-\omega_2-\omega_3)(n_2n_3n+n_2n_3n_1-nn_1n_2-nn_1n_3).\end{aligned} \tag{G.1}$$

This equation can be derived from the primitive Euler equations for gravity waves. This is first obtained in Hasselmann (1962). In spite of the general applicability of (G.1) for predicting wave field evolution, the specific form of the kernel T_{k123} remains controversial due to its inherent complexity. Relevant considerations include Crawford *et al.* (1980); Stiassnie & Shemer (1984); Krasitskii (1994); Zakharov (1999). We leave this as future work to determine the correct form of T_{k123}.

No matter which form we take, T_{k123} holds certain properties of homogeneity and symmetry:

$$T(\epsilon\mathbf{k},\epsilon\mathbf{k}_1,\epsilon\mathbf{k}_2,\epsilon\mathbf{k}_3)=\epsilon^3 T(\mathbf{k},\mathbf{k}_1,\mathbf{k}_2,\mathbf{k}_3), \tag{G.2}$$

$$T_{k123}=T_{1k23}=T_{k132}=T_{23k1}. \tag{G.3}$$

We change the integration in (G.1) into polar integration, and multiply both sides with $kdk/d\omega$ to keep the symmetry. This gives

$$\begin{aligned} k\frac{dk}{d\omega}\frac{dn(\mathbf{k},t)}{dt} =& 4\pi \int_{\theta_1}\int_{\theta_2}\int_{\theta_3}\int_{\omega_1}\int_{\omega_2}\int_{\omega_3} kk_1k_2k_3\frac{dk}{d\omega}\frac{dk_1}{d\omega_1}\frac{dk_2}{d\omega_2}\frac{dk_3}{d\omega_3}|T_{k123}|^2 \\ & \delta(\mathbf{k}+\mathbf{k}_1-\mathbf{k}_2-\mathbf{k}_3)\delta(\omega+\omega_1-\omega_2-\omega_3) \\ & (n_2n_3n+n_2n_3n_1-nn_1n_2-nn_1n_3)d\omega_3d\omega_2d\omega_1d\theta_3d\theta_2d\theta_1. \end{aligned} \tag{G.4}$$

We define $N(\omega) = 2\pi k \cdot (dk/d\omega) \cdot n(k)$, and transforms (G.4) to

$$\begin{aligned} \frac{dN(\omega)}{dt} =& I(\omega) = \iiint U(\omega,\omega_1,\omega_2,\omega_3)(n_2n_3n+n_2n_3n_1-nn_1n_2-nn_1n_3) \\ & \delta(\omega+\omega_1-\omega_2-\omega_3)d\omega_1d\omega_2d\omega_3, \end{aligned} \tag{G.5}$$

where

$$U(\omega,\omega_1,\omega_2,\omega_3) = 128\pi^2 \iiint |T_{k123}|^2\delta(\mathbf{k}+\mathbf{k}_1-\mathbf{k}_2-\mathbf{k}_3)(kk_1k_2k_3)^{3/2}d\theta_1d\theta_2d\theta_3. \tag{G.6}$$

The function U has the same symmetric property as T, and holds the homogeneous property:

$$U(\epsilon\mathbf{k},\epsilon\mathbf{k}_1,\epsilon\mathbf{k}_2,\epsilon\mathbf{k}_3) = \epsilon^{20}U(\mathbf{k},\mathbf{k}_1,\mathbf{k}_2,\mathbf{k}_3). \tag{G.7}$$

Equation G.5 can be re-arranged to eliminate the variable ω_1:

$$I(\omega) = \iint_\Omega d\omega_2d\omega_3U(\omega,\omega_2+\omega_3-\omega,\omega_2,\omega_3)n_2n_{2+3-0}n_0n_3(n_0^{-1}+n_{2+3-0}^{-1}-n_2^{-1}-n_3^{-1}) \tag{G.8}$$

where Ω is the plane for $\omega_2 > 0$ and $\omega_3 > 0$, but without the lower left corner $\omega_2+\omega_3-\omega \le 0$ (see figure G-1) to ensure that $\omega_1 = \omega_2+\omega_3-\omega > 0$.

We divide the region Ω into four sub-regions I, II, III and IV, as shown in figure G-1, and write $I(\omega) \equiv I_I(\omega)+I_{II}(\omega)+I_{III}(\omega)+I_{IV}(\omega)$.

For sub-region II($\omega_2 > \omega$, $\omega_3 > \omega$), we define the Zakharov transformation:

$$\omega_2 = \frac{\omega\omega_2'}{\omega_2'+\omega_3'-\omega}, \quad \omega_3 = \frac{\omega\omega_3'}{\omega_2'+\omega_3'-\omega}. \tag{G.9}$$

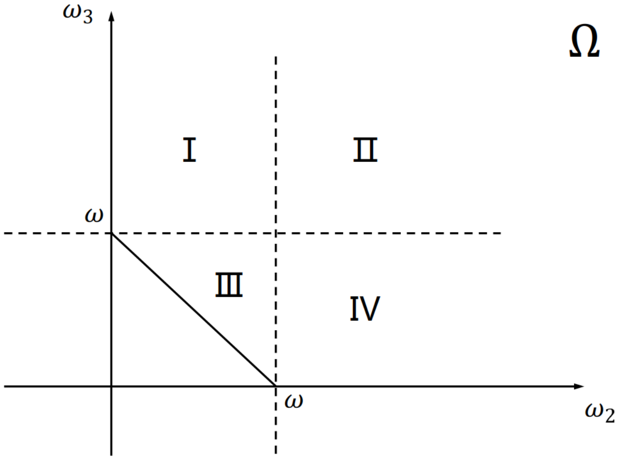

Figure G-1: The division of region Ω into four sub-regions I, II, III and IV.

Equation G.9 transforms the region $(\omega_2 > \omega,\ \omega_3 > \omega)$ to $(0 < \omega_2' < \omega,\ \omega - \omega_2' < \omega_3' < \omega)$. The transformation of (G.8) from ω_2 and ω_3 to ω_2' and ω_3' requires the change of integration variables:

$$\begin{aligned} d\omega_2 d\omega_3 = |J| d\omega_2' d\omega_3' &= |\begin{vmatrix} \frac{d\left[(\omega\omega_2')/(\omega_2'+\omega_3'-\omega)\right]}{d\omega_2'} & \frac{d\left[(\omega\omega_2')/(\omega_2'+\omega_3'-\omega)\right]}{d\omega_3'} \\ \frac{d\left[(\omega\omega_3')/(\omega_2'+\omega_3'-\omega)\right]}{d\omega_2'} & \frac{d\left[(\omega\omega_3')/(\omega_2'+\omega_3'-\omega)\right]}{d\omega_3'} \end{vmatrix}| d\omega_2' d\omega_3' \\ &= \frac{\omega^3}{(\omega_2'+\omega_3'-\omega)^3} d\omega_2' d\omega_3'. \end{aligned} \tag{G.10}$$

Substituting (G.9) and (G.10) into (G.8) (and $n(\omega) = A\omega^x$) for sub-region II, we obtain

$$\begin{aligned} I_{II}(\omega) = \int_0^\omega d\omega_2' \int_{\omega-\omega_2'}^{\omega} d\omega_3' \cdot U(\omega, \frac{\omega^2}{\omega_2'+\omega_3'-\omega}, \frac{\omega\omega_2'}{\omega_2'+\omega_3'-\omega}, \frac{\omega\omega_3'}{\omega_2'+\omega_3'-\omega}) A^3 \\ (\frac{\omega\omega_2'}{\omega_2'+\omega_3'-\omega})^{-x} (\frac{\omega^2}{\omega_2'+\omega_3'-\omega})^{-x} \omega^{-x} (\frac{\omega\omega_3'}{\omega_2'+\omega_3'-\omega})^{-x} \frac{\omega^3}{(\omega_2'+\omega_3'-\omega)^3} \\ \left[\omega^x + (\frac{\omega^2}{\omega_2'+\omega_3'-\omega})^x - (\frac{\omega\omega_2'}{\omega_2'+\omega_3'-\omega})^x - (\frac{\omega\omega_3'}{\omega_2'+\omega_3'-\omega})^x\right]. \end{aligned} \tag{G.11}$$

This can be simplified by using the homogeneity of U and the symmetric property

$U_{0123} = U_{1023}$, which gives (by dropping the primes)

$$I_{II}(\omega) = \int_0^{\omega} d\omega_2 \int_{\omega-\omega_2}^{\omega} d\omega_3 U(\omega, \omega_2+\omega_3-\omega, \omega_2, \omega_3) A^3 \big[\omega_2\omega(\omega_2+\omega_3-\omega)\omega_3\big]^{-x}$$
$$\big[\omega^x + (\omega_2+\omega_3-\omega)^x - \omega_2^x - \omega_3^x\big]\big(\frac{\omega}{\omega_2+\omega_3-\omega}\big)^{23-3x}. \tag{G.12}$$

For sub-region I, we apply the following Zakharov transformation

$$\omega_3 = \frac{\omega^2}{\omega_2'},\ \omega_2 = \frac{\omega(\omega_3'+\omega_2'-\omega)}{\omega_2'}, \tag{G.13}$$

which transforms the region $(0 < \omega_2 < \omega,\, \omega_3 > \omega)$ to $(0 < \omega_2' < \omega,\, \omega - \omega_2' < \omega_3' < \omega)$. The change of integration variables takes the form:

$$d\omega_2 d\omega_3 = |J| d\omega_2' d\omega_3' = |\begin{vmatrix} \frac{d\big[\omega(\omega_3'+\omega_2'-\omega)/\omega_2'\big]}{d\omega_2'} & \frac{d\big[\omega(\omega_3'+\omega_2'-\omega)/\omega_2'\big]}{d\omega_3'} \\ \frac{d(\omega^2/\omega_2')}{d\omega_2'} & \frac{d(\omega^2/\omega_2')}{d\omega_3'} \end{vmatrix}| d\omega_2' d\omega_3'$$
$$= \frac{\omega^3}{\omega_2'^3} d\omega_2' d\omega_3'. \tag{G.14}$$

Making use of the symmetric property $U_{0123} = U_{3201}$ and its homogeneous property, (G.8) for region I can be transformed to (by dropping the primes)

$$I_I(\omega) = \int_0^{\omega} d\omega_2 \int_{\omega-\omega_2}^{\omega} d\omega_3 \cdot U(\omega, \omega_2+\omega_3-\omega, \omega_2, \omega_3) A^3$$
$$\big[(\omega_2+\omega_3-\omega)\omega_3\omega_2\omega\big]^{-x}\big[\omega_2^x + \omega_3^x - (\omega_3+\omega_2-\omega)^x - \omega^x\big]\big(\frac{\omega}{\omega_2}\big)^{23-3x}. \tag{G.15}$$

A similar Zakharov transformation can be applied to I_{IV}. This leaves $I(\omega) \equiv I_I(\omega) + I_{II}(\omega) + I_{III}(\omega) + I_{IV}(\omega)$ as

$$I(\omega) = \int_0^{\omega} d\omega_2 \int_{\omega-\omega_2}^{\omega} d\omega_3 U(\omega, \omega_2+\omega_3-\omega, \omega_2, \omega_3) A^3$$
$$\big[\omega_2\omega(\omega_2+\omega_3-\omega)\omega_3\big]^{-x}\big[\omega^x + (\omega_2+\omega_3-\omega)^x - \omega_2^x - \omega_3^x\big] \tag{G.16}$$
$$\big[1 + \big(\frac{\omega}{\omega_2+\omega_3-\omega}\big)^{23-3x} - \big(\frac{\omega}{\omega_2}\big)^{23-3x} - \big(\frac{\omega}{\omega_3}\big)^{23-3x}\big].$$

There are four solutions of x to the equation $I(\omega; x) = 0$: $x = 0$, $x = 1$, $x = 23/3$, and $x = 8$. The former two solutions correspond to the thermodynamically equilibrium distribution of a flux-less spectrum; and the latter two correspond to the Kolmogorov-Zakharov spectrum. Specifically, $x = 23/3$ corresponds to an inverse wave action cascade (Zakharov *et al.*, 1992), and $x = 8$ corresponds to a direct energy cascade which we next analyze in detail.

The energy flux for the direct energy cascade can be determined from the spectral energy balance equation:

$$\frac{\partial \epsilon_\omega}{\partial t} + \frac{\partial P}{\partial \omega} = 0, \tag{G.17}$$

which, upon integration along ω, gives

$$P = -\frac{1}{4\pi^2}\int_0^\omega \omega \frac{\partial N(\omega)}{\partial t} d\omega = -\frac{1}{4\pi^2}\int_0^\omega \omega I(\omega; x) d\omega. \tag{G.18}$$

We now write $I(\omega; x)$ in normalized form:

$$\begin{aligned} I(\omega; x) =& \omega^{22-3x}\int_0^1 d\xi_2 \int_{1-\xi_2}^1 d\xi_3 U(1, \xi_2+\xi_3-1, \xi_2, \xi_3) A^3 \left[\xi_2\xi_3(\xi_2+\xi_3-1)\right]^{-x} \\ &\left[1 + (\xi_2+\xi_3-1)^x - \xi_2^x - \xi_3^x\right]\left[1 + (\xi_2+\xi_3-1)^{3x-23} - \xi_2^{3x-23} - \xi_3^{3x-23}\right], \end{aligned} \tag{G.19}$$

and (G.18) becomes

$$P = -\frac{1}{4\pi^2}\int_0^\omega \omega^{-y} J(y) d\omega = -\frac{1}{4\pi^2}\frac{\omega^{-y+1}}{-y+1} J(y), \tag{G.20}$$

where $y = 3x - 23$, and

$$\begin{aligned} J(y) = &\int_0^1 d\xi_2 \int_{1-\xi_2}^1 d\xi_3 U(1, \xi_2+\xi_3-1, \xi_2, \xi_3) A^3 \left[\xi_2\xi_3(\xi_2+\xi_3-1)\right]^{-\frac{23+y}{3}} \\ &\left[1 + (\xi_2+\xi_3-1)^{\frac{23+y}{3}} - \xi_2^{\frac{23+y}{3}} - \xi_3^{\frac{23+y}{3}}\right]\left[1 + (\xi_2+\xi_3-1)^y - \xi_2^y - \xi_3^y\right]. \end{aligned} \tag{G.21}$$

For $x = 8$, $y = 1$, L'Hospital's Rule can be used in evaluating (G.20), as

$$
\begin{aligned}
P = \frac{1}{4\pi^2} J'(y)|_{y=1} = &\frac{1}{4\pi^2} \int_0^1 d\xi_2 \int_{1-\xi_2}^1 d\xi_3 U(1, \xi_2 + \xi_3 - 1, \xi_2, \xi_3) A^3 \\
&\left[\xi_2\xi_3(\xi_2 + \xi_3 - 1)\right]^{-8} \left[1 + (\xi_2 + \xi_3 - 1)^8 - \xi_2^8 - \xi_3^8\right] \\
&\left[(\xi_2 + \xi_3 - 1) log(\xi_2 + \xi_3 - 1) - \xi_2 log\xi_2 - \xi_3 log\xi_3\right].
\end{aligned}
\tag{G.22}
$$

The integral in (G.22) can be evaluated numerically, where the only difficulty lies in the evaluation of $U(1, \xi_2 + \xi_3 - 1, \xi_2, \xi_3)$ (see (G.6)). We show that the integral involved in function U can be reduced to numerical summation of integrals in the form of (2.68), and is thus also subject to numerical evaluation.

In evaluation of $U(1, \xi_2 + \xi_3 - 1, \xi_2, \xi_3)$, we consider a Cartesian coordinate system with the abscissa coinciding with the $\mathbf{k}$ vector, and the angles θ_1, θ_2 and θ_3 are measured with respect to the chosen abscissa. We then define $\mathbf{k}' = \mathbf{k} + \mathbf{k}_1$, as a result $\mathbf{k}'$ depends only on θ_1 (and values of ξ_2 and ξ_3 which we consider as constants in a particular evaluation of U). Therefore, $U(1, \xi_2 + \xi_3 - 1, \xi_2, \xi_3)$ can be written as

$$
U(1, \xi_2 + \xi_3 - 1, \xi_2, \xi_3) = 128\pi^2 \sum_{\theta_1} \iint |T_{k123}|^2 \delta(\mathbf{k}'(\theta_1) - \mathbf{k}_2 - \mathbf{k}_3)(kk_1k_2k_3)^{3/2} d\theta_2 d\theta_3 \Delta\theta_1,
\tag{G.23}
$$

where k, k_1, k_2 and k_3 are connected with 1, $\xi_2 + \xi_3 - 1$, ξ_2 and ξ_3 by the dispersion relation of gravity waves. The double integral in (G.23) can be evaluated in a similar way as that of (2.68), with the difference that, in this case, vectors $\mathbf{k}'$, $\mathbf{k}_1$ and $\mathbf{k}_2$ are not necessarily always able to form a triangle.

The above procedure can be straightforwardly performed once the proper form of T_{k123} is determined. The derivation of gravity wave turbulence, including the value of Kolmogorov Constant C (after (G.22) is evaluated) can then be complete.

Bibliography

An, Nguyen Ngoc & Shibayama, Tomoya 1994 Wave-current interaction with mud bed. In *Proc. 24th Coastal Engineering Conference, ASCE*, pp. 2913–2927.

Boyd, John P 2001 *Chebyshev and Fourier spectral methods*. Courier Corporation.

Brazhnikov, M.Y., Kolmakov, GV, Levchenko, AA & Mezhov-Deglin, LP 2007 Observation of capillary turbulence on the water surface in a wide range of frequencies. *EPL (Europhysics Letters)* **58** (4), 510.

Bretherton, Francis P & Garrett, Christopher JR 1968 Wavetrains in inhomogeneous moving media. In *Proceedings of the Royal Society of London A: Mathematical, Physical and Engineering Sciences*, , vol. 302, pp. 529–554. The Royal Society.

Brueckner, Keith A & West, Bruce J 1988 Vindication of mode-coupled descriptions of multiple-scale water wave fields. *Journal of Fluid Mechanics* **196**, 585–592.

Cai, David, Majda, Andrew J, McLaughlin, David W & Tabak, Esteban G 1999 Spectral bifurcations in dispersive wave turbulence. *Proceedings of the National Academy of Sciences* **96** (25), 14216–14221.

Cai, David, Majda, Andrew J, McLaughlin, David W & Tabak, Esteban G 2001 Dispersive wave turbulence in one dimension. *Physica D: Nonlinear Phenomena* **152**, 551–572.

Canuto, Claudio, Hussaini, M Yousuff, Quarteroni, Alfio Maria, Thomas Jr, A *et al.* 2012 *Spectral methods in fluid dynamics*. Springer Science & Business Media.

Caulliez, Guillemette 2013 Dissipation regimes for short wind waves. *Journal of Geophysical Research: Oceans* .

Ceniceros, Hector D & Hou, Thomas Y 1999 Dynamic generation of capillary waves. *Physics of Fluids* **11**, 1042.

Chang, John H, Wagner, Richard N & Yuen, Henry C 1978 Measurement of high frequency capillary waves on steep gravity waves. *Journal of Fluid Mechanics* **86**, 401–413.

Connaughton, Colm, Nazarenko, Sergey & Newell, Alan C 2003 Dimensional analysis and weak turbulence. *Physica D: Nonlinear Phenomena* **184** (1), 86–97.

Connaughton, Colm, Nazarenko, Sergey & Pushkarev, Andrei 2001 Discreteness and quasiresonances in weak turbulence of capillary waves. *Physical Review E* **63** (4), 046306.

Constantin, Adrian 2015 The flow beneath a periodic travelling surface water wave. *Journal of Physics A: Mathematical and Theoretical* **48** (14), 143001.

Cox, C.S. 1958 Measurements of slopes of high-frequency wind waves. *J. Mar. Res.* **213**, 95–109.

Crapper, GD 1957 An exact solution for progressive capillary waves of arbitrary amplitude. *Journal of Fluid Mechanics* **2** (06), 532–540.

Crawford, Donald R, Saffman, Philip G & Yuen, Henry C 1980 Evolution of a random inhomogeneous field of nonlinear deep-water gravity waves. *Wave motion* **2** (1), 1–16.

Deike, Luc, Bacri, Jean-Claude & Falcon, Eric 2013 Nonlinear waves on the surface of a fluid covered by an elastic sheet. *Journal of Fluid Mechanics* **733**, 394–413.

Deike, Luc, Berhanu, Michael & Falcon, Eric 2012 Decay of capillary wave turbulence. *Physical Review E* **85** (6), 066311.

Deike, Luc, Berhanu, Michael & Falcon, Eric 2014*a* Energy flux measurement from the dissipated energy in capillary wave turbulence. *Physical Review E* **89** (6), 023003.

Deike, Luc, Daniel, Fuster, Berhanu, Michael & Falcon, Eric 2014*b* Direct numerical simulations of capillary wave turbulence. *Physical review letters* **112** (1), 234501.

Deike, L., Miquel, B., Gutierrez, P., Jamin, T., Semin, B., Berhanu, M., Falcon, E. & Bonnefoy, F. 2015 Role of the basin boundary conditions in gravity wave turbulence. *Journal of Fluid Mechanics* **781**, 196–225.

Denissenko, Petr, Lukaschuk, Sergei & Nazarenko, Sergey 2007 Gravity wave turbulence in a laboratory flume. *Physical review letters* **99** (1), 014501.

Dommermuth, DG 1994 Efficient simulation of short and long wave interactions with applications to capillary waves. *Journal of fluids engineering* **116** (1), 77–82.

Dommermuth, Douglas G 1993 The laminar interactions of a pair of vortex tubes with a free surface. *Journal of Fluid Mechanics* **246**, 91–115.

Dommermuth, Douglas G & Yue, Dick KP 1987 High-order spectral method for the study of nonlinear gravity waves. *Journal of Fluid Mechanics* **184** (1), 267–288.

Don, Wai Sun & Solomonoff, Alex 1995 Accuracy and speed in computing the chebyshev collocation derivative. *SIAM Journal on Scientific Computing* **16** (6), 1253–1268.

Dyachenko, Alexander I, Korotkevich, Alexander O & Zakharov, Vladimir E 2003 Weak turbulence of gravity waves. *Journal of Experimental and Theoretical Physics Letters* **77** (10), 546–550.

Dyachenko, S, Newell, AC, Pushkarev, A & Zakharov, VE 1992 Optical turbulence: weak turbulence, condensates and collapsing filaments in the nonlinear schrödinger equation. *Physica D: Nonlinear Phenomena* **57** (1), 96–160.

Dysthe, Kristian, Krogstad, Harald E & Müller, Peter 2008 Oceanic rogue waves. *Annu. Rev. Fluid Mech.* **40**, 287–310.

Falcon, E., Laroche, C. & Fauve, S. 2007 Observation of gravity-capillary wave turbulence. *Physical review letters* **98** (9), 94503.

Falkovich, GE, Shapiro, I Ya & Shtilman, L 1995 Decay turbulence of capillary waves. *EPL (Europhysics Letters)* **29** (1), 1.

Fedorov, Alexey V, Melville, W Kendall & Rozenberg, Anatol 1998 An experimental and numerical study of parasitic capillary waves. *Physics of Fluids* **10**, 1315.

Fermi, Enrico, Pasta, J & Ulam, S 1955 Studies of nonlinear problems. *Los Alamos Report LA-1940* **978**.

Filatov, SV, Parfenyev, VM, Vergeles, SS, Brazhnikov, M Yu, Levchenko, AA & Lebedev, VV 2016 Nonlinear generation of vorticity by surface waves. *Physical Review Letters* **116** (5), 054501.

Galtier, S, Nazarenko, SV, Newell, AC & Pouquet, A 2002 Anisotropic turbulence of shear-alfvén waves. *The Astrophysical Journal Letters* **564** (1), L49.

Gerber, Marius 1987 The benjamin-feir instability of a deep-water stokes wavepacket in the presence of a non-uniform medium. *Journal of Fluid Mechanics* **176**, 311–332.

Gramstad, O. & Trulsen, K. 2010 Can swell increase the number of freak waves in a wind sea? *Journal of Fluid Mechanics* **650** (1), 57–79.

Green, Theodore, Medwin, Herman & Paquin, James E 1972 Measurements of surface wave decay due to underwater turbulence. *Nature* **237** (77), 115–117.

Gutiérrez, Pablo & Aumaître, Sébastien 2016 Surface waves propagating on a turbulent flow. *Physics of Fluids (1994-present)* **28** (2), 025107.

Haldenwang, P, Labrosse, G, Abboudi, S & Deville, M 1984 Chebyshev 3-d spectral and 2-d pseudospectral solvers for the helmholtz equation. *Journal of Computational Physics* **55** (1), 115–128.

Hasselmann, Klaus 1962 On the non-linear energy transfer in a gravity-wave spectrum part 1. general theory. *Journal of Fluid Mechanics* **12** (04), 481–500.

Herbert, Eric, Mordant, Nicolas & Falcon, Eric 2010 Observation of the nonlinear dispersion relation and spatial statistics of wave turbulence on the surface of a fluid. *Physical review letters* **105** (14), 144502.

Hjelmervik, Karina B & Trulsen, Karsten 2009 Freak wave statistics on collinear currents. *Journal of Fluid Mechanics* **637**, 267–284.

Holliday, Dennis 1977 On nonlinear interactions in a spectrum of inviscid gravity–capillary surface waves. *Journal of Fluid Mechanics* **83** (04), 737–749.

Hou, Thomas Y, Lowengrub, John S & Shelley, Michael J 1994 Removing the stiffness from interfacial flows with surface tension. *Journal of Computational Physics* **114** (2), 312–338.

Hung, Li-Ping & Tsai, Wu-Ting 2009 The formation of parasitic capillary ripples on gravity-capillary waves and the underlying vortical structures. *Journal of Physical Oceanography* **39** (2), 263–289.

Ignatowsky, WV 1905 Reflexion elektromagnetisches wellen an einem draht. *Annalen der Physik* **323**, 495–522.

Janssen, Peter AEM 2003 Nonlinear four-wave interactions and freak waves. *Journal of Physical Oceanography* **33** (4), 863–884.

Jiang, Lei, Lin, Huan-Jay, Schultz, William W & Perlin, Marc 1999 Unsteady ripple generation on steep gravity-capillary waves. *Journal of Fluid Mechanics* **386**, 281–304.

Kartashova, Elena A 1990 Partitioning of ensembles of weakly interacting dispersing waves in resonators into disjoint classes. *Physica D: Nonlinear Phenomena* **46** (1), 43–56.

Kelly, Samuel M & Lermusiaux, Pierre FJ 2016 Internal-tide interactions with the gulf stream and middle atlantic bight shelfbreak front. *Journal of Geophysical Research: Oceans* **121** (8), 6271–6294.

Kelly, Samuel M, Lermusiaux, Pierre FJ, Duda, Timothy F & Haley Jr, Patrick J 2016 A coupled-mode shallow water model for tidal analysis: Internal-tide reflection and refraction by the gulf stream. *Journal of Physical Oceanography* (2016).

Kolmakov, GV, Levchenko, AA, Brazhnikov, M Yu, Mezhov-Deglin, LP, Silchenko, AN & McClintock, Peter VE 2004 Quasiadiabatic decay of capillary turbulence on the charged surface of liquid hydrogen. *Physical review letters* **93** (7), 074501.

Kolmogorov, A 1941 The local stucture of turbulence in incompressible viscous fluid for very large reynolds numbers. *Dokl. Akad. Nauk SSSR* **30**, 9.

Korotkevich, Alexander O 2008 Simultaneous numerical simulation of direct and inverse cascades in wave turbulence. *Physical review letters* **101** (7), 074504.

Krasitskii, Vladimir P 1994 On reduced equations in the hamiltonian theory of weakly nonlinear surface waves. *Journal of Fluid Mechanics* **272**, 1–20.

Lamy, Morgan, Le Caillec, Jean-Marc, Garello, René & Kenchaf, A 2004 Short wave spectrum modulation by a surface current field and long waves for sar imaging process simulation. In *Geoscience and Remote Sensing Symposium, 2004. IGARSS'04. Proceedings. 2004 IEEE International*, , vol. 5, pp. 3100–3102. IEEE.

Lavrenov, IV 1998 The wave energy concentration at the agulhas current off south africa. *Natural hazards* **17** (2), 117–127.

Lavrenov, IV & Porubov, AV 2006 Three reasons for freak wave generation in the non-uniform current. *European Journal of Mechanics-B/Fluids* **25** (5), 574–585.

Longuet-Higgins, M.S. 1987 The propagation of short surface waves on longer gravity waves. *Journal of Fluid Mechanics* **177**, 293–306.

Longuet-Higgins, M.S. & Stewart, RW 1960 Changes in the form of short gravity waves on long waves and tidal currents. *Journal of Fluid Mechanics* **8** (04), 565–583.

Longuet-Higgins, Michael S 1963 The generation of capillary waves by steep gravity waves. *J. Fluid Mech* **16** (1), 138–159.

Longuet-Higgins, Michael S 1995 Parasitic capillary waves: a direct calculation. *Journal of Fluid Mechanics* **301**, 79–108.

Longuet-Higgins, Michael S & Stewart, RW 1961 The changes in amplitude of short gravity waves on steady non-uniform currents. *Journal of Fluid Mechanics* **10** (04), 529–549.

Lvov, Yuri V, Polzin, Kurt L & Tabak, Esteban G 2004 Energy spectra of the ocean's internal wave field: Theory and observations. *Physical review letters* **92** (12), 128501.

Majda, AJ, McLaughlin, DW & Tabak, EG 1997 A one-dimensional model for dispersive wave turbulence. *Journal of Nonlinear Science* **7** (1), 9–44.

MALLORY, JOHN KENNAWAY 1974 Abnormal waves on the south east coast of south africa. *The International Hydrographic Review* **51** (2).

MCGOLDRICK, LAWRENCE F 1965 Resonant interactions among capillary-gravity waves. *Journal of Fluid Mechanics* **21** (02), 305–331.

MEI, CHIANG C, STIASSNIE, MICHAEL & YUE, DICK K-P 2005 *Theory and applications of ocean surface waves: nonlinear aspects*, , vol. 23. World Scientific.

MELVILLE, W KENDALL & FEDOROV, ALEXEY V 2015 The equilibrium dynamics and statistics of gravity–capillary waves. *Journal of Fluid Mechanics* **767**, 449–466.

MERKOUNE, D, TOUBOUL, J, ABCHA, N, MOUAZÉ, D & EZERSKY, ALEXANDER 2013 Focusing wave group on a current of finite depth. *Natural Hazards and Earth System Science* **13** (11), 2941–2949.

MILDER, D MICHAEL 1990 The effects of truncation on surface-wave hamiltonians. *Journal of Fluid Mechanics* **217**, 249–262.

MIQUEL, BENJAMIN, ALEXAKIS, ALEXANDROS & MORDANT, NICOLAS 2014 Role of dissipation in flexural wave turbulence: From experimental spectrum to kolmogorov-zakharov spectrum. *Physical Review E* **89** (6), 062925.

MIQUEL, BENJAMIN & MORDANT, NICOLAS 2011 Nonstationary wave turbulence in an elastic plate. *Physical review letters* **107** (3), 034501.

MOIN, PARVIZ 2010 *Fundamentals of engineering numerical analysis*. Cambridge University Press.

MUNK, WALTER H 1955 High frequency spectrum of ocean waves. *JOURNAL OF MARINE RESEARCH* **14** (4), 302–314.

NACIRI, M. & MEI, C. 1992 Evolution of a short surface wave on a very long surface wave of finite amplitude. *Journal of Fluid Mechanics* **235**, 415–452.

NEWELL, ALAN C & RUMPF, BENNO 2011 Wave turbulence. *Annual Review of Fluid Mechanics* **43**, 59–78.

NICHOLLS, DAVID P & REITICH, FERNANDO 2001 Stability of high-order perturbative methods for the computation of dirichlet–neumann operators. *Journal of Computational Physics* **170** (1), 276–298.

NWOGU, OKEY G 2009 Interaction of finite-amplitude waves with vertically sheared current fields. *Journal of Fluid Mechanics* **627**, 179–213.

ÖLMEZ, HS & MILGRAM, JH 1995*a* Nonlinear energy transfer to short gravity waves in the presence of long waves. *Journal of Fluid Mechanics* **289** (1), 199–226.

ÖLMEZ, HS & MILGRAM, JH 1995*b* Nonlinear energy transfer to short gravity waves in the presence of long waves. *Journal of Fluid Mechanics* **289**, 199–226.

Onorato, Miguel, Osborne, AR, Serio, M a al, Resio, D, Pushkarev, A, Zakharov, Vladimir E & Brandini, C 2002 Freely decaying weak turbulence for sea surface gravity waves. *Physical review letters* **89** (14), 144501.

Onorato, Miguel, Proment, Davide & Toffoli, Alessandro 2011 Triggering rogue waves in opposing currents. *Physical review letters* **107** (18), 184502.

Pan, Yulin & Yue, Dick KP 2014 Direct numerical investigation of turbulence of capillary waves. *Physical review letters* **113** (9), 094501.

Pan, Yulin & Yue, Dick KP 2015 Decaying capillary wave turbulence under broad-scale dissipation. *Journal of Fluid Mechanics* **780**, R1.

Perlin, Marc, Lin, Huanjay & Ting, Chao-Lung 1993 On parasitic capillary waves generated by steep gravity waves: an experimental investigation with spatial and temporal measurements. *Journal of Fluid Mechanics* **255** (1), 597–620.

Phillips, OM 1959 The scattering of gravity waves by turbulence. *Journal of Fluid Mechanics* **5** (02), 177–192.

Phillips, OM 1981 Dispersion of short wavelets in the presence of a dominant long wave. *Journal of Fluid Mechanics* **107**, 465–85.

Phillips, OM 1985 Spectral and statistical properties of the equilibrium range in wind-generated gravity waves. *Journal of Fluid Mechanics* **156**, 505–531.

Piscopia, R, Polnikov, V, DeGirolamo, P & Magnaldi, S 2003 Validation of the three-wave quasi-kinetic approximation for the spectral evolution in shallow water. *Ocean Engineering* **30** (5), 579–599.

Punzmann, Horst, Francois, Nicolas, Xia, Hua, Falkovich, Gregory & Shats, Michael 2014 Generation and reversal of surface flows by propagating waves. *Nature Physics* **10** (9), 658–663.

Pushkarev, A, Resio, D & Zakharov, V 2003 Weak turbulent approach to the wind-generated gravity sea waves. *Physica D: Nonlinear Phenomena* **184** (1), 29–63.

Pushkarev, AN & Zakharov, VE 1996 Turbulence of capillary waves. *Physical review letters* **76** (18), 3320–3323.

Pushkarev, AN & Zakharov, VE 2000 Turbulence of capillary waves Ů theory and numerical simulation. *Physica D: Nonlinear Phenomena* **135** (1), 98–116.

Russel, J Scott 1838 Report of the committee on waves. *Rept. Brit. Assoc. Advancement Sci* **8** (417-496), 14.

Shyu, Jinn-Hwa & Phillips, OM 1990 The blockage of gravity and capillary waves by longer waves and currents. *Journal of Fluid Mechanics* **217**, 115–141.

Simons, Richard R, Grass, Anthony J & Kyriacou, Andreas 1988 The influence of currents on wave attenuation. *Coastal Engineering Proceedings* **1** (21).

Smith, Ronald 1976 Giant waves. *Journal of Fluid Mechanics* **77** (03), 417–431.

Stiassnie, Michael, Agnon, Yehuda & Shemer, Lev 1991 Fractal dimensions of random water surfaces. *Physica D: Nonlinear Phenomena* **47** (3), 341–352.

Stiassnie, Michael & Shemer, Lev 1984 On modifications of the zakharov equation for surface gravity waves. *Journal of Fluid Mechanics* **143**, 47–67.

Trulsen, Gerd N, Dysthe, Kristian B & Trulsen, Jan 1990 Evolution of a gravity wave spectrum through a current gradient. *Journal of Geophysical Research: Oceans* **95** (C12), 22141–22151.

Tsai, Wu-ting & Hung, Li-ping 2010 Enhanced energy dissipation by parasitic capillaries on short gravity-capillary waves. *Journal of Physical Oceanography* **40** (11), 2435–2450.

Watson, KENNETH M 1999 Interaction of capillary waves with longer waves. part 2. applications to waves in two surface dimensions and to waves in shallow water. *Journal of Fluid Mechanics* **397**, 99–117.

Watson, Kenneth M & Buchsbaum, Steven B 1996 Interaction of capillary waves with longer waves. part 1. general theory and specific applications to waves in one dimension. *Journal of Fluid Mechanics* **321** (1), 87–120.

Watson, Kenneth M & Mcbride, John B 1993 Excitation of capillary waves by longer waves. *Journal of Fluid Mechanics* **250**, 103–119.

West, Bruce J, Brueckner, Keith A, Janda, Ralph S, Milder, D Michael & Milton, Robert L 1987 A new numerical method for surface hydrodynamics. *Journal of Geophysical Research* **92** (C11), 11803–11.

White, Benjamin S & Fornberg, Bengt 1998 On the chance of freak waves at sea. *Journal of fluid mechanics* **355**, 113–138.

Wright, W.B., Budakian, R. & Putterman, S.J. 1996 Diffusing light photography of fully developed isotropic ripple turbulence. *Physical review letters* **76** (24), 4528–4531.

Wu, Chin H & Yao, Aifeng 2004 Laboratory measurements of limiting freak waves on currents. *Journal of Geophysical Research: Oceans* **109** (C12).

Wu, Guangyu 2004 Direct simulation and deterministic prediction of large-scale nonlinear ocean wave-field. PhD thesis, Massachusetts Institute of Technology.

Xia, H., Shats, M. & Punzmann, H. 2010 Modulation instability and capillary wave turbulence. *EPL (Europhysics Letters)* **91** (1), 14002.

Xiao, Wenting, Liu, Yuming, Wu, Guangyu & Yue, Dick KP 2013 Rogue wave occurrence and dynamics by direct simulations of nonlinear wave-field evolution. *Journal of Fluid Mechanics* **720**, 357–392.

Zakharov, V 1999 Statistical theory of gravity and capillary waves on the surface of a finite-depth fluid. *European Journal of Mechanics-B/Fluids* **18** (3), 327–344.

Zakharov, VE 2010 Energy balance in a wind-driven sea. *Physica Scripta* **2010** (T142), 014052.

Zakharov, Vladimir, Dias, Frédéric & Pushkarev, Andrei 2004 One-dimensional wave turbulence. *Physics Reports* **398** (1), 1–65.

Zakharov, VE & Filonenko, NN 1966 The energy spectrum for stochastic oscillation of a fluid surface. *Dokl. Akad. Nauk SSSR* **170**, 1292–1295.

Zakharov, VE & Filonenko, NN 1967 Weak turbulence of capillary waves. *Journal of Applied Mechanics and Technical Physics* **8**, 62–67.

Zakharov, VE, L'vov, VS & Falkovich, G 1992 Kolmogorov spectra of turbulence: Wave turbulence. *Springer, ISBN: 3-540-54533-6* .

Zakharov, Vladimir E 1968 Stability of periodic waves of finite amplitude on the surface of a deep fluid. *Journal of Applied Mechanics and Technical Physics* **9** (2), 190–194.

Zaslavskii, MM & Polnikov, VG 1998 Three-wave quasi-kinetic approximation in the problem of the evolution of a spectrum of nonlinear gravity waves at small depths. *Izvestiya, Atmospheric and Oceanic Physics* **34**, 609–616.

Zhang, Jun, Hong, Keyyong & Yue, Dick KP 1993 Effects of wavelength ratio on wave modelling. *Journal of Fluid Mechanics* **248**, 107–127.

Zhang, J. & Melville, WK 1990 Evolution of weakly nonlinear short waves riding on long gravity waves. *Journal of Fluid Mechanics* **214** (1), 321–346.

Zhang, J. & Melville, WK 1992 On the stability of weakly nonlinear short waves on finite-amplitude long gravity waves. *Journal of Fluid Mechanics* **243** (1), 51–72.

Zhang, Xin 1995 Capillary-gravity and capillary waves generated in a wind wave tank: Observations and theories. *Journal of Fluid Mechanics* **289**, 5–28.

Zhang, Xin 2002 Enhanced dissipation of short gravity and gravity capillary waves due to parasitic capillaries. *Physics of Fluids* **14**, L81.